Universidad Nacional de la Patagonia San Juan Bosco

Doctorado en Ciencias de la Ingeniería - Facultad de Ingeniería

École des Ponts ParisTech

Ecole Doctorale Sciences, Ingénierie et Environnement

TESIS DOCTORAL

Effect of a biopolymer on the mechanical and microstructural behaviour of oil well cement for CO_2 geological storage

---

Juan Cruz Barría

Ingeniero Civil

Diciembre 2021

Universidad Nacional de la Patagonia San Juan Bosco

Doctorado en Ciencias de la Ingeniería - Facultad de Ingeniería

École des Ponts ParisTech

Ecole Doctorale Sciences, Ingénierie et Environnement

DOCTORAL THESIS

Effect of a biopolymer on the mechanical and microstructural behaviour of oil well cement for CO_2 geological storage

---

Juan Cruz Barría

Civil Engineer

Director UNPSJB:

Dr. Ing. Diego Manzanal

Co-Director UNPSJB:

Dra. Ing. Analía Vázquez

Director ENPC:

Dr. Ing. Jean-Michel Pereira

Co-Director ENPC:

Dr. Ing. Siavash Ghabezloo

December 2021

Universidad Nacional de la Patagonia San Juan Bosco

Doctorado en Ciencias de la Ingeniería - Facultad de Ingeniería

École des Ponts ParisTech

Ecole Doctorale Sciences, Ingénierie et Environnement

TESIS DOCTORAL

Effect of a biopolymer on the mechanical and microstructural behaviour of oil well cement for CO_2 geological storage

---

Juan Cruz Barría

Ingeniero Civil

Tribunal nombrado por la Comisión de Doctorado de la Facultad de Ingeniería de la Universidad Nacional de la Patagonia San Juan Bosco :

Prof. J. Carlos Santamarina	KAUST	Presidente
Prof. Antonin Fabbri	Ecole Nationale des Travaux Publics de l'Etat	Vocal
Prof. Celina Bernal	ITPN - CONICET	Vocal
Dr. Martín Sánchez	Y-TEC	Vocal
Dr. Teresa Pique	Universidad de Buenos Aires	Secretaria

Acknowledgement

I am very grateful to my supervisors, Prof. Diego Manzanal and Prof. Jean-Michel Pereira for their guidance, experience and advice during this long journey. Without them this work could not be accomplished. I also thank my previous supervisor, Prof. Analía Vázquez for her support during my first steps. I also thank my co-supervisor Prof. Nicolas Foix for his collaboration, and Dr. Siavash Ghabezloo for his enriching talks.

I thank the thesis examining committee, Prof. J. Carlos Santamarina, Dr. Antonin Fabbri, Dr. Celina Bernal, Dr. Martín Sánchez, and Dr. Teresa Piqué, as well as to the doctoral committee of the UNPSJB led by Dr. Adriana Pajares.

I express my sincere gratitude to the Universidad Nacional de la Patagonia San Juan Bosco (UNPSJB), the Engineering Faculty, and the Rector's Office for their support during the development of this thesis. I also extend this acknowledgement to the École Nationale des Ponts et Chaussées (ENPC), where I had the opportunity to do the Ph.D. in co-supervision.

I am most grateful to the National Scientific and Technical Research Council of Argentina (CONICET) for giving me the opportunity to start my Ph.D. career. I also thank the French Consulate in Argentina and the Ministère de l'Europe et des Affaires étrangères of France for the Eiffel Excellence Scholarship Program of 2018 and the Saint-Exupéry Scholarship 2020-2021.

I would like to make special mention to the support received through the DISCO2 STORE project, which currently involves a large network of researchers from different countries collaborating on climate change mitigation.

The Soils, Concrete and Asphalt Laboratory of the UNPSJB has always provided support from the beginning of my thesis, for which I thank all its staff, especially Alejandra and Oscar. I would like to thank Alberto, Oscar and the staff of Petroquímica Comodoro Rivadavia S.A. for having received us warmly, and for having collaborated with the materials and equipment needed for this work.

I thank the entire CERMES team and the Navier Laboratory of the ENPC for having welcomed me and helped me during all my laboratory experiences. I am happy to have met excellent people and new friends who supported me in times of anguish and joy during my thesis.

The support of my family was a great driving force to continue along this journey, for which I will always be enormously grateful.

Abstract

Storing CO_2 in deep underground reservoirs is key to reducing emissions to the atmosphere and standing against climate change. However, the risk of CO_2 leakage from geological reservoirs to other rock formations requires a careful long-term analysis of the system. Essentially, oil well cement used for the operation must withstand the carbonation process that changes its poromechanical behaviour over time, possibly affecting the system's integrity.

The use of nanoadditives for cement, such as bacterial nanocellulose (BNC), has been increasing in recent years. This biopolymer has particular properties, like high mechanical properties and thermal resistance, that can improve cement performance. For this reason, and in light of the problems that carbonation may pose in the long term in the context of geological storage of CO_2, studies were carried out under supercritical CO_2 conditions analyzing the behaviour of cement with nanocellulose additions.

Rheological, mechanical, thermal, and microstructural tests were performed on samples with different percentages (0%, 0.05%, 0.10%, 0.15%, 0.20%) of bacterial nanocellulose (BNC). 11 free fluid and 6 thickening-time tests were performed to characterize the slurry with BNC. The mechanical behaviour of the hardened state was investigated through the dynamical mechanical analysis (DMA) of 20 samples, measurements of 32 elastic ultrasound waves, 84 unconfined compressive strength (UCS) and 24 triaxial experiments (20 isotropic and 4 compressive tests). A total of 64 cylindrical specimens were subjected to supercritical CO_2 conditions (20 MPa and 90 °C) for 30 and 120 days with several percentages of nanocellulose using two curing methods, one long-term curing at low temperature (36 specimens) and one short-term curing at high temperature (32 specimens). The microstructure and crystalline characterization were studied by means of thermogravimetric analysis (TGA) of 9 samples, mercury intrusion porosimetry (MIP) of 52 samples, water porosity of 60 samples, scanning electron microscopy (SEM) of 6 samples, and X-ray diffraction (XRD) of 10 samples.

These results showed that BNC produces an increase in slurry viscosity but retains a greater amount of water which aids in its subsequent hydration. This could be observed in its microstructure, where a higher degree of hydration, and a decrease in porosity were observed. This increase in hydration was likely the reason why cements with nanocellulose had a uniaxial compressive strength up to 20% higher than neat cement. It was also observed that higher BNC contents improve the thermo-mechanical behaviour under oscillating bending stress.

After carbonation, the microstructure shows that the capillary porosity decreases steadily to values of 5%, which reduces the penetration of carbonic acid into the sample. All cements showed a reduction in mechanical strength, but cements with BNC had a lower degree of

carbonation and better mechanical behaviour, because of the lower capillary porosity prior to carbonation.

However, these effects were not observed when the cement was subjected to a curing process under unfavorable conditions at high temperatures. In this case, the large increase in porosity dulls the short-term hydration effects, and the strength of cements with nanocellulose is lower than neat cement prior to the carbonation process. After carbonation, a relative increase in the strength of the specimens with BNC is higher, however, it is still below the strength of neat cement.

These experimental studies were simulated using a coupled chemo-hydro-mechanical model. The model simulates the carbonation front advance in cement subjected to supercritical CO_2 and the changes generated by the chemical reactions using the classic balance equations of porous continua based on conservation of mass and momentum. Simultaneous dissolution of portlandite and C-S-H, dissolution of calcite, and a damage model were added to the existing code. The carbonation progress of the specimens was represented and extrapolation was made to an oil well based on the parameters obtained from the experiments and simulations.

Keywords: oil well cement, supercritical carbonation, mechanical strength, microstructure, modeling

Résumé

Le stockage du CO_2 dans des réservoirs géologiques profonds est essentiel pour réduire les émissions dans l'atmosphère et lutter contre le changement climatique. Toutefois, le risque de fuite de CO_2 des réservoirs géologiques vers d'autres formations rocheuses implique une analyse minutieuse du système à long terme. Principalement, le ciment des puits pétroliers utilisé pour l'opération doit résister au processus de carbonatation qui modifie son comportement poromécanique au fil du temps, ce qui peut affecter l'intégrité du système.

L'utilisation de nanoadditifs pour le ciment, comme la nanocellulose bactérienne (BNC), a augmenté ces dernières années. Ce biopolymère possède des propriétés particulières, telles que des propriétés mécaniques élevées et une résistance thermique, qui peuvent améliorer les performances du ciment. Pour cette raison, et à la lumière des problèmes que la carbonatation peut poser à long terme dans le contexte du stockage géologique du $_2$, des études ont été menées dans des conditions de $_2$ supercritique pour analyser le comportement du ciment avec des ajouts de nanocellulose.

Des essais rhéologiques, mécaniques, thermiques et microstructurels ont été réalisés sur des échantillons contenant différents pourcentages (0%, 0,05%, 0,10%, 0,15%, 0,20%) de nanocellulose bactérienne (BNC). Des essais de fluide libre et de temps d'épaississement ont été réalisés pour caractériser la suspension avec BNC. Le comportement mécanique de l'état durci a été étudié par l'analyse mécanique dynamique (DMA), les mesures des ondes ultrasonores élastiques, la résistance à la compression non confinée (UCS) et les expériences triaxiales. Ensuite, des échantillons cylindriques ont été soumis à des conditions de CO_2 supercritique (20 MPa et 90 °C) pendant 30 et 120 jours avec plusieurs pourcentages de nanocellulose en utilisant deux méthodes de durcissement, un durcissement à long terme à basse température et un durcissement à court terme à haute température. La microstructure et la caractérisation cristalline ont été étudiées par analyse thermogravimétrique (TGA), porosimétrie par intrusion de mercure (MIP), porosité à l'eau, microscopie électronique à balayage (SEM) et diffraction des rayons X (XRD).

Ces résultats montrent que la BNC produit l'augmentation de la viscosité du coulis mais retient une plus grande quantité d'eau, ce qui facilite son hydratation ultérieure. Cela a pu être observé dans sa microstructure, où un degré d'hydratation plus élevé, et une diminution de la porosité ont été observés. Il est probable que cette augmentation de l'hydratation soit la raison pour laquelle les ciments contenant de la nanocellulose ont une résistance à la compression uniaxiale jusqu'à 20% supérieure à celle du ciment ordinaire. Il a également été observé que des teneurs plus élevées en BNC améliorent le comportement thermo-mécanique sous une contrainte de flexion oscillante.

Après carbonatation, la microstructure montre que la porosité capillaire diminue régulièrement jusqu'à des valeurs de 5%, ce qui réduit la pénétration de l'acide carbonique dans

l'échantillon. Tous les ciments ont montré une réduction de la résistance mécanique, mais les ciments avec BNC ont eu un degré de carbonatation plus bas et un meilleur comportement mécanique, en raison de la porosité capillaire plus basse avant la carbonatation.

Cependant, ces effets n'ont pas été observés lorsque le ciment a été soumis à un processus de durcissement dans des conditions défavorables à haute température. Dans ce cas, la forte augmentation de la porosité atténue les effets de l'hydratation à court terme et la résistance des ciments avec nanocellulose est plus faible avant le processus de carbonatation. Après la carbonatation, une augmentation relative de la résistance des échantillons avec BNC est plus élevée, cependant, elle reste inférieure à la résistance du ciment ordinaire.

Ces études expérimentales ont été simulées à l'aide d'un modèle chimio-hydro-mécanique couplé. Le modèle simule l'avancée du front de carbonatation dans le ciment soumis au $_2$ supercritique et les changements générés par les réactions chimiques en utilisant les équations de conservation classiques des milieux continus relatives à la masse et à la quantité de mouvement. La dissolution simultanée de la portlandite et du C-S-H, la dissolution de la calcite et un modèle d'endommagement ont été considérés. La progression de la carbonatation des échantillons a été représentée et une extrapolation a été faite à un puits pétroliers sur la base des paramètres obtenus à partir des expériences et des simulations.

Mots-clefs: Ciment de puits pétroliers, carbonatation supercritique, résistance mécanique, microstructure, modélisation

Contents

1 Introduction **1**

1.1 Context and motivation 1

1.2 Objectives and outline of the work 2

2 Literature review **5**

2.1 Carbon capture and storage (CCS) 5

2.1.1 A climate change technology 5

2.1.2 Challenges to overcome 7

2.2 Oil well cement 10

2.2.1 Fundamental roles of cement in the oil and gas industry 10

2.2.2 Clinker production and chemical composition 12

2.2.3 Cement hydration 13

2.2.4 API cement testing 18

2.2.5 Mechanical properties of cement 19

2.2.6 Carbonation process 22

2.3 Bacterial nanocellulose (BNC) 29

2.3.1 Introduction 29

2.3.2 BNC Characteristics 29

2.3.3 Feasibility of using nanocellulose as a cement additive 30

3 Materials and experimental methods **33**

3.1 Introduction 33

3.2 Materials 33

3.3 Experimental methods 36

3.3.1 Free fluid test 36

3.3.2 Thickening-time test 37

3.3.3 Dynamical mechanical analysis (DMA) 38

3.3.4 Measurement of elastic ultrasound waves 39

3.3.5 Unconfined compressive strength (UCS) 40

3.3.6 Triaxial experiments 41

3.3.7 Supercritical carbonation test 43

3.3.8 Thermogravimetric analysis (TGA) 45

3.3.9 Mercury intrusion porosimetry (MIP) . . . 46
3.3.10 Water porosity . . . 48
3.3.11 Scanning electron microscopy (SEM) . . . 48
3.3.12 X-ray diffraction (XRD) . . . 49

4 Results and Discussion **51**
4.1 Introduction . . . 51
4.2 Effect of bacterial nanocellulose on non-carbonated cement . . . 51
4.2.1 Free fluid test . . . 51
4.2.2 Thickening-time test . . . 53
4.2.3 Dynamical mechanical analysis (DMA) . . . 54
4.2.4 Unconfined compressive strength (UCS) . . . 58
4.2.5 Triaxial experiments . . . 60
4.2.6 Thermogravimetric analysis (TGA) . . . 64
4.2.7 Mercury intrusion porosimetry (MIP) . . . 66
4.2.8 Conclusion . . . 67
4.3 Effect of bacterial nanocellulose on carbonated cement . . . 68
4.3.1 Supercritical carbonation test . . . 68
4.3.2 Microstructural analysis . . . 72
4.3.3 Porosity measurements by oven drying and porosity variation over time 77
4.3.4 Unconfined compressive strength (UCS) . . . 81
4.3.5 Triaxial tests on carbonated samples . . . 85
4.3.6 X-ray diffraction (XRD) . . . 88
4.3.7 Conclusion . . . 93
4.4 High temperature curing effect and carbonation . . . 95
4.4.1 Supercritical carbonation test . . . 95
4.4.2 Mercury intrusion porosimetry (MIP) and total porosity . . . 97
4.4.3 Measurement of elastic ultrasound waves and unconfined compressive strength (UCS) . . . 102
4.4.4 X-ray diffraction (XRD) . . . 105
4.4.5 Conclusion . . . 108
4.5 Integral assessment of the cement properties obtained . . . 110
4.5.1 Microstructure and mechanical behaviour . . . 110
4.5.2 Permeability estimation . . . 112
4.5.3 Comparative overview . . . 114

5 Modeling the carbonation process **115**
5.1 Introduction . . . 115
5.2 Carbonation degree . . . 115

5.3 Chemo-poro-mechanical model . . . 117
5.3.1 Fundamentals . . . 117
5.3.2 Homogenization of the poroelastic parameters . . . 120
5.3.3 Isotropic damage . . . 121
5.3.4 Damage evolution . . . 121
5.3.5 Dissolution and precipitation of CH, C-S-H and $C\bar{C}$ . . . 122
5.3.6 Modeling in cement cured at room temperature . . . 126
5.3.7 Modeling cements with bacterial nanocellulose cured at reservoir temperature . . . 134
5.3.8 Conclusion . . . 139

6 Conclusions and perspectives **141**
6.1 Conclusions . . . 141
6.2 Perspectives . . . 144

Bibliography **145**

A Appendix **163**
A.1 Unconfined compressive strength (UCS) . . . 163
A.2 Isotropic experiments . . . 164
A.3 Triaxial experiments . . . 167
A.4 Measurement of elastic ultrasound waves . . . 169
A.5 Density variation after supercritical carbonation . . . 170
A.6 Water Porosity . . . 172

List of Figures

1.1 Testing methodology to study the effect of BNC on cement. All microstructural tests are included in Figure 1.2. . . . 3
1.2 Testing methodology to study the effect of carbonation. . . . 3

2.1 Historical record of global CO_2 emissions compared with various projections [7]. 5
2.2 Geological storage options for CO_2. Courtesy of CO2CRC Ltd. . . . 6
2.3 Carbon capture, transport and storage. Courtesy of CO2CRC Ltd. . . . 7
2.4 Plume generated by the injection process and CO_2-water capillary meniscus at the reservoir-caprock interface (after Espinoza et al. [17]). . . . 8
2.5 Diagram of possible leakage pathways through an abandoned well (after Gasda et al. [22]). . . . 9
2.6 Schematic of a cementing operation (after Adjei et al. [23]) . . . 10
2.7 CO_2 phase diagram (after Zhang et al. [34]). . . . 11
2.8 CO_2 attack on cement sheath. . . . 12
2.9 Cement hydration rate periods (after Vázquez et al. [42]). . . . 15
2.10 Strength and heat of hydration of the main cement components (after Niño Hernández et al. [43]). . . . 15
2.11 (a) API mixer, (b) pressurized consistometer, (c) atmospheric consistometer and (d) free fluid diagram. . . . 18
2.12 Strength development as a function of curing temperature (results of cubic specimens of class G cement.). . . . 20
2.13 (A) Porosity and incremental pore volume as a function of temperature after 28 days of curing, (B) Variation of porosity and incremental pore volume as a function of time for samples cured at 20 °C (after Bahafid [60]). . . . 21
2.14 Migration of ions along carbonation and precipitation fronts. The chemical reactions in the figure are given using industry notations. $Ca(OH)_2$ is CH and porous silica is $AmSi$ (after Kutchko et al. [69]). . . . 23
2.15 Volumetric proportions of an elementary volume of the cementitious matrix (after Bagheri et al. [80]). . . . 24
2.16 (a) Uncarbonated cement (b) Carbonated cement (after Shah et al. [68]). . . . 25
2.17 Carbonation breakthrough in specimens subjected to carbonated brine (after Kutchko et al. [69]). . . . 26

2.18 Carbonation breakthrough in specimens subjected to wet $scCO_2$ (After Kutchko et al. [69]). 27
2.19 Reaction zones for samples run with influent pH 2.4 (After Duguid et al. [82]). 28
2.20 *Gluconacetobacter xylinus* bacteria and bacterial nanocellulose (after Cerrutti et al. [103]). 30
2.21 Flexural strength and degree of hydration of cement for different CNF contents. (after Sun et al. [112, 117]). 31
2.22 Schematic of the generation of bacterial nanocellulose network (NC) among cement hydration products (after Hisseine et al. [125]). 32

3.1 (a) BNC in sealed jars, (b) BNC wet-grounded and mixed together with additional water, (c) ultrasonic bath, and (d) BNC final additive. 34
3.2 (a) API mixer (b) uniaxial compression test. 40
3.3 Carbonation system 44

4.1 Free fluid content for different percentages of superplasticizer for Portland Cement (PC) and PC + 0.05% BNC. 52
4.2 Consistometry test for Portland Cement (PC), slurry with 0.05% of BNC + 0.35% SP, and slurry with 0.05% BNC + 0.40% SP. 54
4.3 DMA results of Portland Cement (PC) and PC modified with BNC at 0.05%, 0.10%, 0.15% and 0.20% BWOC samples cured for 28 days. 55
4.4 Normalized storage modulus of Portland Cement (PC) and PC modified with BNC at 0.05%, 0.10%, 0.15% and 0.20% BWOC samples cured for 28 days. . 56
4.5 DMA results in term of tan δ of Portland Cement (PC) and PC modified with BNC at 0.05%, 0.10%, 0.15% and 0.20% BWOC samples cured for 28 days. . 57
4.6 Normalized compressive strength of Portland Cement (PC) and modified cement cured for 7 and 28 days according to the percentage of nanocellulose: Diamonds symbols represent samples cured for 7 days and squares symbols represent samples with 28 days of curing. The values have been normalized to the strength value obtained after 7 days of curing in PC cement. 58
4.7 Unconfined compressive strength for of Portland Cement (PC) and PC modified with BNC at 0.05%, 0.10%, 0.15% and 0.20% BWOC samples at three curing times: 1 day, 7 days and 28 days. 59
4.8 Isotropic compression tests. The Kd and Ku moduli are determined by curve fitting these results. 60
4.9 Bulk modulus of drained (Kd) and undrained (Ku) tests on non-carbonated (NC) PC and 0.05%-BNC cement samples. Results are shown as a function of the initial confinement pressure of each test. 61

4.10 Deviatoric test on non-carbonated (NC) samples. The pore pressure u is the initial value before loading. The legend shows the type of strain, the tested specimen, and the confining pressure value (σ_3). 63
4.11 (a) Example of mass loss calculation for CH in the TGA test (b)TGA result for Portland Cement (PC) and PC modified with BNC at 0.05%, 0.10%, 0.15% and 0.20% BWOC. 64
4.12 DrTGA results for Portland Cement (PC) and cement with BNC at 0.05%, 0.10%, 0.15% and 0.20% BWOC. 65
4.13 Cumulative porosity and pore size distribution of PC, BNC05 and BNC15 in non-carbonated samples. Results are shown up to values of 0.006 μm 67
4.14 Cross section of PC (longitudinal on the left and radial at the top) and BNC05 (longitudinal on the right and radial at the bottom) samples after 120 days of carbonation. 69
4.15 Variation in the coloration of carbonated samples at 30 and 120 days. 71
4.16 Cumulative porosity and pore size distribution of PC before and after 30 and 120 days of carbonation. 72
4.17 Cumulative porosity and pore size distribution of BNC05 before and after 30 and 120 days of carbonation. 73
4.18 Cumulative porosity and pore size distribution of BNC15 before and after 30 and 120 days of carbonation. 74
4.19 Carbonation front of BNC15 after 120 days of carbonation. 75
4.20 Pore size distribution variation in time for a point near the exposed surface of PC samples. Non-carbonated (Time 1), 30 days of carbonation (Time 2) and 120 days of carbonation (Time 3). 76
4.21 The outer rim shows larger calcite crystals in a more porous zone, while the carbonated zone shows fewer voids because the dissolution front has not yet reached this zone. 78
4.22 Total porosity of samples carbonated after 120 days (PC, BNC05, BNC15). . . 79
4.23 Variation of total, capillary and gel porosities over time for samples PC, BNC05 and BNC15 for 30 days and 120 days of carbonation (near the exposed surface) 80
4.24 Development of the compressive strength (red) and Young's modulus (blue) of PC (a), BNC05 (b) and BNC15 (c) over the carbonation time. 81
4.25 Cracks formed around a pore with calcium carbonate growth. 83
4.26 Cement samples being filled with calcium carbonates after 120 days of carbonation. 83
4.27 Pore with bacterial nanocellulose in carbonated cement (BNC15). A small network linking different vertices of the cement structure can be observed. . . 84

4.28 Bulk modulus of drained (Kd) and undrained (Ku) tests on carbonated (C) samples. Results are shown as a function of the initial confinement pressure of each test. 86
4.29 Edge exposed to CO_2 in supercritical state after 120 days of carbonation. It is observed that the zone closer to the surface has more voids, indicating that $CaCO_3$ is dissolving. 87
4.30 Structure of carbonated cement after 120 days. The precipitation of $CaCO_3$ crystals generates a zone with low porosity. 88
4.31 XRD patterns at the core (Int) and near the outer rim (Ext) of PC and BNC15 samples exposed to supercritical CO_2 for 120 days. 89
4.32 Non-carbonated cement structure. The images show portlandite crystals surrounded by C-S-H. 90
4.33 TGA results for Portland Cement (PC) and BNC05 near the exposed surface of samples carbonated for 120 days. 91
4.34 (a) Structure of the carbonated cementitious matrix (b) Types of calcium carbonate crystals (c) Carbonation zones of the cement (d) Calcite crystal in carbonated cementitious matrix. 92
4.35 TGA results for PC and BNC05 at the core of samples carbonated for 120 days. 93
4.36 Samples cured at 90 °C and carbonated for 30 days (left: PC, and right: BNC05). 96
4.37 Cracks in samples of cement cured under unfavorable conditions and carbonated for 120 days. 97
4.38 Pore size distribution of oven-dried (curing method B) and freeze-dried samples. 98
4.39 Pore size distribution of 30-days carbonated and non-carbonated PC samples cured at 90 °C. The red curve corresponds to the cement core, while the green curve corresponds to a sector near the exposed surface. 99
4.40 Pore size distribution of 30-days carbonated and non-carbonated BNC05 samples cured at 90 °C. The red curve corresponds to the cement core, while the green curve corresponds to a sector near the exposed surface. 99
4.41 Pore size distribution of 120-days carbonated and non-carbonated PC samples cured at 90 °C. The red curve corresponds to the cement core, while the green curve corresponds to a sector near the exposed surface. 100
4.42 Pore size distribution of 120-days carbonated and non-carbonated BNC05 samples cured at 90 °C. The red curve corresponds to the cement core, while the green curve corresponds to a sector near the exposed surface. 101
4.43 Compressive strength after carbonation of PC and BNC05 samples for 30 and 120 days. 103
4.44 Young's Modulus after carbonation of PC and BNC05 samples for 30 and 120 days. 103

4.45 XRD patterns of non-modified cement (PC) and modified cement (BNC05) cured at 90°C before carbonation (NC), and after 30-days of carbonation (C). 105
4.46 BNC05 carbonated for 120 days. The image below shows a zoom of the red rectangle. 106
4.47 Zoom of a BNC05 sample carbonated for 120 days. 107
4.48 Crystal growth inside pores. BNC05 sample cured at 90 °C and carbonated for 120 days. 107
4.49 Crystal growth inside pores. BNC05 sample cured at 90 °C and carbonated for 120 days. 108
4.50 Effect of carbonation on porosity and mechanical strength of specimens cured at low temperature for 28 days. 110
4.51 Effect of carbonation on chemical composition and bulk modulus of specimens cured at low temperature for 28 days. (Data from Section 4.3) 111

5.1 Results of the carbonation degree and extrapolation to 100 years for PC, BNC05 and BNC15. 117
5.2 1D cement carbonation model. 125
5.3 Volumetric proportions of the 1D carbonation model. 125
5.4 Variation in the number of moles as a function of time. These results are those obtained at the outer edge in contact with supercritical CO_2. 126
5.5 2D model representation of one-quarter sample subjected to carbonation using the code BIL. Case (a) uniaxial test. Case (b) supercritical carbonation. 127
5.6 Uniaxial compressive stress for a non-carbonated sample. 128
5.7 Total displacements in the X and Y direction. 129
5.8 Behaviour of the elastic modulus when damage is applied to the sample. . . . 129
5.9 Behaviour of the compressibility modulus when damage is applied to the sample. 130
5.10 Variation of the modulus of compressibility as a function of damage. 131
5.11 Damage evolution under uniaxial loading. 131
5.12 CO_2 concentration and capillary porosity after 30 days of supercritical carbonation. 132
5.13 Number of moles of portlandite, C-S-H and calcite after 30 days of supercritical carbonation. 133
5.14 Variation in uniaxial strength after 30 days of carbonation. 133
5.15 Left: Results of the simulation showing the variation of porosity in the experimental BNC05 sample of 38 mm by 78 mm for values of $k_0 = 350$ and $d^0_{eff} = 160$. Right: Results of porosity in 1D. 137

5.16 Dissolution and carbonation fronts development over time. The blue line corresponds to the starting point of the chemical reaction of CH, while the red line is the limit between the carbonation process and where the hydrated products have already been completely carbonated 138
5.17 Permeability variation over time along the annular cement thickness of 3/4 inch 139

A.1 Isotropic triaxial tests on non-carbonated specimens (undrained tests) 164
A.2 Isotropic triaxial tests on non-carbonated specimens (drained tests) 165
A.3 Isotropic undrained tests. The slopes correspond to Skempton coefficient B . . 166
A.4 Undrained triaxial test on DEV-00-U (σ_3 = 14 MPa) 167
A.5 Undrained triaxial test on DEV-00-U (σ_3 = 30 MPa) 167
A.6 Undrained triaxial test on DEV-05-U (σ_3 = 30 MPa) 168
A.7 Undrained triaxial test on DEV-15-U (σ_3 = 30 MPa) 168

List of Tables

2.1 Cement composition . . . 13
2.2 Main components of anhydrous cement. . . . 13
2.3 Main components of hydrated cement. . . . 17
2.4 Secondary components of hydrated cement. . . . 17

3.1 Class G cement composition. . . . 34
3.2 Bacterial Nanocellulose content in cement paste. . . . 36
3.3 Free fluid experiments. . . . 37
3.4 Consistometry experiments. . . . 38
3.5 DMA experiments. . . . 39
3.6 UWM on specimens cured at 90 °C. . . . 39
3.7 UCS experiments on cubic specimens. . . . 40
3.8 UCS experiments on cylindrical specimens. . . . 41
3.9 Triaxial experiments. . . . 43
3.10 Carbonation experiments. . . . 45
3.11 TGA experiments on non-carbonated samples. . . . 46
3.12 TGA experiments on carbonated samples. . . . 46
3.13 MIP experiments on samples cured at 20 °C. . . . 47
3.14 MIP experiments on samples cured at 90 °C. . . . 47
3.15 Water porosity test on samples cured at 20 °C. . . . 48
3.16 Water porosity test on samples cured at 90 °C. . . . 48
3.17 XRD tests on samples cured at 20 °C. . . . 49
3.18 XRD tests on samples cured at 90 °C. . . . 49

4.1 Consistometry tests. . . . 53
4.2 Bulk modulus values for non-carbonated specimens subjected to different confining pressures. . . . 61
4.3 Triaxial compressive strength of non-carbonated samples. . . . 62
4.4 Undrained Young's modulus, Poisson ratio and final pore pressure of non-carbonated samples. . . . 63
4.5 CH content and DOH of the samples. . . . 65
4.6 Average values of density and mass uptake after carbonation. . . . 68

4.7 Total porosity near the exposed surface of the samples at different carbonation times. . . . 77
4.8 Bulk modulus values for carbonated specimens subjected to different confining pressures. . . . 85
4.9 Averages bulk modulus values of CP and BNC05 obtained from isotropic tests at different confinement pressures. . . . 86
4.10 Quantification of crystalline phases from XRD results (120 days of carbonation). 89
4.11 Content of portlandite and calcium carbonates near the exposed surface after 120 days of carbonation . . . 91
4.12 Density and mass gained after carbonation. . . . 96
4.13 MIP experiments on samples cured at 90 °C. . . . 98
4.14 Water porosity on samples cured at 90 °C. . . . 101
4.15 Elastic properties obtained from elastic waves velocities V_P and V_S. . . . 102
4.16 Quantification of crystalline phases from XRD results. . . . 105
4.17 Intrinsic permeabilities. . . . 113
4.18 Summary based on the results obtained. . . . 114

5.1 Carbonation degree and its deviation after 30 and 120 days of carbonation calculated from the mass balance. . . . 116
5.2 Initial properties of cement with bacterial nanocellulose cured at room temperature. BNC values are conservative and determined from the literature [214, 215, 216]. . . . 128
5.3 Initial media properties for simulations. . . . 135
5.4 Molar volumes in cm^3/mol. . . . 135
5.5 Initial properties of cement with bacterial nanocellulose for the simulation under downhole conditions. . . . 136
5.6 Values of k for different values of k_0. . . . 136
5.7 Values of d_{eff} for different values of d^0_{eff}. . . . 136

A.1 UCS test results on cubic specimens. . . . 163
A.2 UCS test results on cylindrical specimens. . . . 163
A.3 Bulk modulus values for non-carbonated specimens subjected to several confining pressures. (*) Skempton coefficient = 0.32 (**) Skempton coefficient = 0.30. . . . 164
A.4 Bulk modulus values for carbonated specimens subjected to several confining pressures.(*) Skempton coefficient = 0.34 (**) Skempton coefficient = 0.35. 165
A.5 Elastic ultrasound waves of cylindrical specimens after 30 days of carbonation (curing method B). . . . 169

A.6 Elastic ultrasound waves of cylindrical specimens before 120 days of carbonation (curing method B). . . . 169
A.7 Elastic ultrasound waves of cylindrical specimens after 120 days of carbonation (curing method B). . . . 169
A.8 Density values of cylindrical specimens before 30 days of carbonation (curing method A) . . . 170
A.9 Density values of cylindrical specimens after 30 days of carbonation (curing method A) . . . 170
A.10 Mass uptake of cylindrical specimens after 30 days of carbonation (curing method A) . . . 170
A.11 Density values of cylindrical specimens before 120 days of carbonation (curing method A) . . . 170
A.12 Density values of cylindrical specimens after 120 days of carbonation (curing method A) . . . 170
A.13 Mass uptake of cylindrical specimens after 120 days of carbonation (curing method A) . . . 170
A.14 Density values of cylindrical specimens before 30 days of carbonation (curing method B) . . . 171
A.15 Density values of cylindrical specimens after 30 days of carbonation (curing method B) . . . 171
A.16 Mass uptake of cylindrical specimens after 30 days of carbonation (curing method B) . . . 171
A.17 Density values of cylindrical specimens before 120 days of carbonation (curing method B) . . . 171
A.18 Density values of cylindrical specimens after 120 days of carbonation (curing method B) . . . 171
A.19 Mass uptake of cylindrical specimens after 120 days of carbonation (curing method B) . . . 171
A.20 Water porosity of PC samples (curing method A) . . . 172
A.21 Water porosity of BNC05 samples (curing method A) . . . 172
A.22 Water porosity of BNC15 samples (curing method A) . . . 172
A.23 Water porosity of PC samples (curing method B) . . . 173
A.24 Water porosity of BNC05 samples (curing method B) . . . 173

List of abbreviations and nomenclature

Abbreviations

a_{Ri}	Stoichiometric coefficient of the reaction Ri
b_{J}	Generalized Biot coefficient
C_{CO_2}	CO_2 concentration in fluid
c_c	Modeling parameter
d_{i}	Pore diameter
d_{eff}	Diffusion coefficient
f_d	Yield surface
f_f	Modeling parameter
f_r	volumetric proportion of the phase r
i	Hydraulic gradient
n	Total number of pores of different diameters
n_{CO_2}	Apparent CO_2 concentration
p	Mercury pressure
p_f	Fluid pressure
q	Deviatoric stress
$\boldsymbol{u}$	Skeleton displacement vector
AmSi	Amorphous silica
API	American Petroleum Institute
A_v^i	Strain localization coefficients
BNC	Bacterial nanocellulose
BWOC	By weight of cement
C_3S	Alite
C_2A	Calcium aluminate
C_2S	Belite
C_4AF	Calcium alumino-ferrite
CH	Calcium hydroxide (Portlandite)

CO_2	Carbon dioxide
C-S-H	Calcium silicate hydrate
CBW	Chemical bound water
DMA	Dynamic mechanical analysis
DOH	Degree of hydration
DrTGA	Derivative of thermogravimetric analysis
E	Young's modulus
EOR	Enhanced oil recovery
G	Shear modulus
H_2CO_3	Carbonic acid
K	Bulk modulus
K_f	Fluid bulk modulus
L_i	Cylinder length of diameter i
L_e	Average pore length
MFC	Microfibrillated nanocellulose
MIP	Mercury intrusion porosimetry
N_{JK}	Generalized poroelastic coupling moduli
NCC	Nanocrystalline cellulose
PC	Portland Cement
PSD	Pore size distribution
$scCO_2$	Supercritical CO_2
S	Cross-section of a cubic specimen
SP	Superplasticizer
TGA	Thermogravimetric analysis
UCS	Unconfined compressive strength
UWM	Ultrasonic waves measurement
V_i	Volume of mercury intrusion into the pore of diameter i
V_S	Elastic S-wave velocity
V_t	Total apparent volume of the MIP sample
V_P	Elastic P-wave velocity
W/C	Water to Cement ratio
XRD	X-ray diffraction
XRF	X-ray fluorescence
Y_{Ri}	Variable that depends of the molar volumes of reactive species

Greek nomenclature

δ_{C}	Pore volume occupied by carbonate crystals
$\Delta \mathrm{P_i}$	Mercury pressure step
$\Delta \mathrm{P_t}$	Total pressure increase in meters' water column measured in the MIP
$\boldsymbol{\epsilon}$	Infinitesimal strain tensor
ε_v	Volumetric strain (tr($\boldsymbol{\epsilon}$))
η	Dynamic viscosity of the fluid phase
θ	Mercury contact angle
κ	Intrinsic permeability
μ	Strength average
ν	Poisson's ratio
ξ_{Ri}	Reaction advance
ξ_{max}	Maximum possible advancement calculated from the quantities of reactants present
ρ	Bulk density of the specimen
ρ_f	Fluid density
σ	Standard deviation
σ_m	Effective mean stress
$\boldsymbol{\sigma}$	Stress tensor
τ	Time constant
ν	Mercury surface tension
φ	Friction angle of the material
φ_{C}	Deformation of the porous medium filled by calcite phase
φ_{F}	Deformation of the porous medium filled by fluid phase
φ_{J}	Deformation of the porous volume occupied by the phase J
ϕ	pore space per unit of initial volume of porous medium which is not occupied by the solid phase
ϕ_{F}	Pore volume occupied by the in-pore fluid per unit volume of porous medium
ϕ_{L}	Porosity due to leaching of cement matrix
ϕ_{P}	Porosity filled by calcite precipitation

1 Introduction

1.1 Context and motivation

The increase in energy demand due to the world's economic growth has led to an increase in CO_2 emissions [1]. This has a negative impact on the environment, damaging ecosystems, air quality and promoting the greenhouse effect. As a result, new technologies are being developed to reduce the concentration of CO_2 in the atmosphere. One of the several solutions to reduce atmospheric pollution today is carbon capture and storage (CCS). This technology consists of capturing CO_2 during industrial processes and diverting its flow to suitable reservoirs [2]. These reservoirs have a large volume adequate to store these gases [3].

The use of nanoadditives for cement, such as bacterial nanocellulose (BNC), has been increasing in recent years due to its high mechanical properties and thermal resistance. However, the influence of BNC addition on the mechanical properties of the cement is not widely studied. The modification of cement to improve some properties is a subject of interest in the cement wellbore industry, and evidence shows that nanocellulose can be used as a crack inhibitor to avoid cement damage and thus prevent CO_2 leakage through the upper formations. The induced reduction of permeability, and other transport properties such as diffusivity, would be essential to prevent the entry of carbonic acid into the cementitious matrix. Therefore, the study of bacterial nanocellulose as an additive for oil well class G cement is a promising alternative to improve cement performance in petroleum engineering applications, especially in the context of geological storage of CO_2.

This study aims to contribute to the behaviour of modified petroleum cements in a context of carbon dioxide injection in geological reservoirs. The characterization of one of the constituent elements of the triple interface (cement annulus, cap rock and reservoir rock) of an injection well: oil cements modified with bacterial nanocellulose (NCB). The aim is to understand the micro and macro structural interaction of the modified cements under a supercritical CO_2 environment similar to that of a CO_2 geological storage. The experimental results will provide the key parameters for a constitutive and numerical study of possible simplified injection scenarios including thermal, hydraulic, mechanical and chemical (THMC) couplings at the triple interface. The expected results are intended to provide insight into the above interactions and their consequences in the depleted oil basin for future CO_2 and other gas storage ventures.

1.2 Objectives and outline of the work

The objective of this work is to expand the current knowledge on the mechanical and microstructural behaviour of cement after a supercritical carbonation process and to compare it with bacterial nanocellulose-containing specimens.

For this purpose, we examine the rheological behaviour of an oil well cement slurry modified with different percentages of BNC by performing free fluid and consistometry tests. The thermal and mechanical behaviour of class G cement with different BNC content is analyzed by dynamic mechanical analysis (DMA) and unconfined compression strength (UCS) tests. In addition, the degree of hydration (DOH) of the cement paste with the addition of BNC is investigated using thermogravimetric analysis (TGA).

This work also presents results on the porous structure and mechanical properties of cement modified with bacterial nanocellulose after carbonation under supercritical CO_2 conditions representative of CO_2 geological storage conditions. Specimens with BNC addition were cured for 28 days at 20 °C and then subjected to supercritical CO_2 for 30 and 120 days in an environment at 20 MPa of pressure, with a temperature of 90 °C. Mercury intrusion porosimetry (MIP), porosity measurement by oven-drying, X-ray diffraction (XRD), scanning electron microscopy (SEM), TGA, UCS, and triaxial tests were performed on cylindrical carbonated specimens.

To determine the properties of cement curing under extreme conditions, one group of specimens was cured at 90 °C, unmolded after 24 h, and kept underwater for 48 h. Then, they were dried at 85 °C for one week. This method provides information on cements cured under unfavorable conditions, simulating dry curing after being 48 hours underwater in the wellbore and subsequent carbonation.

Figure 1.1 shows a diagram of the tests performed on cement samples with bacterial nanocellulose, while Figure 1.2 shows the layout of the tests performed on carbonated samples. All microstructural tests are included in Figure 1.2.

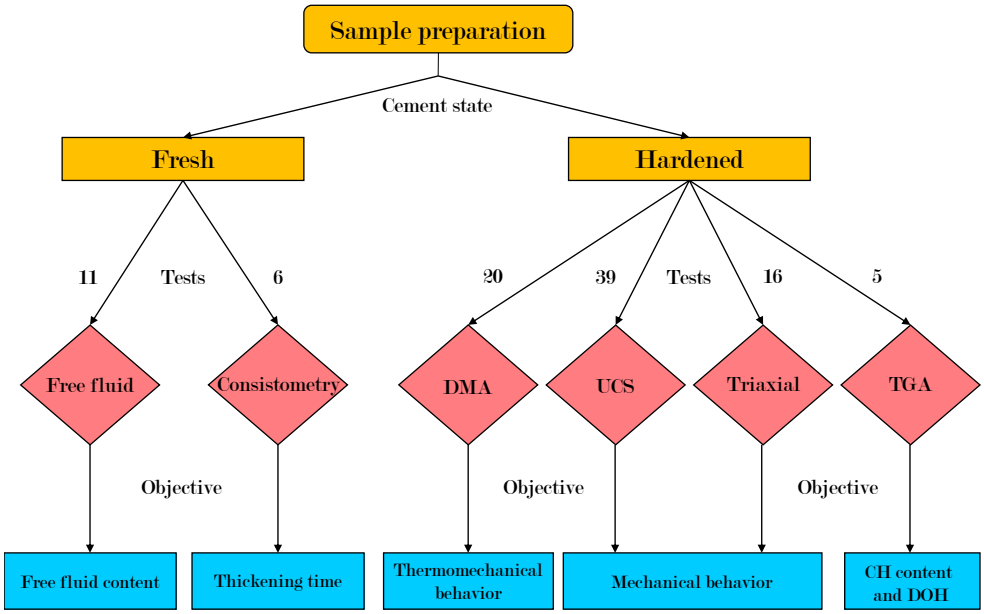

Fig. 1.1.: Testing methodology to study the effect of BNC on cement. All microstructural tests are included in Figure 1.2.

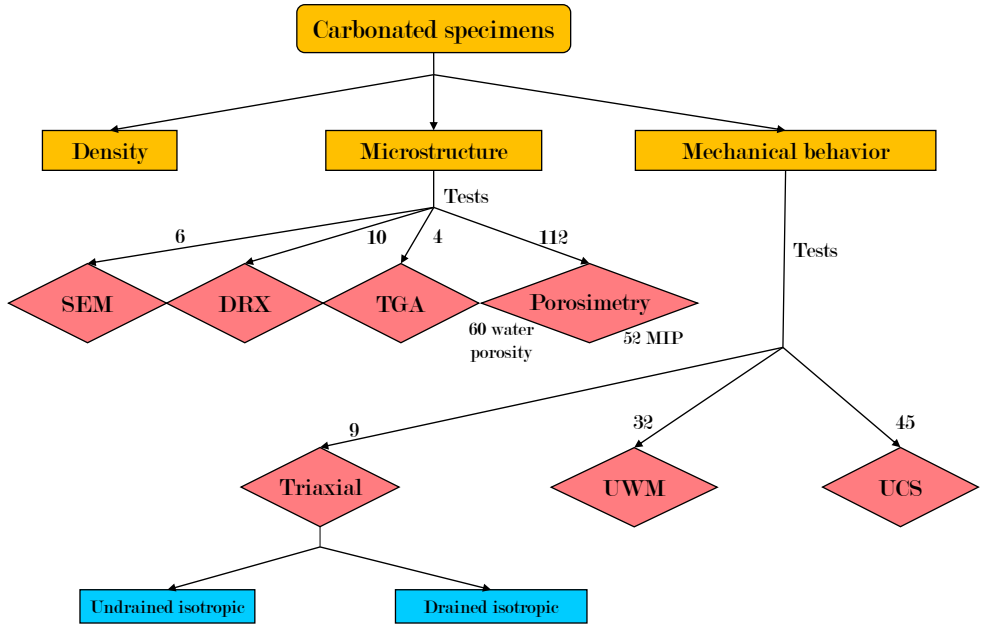

Fig. 1.2.: Testing methodology to study the effect of carbonation.

The structure of the following chapters is presented below:

- Chapter 2: This chapter is dedicated to a review of the literature relevant to the present work. Is divided into three sections, namely the geological CO_2 storage technology, the fundamental roles of cement, and a study of bacterial nanocellulose.
- Chapter 3: This chapter describes to the materials and methods used for the characterization of class G cement paste with the addition of bacterial nanocellulose.
- Chapter 4: The results are presented and discussed in this chapter. They are divided into three sections. The first shows the effects of bacterial nanocellulose on cement in the fresh and hardened state. The second one presents the influence on mechanical strength and microstructure due to supercritical carbonation. And the last one shows the variation in the performance that can be obtained in these modified cements if the curing conditions are unfavorable.
- Chapter 5: In this chapter, the degree of carbonation of laboratory specimens is determined, and a simulation is carried out using a chemo-hydro-mechanical model implemented in a finite element code. Modifications were made to the base code to account for the simultaneous dissolution of CH and C-S-H, and also the dissolution of calcite when the supercritical CO_2 concentration is high enough.
- Chapter 6: Conclusions and perspectives are presented in this chapter.

Literature review

2

2.1 Carbon capture and storage (CCS)

2.1.1 A climate change technology

There is an increasing rate of greenhouse gas emissions into the atmosphere [4]. This can have consequences for different ecosystems and human health[5]. Even though some developed countries are reducing their CO_2 emissions, some developing countries such as India, China, and the rest of the world are still increasing their consumption of fossil fuels [4]. Although new technologies are being developed to replace fossil fuels, humankind is still dependent on them. During this transition, reducing greenhouse gas emissions will be crucial. The mitigation options include energy efficiency, use of less carbon-dependent fuels, such as nuclear power, and obtaining new renewable energy sources. It should be borne in mind that no single technology option will provide all the emission reductions needed to achieve stabilization; more likely, several mitigation measures will be required. Figure 2.1 shows the evolution of CO_2 emissions over the years. As a result of the awareness of a large part of society, it has been possible to reduce some future emissions, although they could be reduced even further. To this end, the Intergovernmental Panel on Climate Change (IPCC) proposed a target for 2050 so that global warming does not raise the Earth's temperature by more than 1.5 °C [6].

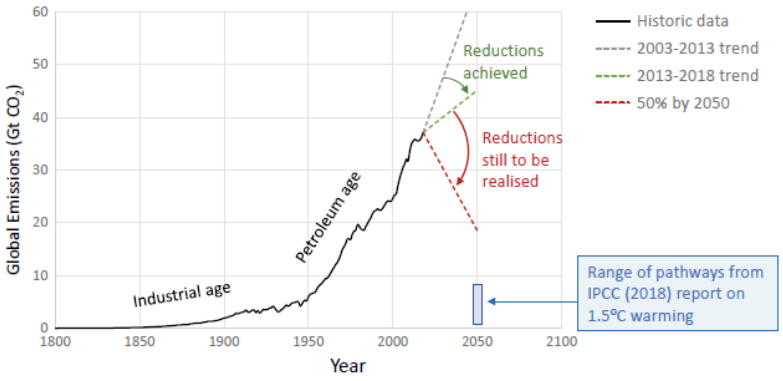

Fig. 2.1.: Historical record of global CO_2 emissions compared with various projections [7].

The carbon dioxide capture and storage (CCS) technology is an effective solution to reduce these emissions of CO_2 [7]. CCS is a process that involves the separation of CO_2 emitted by industries or sources, its transport to a storage site, and its long-term atmospheric isolation [8]. This technology allows storing massive amounts of CO_2 underground in geological reservoirs[3, 9], such as abandoned oil reservoirs, deep saline aquifers, basaltic rocks, or coal seams [10, 11]. Figure 2.2 shows the different alternatives for CO_2 storage.

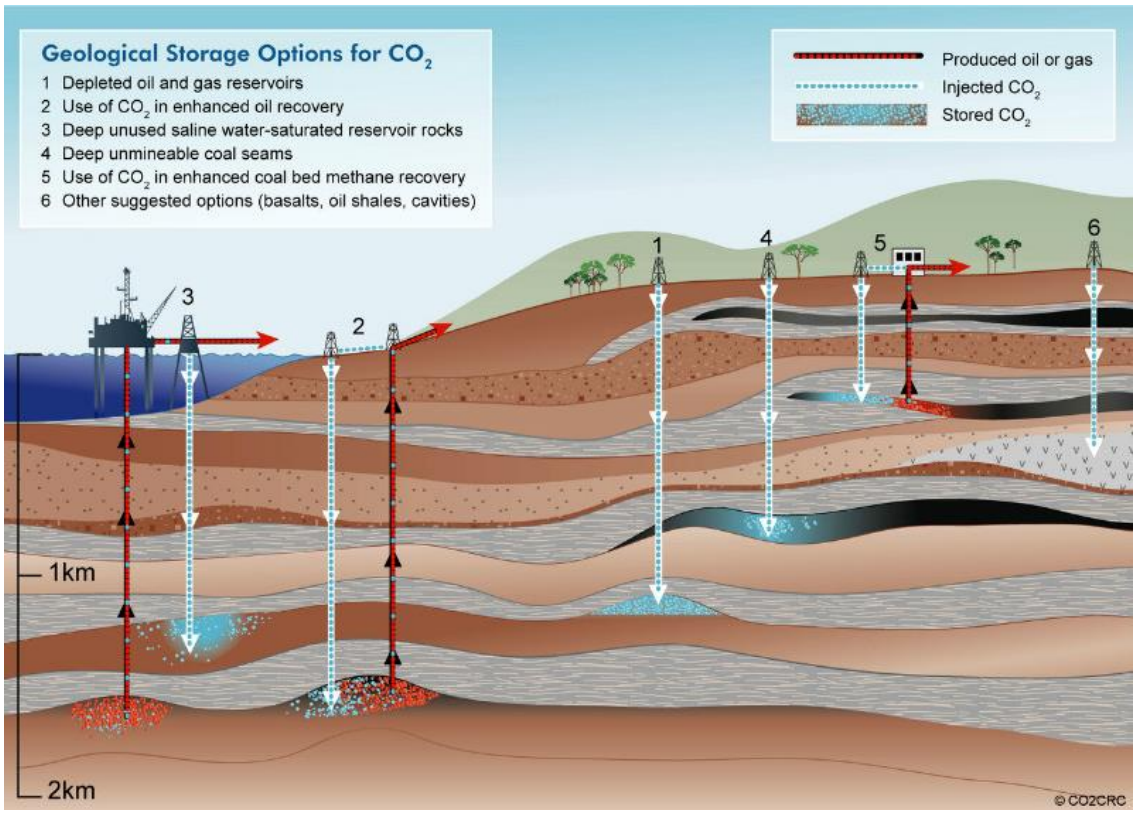

Fig. 2.2.: Geological storage options for CO_2. Courtesy of CO2CRC Ltd.

It is important to know the storage capacity of the reservoir, but this highly depends on temperature and pressure [1]. High pressures and temperatures just above the supercritical point considerably increase the fluid density, and therefore the amount of CO_2 that can be stored [7]. Therefore, reservoirs deep enough to store CO_2 in a supercritical state ($scCO_2$) present considerably higher capacities compared to shallower reservoirs with similar pore volume. Other key factors are the porosity and permeability of the reservoir rock. For instance, the "Sicily Channel" and "Abruzzi Offshore" reservoirs are candidates for geological storage, with porosities reaching 25.6% and permeability of 358 mD [12]. On the other hand, shale formations can also be considered for storage of CO_2, as indicated by studies on the SACROC Unit reservoir, since shale rock have porosities of around 10% and permeability of 10-100 mD, ensuring that their sealing capacity can be maintained for decades [13].

2.1.2 Challenges to overcome

CCS technology consists of three parts: capture, transport, and storage. Figure 2.3 describes the linear process that leads to store CO_2 from its capture. In turn, these three parts have their drawbacks, for which new alternatives are being developed to make these tasks more effective.

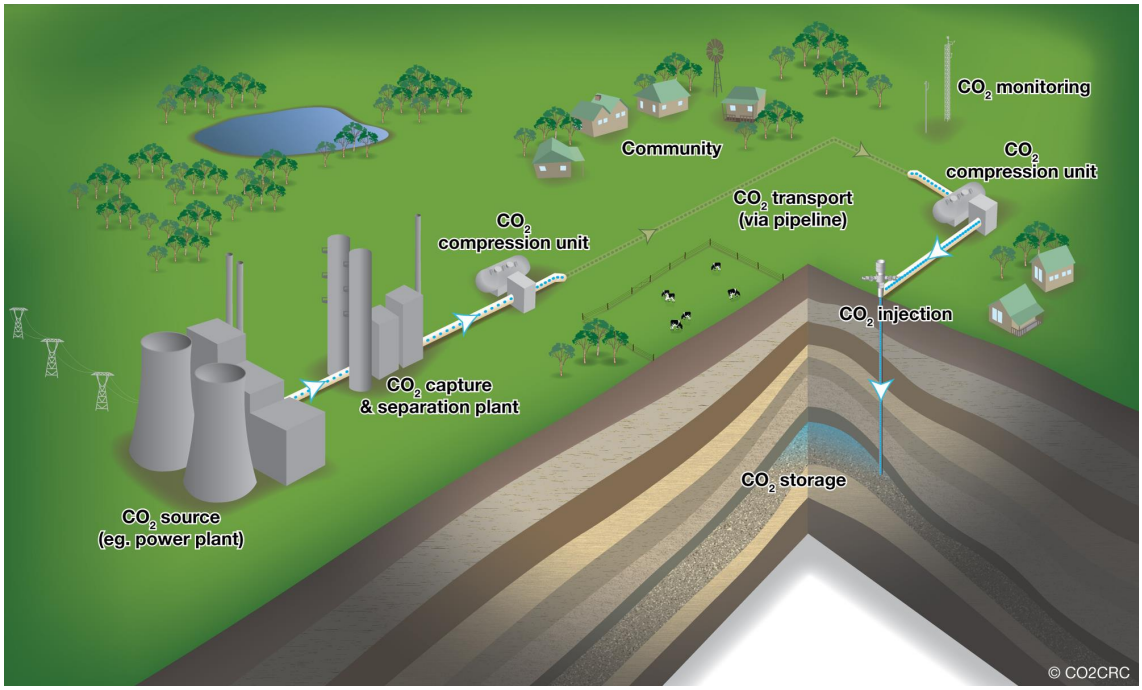

Fig. 2.3.: Carbon capture, transport and storage. Courtesy of CO2CRC Ltd.

One of the main problems with CCS is that it is currently too expensive and energy-intensive. The facilities, the supplies used to separate the materials, their consumption, and maintenance involve considerable expenses [14]. The development of this technology will depend on the costs of its implementation being relatively reasonable compared to the cost of emitting CO_2.

There are two ways to separate CO_2 from the power plants: pre-combustion and post-combustion. So far, the dominant CO_2 capture process is solvent-based using mono-ethanol-amine (MEA) as the solvent [7]. However, it is a complex process that consumes a lot of energy, so researchers are focused on making the CO_2 absorption more efficient, reducing the energy demand, and obtaining more effective recycling of the amine solution.

The location of the CO_2 separation site must be strategically chosen. Infrastructure costs will depend on the amount of piping needed to transport the CO_2 to the injection well [15, 16]. CO_2 transport is still relatively unexplored, but some aspects must be taken into account: it is necessary to determine the phases through which CO_2 can pass during

transport (gas, liquid or supercritical). If it is mixed with an aqueous phase, the mixture becomes corrosive. It must also be taken into account that this fluid may also have other components (such as hydrocarbons, nitrogen, or oxygen).

Concerning the injection process and storage, there are two stages during which the integrity of the system must be guaranteed. The first refers to the reservoir behaviour under CO_2 injection, and the second one to the long-term behaviour of the storage system.

During the injection stage, the temperature and pressure conditions of the reservoir must be determined, as well as its stress state and possible existing faults. The properties of the CO_2 must also be estimated at the time of injection, and need to be monitored throughout this stage. A massive injection of CO_2 into an aquifer reservoir will alter the equilibrium of the geochemical system composed of the porous rock and the formation water. Figure 2.4 shows the plume generated when CO_2 is injected into the reservoir and the meniscus effect produced between CO_2 and water at the reservoir-caprock interface. This caprock must resist the short-term excess injection pressure, and the long-term buoyancy pressure [17]. The dissolution of supercritical CO_2 to the formation water will control the rate of dissolution and precipitation of the minerals that constitute the porous rock.

Several problems may arise during injection, two of which are temperature gradients [18] and induced seismic activity [19]. These effects change the stress states and can lead to failure of the materials involved.

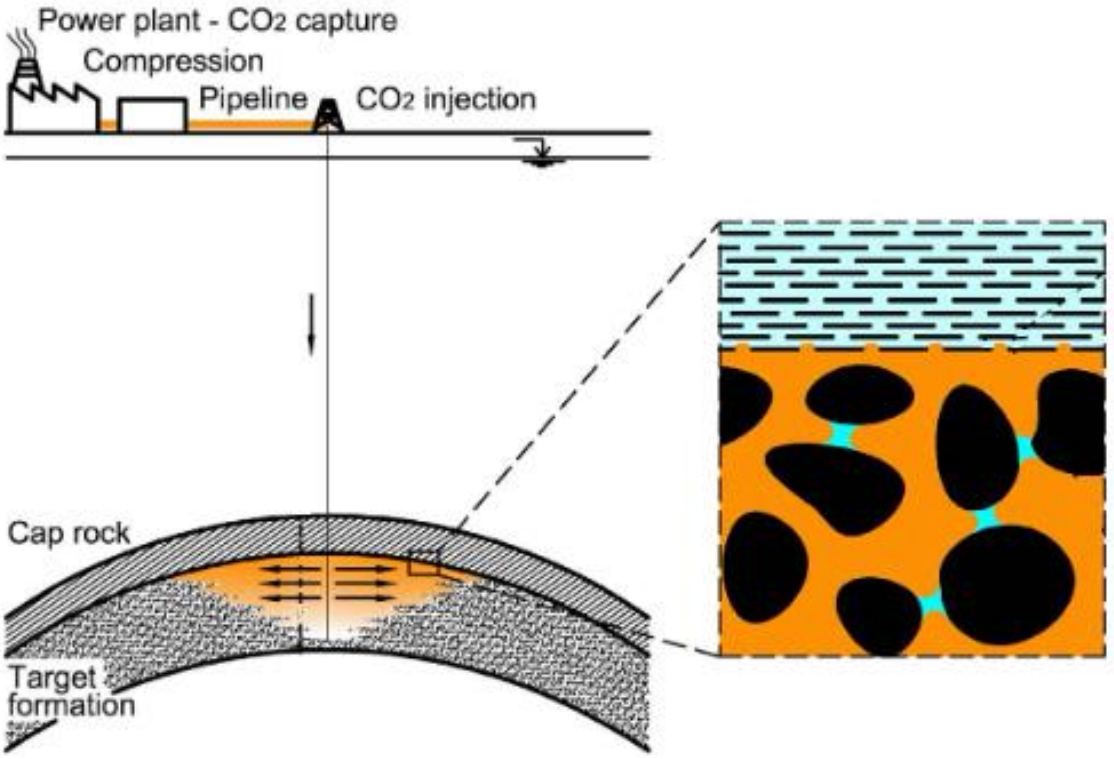

Fig. 2.4.: Plume generated by the injection process and CO_2-water capillary meniscus at the reservoir-caprock interface (after Espinoza et al. [17]).

Predicting long-term behaviour is essential for the proper functioning and integrity assessment of the geosystem.

An interesting aspect to study is the behaviour of the wellbore-caprock interface. Here is where the higher heterogeneity is found, as reservoir rock, caprock, and cementation are in contact. During drilling, the near-wellbore zone is damaged, and faults/fractures in the caprock could provide leakage pathways for $scCO_2$ to upper environments. To ensure the long-term integrity of the storage, it is necessary to study the behaviour of this zone, since the presence of artificial interfaces around wells and cracks due to the excavation damaged zone (EDZ) allow carbonate water to seep in. This generates mineral precipitation and possibly induces the evolution of cracks due to the concentration of tensile stresses. Figure 2.5 shows the possible leakage along several interfaces and cracks.

Furthermore, Class G cement used in the oil industry is chemically unstable against CO_2 and $scCO_2$ [20]. It requires a high pH to remain in chemical equilibrium, while conditions in CO_2-bearing geological reservoirs create an acidic environment. This supercritical CO_2 or dissolved CO_2 can react chemically with cement seals, creating potential leakage pathways through the wellbores [21].

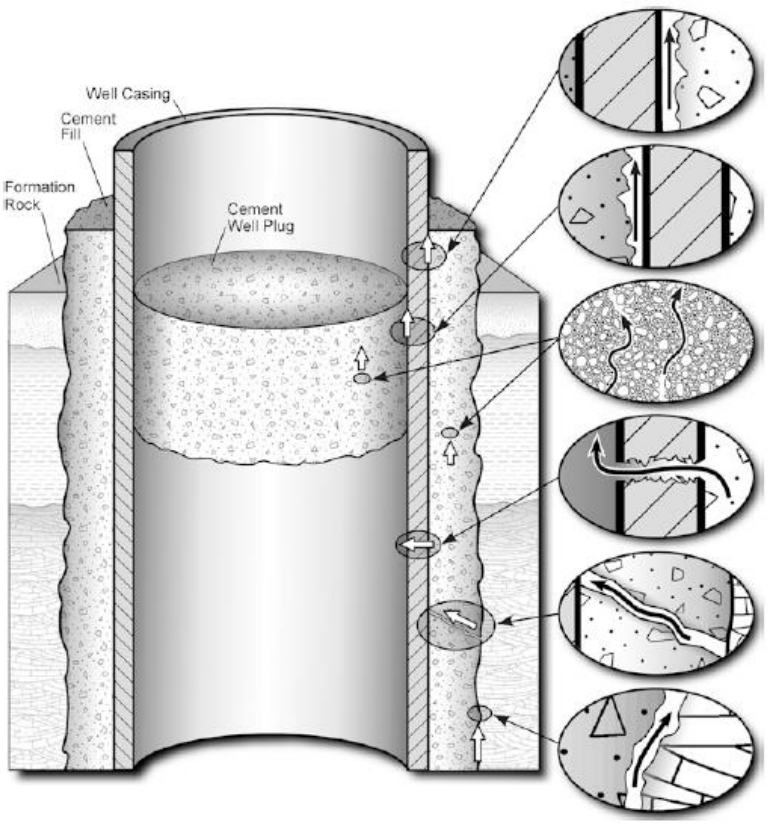

Fig. 2.5.: Diagram of possible leakage pathways through an abandoned well (after Gasda et al. [22]).

2.2 Oil well cement

2.2.1 Fundamental roles of cement in the oil and gas industry

The way to inject CO_2 into a geological reservoir is to drill a well to the desired depth and inject CO_2 through it under pressure. However, this task requires the injection well to be stable and safe. In practice, a steel pipe (called casing) is placed perfectly centered in the wellbore. Cement slurry is pumped through the casing and placed between the casing and the formation rocks during the well completion (Figure 2.6). This annular cement sheath ensures stability, protects the casing against corrosion, and, most importantly, ensures wellbore sealing and zonal isolation after the drilling fluids are removed.

The caprock formation is an impermeable barrier that covers the upper part of the reservoir and prevents CO_2 leakage to other geological formations. Along with the caprock, the cement sheath constitutes the hydraulic barrier against CO_2 leakage during injection and after it is finished [22].

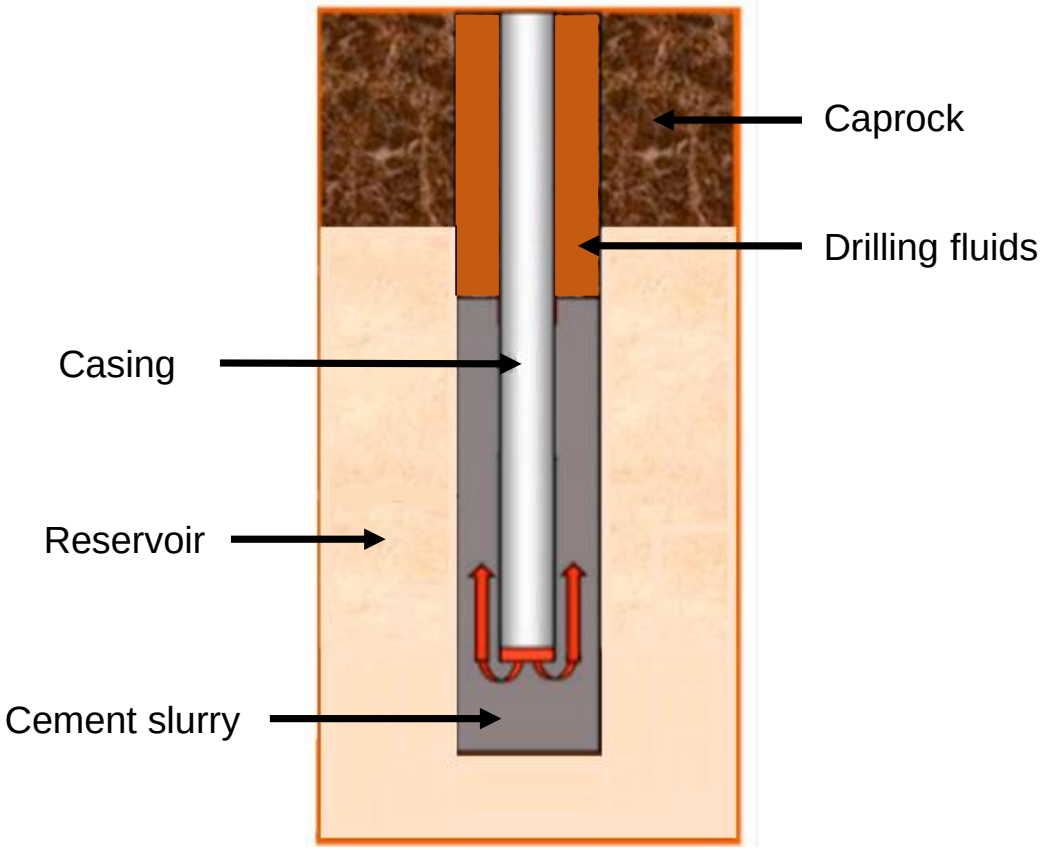

Fig. 2.6.: Schematic of a cementing operation (after Adjei et al. [23])

Oil well cementing is a complex procedure in wellbore operations [24]. The cement must ensure the oil well integrity and prevent links between formations [25, 26]. The slurry used differs for each particular well condition, changing its additives and quantities as needed. This cement mixture must meet a series of requirements according to Standards. It will be subjected to several stress loadings throughout its life span. Different problems arise during these stages, but the low tensile strength, cracks propagation of the set cement, and its temperature resistance are essential properties to be optimized [27, 28]. Temperatures in the various geological reservoirs (coal beds, deep saline aquifers, or depleted oil and gas reservoirs) can vary depending on the depth at which they are found. The depth at which the reservoir is located will also influence the determination of the pressures to which it is subjected. In some reservoirs, the temperature can vary from 60 to 160 °C [29], being 90 °C a value usually used by other authors testing oil well cement [30, 31, 32, 33].

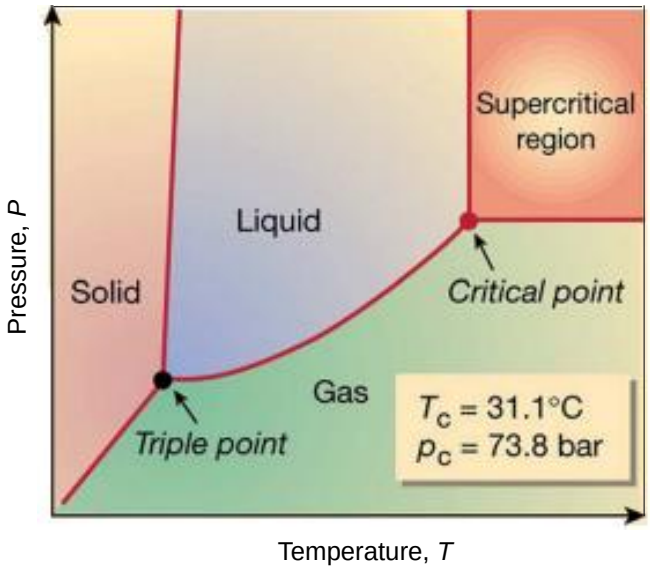

Fig. 2.7.: CO_2 phase diagram (after Zhang et al. [34]).

The hardened cement paste will then be in contact with the casing, rock formation (caprock and reservoir), geological formation fluids, and injected gases. These interfaces (cement-caprock, cement-reservoir rock, and cement-casing) will be subjected to CO_2 throughout the injection process and the accumulation of the gas in the reservoir during its lifetime. The integrity of the wellbore must be maintained against supercritical CO_2 ($scCO_2$) attack on the cement, especially at the cement-caprock-reservoir rock interface. A supercritical fluid is at temperature and pressure above its critical point, as shown in Figure 2.7. These fluids are characterized by diffusing like gas, but their density is higher like that of a liquid.

One of the problems with using cement to seal CO_2 in geologic reservoirs is that ordinary unmodified cement cannot withstand supercritical CO_2 in contact with the hydrated products of cement [35]. The chemical reactions induce cracks and potential CO_2 escape pathways to the surface or upper formations [36].

In the presence of CO_2 in the reservoir rock, carbonation of the cementitious materials starts from the external surface of the cement sheath. The process is intensified by the high pressure and high-temperature conditions at reservoir depth (Figure 2.8). The carbonation process affects the mechanical properties and permeability of the cement paste, and may alter its role in ensuring zonal isolation [37].

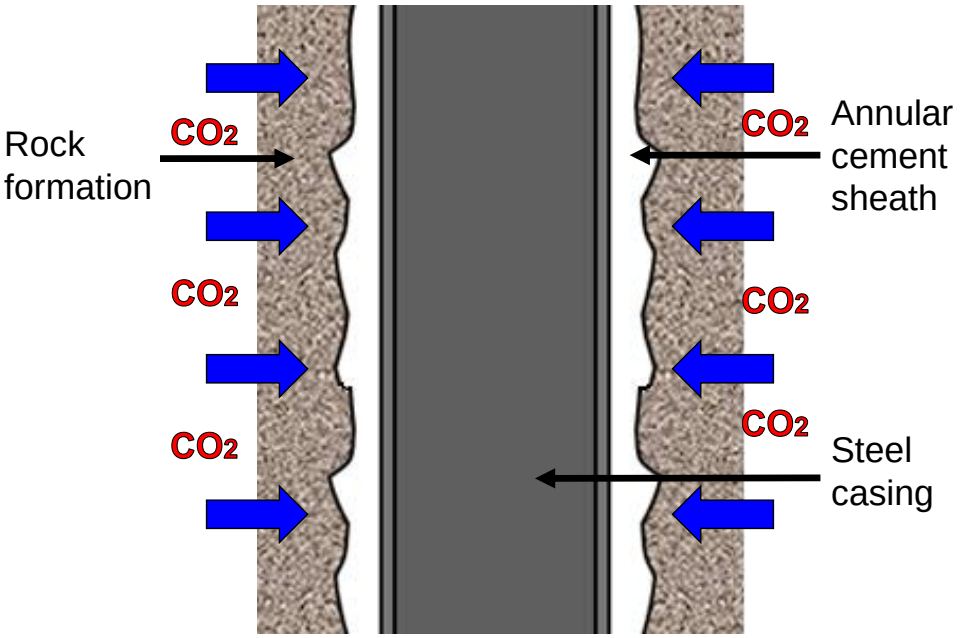

Fig. 2.8.: CO_2 attack on cement sheath.

To understand these chemical reactions that can damage cement, it is necessary to identify the composition of the Portland cement used for these operations.

2.2.2 Clinker production and chemical composition

The raw materials used for clinker production must contain calcium, silica, aluminum, and iron. The Portland cement manufacturing process consists of finely grinding and mixing the limestone and clay materials so that the calcium oxide (CaO) from the limestone and the clay components (silica, alumina, and iron oxides) are adequately homogenized. These materials are calcined at temperatures comprised between 1400 and 1600 °C, where they melt. The resulting product is clinker. The oxides that are produced during this process are summarized in Table 2.1.

Component	Nomenclature	Formula
Lime	C	CaO
Silica	S	SiO_2
Alumina	A	Al_2O_3
Iron	F	Fe_2O_3
Magnesium Oxide	M	MgO
Sulfuric Anhydride	$\hat{S}$	SO_3
Sodium Oxide	N	NaO
Potassium Oxide	K	K_2O

Tab. 2.1.: Cement composition

The clinker is then allowed to cool and generates the main components of Portland cement, the anhydrous products. There are also other oxides in smaller proportions, such as magnesium, sodium or potassium oxides. Sodium and potassium oxides are jointly called total equivalent alkalis. The main products are called alite (C_3S), belite (C_2S), celite (C_3A) and felite (C_4AF). Their chemical formulation and approximate proportions within the cement are listed in Table 2.2. The clinker is mixed with gypsum (about 5%) and then ground to a certain fineness to obtain Portland cement, which is the final product.

Component	Formula	Abbreviation	Proportion
Tricalcium silicate (alite)	$3CaO.SiO_2$	C_3S	40-60
Dicalcium silicate (belite)	$2CaO.SiO_3$	C_2S	20-30
Tricalcium aluminate (celite)	$3CaO.Al_2O_3$	C_3A	8-15
Tetracalcium aluminoferrite (felite)	$4CaO.Al_2O_3.Fe_2O_3$	C_4AF	4-13

Tab. 2.2.: Main components of anhydrous cement.

Regarding petroleum cements, the American Petroleum Institute (API) classified cement into 8 classes (from A to H) corresponding to the different conditions to which the cement may be subjected [38]. The most commonly used are class G and class H cements. Their chemical composition is the same, but Class G cement is more finely ground. They can be found in moderate (MSR) or high sulfate-resistant grade (HSR). Both cements must satisfy a series of physical requirements according to the API in order to be approved for use, both in terms of fluidity, and mechanical strength. The only difference between the two is that a water to cement ratio of 0.44 is used with class G cement for these standards tests, while a ratio of 0.38 is used for class H cement.

2.2.3 Cement hydration

When cement is mixed with water, it forms stable hydrated components that have the property of adhering to each other, improving the mechanical properties of the cement as the hydration process progresses.

C_3S is the most important component for obtaining higher initial strengths, being its hydration rate high. Unlike C_3S, C_2S has a slow hydration rate [39]. Its low hydration rate prevents its rapid development of strength, so its contribution becomes important over longer time periods. The reaction of C_3A with water is very fast and leads to immediate hardening of the paste. To avoid this, gypsum ($CaSO_4 \cdot 2H_2O$) is added to the cement clinker, which decreases the solubility of C_3A. C_3A reduces the firing temperature of the clinker and facilitates the combination of lime and silica; for this reason, C_3A is useful in the manufacture of cement. Nevertheless, it hardly contributes to strengthen it, except at very early ages [40]. The iron in C_4AF is of great importance as it favors the melting in the clinker calcination stage. It is responsible for the greenish-gray color of Portland cements [41]. It is a relatively inactive component that contributes little to cement strength. Its hydration is rapid although less than that of C_3A. The main alkaline materials are sodium and potassium. The effects of alkalis on strength development are difficult to predict, as they can increase compressive strength and can also be detrimental if they are in contact with reactive aggregates. Therefore, the amount of these substances is usually small (<1%).

The volume of formed hydration products is less than the sum of the volumes of reacting cement and water. Therefore, the hydration product does not completely fill the volume available to it. This effect is called shrinkage. On the other hand, if the hydration process continues, the new hydration products will fill more and more the available spaces. This exothermic process causes the cement paste to increase in consistency over time and forms a structure with mechanical and hydraulic properties. Cement hydration consists of 5 well-distinguished stages based on its heat release rate (Figure 2.9):

- Pre-induction period: It lasts only a few minutes, during and immediately after mixing. This stage is greatly exothermic.
- Induction period: This period lasts until critical supersaturation is reached and the first cement hydrates begin to precipitate, signaling the end of the induction period.
- Acceleration period: The acceleration is known as the setting period, representing the interval of most rapid hydration. During the acceleration period, the hydration products precipitate and are deposited on the available water-filled space. The acceleration period ends when the peak of heat release rate is reached.
- Deceleration period: The porosity of the system decreases as a consequence of hydrate deposition. Eventually the transport of ions and water through the hydration products network is hindered, and the rate of hydration slows down.
- Diffusion period: It can also be considered as within the deceleration period, and it can last for years. The network of hydrated products becomes denser and denser, and the process is controlled by diffusion.

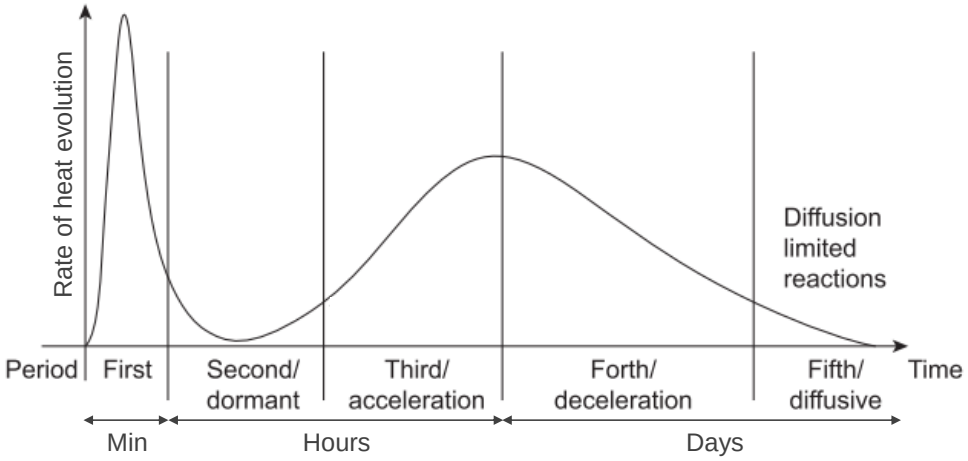

Fig. 2.9.: Cement hydration rate periods (after Vázquez et al. [42]).

After the induction period, heat release eventually resumes and the hydration rate of C_3S exceeds that of C_2S by a wide margin. The hydration of C_3S is mostly responsible for the initiation of set and the development of initial strength, due to its abundance and associated massive C-S-H gel formation. C_2S hydration is significant only in terms of the ultimate strength of the hardened cement. Aluminates are more reactive at short hydration times. The hydration of C_4AF is similar to that of C_3A but much slower. Although their abundance is considerably lower than silicates, they have a great influence on the rheology of the cement slurry and the early strength developed in the cement set. Figure 2.10 shows the heat release of the main components and the development of their strength.

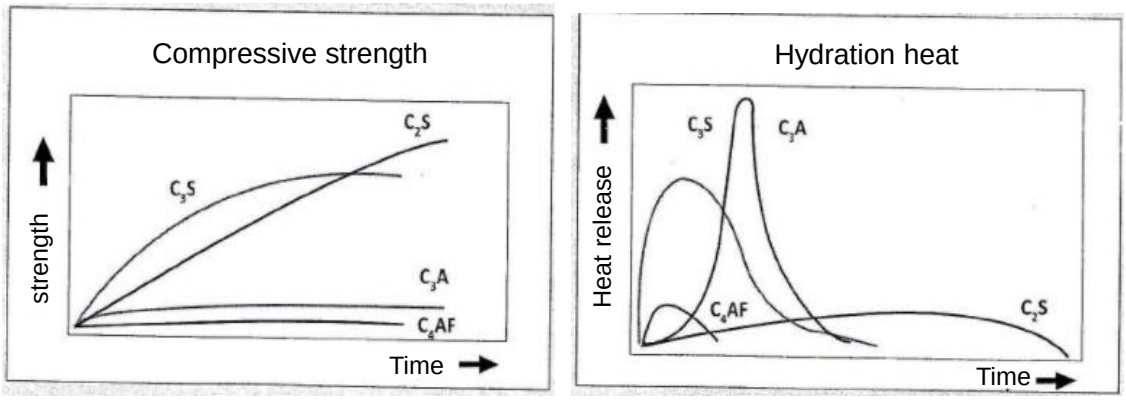

Fig. 2.10.: Strength and heat of hydration of the main cement components (after Niño Hernández et al. [43]).

Silicate phases are the most abundant in cement, with C_3S being the main one. The silicates hydrate to form amorphous calcium silicate hydrate (C-S-H) and highly crystalline calcium hydroxide (CH). C-S-H is the main component of hardened cement and comprises approximately 70%, while CH is in proportions of 15 to 20%.

The hydration reactions of C_3S and C_2S are shown in Equation 2.1 and Equation 2.2, where x represents the C/S (calcium/silicate) ratio and y the H/S (water/silicate) ratio of C-S-H [44].

$$C_3S + (3 - x + y)\,H \rightarrow C_x - S - H_y + (3 - x)\,CH \tag{2.1}$$

$$C_2S + (2 - x + y)\,H \rightarrow C_x - S - H_y + (2 - x)\,CH \tag{2.2}$$

The C/S content is usually set at 1.7, and H/S between 1.2 and 1.5. The value of y actually depends on the drying conditions [45]. If we take $y = 1.5$, we can obtain Equation 2.3 and Equation 2.4:

$$C_3S + 2.8H \rightarrow C_{1.7} - S - H_{1.5} + 1.3CH \tag{2.3}$$

$$C_2S + 1.8H \rightarrow C_{1.7} - S - H_{1.5} + 0.3CH \tag{2.4}$$

Hydration of C_3A is controlled by adding 3 to 5 % gypsum ($C\hat{S}H_2$) to the clinker before grinding. On contact with water, part of the gypsum dissolves. The calcium ions and sulfate released in solution react with the aluminate and hydroxyl ions are released from the C_3A to form calcium trisulfoaluminate hydrate (Equation 2.5), known as ettringite (AFt). Ettringite forms crystalline needles that precipitate on the surface of C_3A, hindering rapid hydration [46]. Therefore, an "induction period" is artificially created. During this period, gypsum is gradually consumed and ettringite continues precipitating. Finally, ettringite becomes unstable and converts to a calcium monosulfoaluminate hydrate (AFm) (Equation 2.6).

$$2C_3A + 3C\hat{S}H_2 + 26H \rightarrow C_6A\bar{S}_3H_{32} \tag{2.5}$$

$$2C_3A + C_6A\bar{S}_3H_{32} + 4H \rightarrow 3C_4A\bar{S}H_{12} \tag{2.6}$$

Any other non-hydrated C_3A forms calcium aluminate hydrate as indicated in Equation 2.7. Calcium aluminate hydrates are metastable and form hexagonal crystals. They are eventually converted to a more stable cubic form, C_3AH_6 as shown in Equation 2.8. This reaction occurs over several days at room temperature [39]:

$$2C_3A + 27H \rightarrow C_2AH_8 + C_4AH_{19} \tag{2.7}$$

$$C_2AH_8 + C_4AH_{19} \rightarrow 2C_3AH_6 + 15H \tag{2.8}$$

The chemical reactions involving C_4AF are similar, but some aluminum is replaced by iron to form ferrite-ettringite. In turn, this phase also becomes unstable and converts to a phase similar to monosulfoaluminate containing iron ($3C_4(A,F)\bar{S}_3H_{12}$).

$$C_4AF + 3C\hat{S}H_2 + 21H \rightarrow C_6\left(A,F\right)\bar{S}_3H_{32} + \left(F,A\right)H_3 \tag{2.9}$$

$$C_4AF + C_6\left(A,F\right)\bar{S}_3H_{32} + 7H \rightarrow 3C_4\left(A,F\right)\bar{S}_3H_{12} + \left(F,A\right)H_3 \tag{2.10}$$

The main components of portland cement are summarized in Table 2.3.

Component	Formula	Abbreviation
Calcium silicate hydrate	$xCaO\text{-}ySiO_2\text{-}zH_2O$	C-S-H
Calcium hydroxide	$Ca(OH)_2$	CH (portlandite)
Calcium trisulphoaluminate hydrated	$3CaO\ Al_2O_3\ 3CaSO_4\ 32H_2O$	AFt (ettringite)
Calcium monosulphoaluminate hydrated	$3CaO\ (Fe,Al)_2O_3\ CaSO_4\ 12H_2O$	AFm

Tab. 2.3.: Main components of hydrated cement.

The secondary components of portland cement are summarized in Table 2.4. These products amount to a very low percentage of the cement matrix, and they can be neglected in some cases.

Component	Formula	Abbreviation
Magnesium hydroxide	$Mg(OH)_2$	MH
Calcium aluminate hydrate	$4CaO\ Al_2O_3\ 13H_2O$	C_4AH_{13}
Calcium trisulphoferrite hydrated	$3CaO\ (Fe,Al)_2O_3\ 3CaSO_4\ 32H_2O$	AFt-(Fe)
Calcium monosulphoferrite hydrated	$3CaO\ (Fe,Al)_2O_3\ CaSO_4\ 12H_2O$	AFm-(Fe)

Tab. 2.4.: Secondary components of hydrated cement.

The anhydrous cement grains in the hydrated paste are a minority phase. Because of the limited space available between the particles, the products generated during hydration tend to crystallize around the cement particles. At prolonged ages, hydration of these particles results in the formation of high-density hydration products, such as high-density C-S-H.

2.2.4 API cement testing

Cement displaces drilling fluids during the cementing process to the top because cement has a higher density (Figure 2.6). During this process, it is necessary to know the rheological properties of cement for designing cementing operations and selecting equipment, and techniques to complement well-completion practices [47]. These properties vary depending on the type of cement used, the pressure in the wellbore and its temperature.

The API establishes the minimum conditions that anhydrous cement must meet before being used in well cementing operations [38], reflected in the thickening time and free fluid tests (Figure 2.11). These mixtures are made with a mixer standardized by the API. The pumpability of cement is determined from the thickening-time test using a pressurized consistometer, which establishes a maximum initial consistency, and an admissible range of pumpability time, depending on a fixed temperature schedule. The free-fluid test allows the stability of the slurry to be analyzed once cement is no longer pumped. For this, a sample is conditioned in an atmospheric consistometer and then the sample is allowed to stand for two hours. Later, the water that remains on top is collected and weighed. The volume fraction for oil well cement classes G and H shall not exceed 5.9 %. For more detailed rheological behaviour, viscosity tests can be performed with a standard viscometer [48].

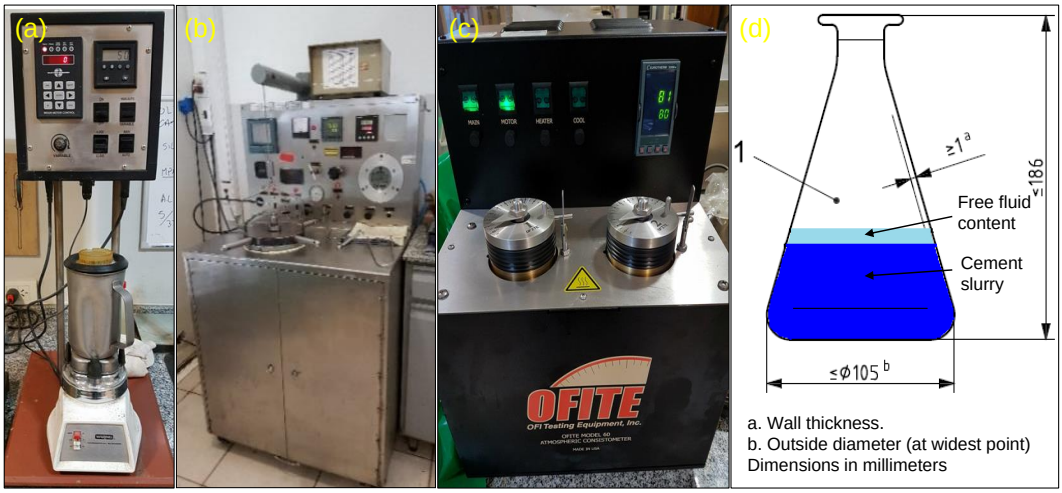

Fig. 2.11.: (a) API mixer, (b) pressurized consistometer, (c) atmospheric consistometer and (d) free fluid diagram.

Once the cement is in a hardened state, the sedimentation produced in a cement column can be analyzed by cutting the column into equal parts and taking their weights. The smaller the difference in density between the top and bottom, the more stable the sample has been during the hardening process. These cements must also meet a minimum compressive strength to be used in cementing operations. This topic will be developed in the next section as an introduction to the results obtained later in this work.

2.2.5 Mechanical properties of cement

Mechanical properties and microstructure are intimately related. The homogenization models start from the cement microstructure considering its main components, such as high and low densities C-S-H, CH, aluminates, and the remaining anhydrous cement [49]. However, porosity must also be considered in order to predict the effective mechanical and physical properties via a multiscale process [50, 51].

In saturated conditions, the effective stress ($\boldsymbol{\sigma_d}$) of a material is given by the Terzaghi equation subtracting the pore pressure (p_f) from the total stress ($\boldsymbol{\sigma}$). b is the Biot coefficient.

$$\boldsymbol{\sigma_d} = \boldsymbol{\sigma} - bp_f \tag{2.11}$$

The theory of elasticity explains how a solid deforms as a function of external forces. A material is in the elastic zone when the deformations are reversible, i.e. the material returns to its initial configuration when the applied load is removed, meaning that there was no energy dissipation during loading. Among the most used elastic properties are Young's modulus (E) and Poisson's ratio (ν). The former is the slope of the straight line produced in a stress-strain diagram in a quasi-static compression test. While the second indicates the ratio between radial deformation (ε_{trans}) and axial deformation (ε_{long}), with values that can typically range from 0.1 to 0.45 for rocks or cements. Under uniaxial compression, these values are determined according to Equation 2.12.

$$E = \frac{\sigma_{axial}}{\varepsilon_{long}} \ , \ \nu = -\frac{\varepsilon_{trans}}{\varepsilon_{long}} \tag{2.12}$$

These two elastic parameters are sufficient to determine the stress-strain relationship of a isotropic linear elastic material. Another relevant elastic parameter is the bulk modulus of a material (K), which measures the volumetric stiffness, indicating the amount of pressure required to cause a unit decrease in volume.

Cement is usually considered a poroelastic material, and its mechanical behaviour is related to its microstructural properties. This behaviour will also depend on the type of load applied and its duration, saturation level and pore size distribution within its matrix. For these types of materials, different stiffness moduli can be defined under saturated conditions. The variations of the total volume of a specimen (V) and the pore volume (V_ϕ) are given by the drained bulk modulus K_d and the modulus K_p (Equation 2.13) [52]. The unjacketed modulus K_s is given by the variation of the volume of the specimen with respect to the applied pressure, while the modulus K_ϕ is given by the variation of the pore volume

evaluated from the quantity of fluid exchanged between the specimen and the pore pressure generator [53].

$$\frac{1}{K_d} = -\frac{1}{V}\left(\frac{\partial V}{\partial \sigma_d}\right)_{p_f} \ , \ \frac{1}{K_p} = -\frac{1}{V_\phi}\left(\frac{\partial V_\phi}{\partial \sigma_d}\right)_{p_f} \tag{2.13}$$

$$\frac{1}{K_s} = -\frac{1}{V}\left(\frac{\partial V}{\partial p_f}\right)_{\sigma_d} \ , \ \frac{1}{K_\phi} = -\frac{1}{V_\phi}\left(\frac{\partial V_\phi}{\partial p_f}\right)_{\sigma_d} \tag{2.14}$$

K_d becomes K_u if the specimen is not allowed to drain during the loading process. The Biot coefficient can be determined from the modulus K_d and K_s, and from it the Skempton coefficient could also be determined:

$$b = 1 - \frac{K_d}{K_s} \ , \ B = \frac{1 - K_d/K_u}{b} \tag{2.15}$$

Regarding the microstructure of the cement, it varies with curing conditions. It is recommended to enable a constant supply of water to the cement during the curing process so that it continues to hydrate and develop its microstructure. Curing temperature is an important variable that substantially influences the development of its poromechanical properties [54]. Figure 2.12 shows the strength development of a cement cured at 20 °C and at 38 °C.

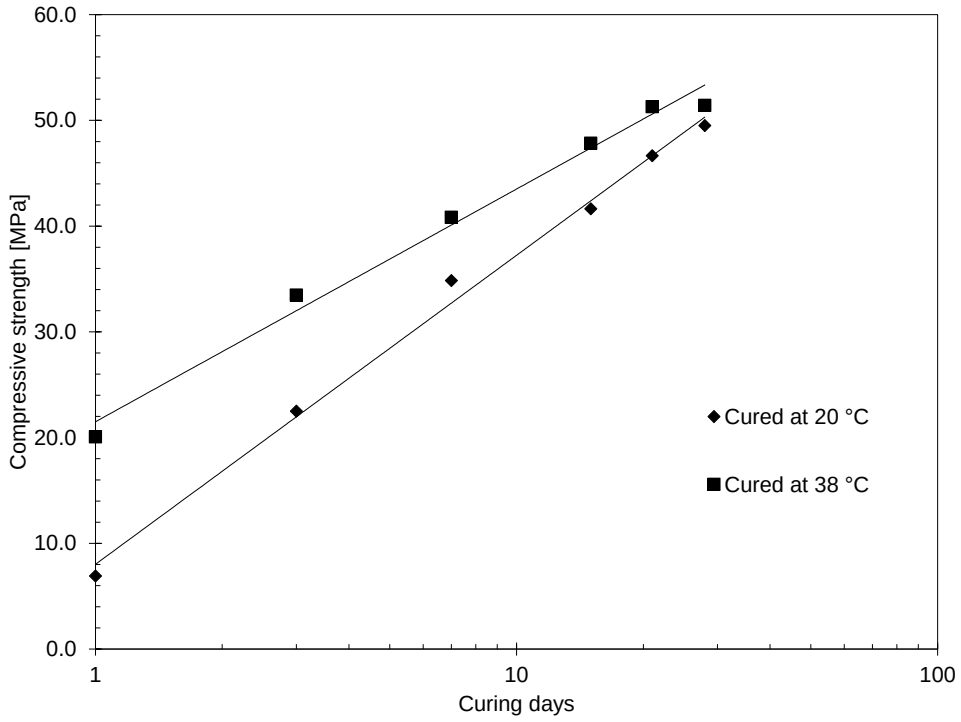

Fig. 2.12.: Strength development as a function of curing temperature (results of cubic specimens of class G cement.).

At first, a cement cured at high temperature will develop higher strength than a cement cured at low temperature. But at long curing times, the low-temperature cement will outperform the high-temperature cement in strength [55, 56, 57], as the trend in Figure 2.12 shows.

Porosity decreases as curing time increases. In turn, capillary porosity increases with higher curing temperatures [58]. Furthermore, temperature modifies the hydration products of cement, generating denser C-S-H and katoite phases [54]. However, obtaining this denser structure does not compensate for the loss of strength due to the increase in capillary porosity [59]. The porosity development over time depends mainly on the water to cement ratio and the curing conditions. Figure 2.13 shows that porosity decreases as the curing temperature decreases. It also indicates that with a higher hydration degree, cement will have lower porosity for a given curing temperature.

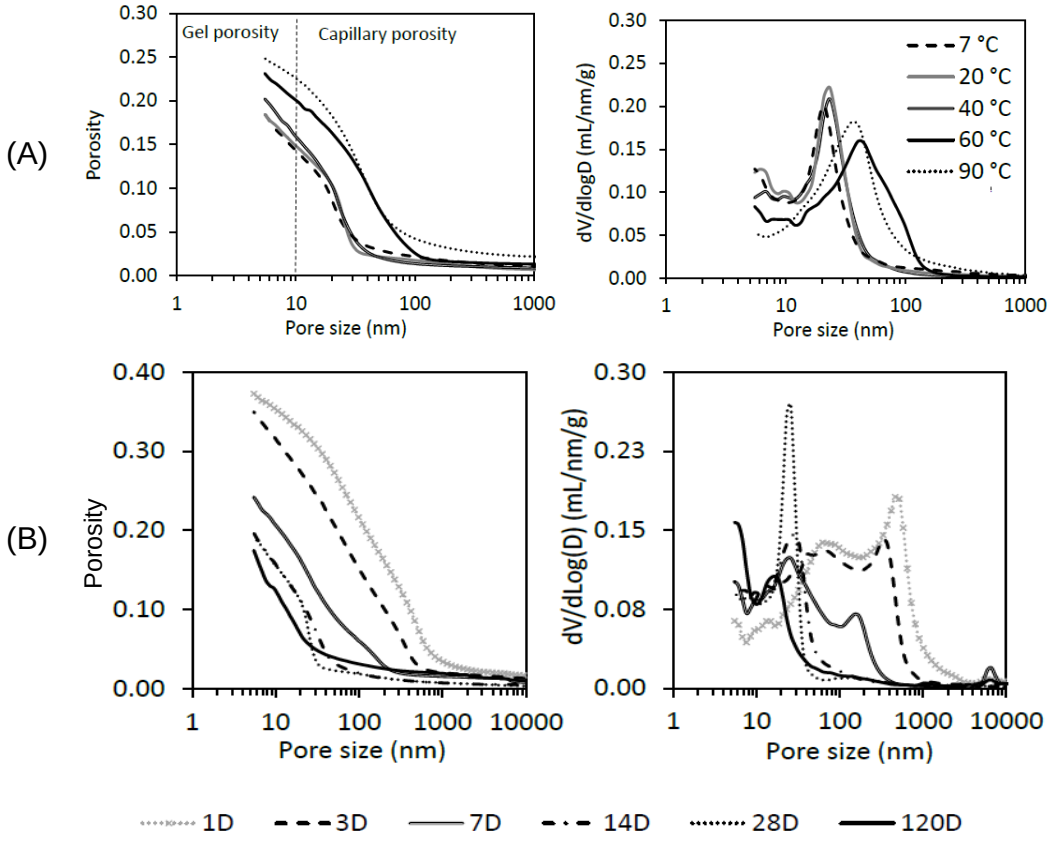

Fig. 2.13.: (A) Porosity and incremental pore volume as a function of temperature after 28 days of curing, (B) Variation of porosity and incremental pore volume as a function of time for samples cured at 20 °C (after Bahafid [60]).

2.2.6 Carbonation process

When injected in a geological reservoir, CO_2 first dissolves in the aqueous phase, generating carbonic acid and reducing the pH of the phase. This carbonic acid (H_2CO_3) is unstable, so most of it dissociates into bicarbonate ions (HCO_3^-) and a small part into carbonate ions (CO_3^{2-}) in the pore solution, depending on the pH at the equilibrium:

$$CO_2 + H_2O \leftrightarrow H_2CO_3 \leftrightarrow H^+ + HCO_3^- \leftrightarrow 2H^+ + CO_3^{2-} \tag{2.16}$$

Geochemical studies of cement paste carbonation show that the advance of carbonic acid through the paste mainly induces chemical reactions with the portlandite (CH) and hydrated calcium silicates (C-S-H). The carbonation of saturated specimens is considered to be a diffusion-dominated process [61]. These chemical reactions induce changes in porosity and the mineral composition of the solid phase.

Both reactions lead to the precipitation of calcium carbonate ($CaCO_3$) [62] in its various forms: calcite, aragonite, or vaterite [63]. The first cement component to react with dissolved CO_2 is calcium hydroxide:

$$CH + CO_2 \rightarrow CaCO_3 + H_2O \tag{2.17}$$

This reaction dissolves CH, reduces the equilibrium pH of the cement matrix, and leads to the precipitation of $CaCO_3$. The drop in pH then allows the C-S-H to be decalcified in contact with CO_2. Some works consider water release during carbonation [64, 65]. However, new studies have demonstrated that C-S-H carbonation does not release it, and the only effects are C-S-H decalcification and amorphous silica (AmSi) formation [66, 67]:

$$C - S - H + 1.7CO_2 \leftrightarrow 1.7CaCO_3 + AmSi \tag{2.18}$$

Nevertheless, it has been found that dissolution of CH and C-S-H occurs simultaneously [67, 68], even though thermodynamically, C-S-H should be dissolved after CH depletion [69]. The formation of amorphous silica from C-S-H could increase porosity, depending on the C-S-H structure [68], and may reduce the structural integrity of the cementitious material.

Since C-S-H is the component with the most important influence on the cement mechanical characteristics, its loss will reduce the mechanical properties and could compromise the wellbore integrity, while the reduction of pH may induce corrosion of the steel casing.

Furthermore, $CaCO_3$ precipitated in a water acidified medium in the presence of CO_2 is in turn prone to dissolution (Figure 2.14) [70].

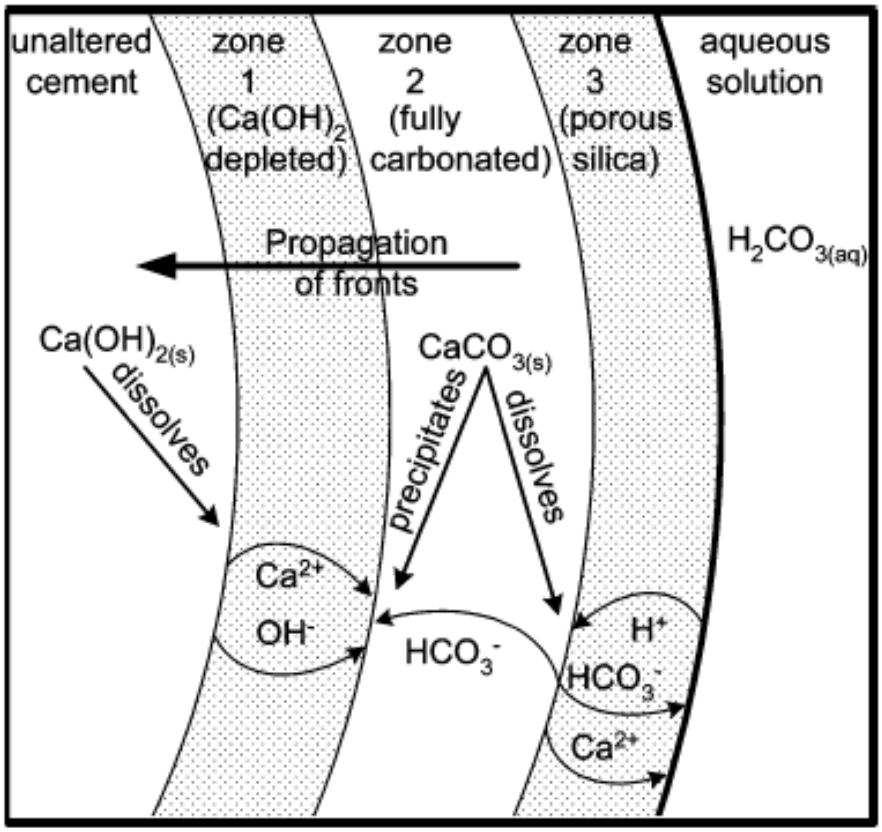

Fig. 2.14.: Migration of ions along carbonation and precipitation fronts. The chemical reactions in the figure are given using industry notations. $Ca(OH)_2$ is CH and porous silica is $AmSi$ (after Kutchko et al. [69]).

The pressure and temperature in the geological reservoirs considered for CO_2 storage are above the critical point for CO_2 (31.6 °C and 7.3 MPa). These conditions result in a high CO_2 content per unit volume and a gas-like viscosity, and accelerate the carbonation process of the cement. Thus, the carbonation front might not be stopped by the carbonate barrier and continue its progression through the material. This barrier constituted by $CaCO_3$ can be dissolved by the CO_2–rich environment surrounding the cement sheath, which would increase its porosity again [32, 71, 72, 73]:

$$H^+ + HCO_3^- + CaCO_3 \rightarrow Ca^{2+} + 2HCO_3^- \tag{2.19}$$

This dissolution continues until thermodynamic equilibrium is reached [74], increasing porosity, permeability, and reducing compressive strength [75]. The cement matrix, after complete carbonation and degradation, may result in a porous medium of low resistance,

unable to maintain the integrity of the borehole or its sealing ability against leakages towards upper formations [76, 77].

The carbonation process and a brief summary of the evolution of cement components can be seen in Figure 2.15. Cement carbonation produces a leaching front, which is characterized by an increase in porosity, followed by a $CaCO_3$ precipitation zone of low porosity [69], and finally, near the exposed front, a degraded zone of low pH, high porosity, and low strength is generated [71]. This front exposed to the high level of carbonic acid is capable of leaving a zone of high porosity and only reinforced with silica gel. These fronts are of variable penetration and thickness, depending on the cement curing conditions [78] and density [79].

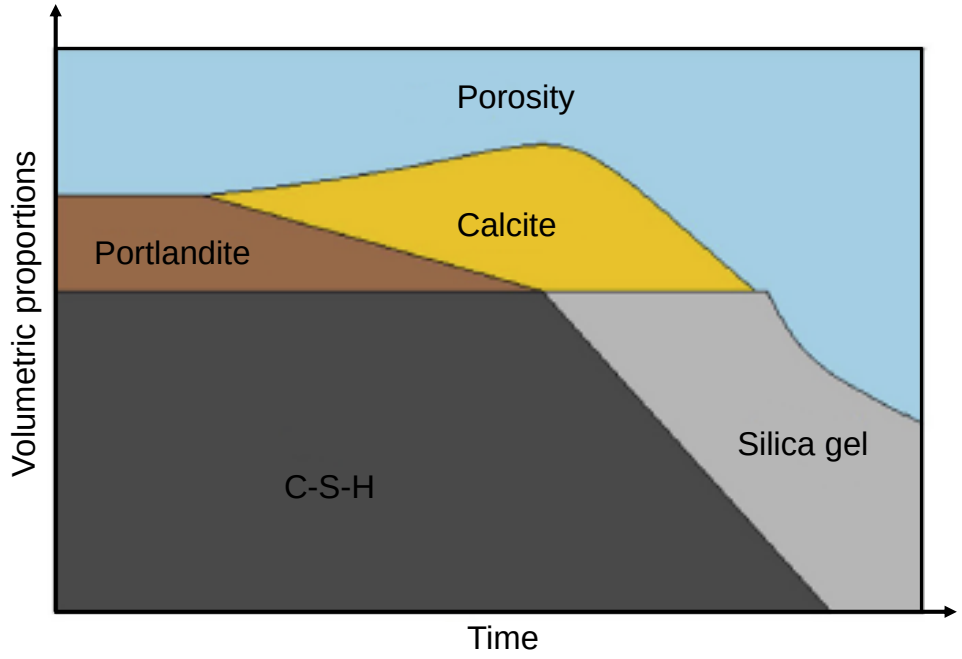

Fig. 2.15.: Volumetric proportions of an elementary volume of the cementitious matrix (after Bagheri et al. [80]).

The microscopic structure of an uncarbonated cement and a cement exposed to carbonation can be observed in Figure 2.16 through an scanning electron microscopy. The image on the left is a non-carbonated cement, while the image on the right is carbonated cement at atmospheric pressure and 27 °C temperature. The brightest region corresponds to anhydrous cement grains, light grey region corresponds to calcium hydroxide and C-S-H and black colour represents pores. After carbonation, brighter products begin to appear, these are the calcium carbonates that precipitate. It can also be observed that the zone is denser with the precipitation of these products.

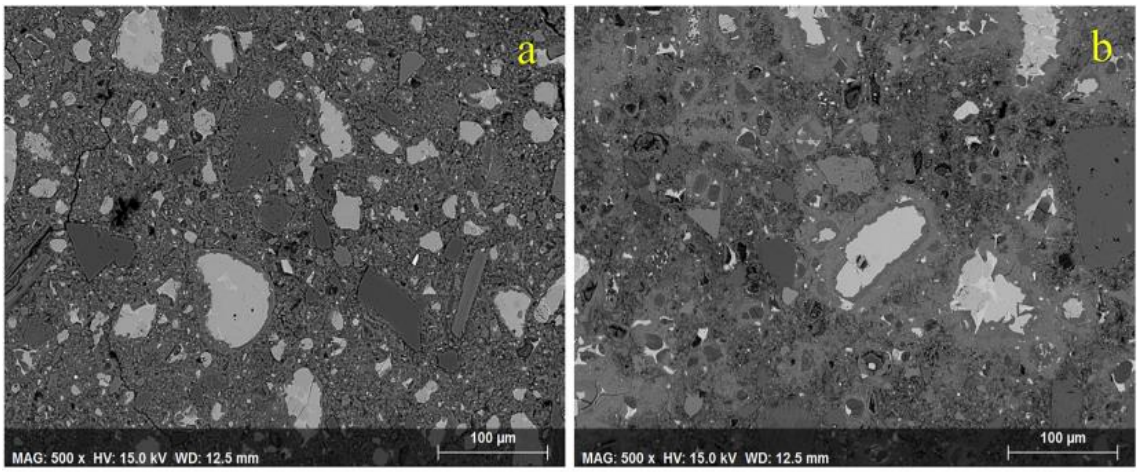

Fig. 2.16.: (a) Uncarbonated cement (b) Carbonated cement (after Shah et al. [68]).

Experiments have been carried out to determine the behaviour while the hydration process evolves, as well as the effects produced when supercritical carbonation is occurring. These experiments can be under static conditions [81] or in a dynamic system [82, 83]. Furthermore, there are different states of supercritical carbonation to which a specimen can be subjected:

- Supercritical carbon dioxide, at temperatures higher than 31 °C and pressures higher than 7.38 MPa. [30, 84, 85]
- Supercritical carbon dioxide dissolved in brine. Brine is a salt solution containing little or no suspended solids. [73, 86, 87, 88]
- Supercritical carbon dioxide dissolved in pure water. [89, 90, 91, 92]
- Supercritical carbon dioxide dissolved in acidified water. [82, 93, 94]

Kutchko et al. [84] performed experiments on Class H Portland cement with a w/c ratio of 0.38 by subjecting it to curing and also carbonation under pressure and temperature conditions representative of geostorage.

They analyzed two types of chemical aggressors: carbonated brine and wet $scCO_2$. With a scanning electron microscope (SEM) equipped with a backscattered electron imaging detector (BSE) and energy dispersive spectroscopy (EDS) they were able to observe the advance of the carbonation front within the mixtures. They were able to contemplate that there is a difference in physical reaction of the cement using carbonated brine and $scCO_2$. In the case of aqueous aggressor, 4 zones can be observed in the cement (Figure 2.17), which are the unaltered cement, the CH depleted zone, the $CaCO_3$ barrier and the degraded zone.

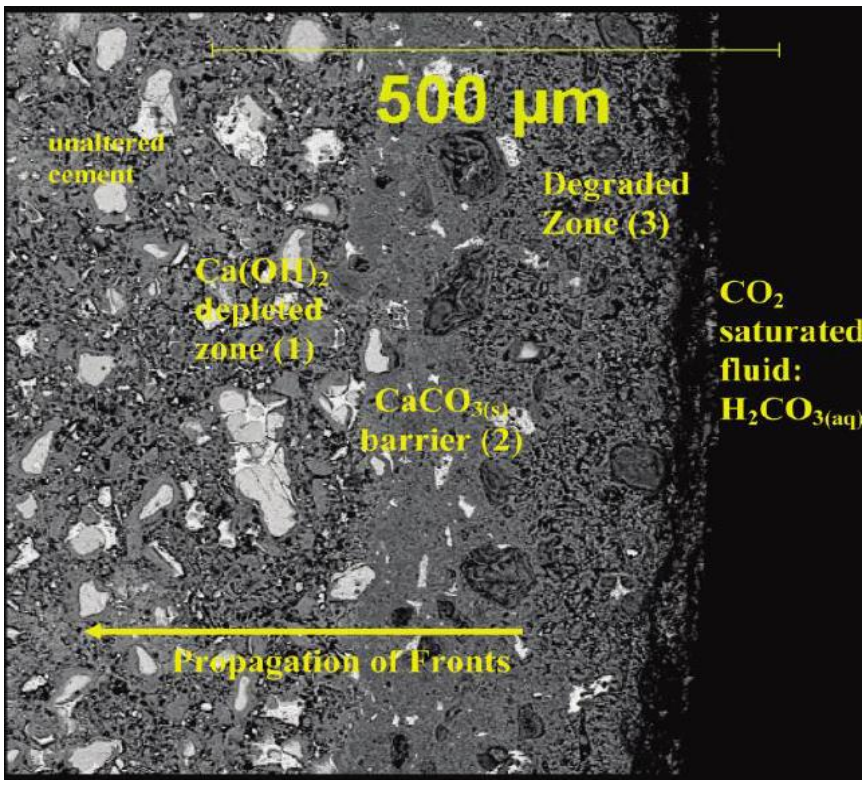

Fig. 2.17.: Carbonation breakthrough in specimens subjected to carbonated brine (after Kutchko et al. [69]).

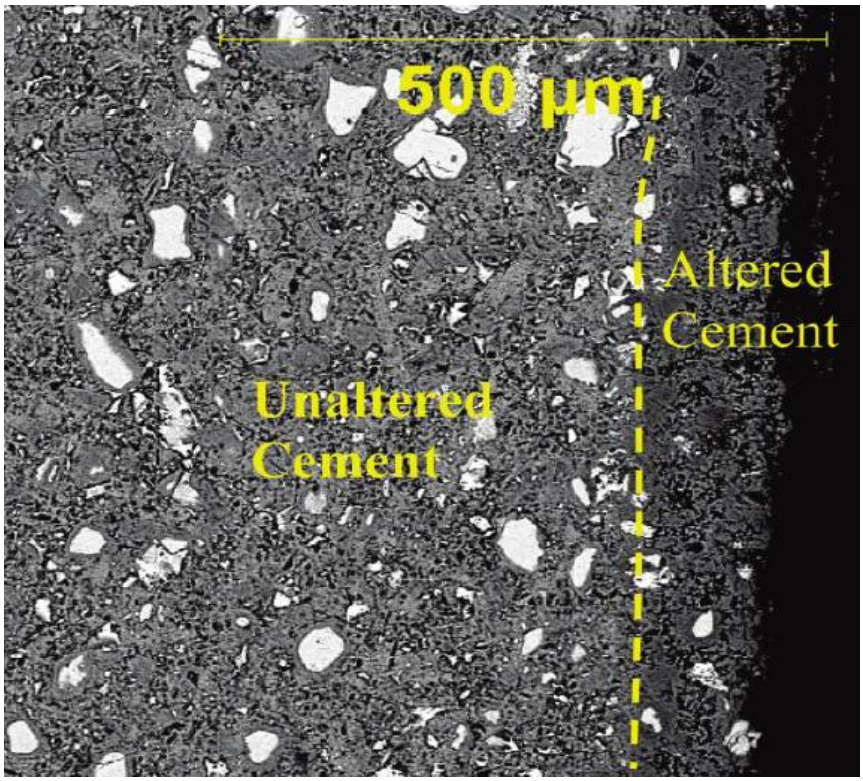

Fig. 2.18.: Carbonation breakthrough in specimens subjected to wet $scCO_2$ (After Kutchko et al. [69]).

The degraded zone is the one closest to the aggressive atmosphere where chemical reactions are more advanced, so it is the most porous and has poor mechanical properties. The $CaCO_3$ barrier may advance towards the core of the cement paste depending on the permeability of the $CaCO_3$ barrier and CH depleted phases which may or may not block the advance of the carbonate brine. Another question to determine is whether or not the formation of $CaCO_3$, depending on their crystalline phase, can induce tensile stresses within the cement matrix and crack it, and allow the carbonated brine to pass through.

In contrast, cement exposed to $scCO_2$ produced a slow penetration into the paste that did not develop individual distinct alteration zones, this penetration is seen in Figure 2.18. This may be due to the lack of water to diffuse ions out of the cement matrix. SEM-EDS revealed that in these samples the $CaCO_3$ precipitates in place and is not as dense compared to the previous experience.

The difference between supercritical carbonation in brine, pure water or acidic water is essentially the pH level of the solution. Barlet-Gouédard et al. [87, 73] showed that after 2 days of reaction with CO_2-saturated brine, the alteration front was only a tenth of what was observed in the reaction with CO_2-pure water [89]. Finally, Duguid's experiments [82] showed that CO_2 dissolved in water at very low pH significantly affects the structure of

cement, with distinct observable fronts of various colors as shown in Figure 2.19. However, here it is more difficult to separate the two effects of acid and carbonation.

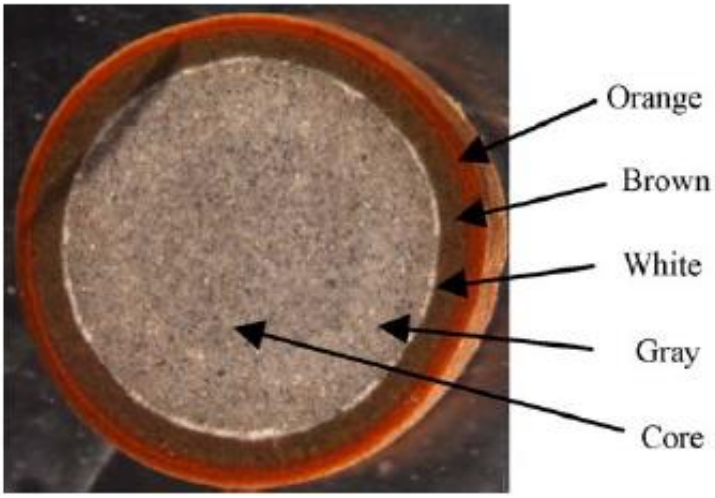

Fig. 2.19.: Reaction zones for samples run with influent pH 2.4 (After Duguid et al. [82]).

2.3 Bacterial nanocellulose (BNC)

2.3.1 Introduction

A polymer is a chemical compound in which the molecules are made up of long chains in which a basic unit called a monomer is repeated. Each polymer has certain properties. One polymer or another can be chosen depending on the properties required of a material for a particular use. These polymers can be found naturally in the environment or can be synthesized in laboratories.

Cellulose is a material found in nature: it is a renewable and degradable material, non-toxic and therefore safe to use. It is also the most abundant biopolymer in nature and, together with lignin, is one of the structural components of plants. Bacteria also produce this material, which is composed of glucose units linked together by chemical bonds. This material is composed of amorphous parts and of ordered crystalline parts. The crystalline part has the shape of a rectangular prism, whose dimensions vary according to the source of the cellulose [95]. Their length varies from 10 to 200 nanometers and the width is from 3 to 50 nanometers. When the amorphous parts of the cellulose are removed, the crystalline parts remain, which, due to their arrangement, have very high mechanical properties. These crystalline parts are called cellulose nanocrystals or nanocellulose, because they have dimensions in the nanometer range [96]. There are three types of nanocellulose depending on how it is produced; microfibrillated nanocellulose (MFC), nanocrystalline cellulose (NCC), and bacterial nanocellulose (BNC).

2.3.2 BNC Characteristics

Bacterial nanocellulose is an environmentally friendly material [97] produced by several bacteria types in different culture media. It is a bio-polymer non-soluble in aqueous solutions, with high mechanical properties, and thermally resistant. For instance, Gatenholm et al. [98] compares the mechanical strength with other polymers, such as polypropylene or cellophane, and shows that BNC has a Young's modulus between 4 and 10 times higher, while the tensile strength is between 2 to 5 times higher on average.

In particular, *Gluconacetobacter xylinus* bacteria is one of the primary microbial producers of this material (Figure 2.20), on which research is still ongoing [99], with essential advances about bacterial cultivation [100, 101]. Bacterial nanocellulose has the same molecular formula as plant cellulose, but it is different in its nanofiber architecture. Bacteria-produced

ribbons normally show rectangular cross-sections with thicknesses around 3–10 nm., 30–100 nm in width, and 1–9 mm in length [102].

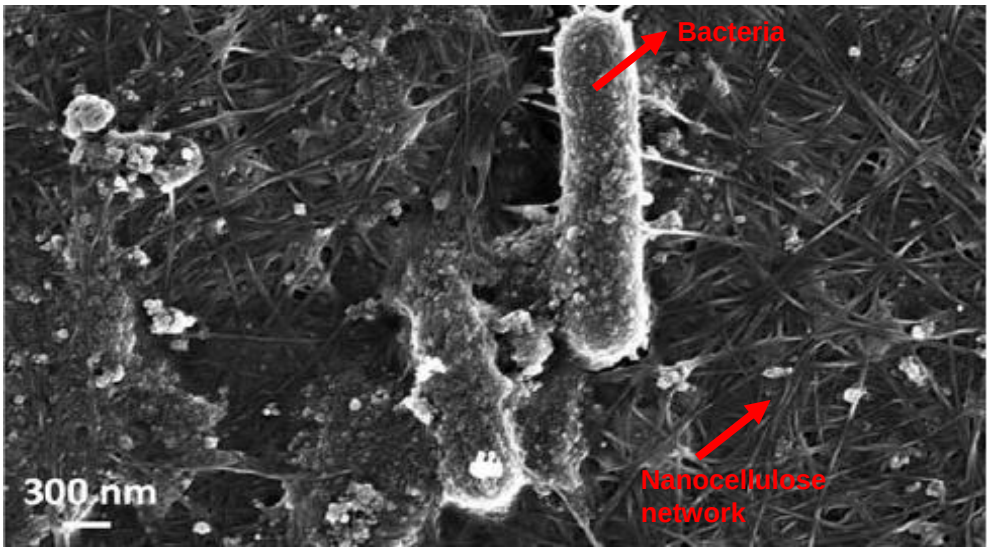

Fig. 2.20.: *Gluconacetobacter xylinus* bacteria and bacterial nanocellulose (after Cerrutti et al. [103]).

New studies on the cost-effectiveness of culture media are making bacterial nanocellulose production a significant subject of interest for industrial applications [104]. Recently, there has been new methods of production of bacterial nanocellulose utilizing residues from the wine industry and using corn steep liquor, which demonstrated a four-time higher yield of this product in an inexpensive fermentation medium [103]. This increase in quantity becomes significant after 21 days of incubation. Furthermore, its structure is more compact and dense because it generates a more substantial number of branches that intertwine with each other [105]. These denser nanocellulose fibers are obtained with nanometric widths in the range of 18 to 57 nm and micrometers in length, thus obtaining a high specific surface area material.

2.3.3 Feasibility of using nanocellulose as a cement additive

Additions to the cementitious mix, such as silica fume [106], epoxy resins [107] or latex [108], are currently being studied to improve resistance to CO_2 exposure. Nowadays, there has been a growing interest in nanocellulose technology [109]. Nanocellulose has a background in reducing micro-cracking [110, 111]. Its addition to cement is very likely to induce an increment in tensile strength and prevent the propagation of cracks caused by external loads. There are three types of nanocellulose according to how it is produced: microfibrillated nanocellulose (MFC), nanocrystalline cellulose (NCC), and bacterial nanocellulose (BNC).

Several authors have proved that nanocellulose improves the mechanical and microstructural properties of cement-based components [101, 112]. These studies are mainly focused on the research of microfibrillated nanocellulose (MFC) and nanocrystalline cellulose (NCC). The properties that were improved were flexural and compressive strength, thermal performance, degree of hydration, viscosity and water retention properties of cement [113, 114, 115, 116].

For example, Sun et al. [112] determined that the addition of cellulose nanofibers (CNF) improved the tensile strength. He explains this by arguing that the addition of CNF is more resistant to tensile strength than cement, so the strength of fiber reinforced composites increases when the amount of CNF increases. In a subsequent work [117], they indicated that compressive strength also increased. In this study, they determined the degree of cement hydration with a thermogravimetric analysis (TGA). This technique consists of measuring the mass of a sample over time as temperature is applied. Thus, it is possible to determine at what temperature the hydration products of cement dissociate, and to determine their quantity. They observed that the amount of portlandite and degree of hydration increased as the amount of CNF increased Figure 2.21. Therefore, the addition of CNF could increase the strength of the cement from its intrinsic mechanical characteristics and also from the effect that these fibers produce in the cement hydration process.

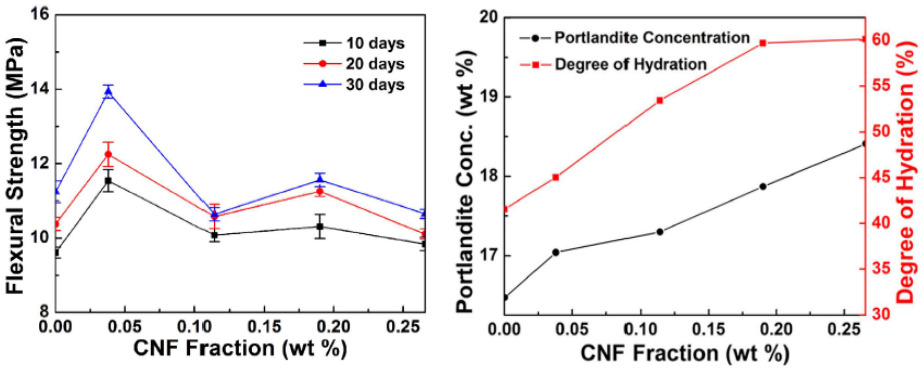

Fig. 2.21.: Flexural strength and degree of hydration of cement for different CNF contents. (after Sun et al. [112, 117]).

Nevertheless, there are few studies on the bacterial nanocellulose (BNC) [118, 119], and there are no studies on carbonating BNC-containing cement under supercritical conditions. Recently, BNC has been used to modify properties of the drilling fluids, enhance oil recovery (EOR), and oil well cementing [120]. BNC is expected to have an effect on cement similar to that of MFC and NCC. The use of BNC in cement mortars shows an improvement in flexural and compressive strength [121]. Moreover, studies show that nanofibers act as bridges over cracks creating reinforcement mechanisms as described in Figure 2.22, which prevents crack propagation at the microestructural level [121, 122]. Overall, these benefits make

this material to be considered as an admixture for cement-based materials [101, 123], and also for other uses in the oil and gas industry [123, 124].

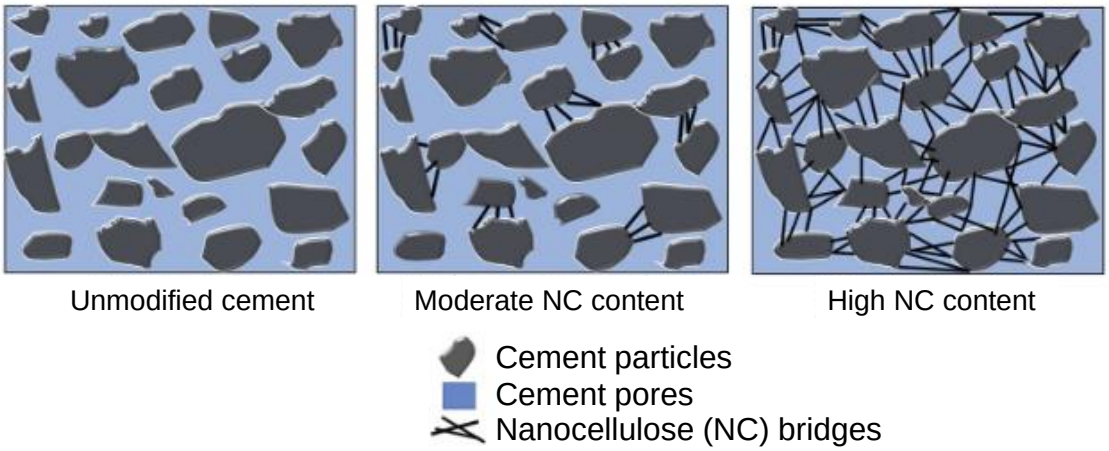

Fig. 2.22.: Schematic of the generation of bacterial nanocellulose network (NC) among cement hydration products (after Hisseine et al. [125]).

The modification of cement to improve some properties is a subject of interest in the cement wellbore industry. Evidence shows that nanocellulose can be used as a crack-inhibitor to avoid cement damage and thus prevent CO_2 leakage through the upper formations [110, 111]. Furthermore, nanocellulose can be considered as a potential additive to improve cement properties, such as mechanical or thermal resistance, and to reduce transport properties by reducing cement porosity [115, 126]. Low permeability is essential for oil well cement in the context of CCS because it prevents or slows down the external supply of CO_2-bearing fluids. Any improvement in avoiding CO_2 income could lead to a considerable extension of cement durability.

Therefore, the study of bacterial nanocellulose as an additive for oil well class G cement is an promising alternative to improve cement performance in petroleum engineering applications, especially in the context of geological storage of CO_2.

Materials and experimental methods 3

3.1 Introduction

This chapter is dedicated to the materials and methods used for the characterization of class G cement paste with the addition of bacterial nanocellulose.

The materials section lists the components used in the cementitious mixture and explains the preparation of the slurry.

The methods section details the tests performed on the slurry and hardened cement paste. Free fluid and thickening-time tests were performed to characterize the slurry with BNC. The mechanical behaviour of the hardened state was investigated through the dynamical mechanical analysis (DMA), measurements of elastic ultrasound waves, unconfined compressive strength (UCS) and triaxial experiments. The set up and operation of the carbonation cell is also described in this section. The microstructure and crystalline characterization were studied by means of thermogravimetric analysis (TGA), mercury intrusion porosimetry (MIP), water porosity, scanning electron microscopy (SEM) and X-ray diffraction (XRD).

3.2 Materials

Cement

The cement used in this study was class G API Portland Cement, provided by PCR S.A (Petroquímica Comodoro Rivadavia S.A. - Argentina). The clinker and calcium sulfate were dosed to satisfy the chemical requirements of the American Petroleum Institute (API) Standard 10A for cement [38]: C_3S 52.8%, C_3A 1.6%, C_2S 21.1% and C_4AF 15.5%. To obtain a high sulfate resistance grade, this cement is characterized by a very low aluminate content compared to other types of cements. The chemical composition obtained by PCR S.A. through X-ray fluorescence (XRF) is given in Table 3.1 and its Blaine specific surface is 367 m^2/kg. The XRF system consists of an X-ray generator tube, collimators, crystals, and beam detectors. The excitation of the atoms from the X-rays emits radiation that is detected by the equipment, thus quantifying the chemical composition of the cement.

Componente	Value [%]
CaO	62.39
SiO_2	21.23
MgO	2.22
Al_2O_3	3.84
Fe_2O_3	5.07
NaO	0.3
K_2O	0.34

Tab. 3.1.: Class G cement composition.

Water

Fresh deionized water was used at a temperature of 23 °C ± 1 °C. This water does not contain impurities of any kind and is suitable for its use because it does not affect the properties in fresh or hardened state of cement.

Bacterial nanocellulose

Bacterial nanocellulose (BNC) is a polymer derived from cellulose obtained from the aerobic fermentation of bacteria of the genus *Gluconacetobacter* as the primary extracellular metabolite [109]. It was provided by the ITPN-CONICET in the form of a membrane in sealed jars [103].

BNC membranes were wet-grounded to obtain the BNC additive. Then, the BNC-distilled water mixture was conditioned in a 6.5 L Arcano ultrasonic bath with a frequency of 40,000 Hz for 30 min (Figure 3.1). This procedure breaks up the nanocellulose agglomerated fibers. The use of the ultrasound technique improves the mechanical properties of the mixture by dispersing the nanocellulose and generating a more homogeneous paste [127]. The BNC proportion was determined by weighing three representative samples from the additive before and after placing the samples inside an oven for 24 h. Free water was evaporated, and the average quantity of BNC obtained was approximately 0.46% of the total weight. The additive was sealed in glass jars and stored in a refrigerator. They were taken to room temperature at the moment of use.

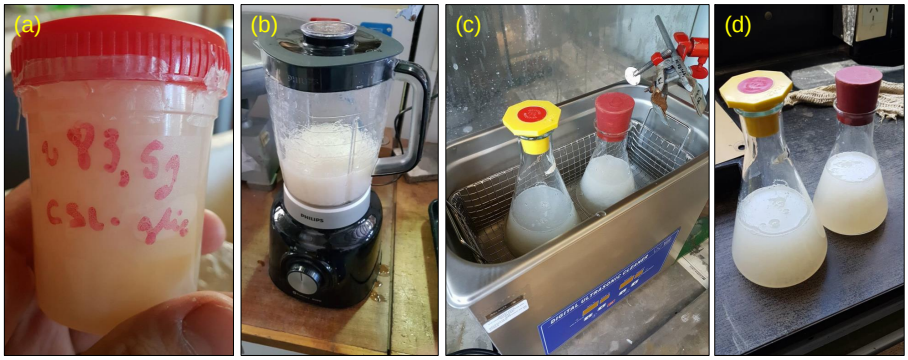

Fig. 3.1.: (a) BNC in sealed jars, (b) BNC wet-grounded and mixed together with additional water, (c) ultrasonic bath, and (d) BNC final additive.

Superplasticizer

Superplasticizer was used in this work to give an adequate flow to the slurry once containing the BNC. Due to the water retention properties of the BNC, the viscosity of the slurry increases, which degrades its performance when BNC is incorporated.

The superplasticizer utilized was the ADVA 175 LN, a commercial product based on polycarboxylates listed as a high performance water reducing additive, with a density of 1.06 g/cm^3 [128]. The recommended dose for this type of superplasticizer varies between 0.4% and 1% by weight of cement (BWOC), but it depends on the type of cement utilized, temperature, transportation time, and application conditions.

Slurry preparation

The slurry was mixed according to API specifications. A high-speed mixer with an API standard blade type was used [38]. The mixing procedure consisted of 15 s at a rotation speed of 4,000 ± 200 rpm, and then, 35 s at 12,000 ± 500 rpm. The cement was passed through an ASTM No. 20 sieve. Each slurry was prepared with 792 ± 0.5 g of cement and 349 ± 0.5 g of distilled water at a temperature of 23 ± 1 °C, obtaining a water to cement (w/c) ratio of 0.44, whatever the BNC content. The BNC additive already contains water, so this amount of water must be taken into account. The amount of additional water to obtain a w/c ratio of 0.44 by weight is calculated by:

$$W_{AD} = W_T - W_{BNC} \tag{3.1}$$

being: W_T = total amount of water = 349 g; W_{BNC} = BNC-distilled water; W_{AD} = water needed to reach W_T.

The additive was first placed in the mixer. The extra water needed was later introduced along with the superplasticizer in the mixer and it started with a rotation speed of 4.000 ± 200 RPM while the cement was added during the first 15 seconds. Then, the revolutions were automatically raised to 12.000 ± 500 RPM for 35 seconds. The tests carried out were for Portland cement (PC) and Portland cement with percentages of nanocellulose of 0.05%, 0.1%, 0.15% and 0.20% BWOC. Table 3.2 shows the cement dosages used.

Reference	Additive [g]	BNC [g]	W_{BNC} [g]	W_{AD} [g]	Total water [g]	Cement [g]	BNC content [%]
PC	0.00	0.00	0.00	349.00			0.00
BNC05	89.09	0.40	85.69	263.31			0.05
BNC10	172.17	0.79	171.38	177.62	349	792	0.10
BNC15	258.26	1.19	257.07	91.93			0.15
BNC20	342.80	1.58	341.22	7.78			0.20

Tab. 3.2.: Bacterial Nanocellulose content in cement paste.

To determine the effect of BNC on non-carbonated specimens, the slurry was poured into standard cubic molds of 5 cm side following the API specifications (ASTM International, 1999). The slurry was compacted 27 times in two layers with a puddling rod. The molds were placed in the curing chamber at a temperature of 20 ± 1 °C, and after 24 h inside the molds, the specimens were removed and put under water saturated with limestone until testing. The same procedure was followed to produce 38 mm x 100 mm cylindrical specimens for carbonation. Two curing methods were considered for the cylindrical specimens.

A. Specimens cured for 28 days under water saturated with limestone. This method provides information on cements cured under optimal conditions.

B. Specimens cured in a 90 °C batch, unmolded after 24 h and kept underwater for 48 h. Then, they were dried at 85 °C for 1 week. This method provides information on cements cured under unfavorable conditions, simulating a dry curing after being 48 hours under water in the wellbore.

After setting, the top and bottom of the cylindrical specimen were cut with a diamond wire saw to a geometry of 38 mm x 76 mm.

3.3 Experimental methods

3.3.1 Free fluid test

The free fluid or free water content is the volume of fluid that separates from the cement slurry once the slurry remains at rest. PC and modified PC with BNC slurries were prepared in accordance with the API Standard 10A [38]. After the high-speed mixing, the slurry was placed in an atmospheric consistometer. The atmospheric consistometer consists of a rotating cylindrical slurry container equipped with a stationary pallet system. The rotational speed is 150 ± 15 RPM. The vessel was kept at a controlled temperature of 27 ± 2 °C in an oil bath. After stirring the slurry for 20 min ± 30 s in the atmospheric consistometer,

760 ± 5 g of slurry were transferred directly to a 0.5 L Erlenmeyer flask within 1 min of completion of mixing. The flask was kept on an anti-vibration surface for 2 h, and the excess liquid at the top was removed and measured with a pipette. The percentage of free liquid was calculated using the following formula:

$$\varphi = \frac{V_{FF} * \rho}{m_s} \times 100 \tag{3.2}$$

where φ is the volume fraction of free fluid expressed as a percentage, V_{FF} is the volume collected with the pipette, m_s is the mass of the slurry in grams and ρ is the density of the slurry in g/cm^3 which is associated with the cement density. The cement density was obtained following the IRAM 1624 Standard: cement (64 g) was placed into a Le Chatelier flask containing 0.5 cm^3 of kerosene at room temperature of 20 ± 2 °C and relative humidity 50%. After removing the retained air, the final reading was measured after 150 ± 30 min. The cement density obtained was 3.18 ± 0.01 g/cm^3. The associated slurry density is 1.91 g/cm^3. The performed tests are listed in Table 3.3.

Test	Reference	SP [%]	BNC content [%]
1	FF-1	0.00	0.00
2	FF-2	0.10	0.00
3	FF-3	0.20	0.00
4	FF-4	0.30	0.00
5	FF-5	0.40	0.00
6	FF-6	0.50	0.00
7	FF-7	0.10	0.05
8	FF-8	0.25	0.05
9	FF-9	0.35	0.05
10	FF-10	0.40	0.05
11	FF-11	0.45	0.05

Tab. 3.3.: Free fluid experiments.

3.3.2 Thickening-time test

Cementing a wellbore requires a cement slurry capable of maintaining an adequate state of pumpability under downhole conditions over a specific period of time. Thickening time was determined with a high-temperature and high-pressure consistometer following the API Specification 10A. The consistency of the slurry over time is measured in Bearden units (B_C).

The cement slurry was poured into a standardized container and stirred at a constant speed. A ramp of temperature and pressure over time was applied to the system until Bearden unit of consistency reached 100 B_C for a specific time. This time is known as the

thickening time of cement. The consistency should be less than 30 B_C between 15 and 30 min after the beginning of the test to ensure adequate initial consistency. In the field, the time to 100 Bearden units represents the amount of time cement remains pumpable under well conditions. Bearden units are dimensionless, cannot be converted to any viscosity unit, and can only be determined by the high pressure and temperature consistometer. The performed tests are listed in Table 3.4.

Test	Reference	SP [%]	BNC content [%]
1	CONS-1	0.00	0.00
2	CONS-2	0.05	0.05
3	CONS-3	0.15	0.05
4	CONS-4	0.30	0.05
5	CONS-5	0.35	0.05
6	CONS-6	0.40	0.05

Tab. 3.4.: Consistometry experiments.

3.3.3 Dynamical mechanical analysis (DMA)

Cement undergoes temperature variations during its life span when it is used as annular protection for the wellbore. Cement is mechanically affected when a temperature increment is applied to it.

In order to evaluate the thermo-mechanical properties of cement, a dynamic mechanical analysis (DMA) was performed. DMA measures these properties as a function of time and temperature while the material is subjected to a periodic oscillatory force [129]. In this case, oscillatory bending stress was applied. The storage modulus (E') is the stiffness of the material and represents the capacity of the material to store the applied energy. The loss modulus (E'') is the capacity of the material to dissipate the applied energy and is also related to the viscous response of the material [130]. The vector composition between the storage modulus and loss modulus is the complex modulus ($E*$). The angle formed by these vectors is the mechanical damping factor of the material (δ) [131]. A material that can store a large amount of applied energy will have a small angle δ (high elasticity).

The dynamic mechanical analysis was performed with a Perkin- Elmer DMA 8000 instrument using the three-point bending mode. The deformation imposed on each pulse was 0.001 mm, with a pulse frequency of 1 Hz. The test began at room temperature and increased until 200 °C with a constant rate of 2 °C/min. For each pulse, the storage modulus was measured. A total of 20 samples of 3 mm × 9 mm × 30 mm were tested, four for each nanocellulose percentage (0%; 0.05%; 0.1%; 0.15%; 0.20% BWOC). The performed tests are listed in Table 3.5.

Test	Reference	SP [%]	Quantity	Final temperature [°C]
1	DMA-00	0.00	4	
2	DMA-05	0.05	4	
3	DMA-10	0.10	4	200
4	DMA-15	0.15	4	
5	DMA-20	0.20	4	

Tab. 3.5.: DMA experiments.

3.3.4 Measurement of elastic ultrasound waves

A portable OLYMPUS EPOCH XT was used to allow P and S ultrasonic waves measurements (UWM). Two transducers were placed on the top and bottom surfaces with a thin layer of gel to ensure full contact between the specimen surfaces and the transducers. The time it takes for the P and S elastic wave signals to travel through the specimen was measured and divided by the length of the specimen. The dynamic shear and bulk moduli are then calculated as follows:

$$G = \rho V_S^2 \tag{3.3}$$

$$K = \rho \left(V_P^2 - \frac{4}{3} V_S^2 \right) \tag{3.4}$$

While the Young's modulus and Poisson ratio are calculated by:

$$E = \frac{9KG}{3K + G} \tag{3.5}$$

$$\nu = \frac{3K - 2G}{6K + 2G} \tag{3.6}$$

The list of performed tests is shown in Table 3.6. All specimens were saturated before testing. The references are UWM-W-XX-ZZ, where W is the curing method (A or B), XX is the BNC percentage (0, 0.05 or 0.15%) and ZZ is the number of days under carbonation.

Test	Specimen condition	Reference	Quantity	BNC [%]
1	Non-carbonated	UWM-B-00-00	8	0.00
2		UWM-B-05-00	8	0.05
3	Carbonated	UWM-B-00-30	4	0.00
4		UWM-B-05-30	4	0.05
5		UWM-B-00-120	4	0.00
6		UWM-B-05-120	4	0.05

Tab. 3.6.: UWM on specimens cured at 90 °C.

3.3.5 Unconfined compressive strength (UCS)

Cubic specimens

After mixing according to Section 3.2, the slurry was poured into standard cubic molds of 5 cm per side following the API specifications for the subsequent compressive strength tests [132]. The molds were placed in the curing chamber at a temperature of 20 ± 1 °C, and after 24 h inside the molds, the specimens were removed and put back inside the chamber. Once the curing time had passed, the axial compression test was performed with planar metal heads according to the API at a loading rate of 72 ± 7 kN/min (Figure 3.2).

Fig. 3.2.: (a) API mixer (b) uniaxial compression test.

Test	Reference	Curing days	Quantity	BNC content [%]
1	UCS-00-01	1	3	0.00
2	UCS-05-01	1	3	0.05
3	UCS-10-01	1	3	0.10
4	UCS-15-01	1	3	0.15
5	UCS-20-01	1	3	0.20
6	UCS-00-07	7	3	0.00
7	UCS-05-07	7	3	0.05
8	UCS-10-07	7	3	0.10
9	UCS-15-07	7	3	0.15
10	UCS-20-07	7	3	0.20
11	UCS-00-28	28	3	0.00
12	UCS-05-28	28	3	0.05
13	UCS-10-28	28	3	0.10
14	UCS-15-28	28	3	0.15
15	UCS-20-28	28	3	0.20

Tab. 3.7.: UCS experiments on cubic specimens.

The tests were performed using bacterial nanocellulose with percentages of 0.05%, 0.10%, 0.15%, and 0.20%, with adequate percentages of SP to obtain workability. Specimens were

cured for 1, 7 and 28 days to know the evolution over time of the compressive strength. The results are obtained from an average of 3 specimens for each percentage of BNC used. The absolute variation from the average was considered for the analysis. Table 3.7 shows the tested specimens. The references are UCS-XX-YY, where XX is the BNC percentage (0, 0.05 or 0.15%) and YY is the number of days of curing.

Cylindrical specimens

Unconfined compression tests were performed on a 100 kN testing machine with a loading rate of 0.5 mm/min. Vertical displacement and applied force were monitored during the compression tests. The compressive strength and Young's modulus were calculated for all specimens. The averages of strength values and Young's modulus were calculated from 3 specimens. Table 3.8 shows the specimens tested. The references are UCS-W-XX-ZZ, where W is the curing method (A or B), XX is the BNC percentage (0, 0.05 or 0.15%) and ZZ is the number of days under carbonation.

Test	Reference	Quantity	Curing method	Carbonation days	BNC [%]
1	UCS-A-00-00	3	A	0	0.00
2	UCS-A-05-00	3			0.05
3	UCS-A-15-00	3			0.15
4	UCS-A-00-30	3		30	0.00
5	UCS-A-05-30	3			0.05
6	UCS-A-15-30	3			0.15
7	UCS-A-00-120	3		120	0.00
8	UCS-A-05-120	3			0.05
9	UCS-A-15-120	3			0.15
10	UCS-B-00-00	3	B	0	0.00
11	UCS-B-05-00	3			0.05
12	UCS-B-00-30	3		30	0.00
13	UCS-B-05-30	3			0.05
14	UCS-B-00-120	3		120	0.00
15	UCS-B-05-120	3			0.05

Tab. 3.8.: UCS experiments on cylindrical specimens.

3.3.6 Triaxial experiments

Triaxial tests were performed in cement specimens to determine the mechanical properties at different confinement conditions, simulating underground conditions.

Cylindrical cement specimens of 38 mm of diameter and 78 mm height were placed inside a neoprene membrane. Two linear variable differential transformers (LVDT) were positioned in the axial direction and four in a radial direction touching a thin aluminum sheet glued to four radial pierced holes in the membrane. This aluminum plate is in contact with the specimen and accompanies its deformation. The LVDT's are not positioned directly

on the membrane because it is less rigid than aluminum and the readings taken would be influenced by its deformation.

Metallic porous disks were placed on the top and bottom of the specimen to allow a homogeneous pore pressure distribution. Pore pressure, confinement pressure and deviatoric loading were measured by electronic transducers and controlled by a software linked to hydraulic pumps.
The performed tests were:

- Undrained isotropic tests
- Drained isotropic tests
- Triaxial compression tests

The specimen was vacuumed by an air pump connected to the pore pressure pipelines and the confinement cell was filled with oil at a pressure of 0.8 MPa. Once the cell was filled, the confinement pressure was increased up to 2 MPa and both pore pressures were increased to 1 MPa. As the vacuum partially dried the specimen, a saturation condition was maintained during 3 days before testing.

The isotropic tests were performed with initial confining values ranging from 5 to 30 MPa. The isotropic load increases to a certain value and then decreases to the initial value. The bulk modulus of the specimen is measured from the load curve. In the undrained isotropic test, the pore pressure exit valve is closed, preventing mass exchange. The loading rate was 0.1 MPa/min. In this case, the increase in pore pressure within the specimen is measured through pressure sensors. For the drained isotropic test, the confinement pressure and pore pressure were set at an initial value. The pore pressure valves were open and the confinement pressure was increased. The loading rate was 0.02 MPa/min. Under these conditions, the pore pressure was maintained at the same value and the volumetric strains increments were measured. This slow loading rate allows pore pressure to dissipate and avoids pressure jumps.

The triaxial compression test consists of applying a confining pressure σ_3 and then applying a deviatoric load q ($q = \sigma_1 - \sigma_3$) until failure. The test was performed under undrained conditions for non-carbonated specimens. The deviatoric load is applied after reaching desired initial values of confinement and pore pressures. The loading rate used was 0.5 MPa/min. Once the deviatoric pump flow rate was known to obtain this velocity, the load mode was changed to strain-controlled with a constant flow rate for safety to avoid large load increases if the specimen failed. Pore pressure variation (p), deviatoric stress (q), axial strain (ε_{long}) and radial strain (ε_{trans}) were measured.

The parameters obtained during triaxials tests were: undrained bulk modulus (K_u), drained bulk modulus (K_d), Skempton coefficient (B), Young's modulus (E) and Poisson ratio (ν). The performed tests are listed in Table 3.9.

Test	Reference	Quantity	Loading path	BNC content [%]
1	KD-00	3		0.00
2	KD-05	3	Isotropic drained test	0.05
3	KU-00	4		0.00
4	KU-05	6	Isotropic undrained test	0.05
4	KU-15	1		0.15
5	DEV-00-U	2		0.00
6	DEV-05-U	1	Deviatoric undrained test	0.05
7	DEV-15-U	1		0.15

Tab. 3.9.: Triaxial experiments.

3.3.7 Supercritical carbonation test

The carbonation tests were carried out in a titanium vessel of 16 cm inner diameter and 20 cm high, under static conditions. Neat and BNC-modified cement samples were carbonated under wet supercritical CO_2 at 20 MPa and 90 °C, for 30 days and 120 days. Before carbonation, the container with the specimens under water was placed inside a vacuum vessel for removing the air bubbles possibly trapped inside the specimens. The set up of the equipment was as follows:

The saturated specimens were identified, measured, weighed, and placed on a container grid. A water layer was poured at the bottom of the vessel for maintaining humidity (500 ml). One o-ring was positioned on the top part of the vessel to prevent pressure leakage when the device was assembled. A safety valve of 23 MPa was installed on the top of the cell. The grid was placed inside the cell, avoiding contact between the samples and the water layer. The cell was then sealed and connected to the CO_2 pressure line, equipped with a manometer. CO_2 pressure was increased until 8 MPa. The heating system was turned on until 90 °C and the pressure regulated at 20 MPa with the leak valve, removing the remaining air at the top of the vessel. Once the desired pressure and temperature were reached, they were maintained throughout the entire test in static conditions. This process allowed the water to remain liquid. In contrast, the CO_2 went from a gaseous state, then liquid, and finally to a supercritical state when the pressure reached 7.4 MPa and the temperature 31.6 °C. These conditions allow the samples to remain saturated and CO_2 to penetrate by diffusion. The ratio of specimens-volume/vessel-volume was 0.38, and the ratio of specimen-volume/CO_2-volume was 0.79. A diagram of the carbonation system is presented in Figure 3.3.

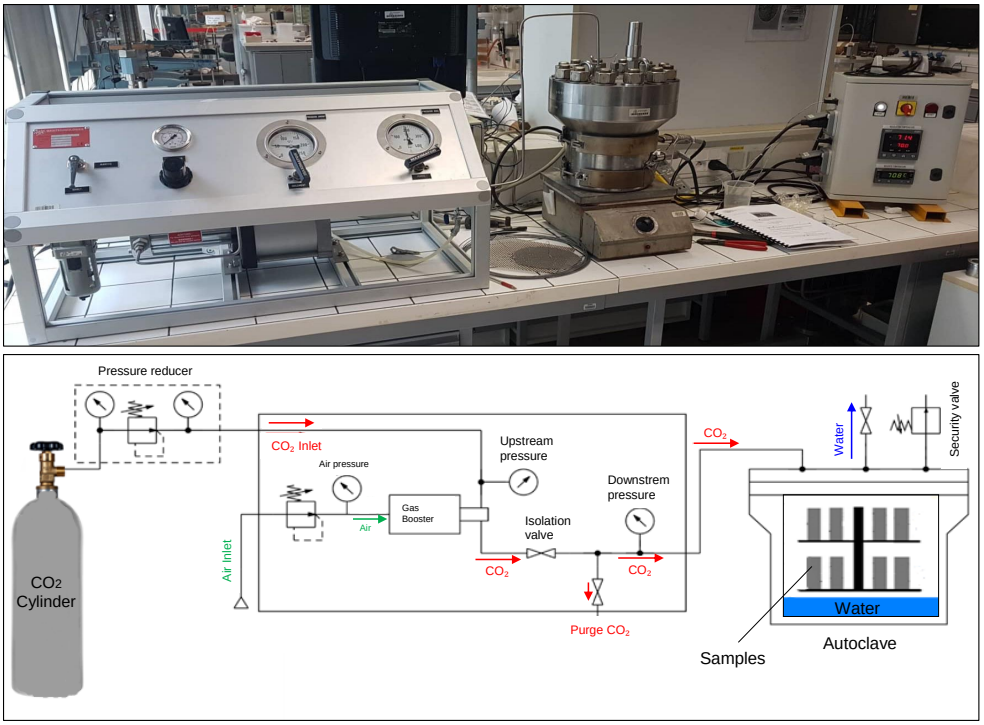

Fig. 3.3.: Carbonation system

To remove the samples, the heating system was first turned off, and temperature was allowed to drop to ambient temperature. The pressure was slowly released for two hours until it dropped to atmospheric pressure. The top lid of the vessel was separated and the grid was removed from the interior. The specimens were recovered, weighed, and photographed. The pH level was measured after carbonation.

In the first stage, a total of 18 specimens were carbonated for 30 days, of which, 6 were neat cement paste (PC), 6 had bacterial nanocellulose content of 0.05% (BNC05), and 6 of 0.15% (BNC15). Another group of 18 samples with the same percentages as before was placed inside the cell for 120 days. All these samples were cured at 20 °C.

In a second stage, a total of 16 samples were carbonated for 30 days, of which, 8 were neat cement paste (PC) and 8 had bacterial nanocellulose content of 0.05% (BNC05). Another group of 16 samples with the same percentages as before was placed inside the cell for 120 days. All these samples were cured at 90 °C.

After carbonation, 3 samples of each BNC percentage were used for compressive strength tests and one for traxial test. The other samples were cut radially and longitudinally to see the penetration depth for the different cement types and to perform the microstructural analysis. The performed tests are listed in Table 3.10. The references are W-XX-ZZ, where W is the curing method (A or B), XX is the BNC percentage (0, 0.05 or 0.15%) and ZZ is the number of days under carbonation.

Test	Reference	Quantity	BNC [%]	Curing method	Carbonation conditions
I 30 days	A-00-30	6	0.00	A	Static – No fluid flow Cell temperature: 90 °C Cell pressure: 20 MPa
	A-05-30	6	0.05		
	A-15-30	6	0.15		
I 120 days	A-00-120	6	0.00		
	A-05-120	6	0.05		
	A-15-120	6	0.15		
II 30 days	B-00-30	8	0.00	B	
	B-05-30	8	0.05		
II 120 days	B-00-120	8	0.00		
	B-05-120	8	0.05		

Tab. 3.10.: Carbonation experiments.

3.3.8 Thermogravimetric analysis (TGA)

Cement is a porous multi-phasic material whose main components are hydrated calcium silicate, calcium hydroxide, and calcium aluminate hydrates. When comparing two different cement types of the same age, the calculation of the hydration degree is useful. It estimates the amount of anhydrous cement that has reacted with water to form the cement hydrates.

The determination of non-evaporable water, calcium hydroxide (CH), calcium carbonates ($C\bar{C}$) and hydration degree (DOH) was carried out by the technique of thermogravimetric analysis. The TGA-50 Shimadzu equipment consists of a precision balance, where the sample is placed inside a platinum tray in a nitrogen atmosphere and a furnace that is programmed to increase the temperature at a constant heating rate of 10 °C/ min.

A total of five non-carbonated samples were crushed and analyzed, one for each percentage of nanocellulose (0%; 0.05%; 0.10%; 0.15%; 0.20% BWOC). Four PC and BNC05 samples taken from the core and near the surface exposed to carbonation were also analyzed. Each sample had an approximate weight of 0.008 g. The powdered material was dried at 110 °C for 24 h to remove free water [133]. The portlandite content is obtained with the technique proposed by [112]:

$$CHcontent[\%] = \frac{M_{CH}}{M_{H_2O}} \times WL_{CH} \tag{3.7}$$

The calcite content is obtained in the same way:

$$C\bar{C}content[\%] = \frac{M_{C\bar{C}}}{M_{CO_2}} \times WL_{C\bar{C}} \tag{3.8}$$

where WL_{CH} or $WL_{C\bar{C}}$ are the percentage of weight loss during the test. M_{CH}, M_{H_2O}, $M_{C\bar{C}}$ and M_{CO_2} are the molar mass of CH, H_2O, $C\bar{C}$ and CO_2, respectively.

The degree of hydration (DOH) is determined by relating chemically bound water (CBW) burned to the maximum CBW burned for cement. The maximum CBW value in ordinary cement is 0.23 g of bound water per g of a burned sample [134]. Therefore, the percentage value of the DOH can be calculated as the weight of CBW burned between 140 °C (W_{140}) and the final temperature (W_F):

$$DOH = \frac{W_{140} - W_F}{W_F \times 0.23} \times 100 \tag{3.9}$$

The performed tests are listed in Table 3.11 and Table 3.12.

Test	Reference	BNC [%]	Final temperature [°C]
1	TGA-00	0.00	800
2	TGA-05	0.05	
3	TGA-10	0.10	
4	TGA-15	0.15	
5	TGA-20	0.20	

Tab. 3.11.: TGA experiments on non-carbonated samples.

Test	Reference	BNC [%]	Final temperature [°C]
1	TGA-00-INT	0.00	1200
2	TGA-00-EXT	0.05	
3	TGA-05-INT	0.00	
4	TGA-05-EXT	0.05	

Tab. 3.12.: TGA experiments on carbonated samples.

3.3.9 Mercury intrusion porosimetry (MIP)

The MIP allows to characterize the pore structure of a sample in terms of porosity and pore size distribution. Mercury is a non-wetting fluid that can enter the pore structure of the cement when an external pressure is applied. The basic assumption to interpret MIP data is that pores are cylindrical and interconnected, thus allowing a simple calculation through the Jurin or Washburn equation:

$$p = -\frac{4\Upsilon cos\,(\theta)}{d} \tag{3.10}$$

where Υ = mercury surface tension = 0.485 N/m, θ = mercury contact angle = 130°, p = mercury pressure, d = pore diameter [135]. This relation permits to calculate a particular pore entry diameter for each pressure step applied. According to the amount of mercury that penetrated the sample, it is then possible to calculate the total capillary porosity and

the pore size distribution. However, the technique does not allow the characterization of isolated pores.

Before the MIP tests, the samples were dried by the freeze-drying method. This method was performed by immersing 1 cm-side cubic samples in liquid nitrogen for 5 minutes, lowering the pressure and vacuuming for 24 h (more details are available in [136]). Samples were then removed and kept sealed in containers with silica-gel to prevent rehydration until the MIP test was performed. The equipment utilized was a Micromeritics AutoPore IV 9500 with a maximum pressure of 230 MPa. The list of tests carried out is given in Table 3.13 and Table 3.14. All non-carbonated MIP samples were taken from a representative zone near the core. In the case of the carbonated cement, samples were taken near the core and near the outer rim. The references are MIP-W-XX-ZZ, where W is the curing method (A or B), XX is the BNC percentage (0, 0.05 or 0.15%), and ZZ is the number of days under carbonation. Samples taken from the core are denoted as INT, and from near the outer rim are denoted as EXT.

Test	Sample condition	Reference	Quantity	BNC [%]
1	Non-carbonated	MIP-A-00	3	0.00
2		MIP-A-05	3	0.05
3		MIP-A-15	3	0.15
4	Carbonated	MIP-A-00-30-EXT	2	0.00
5		MIP-A-05-30-EXT	3	0.05
6		MIP-A-15-30-EXT	2	0.15
7		MIP-A-00-120-INT	2	0.00
8		MIP-A-00-120-EXT	3	0.00
9		MIP-A-05-120-INT	2	0.05
10		MIP-A-05-120-EXT	3	0.05
11		MIP-A-15-120-INT	2	0.15
12		MIP-A-15-120-EXT	3	0.15

Tab. 3.13.: MIP experiments on samples cured at 20 °C.

Test	Sample condition	Reference	Quantity	BNC [%]
1	Non-carbonated	MIP-B-00	3	0.00
2		MIP-B-05	2	0.05
3	Carbonated	MIP-B-00-30-INT	2	0.00
4		MIP-B-00-30-EXT	2	0.00
5		MIP-B-05-30-INT	2	0.05
6		MIP-B-05-30-EXT	2	0.05
7		MIP-B-00-120-INT	2	0.00
8		MIP-B-00-120-EXT	2	0.00
9		MIP-B-05-120-INT	2	0.05
10		MIP-B-05-120-EXT	2	0.05

Tab. 3.14.: MIP experiments on samples cured at 90 °C.

3.3.10 Water porosity

Cement is a complex multiscale porous material with pore sizes ranging from some nanometers to some micrometers. For the sake of simplification, capillary porosity (pore size higher than 0.010 μm) is separated from gel porosity (pore size less than 0.010 μm) [137]. The sum of both porosities gives the total porosity of cement.

Total porosity was estimated as the porosity measured by weighing before and after drying small saturated samples in an oven at 105 °C for 24 h [138]. It is worth noting that these values overestimate the real total porosity since interlayered water is partially evaporated during this process and the C-S-H structure will be modified. The performed tests are listed in Table 3.15 and Table 3.16. The references are WP-XX-ZZ, where XX is the BNC percentage (0, 0.05 or 0.15%) and ZZ is the number of days under carbonation. Samples from near the outer rim are denoted as EXT, while for the 120-day carbonate cements, samples were taken from 4 different zones.

Test	Sample condition	Reference	Quantity	BNC [%]
1	Non-carbonated	WP-00-00	3	0.00
2		WP-05-00	3	0.05
3		WP-15-00	3	0.15
4	Carbonated	WP-00-30-EXT	3	0.00
5		WP-05-30-EXT	3	0.05
6		WP-15-30-EXT	3	0.15
7		WP-00-120-Zone1-2-3-4	4x2	0.00
8		WP-05-120-Zone1-2-3-4	4x2	0.05
9		WP-15-120-Zone1-2-3-4	4x2	0.15

Tab. 3.15.: Water porosity test on samples cured at 20 °C.

Test	Sample condition	Reference	Quantity	BNC [%]
1	Non-carbonated	WP-00-00	4	0.00
2		WP-05-00	4	0.05
3	Carbonated	WP-00-120-INT	3	0.00
4		WP-00-120-EXT	6	0.00
5		WP-05-120-INT	3	0.05
6		WP-05-120-EXT	6	0.05

Tab. 3.16.: Water porosity test on samples cured at 90 °C.

3.3.11 Scanning electron microscopy (SEM)

The microscope FE-SEM Σ used has a Schottky field emission electron cannon optimized to work at high and low currents. It also has secondary and back-scattered electron detectors which allow the simultaneous collection of topographic and chemical contrast information.

The joint optical system allows views with magnifications from 12 X to 500,000 X. The accelerating voltage can be varied between 0.1 kV and 30 kV in 100 V steps. SEM samples were metallized with chromium to make them conductive and placed under vacuum. The maximum resolution of the images is 3072×2304 pixels at 24 bits, and they can be presented in multiple frames, allowing the simultaneous recording of images acquired with different detectors.

3.3.12 X-ray diffraction (XRD)

XRD analysis was performed on a Philips 3020 diffractometer using CuKα radiation with a Ni-filter (35 kV, 40 mA). Scanning was performed between 3° and 70° 2θ, with a step of 0.04° and a count time of 2 s/step. No monochromator was used, and openings were 1° for divergence, 0.2° for the reception, and 1° for dispersion. The identification of the mineral phases in the material was performed using the X'Pert High Score program. For identification and quantification, the procedures described by Moore and Reynolds [139] were followed, while quantification was based on the work of Biscaye [140]. The references are XRD-W-XX-ZZ, where W is the curing method (A or B), XX is the BNC percentage (0, 0.05 or 0.15%) and ZZ is the number of days under carbonation. Samples taken from the core are denoted as INT, and from near the outer rim are denoted as EXT. The performed tests are listed in Table 3.17 and Table 3.18.

Test	Sample condition	Reference	BNC [%]
1	Non-carbonated	XRD-A-00	0.00
2		XRD-A-15	0.15
3	Carbonated	XRD-A-00-120-INT	0.00
4		XRD-A-00-120-EXT	0.00
5		XRD-A-15-120-INT	0.15
6		XRD-A-15-120-EXT	0.15

Tab. 3.17.: XRD tests on samples cured at 20 °C.

Test	Sample condition	Reference	BNC [%]
1	Non-carbonated	XRD-B-00	0.00
2		XRD-B-05	0.05
3	Carbonated	XRD-B-00-30	0.00
4		XRD-B-05-30	0.05

Tab. 3.18.: XRD tests on samples cured at 90 °C.

Results and Discussion

4

4.1 Introduction

This section deals with the discussion of the experimental results on cement containing bacterial nanocellulose. The results are separated into 3 subsections. The first shows the effects of bacterial nanocellulose on cement in the fresh and hardened state. The second one presents the effects on mechanical strength and microstructure due to supercritical carbonation. And the last one shows the variation in the performance that can be obtained in these modified cements if the curing conditions are unfavorable.

4.2 Effect of bacterial nanocellulose on non-carbonated cement

4.2.1 Free fluid test

Once the oil well-cementing procedure is completed, the cement slurry is required to keep the cement solids in suspension in the early and middle hydration periods. If the slurry stability increases, it helps in preventing fluid breakout. This effect of fluid breakout is usually accompanied by longitudinal fluid channeling, which allows gas migration [141, 39, 142]. If the free-fluid content of the slurry is lower, lower will be the risk of having a fluid breakout.

Figure 4.1 shows the evolution of the free fluid content of Portland cement (PC) and PC + 0.05% BNC slurries with the addition of SP. PC slurry shows 1.89% of free fluid content, as determined by Equation 3.2. For slurries without nanocellulose addition, the free fluid is reduced by 5% and 36% for PC + 0.10% SP and PC + 0.30% SP, respectively. The results show a clear decreasing trend of the free fluid content of the PC slurries with the addition of SP. However, large amounts of these additions will allow more air bubbles to enter into the cement paste, thus increasing cement porosity and decreasing long-term mechanical properties and durability. The reduction in the free fluid with SP has been already studied, and the stabilization in the slurry occurs because of the content of polycarboxylates which chemically modifies the behaviour of the cement in the fresh state [143].

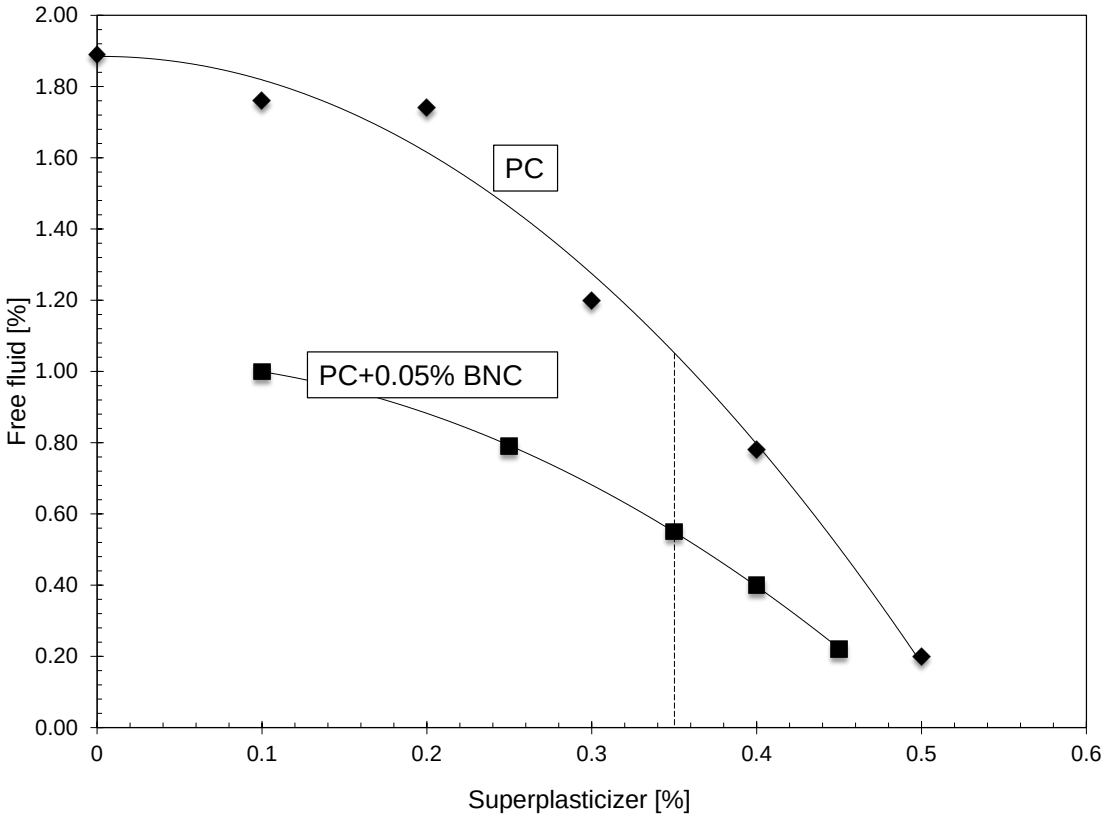

Fig. 4.1.: Free fluid content for different percentages of superplasticizer for Portland Cement (PC) and PC + 0.05% BNC.

A similar trend is observed for slurries with the addition of 0.05% of BNC. The free fluid is significantly reduced by the addition of the BNC for a given SP value, as is shown in Figure 4.1. For the addition of 0.10% SP, the free fluid observed in PC + 0.05 %BNC slurry is reduced by 76% in comparison with the PC slurry. This gap decreases as the amount of SP increases. For instance, the free fluid content of samples with 0.05 %BNC is reduced by 52% in comparison with the PC slurry for the addition of 0.35% SP. Thereby, ensuring that the limitations and correct doses of SP are critical.

Results for the cement slurries modified with BNC might be explained by the water retention capacity of the BNC fibers [114]. Water adheres to the surface of BNC fibers, which thickens the slurry [144]. We can see in previous studies that no water can be extracted if the quantity of nanocellulose applied is excessive [126]. Results show that when using both nanocellulose and superplasticizer, the slurry stability increases, which helps to prevent a fluid breakout.

4.2.2 Thickening-time test

During wellbore cementing operations, if the cement slurry maintains a liquid state for a short time, the constant pumping will damage the cementitious structure generated by its initial setting. On the other hand, if the liquid state is maintained for a long time, it may delay the commissioning of the well. With the addition of BNC to the cement slurry, an increase in the yield stress is observed [126, 112]. However, there is no clear understanding of the dynamic behaviour of the modified slurry concerning temperature changes. In order to observe the rheological behaviour under temperature and pressure of the cement modified with BNC, consistometry tests were performed on PC and cement with the addition of 0.05% BNC. The initial consistency and the thickening time were evaluated for different percentages of SP to obtain slurry workability similar to PC. The results are shown in Table 4.1.

Test	BNC[%]	SP[%]	Initial consistency [Bearden]	Thickening time [min]
1	0.00	0	15	99
2	0.05	0.05	Excessively viscous	-
3		0.15	Excessively viscous	-
4		0.30	Excessively viscous	-
5		0.35	32	99
6		0.40	12	126

Tab. 4.1.: Consistometry tests.

Three different tests are shown in Figure 4.2: tests 1 (Portland cement), 5 and 6 (Slurry with 0.05% BNC). Consistencies are shown along the Y-axis versus time along the X-axis. Test 1 describes the ordinary curve for unmodified class G oil-well cement. In the cases of BNC-modified slurries, with additions of SP less than 0.30%, samples quickly become very viscous, reducing workability with consistency values above the tolerable value (30 Bc). This behaviour is different from other polymers. For instance, it has been found that a natural cellulose polymer increases thickening time [145]. In that experiment the natural cellulose polymer acted as a retarding agent, allowing the slurry to remain in a liquid state. In our case, BNC acts like a water retainer, adsorbing water, and reducing its availability for workability. This effect reduces the initial cement hydration, but at the same time, it considerably increases consistency in Bearden units, reducing thickening time. BNC fibers have a width ranging between 18 and 57 nm and micrometers in length [103], which leads to a specific surface area varying between 150 and 250 m^2/g [146]. Hence, the water employed for cement workability is now reduced to wet this new surface. The addition of 0.10% of BNC considerably increases the yield stress [126], while an increment of 0.40% leads to a cement paste that is impossible to flow.

The consistency of BNC-modified slurries with 0.35% SP additions approximates the behaviour of PC. Despite this behaviour being erratic through time, the final thickening time is similar to the reference cement. However, these BNC-modified slurries with SP additions of 0.35% have an initial consistency higher than the PC slurry, due to a higher initial yield stress. On the other hand, the modified slurries with additions of 0.40% present a smaller initial consistency, and their thickening time is 25 min longer than those observed for the PC and modified slurries with SP additions of 0.35%. This effect is caused by the SP, which makes the mixture more fluid, needing more time to thicken. Larger quantities of SP reduce the initiation of the hydration reaction and the precipitation of solid cement particles during the first hours, allowing the sample to remain in a liquid state for longer.

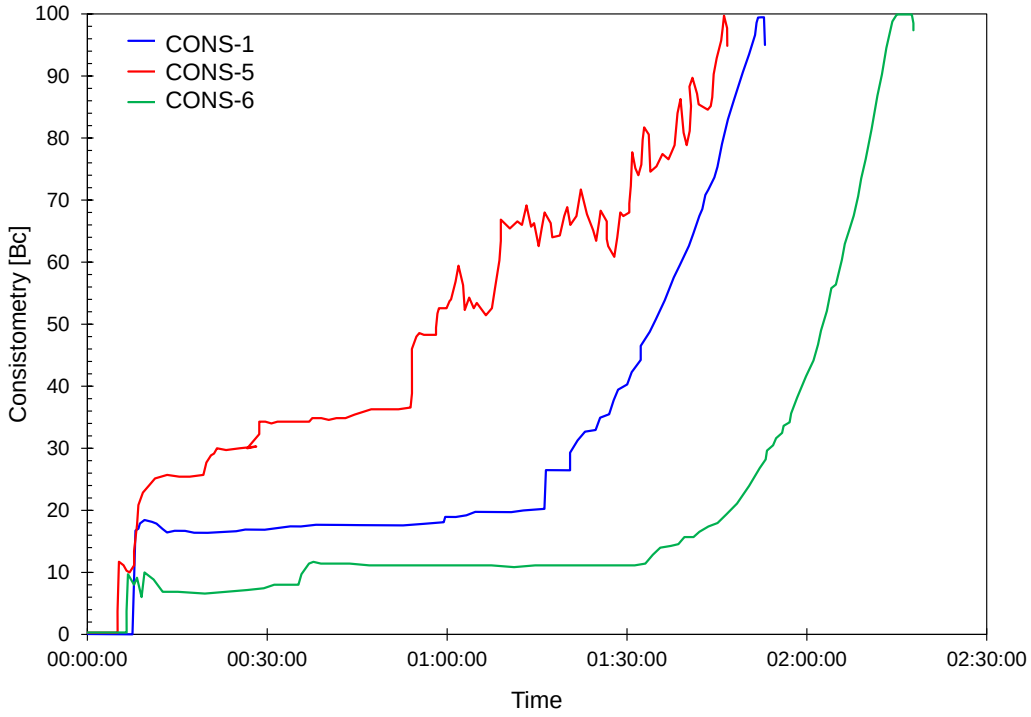

Fig. 4.2.: Consistometry test for Portland Cement (PC), slurry with 0.05% of BNC + 0.35% SP, and slurry with 0.05% BNC + 0.40% SP.

4.2.3 Dynamical mechanical analysis (DMA)

Stiffness of the material is calculated from the deformation under load. The storage modulus E' is a function of the elastic properties of the samples, and it is analogous to the static modulus of elasticity or Young's Modulus.

The values obtained by the DMA results of the storage modulus are observed on a logarithmic scale in Figure 4.3. This modulus is reduced when temperature increases. Samples with 0.15% and 0.20% of BNC maintain higher stiffness magnitudes than PC samples from 20 °C to 200 °C, while 0.05% of BNC has lower values throughout the

test. Observable effects of BNC addition on elastic properties are maintained, while the temperature is rising in the medium, which is attributable to its thermal stability up to 350 °C [126]. The reduction of the stiffness (E' values) during the first stage until 110 °C is due to dehydration of the free adsorbed water and some interlayered water [147] which initiates micro-cracking within the sample [148].

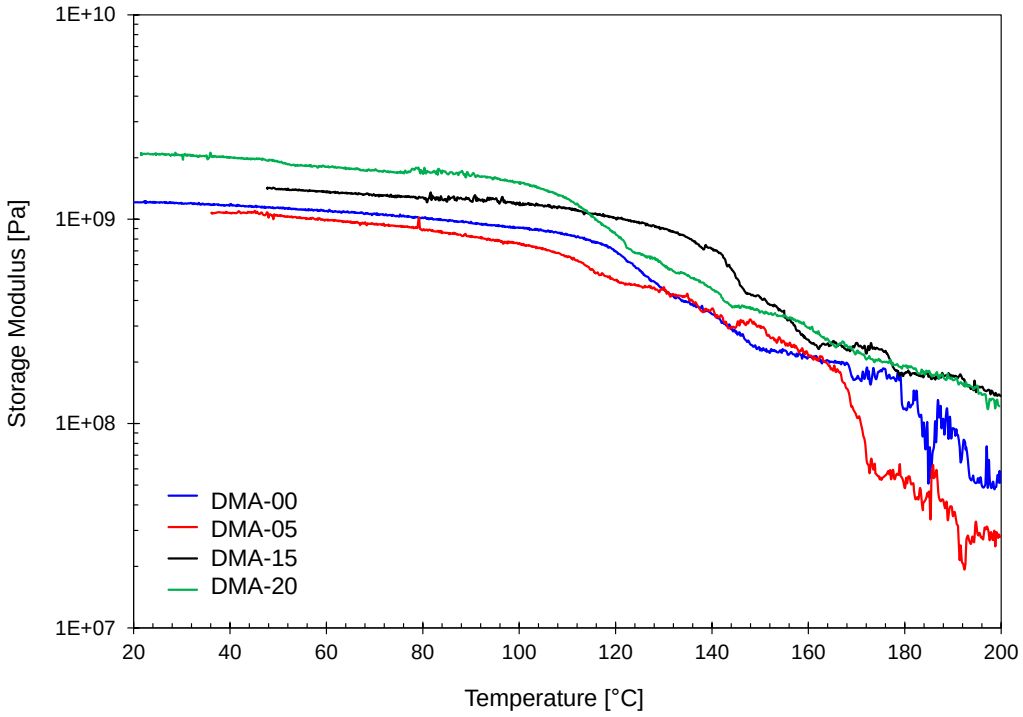

Fig. 4.3.: DMA results of Portland Cement (PC) and PC modified with BNC at 0.05%, 0.10%, 0.15% and 0.20% BWOC samples cured for 28 days.

In Figure 4.4, we normalized the storage moduli to their initial values. The normalized storage modulus is obtained by dividing the modulus measured at a certain temperature (Ti) by its initial value (at T0) for each tested sample. An important drop is observed between 110 and 140 °C, where cement samples lose between 50% and 80% of their storage modulus. This drop can be explained by water evaporation from the samples and by C-S-H dehydration, starting at approximately 110 °C [149]. The dehydration begins to degrade the properties of the cementitious matrix because the water acts as a stabilizer of the C-S-H structure. Here, cement with 0.15% of BNC has a better performance than PC and cement modified with 0.05% or 0.20% of BNC. These samples are the most stable mixtures, because that quantity is more distributed in the sample. For the other samples, dehydration is more rapidly accompanied by a collapse of the C-S-H structure. Thus, the presence of more sliding sites in the C-S-H structure increases the damping factor [150], and it should also be mentioned that tan δ and E' act in opposite directions in cement-based materials [151], i.e. when the elasticity of the specimen decreases, the damping increases, consequently

decreasing more quickly the value of E' with temperature. At 130 °C, PC sample shows a 70% loss of its modulus, while samples with 0.15% of BNC only lost 30%.

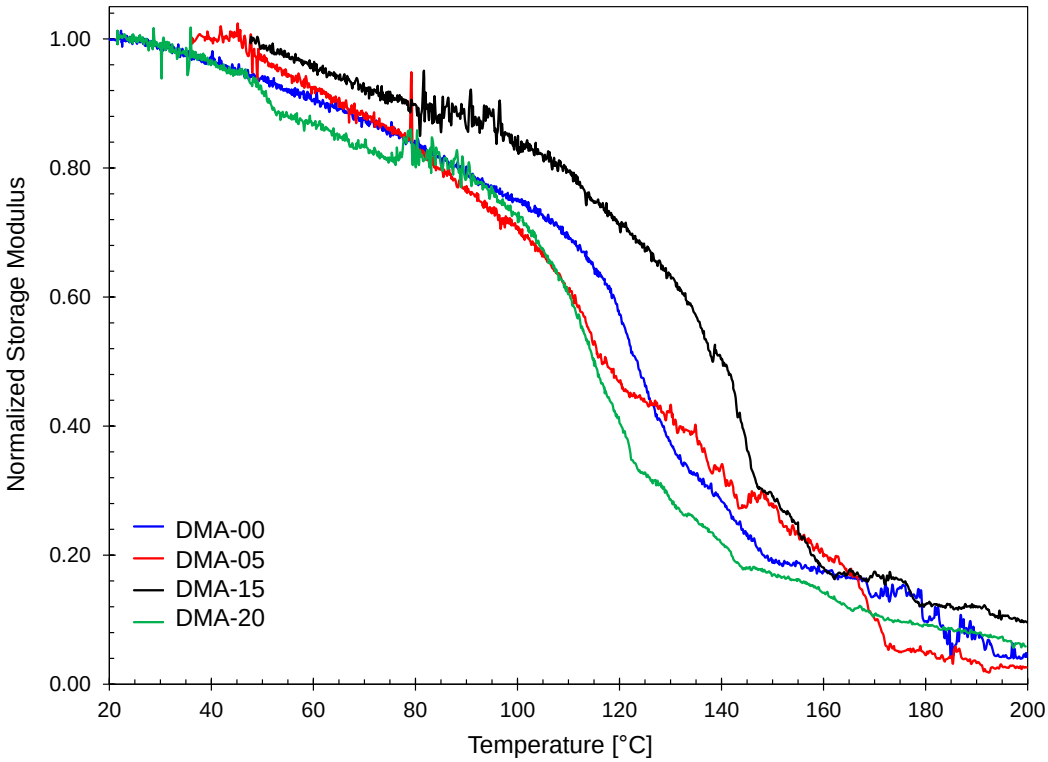

Fig. 4.4.: Normalized storage modulus of Portland Cement (PC) and PC modified with BNC at 0.05%, 0.10%, 0.15% and 0.20% BWOC samples cured for 28 days.

On the other hand, the storage modulus of samples with 0.05% of BNC is smaller than for the PC samples for most of the test, except between 130 and 160 °C. However, the normalized module graph shows better behaviour after 120 °C in terms of thermal resistance. This means that this small addition of BNC changes the thermal properties but does not change the bending stiffness.

Figure 4.5 shows that temperature provokes a significant impact on the PC sample, inducing higher tan δ (see Section 3.3.3), which represents the applied energy that the sample can store. This effect starts to be detected at 150 °C and lasts until 200 °C. Cements with a high percentage of BNC (0.15% and 0.20%) are not affected as the previous one. They have maintained a lower loss modulus factor (85% less than PC at 200 °C). This is not the case for the percentage of 0.05%, where the reduction is 50%. Considering the nanostructural analysis performed by Alizadeh [150], the response δ of PC and 0.05%-BNC cement in terms of tan δ is different from that of 0.15 and 0.20%-BNC. This can be related to the different microstructure induced by the formation of aggregates of BNC in the mixture with PC. Alizadeh et al. related the higher tan δ value to higher E", and sliding frictional effects that occur when water is evaporated from adsorbed water because water restrains the C-S-H sheets. The decrease of tan δ or damping effect is the consequence of higher

rigidity of the nanostructure. This is the result of a higher bridging of the C-S-H sheets due to the increase in the number of strong bonds between SI and O or Si–O-Ca. These bonds are due to the dehydration of water interlayer of C-S-H, which is larger for a higher content of BNC.

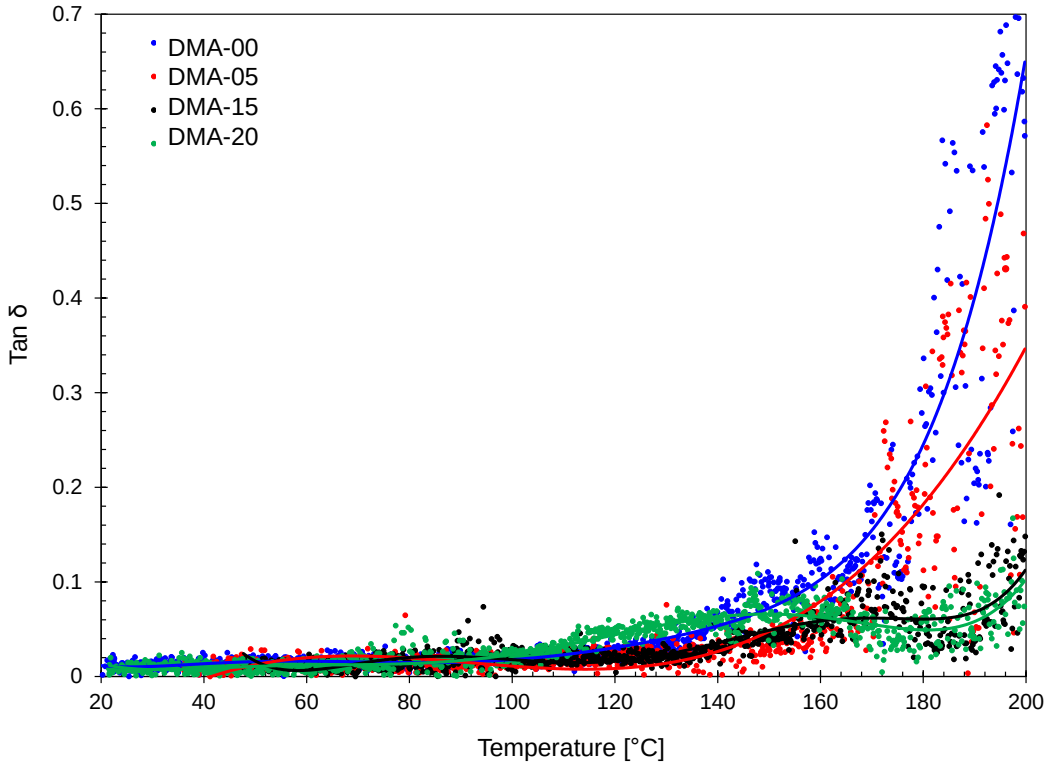

Fig. 4.5.: DMA results in term of tan δ of Portland Cement (PC) and PC modified with BNC at 0.05%, 0.10%, 0.15% and 0.20% BWOC samples cured for 28 days.

As will be shown in the TGA experiments (Section 4.2.6), PC has the lowest degree of hydration compared to the other cements with added BNC. The lower quantities and shorter length chains of C-S-H are making this cement more susceptible to creep [152], while samples with higher hydration degrees withstand the oscillatory loading relatively better. On the other hand, cement samples under bending mode are very dependent on the material tensile strength. Fatigue crack propagation depends on the applied stress, the initial crack size, and the material toughness. As the applied stresses are the same (bending load and temperature rate changes), the samples reinforced with BNC experience two types of changes. The first change occurs on the pre-testing crack size (tensile strength improvement) and the second one on the fracture toughness (hydration improvement). These changes explain the behaviour of the samples at 200 °C, where all samples modified with BNC have shown higher storage modulus than PC samples, except for 0.05%-BNC cement.

Previous studies have worked with other polymers and also found that fibers improve flexural strength in cement [153, 154]. Our results confirms this trend on flexural strength,

and additionally shows improvement under thermal stresses. Samples with 0.15 and 0.20% BNC show increased properties at room temperature and up to 200 °C.

4.2.4 Unconfined compressive strength (UCS)

Figure 4.6 shows the normalized compressive strength of cement cured for 7 and 28 days as a function of BNC percentages for cubic specimens. The strength values (Δ) are normalized to the strength value obtained after 7 days of curing in PC cement (Δ_0). The error bars show the absolute variation observed in the tests. The unconfined compressive strength of PC, and the mixtures with 0.05%, 0.10%, 0.15% and 0.20% BNC for different curing times is presented in Figure 4.7. The errors in PC and 0.05% samples are very small in Figure 4.6, so their error bar is not visible in the graph. To plot Figure 4.7, only the average values of the results were used.

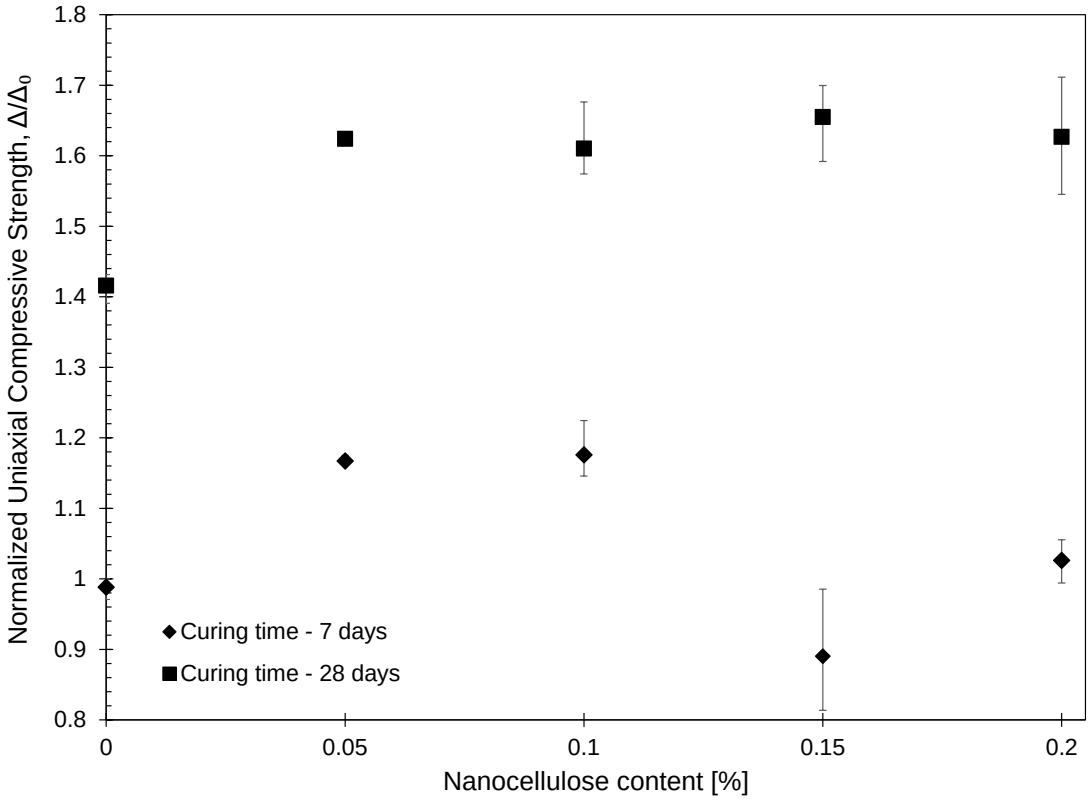

Fig. 4.6.: Normalized compressive strength of Portland Cement (PC) and modified cement cured for 7 and 28 days according to the percentage of nanocellulose: Diamonds symbols represent samples cured for 7 days and squares symbols represent samples with 28 days of curing. The values have been normalized to the strength value obtained after 7 days of curing in PC cement.

The results show an enhancement in strength for cement samples with the addition of BNC. However, the additions of 0.15% and 0.20% at 7 days show a decrease in the strength influenced by the segregation in the mixture due to the SP [155]. It is known that other

types of nanocellulose increase compressive strength as well [110, 156, 115]. The increase in tensile stress [157], compressive strength, and hydration degree supports the use of BNC as a long-term reinforcement. The hydrophilic characteristic of BNC avoids fast water loss during cement hydration and prevents the propagation of thermally induced cracks [144]. By decreasing these cracks, the probability that they initiate failure for a given stress is decreased [28, 156], allowing the sample to withstand higher loads. In addition, nanocellulose has higher tensile strength, thus aiding in overall mechanical performance.

The strength tends to increase with the percentage of nanocellulose. A small increment in BNC (0.05%) produces an important increment in compressive strength, both at 7 days and at 28 days. The addition of 0.05% BNC increases by 18% and 20% the strength in comparison with cement sample (PC) cured at 7 days and 28 days, respectively. Other authors also obtained a significant rise in strength for small percentages of nanocellulose addition [110, 112]. The results are encouraging the use of BNC in future admixtures for the low amounts required and the small induced change in the mixture viscosity.

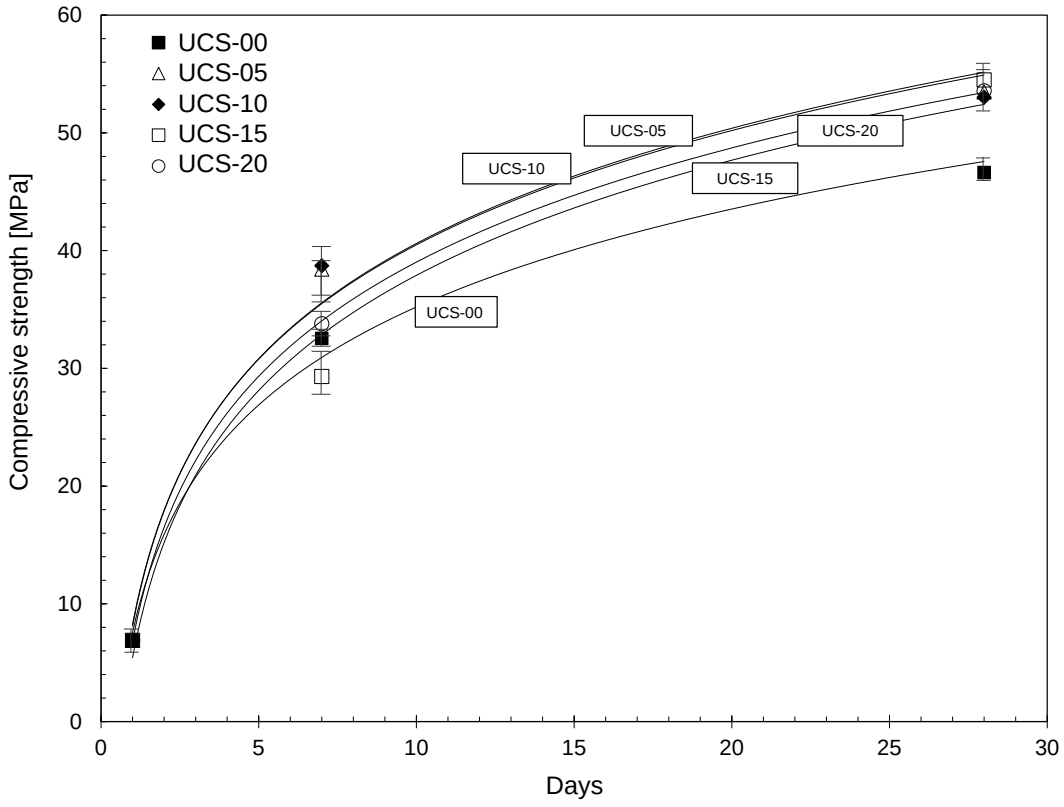

Fig. 4.7.: Unconfined compressive strength for of Portland Cement (PC) and PC modified with BNC at 0.05%, 0.10%, 0.15% and 0.20% BWOC samples at three curing times: 1 day, 7 days and 28 days.

4.2.5 Triaxial experiments

The isotropic stress ramp generates volumetric deformations that can be calculated from the LVDT's measures. The slope of the curve in the confinement-volumetric deformation graph is the compressibility modulus. Figure 4.8 shows typical results for a drained (Kd) and a undrained (Ku) test. The undrained slopes are steeper than the drained slopes. This is because drained samples allow poral water to escape, making them more compressible.

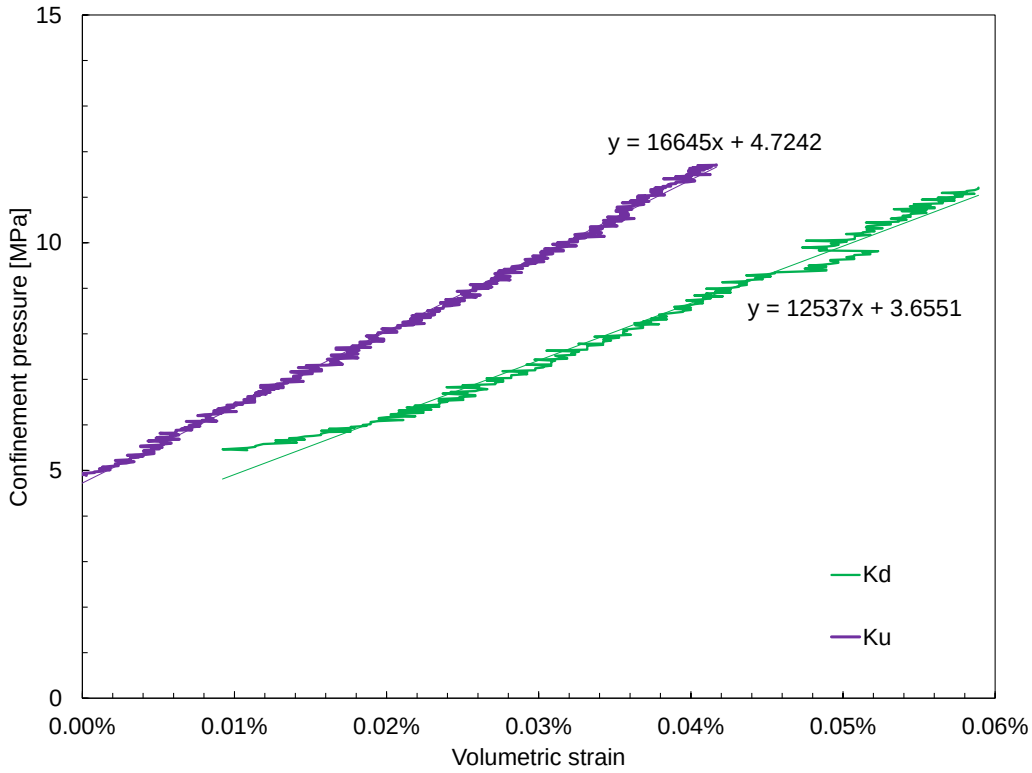

Fig. 4.8.: Isotropic compression tests. The Kd and Ku moduli are determined by curve fitting these results.

The Skempton coefficient B can be obtained from undrained isotropic test, plotting pore pressure variations u versus confining stress σ_3. This coefficient corresponds to the slope of the pressure increase curve as a function of the applied isotropic load [158]. This coefficient is influenced by the degree of saturation of the sample. If the sample is not completely saturated, the measured Skempton coefficient will be lower compared to that of the saturated sample. The values measured in the tests were 0.32, consistent with previous works [33].

The list of isotropic triaxial tests performed for non-carbonated samples is given in Table 4.2. The isotropic tests of non-carbonated samples as function of the initial confinement stress are shown in Figure 4.9. The x-axis indicates the initial confinement pressure at the time of the tests, and the y-axis indicates the drained or undrained value of the compressibility modulus for that initial confinement.

Sample	Condition	Initial confinement pressure [MPa]	Final confinement pressure [MPa]	Bulk modulus [MPa]
PC	Undrained	5.00	12.00	16.60
PC		6.00	10.00	14.10
PC		30.00	40.00	17.00
BNC05		5.00	9.00	15.50
BNC05		11.00	21.00	15.40
BNC05		11.00	21.00	15.80
BNC05		28.00	36.00	18.00
BNC05		28.00	36.00	17.20
PC	Drained	5.00	12.00	11.60
PC		29.00	39.00	12.50
BNC05		10.00	20.00	12.80
BNC05		10.00	27.00	12.10

Tab. 4.2.: Bulk modulus values for non-carbonated specimens subjected to different confining pressures.

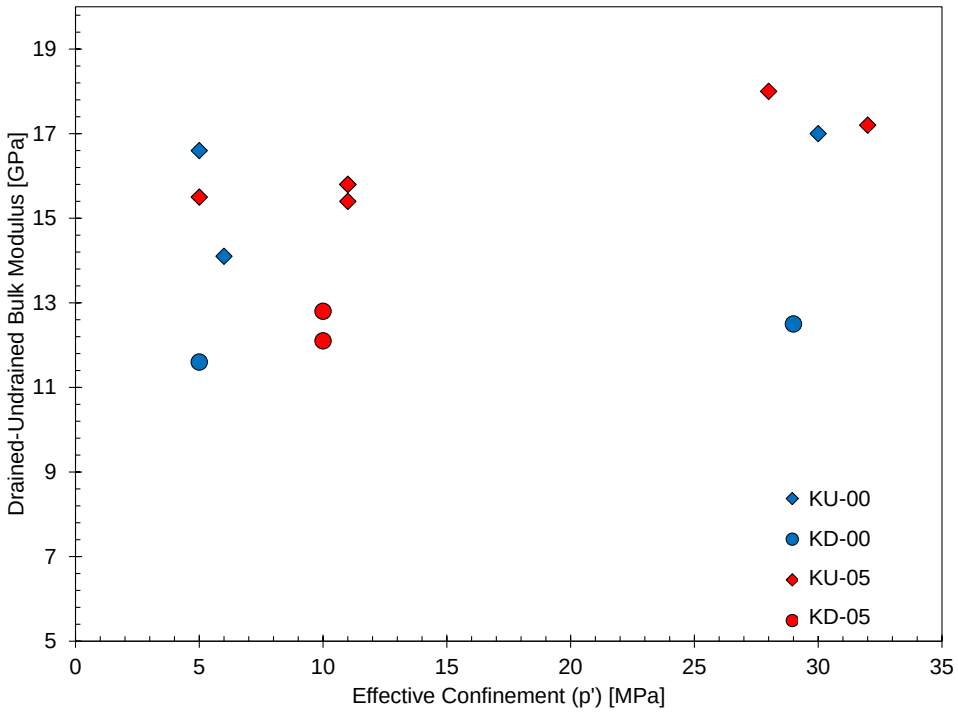

Fig. 4.9.: Bulk modulus of drained (Kd) and undrained (Ku) tests on non-carbonated (NC) PC and 0.05%-BNC cement samples. Results are shown as a function of the initial confinement pressure of each test.

The values of drained and undrained compressibility modulus are similar to previous values obtained in the literature [53, 33]. The increment in the bulk modulus when the initial confinement pressure is increased indicates that the elastic properties are dependent on the initial stress state of the sample. Indeed, in a porous material, the pore structure varies depending on the stress state. Thus, if the confinement increases, the porous volume is reduced, and there is more solid material per unit of volume available to resist the new stress state. Moreover, the increase of the stress within the solid phase (including intergranular forces) is expected to significantly affect the elastic modulus of the material.

Samples with BNC present a slight increment compared to neat Portland cement, on an overall average. The undrained modulus increase from 15.30 for PC to 16.30 for BNC05, while the drained modulus is 12 GPa por PC and 12.50 GPa for samples with the addition of BNC. The increase of this value is related to the effect of bacterial nanocellulose that allows greater hydration. Furthermore, the bacterial nanocellulose fibers have high tensile strength, which may reduce the cracks caused by cement shrinkage [98].

Due to the low permeability of cement, drained experiments would be lengthy, and undrained deviatoric triaxial tests with pore pressure measurement were performed to determine its strength. The results of these tests are shown in Figure 4.10. The ultimate strength of the triaxial compression tests are given in Table 4.3.

Sample	Triaxial compressive strength q [GPa]
PC (σ_3 = 14 MPa)	48.00
PC (σ_3 = 30 MPa)	59.80
BNC05 (σ_3 = 30 MPa)	57.70
BNC15 (σ_3 = 30 MPa)	64.30

Tab. 4.3.: Triaxial compressive strength of non-carbonated samples.

The drained cohesion and internal friction angle could not be obtained because the pore pressure did not increase in some cases, indicating that the specimens were not fully saturated or that there was a leak during the tests.

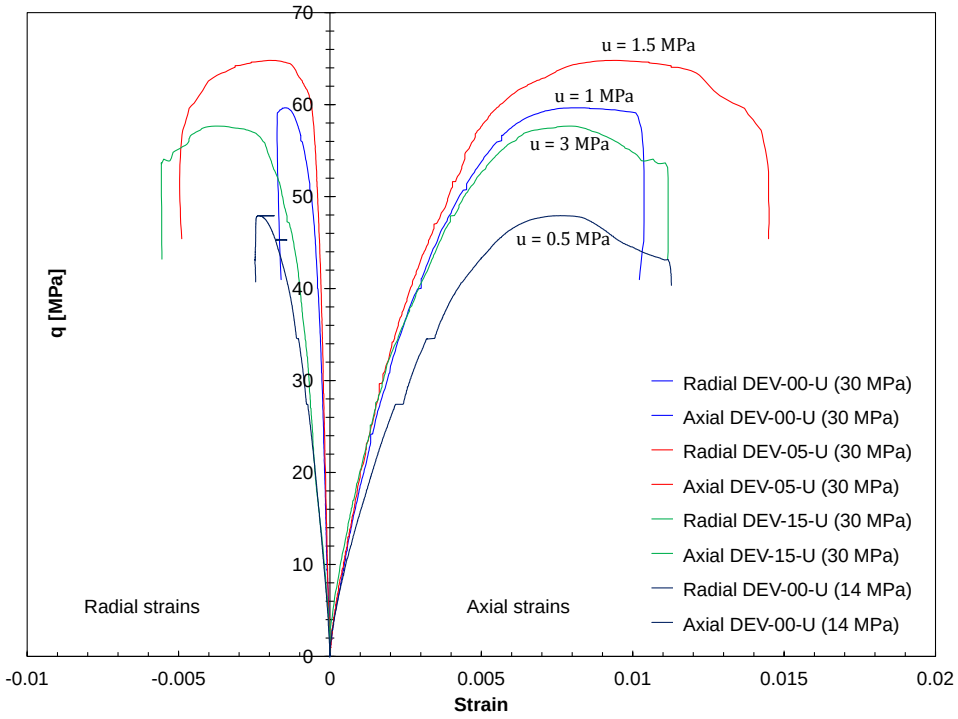

Fig. 4.10.: Deviatoric test on non-carbonated (NC) samples. The pore pressure u is the initial value before loading. The legend shows the type of strain, the tested specimen, and the confining pressure value (σ_3).

In this undrained state, the samples reach a maximum strength level and then have softening until rupture. The undrained Young's modulus and Poisson ratio are taken from the elastic zone (up to an axial strain of 0.001). Both parameters are taken from the same range of load application. Table 4.4 shows the obtained values of Young's modulus and Poisson ratio for non-carbonated samples.

Sample	E_u [GPa]	ν	u_{final} [MPa]
PC (σ_3 = 14 MPa)	18.10	0.23	12
PC (σ_3 = 30 MPa)	19.20	0.20	1.1
BNC05 (σ_3 = 30 MPa)	22.60	0.20	5.5
BNC15 (σ_3 = 30 MPa)	20.40	0.20	10

Tab. 4.4.: Undrained Young's modulus, Poisson ratio and final pore pressure of non-carbonated samples.

For our results, increasing the confinement stress also increases Young's modulus and ultimate strength of cement. For instance, PC increases its strength from 45 to 60 MPa, when it goes from σ_3 = 14 Mpa to σ_3 = 30 MPa. Specimens with BNC with a σ_3 = 30 MPa show a higher Young's modulus than PC. BNC05 has the highest strength at 30 MPa confinement, followed by PC and then BNC15.

4.2.6 Thermogravimetric analysis (TGA)

TGA and DrTGA results are shown in Figure 4.11 and Figure 4.12, respectively. The content of each material phase was calculated by drawing three tangential lines on the TGA graph, and the vertical difference of mass percentage between the intersections is considered the decomposition of the material [159, 112, 160]. The continuous loss of mass on the graph is due to the dehydration of C-S-H and other components that starts at 105 °C and continue until the end of the test [161, 133]. The drop in mass between 420 and 480 °C is due to the portlandite decomposition into Ca^{2+} ions and $2HO^{-}$ from which CaO and H_2O are produced [162]. We can also see a small drop between 600 and 650 °C, which is the decomposition of calcite. But considering that this cement was kept under alkaline distilled water with negligible carbonation in the samples during 28 days [163] and given the fact that the samples were dried in an oven at 110 °C during 24 h, we can assume that this calcite is, in fact, portlandite that was carbonated during drying and precipitated into calcite due to accelerated carbonation in the oven, increasing the CO_2 uptake [164]. The shape of the curves is similar for those samples with and without BNC or SP additions, and they do not show new products due to the addition [165]. The curves corresponding to the 0.05% and 0.15% additions of BNC cannot be distinguished.

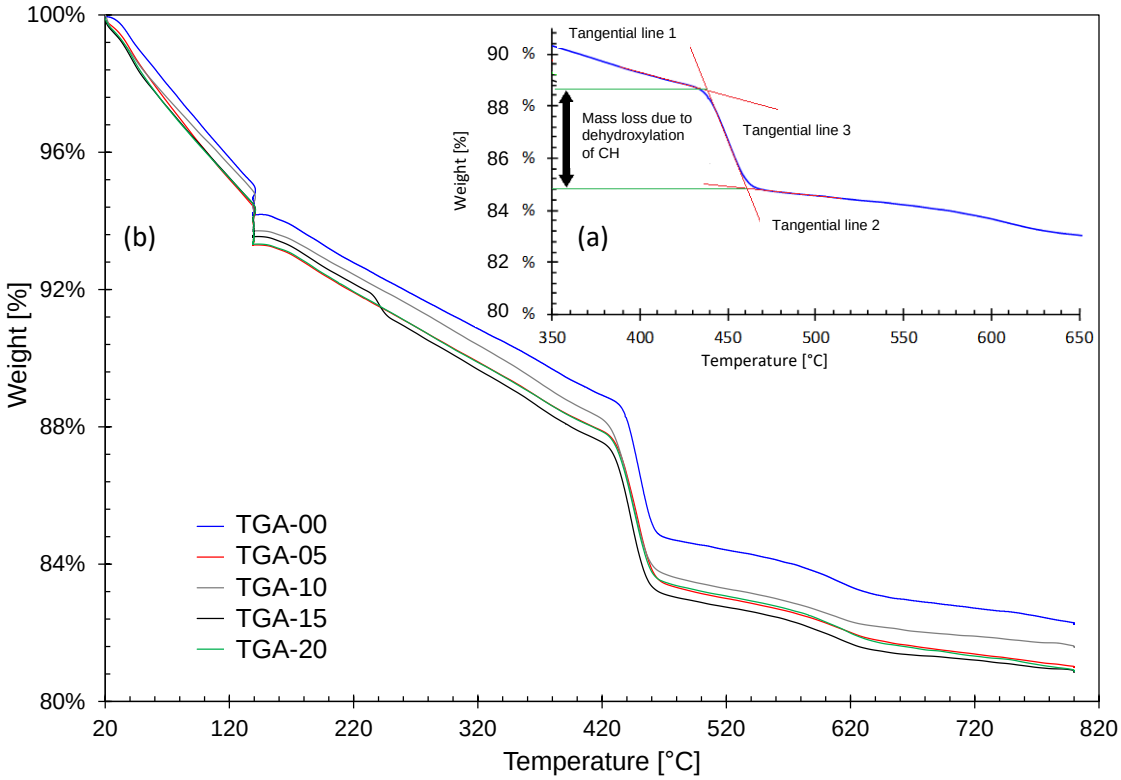

Fig. 4.11.: (a) Example of mass loss calculation for CH in the TGA test (b)TGA result for Portland Cement (PC) and PC modified with BNC at 0.05%, 0.10%, 0.15% and 0.20% BWOC.

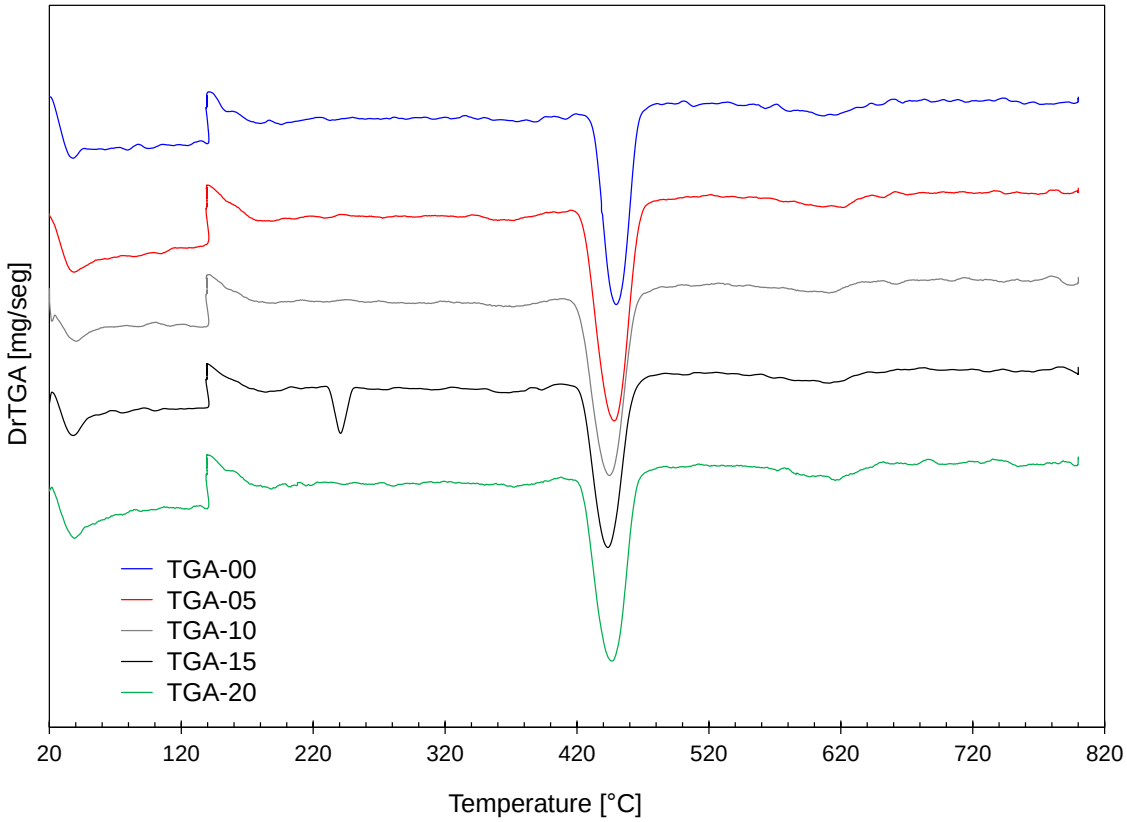

Fig. 4.12.: DrTGA results for Portland Cement (PC) and cement with BNC at 0.05%, 0.10%, 0.15% and 0.20% BWOC.

Portlandite content increases with the BNC content, as we can see in Table 4.5. The BNC water retainer effect generates an additional source of water, which enhances the generation of hydration products [114, 110]. Indeed, the degree of hydration (DOH) is higher for all percentages of BNC compared to PC. Similar behaviour can be found in the literature [112]. It should be noted that, in the present study, the DOH values are underestimated because they were obtained at 800 °C instead of 1200 °C. However, a consisted trend is observed for all the samples analyzed.

Test	BNC[%]	CH [%]	DOH [%]
1	0.00	19.92	62.96
2	0.05	22.16	66.13
3	0.10	22.45	64.62
4	0.15	22.67	68.34
5	0.20	22.58	66.88

Tab. 4.5.: CH content and DOH of the samples.

Cement hydration and development of the microstructure over time are complex processes whose study is not the objective of this work. However, an explanation of the increment in DOH and CH content is necessary. The surface free energy (SFE) is an indicator that can

characterize if a surface is more or less hydrophobic. The sum of the dispersive and polar energy components gives the SFE. According to the literature, dispersive surface energy can increase up to 138% by adding BNC to the cement sample [119]. This causes more hydration reactions due to the increased amount of water on the surfaces of the cement microstructure. Therefore, the increase in SFE explains the increase in portlandite (CH) and DOH. Calorimetry tests on modified cements with nanocellulose have shown an increase in heat release [157, 156], thus leading to a higher hydration degree. However, initially, nanocellulose acts as a retarder for cement [166, 167]. Hisseine [110] suggested that the heat increment during the calorimetry test is associated with the alkaline hydrolysis of cellulose, which promotes cement hydration. Furthermore, cellulose filaments tend to release water during hydration [111]. In our experiments, observed effects of BNC additions are in line with the nanocellulose effects on cement mentioned in the literature: they correspond to an increase of the hydration degree and portlandite content.

4.2.7 Mercury intrusion porosimetry (MIP)

An important issue is related to transport parameters and their evolution. Cement initial porosity and pore size distribution are key factors in allowing CO_2 to enter the cement, which in turn determine the carbonation progress [168]. From this point on, the capillary porosity (pore size higher than 0.010 μm) will be separated from the gel porosity (pore size less than 0.010 μm) [137]. The sum of both porosities will be the total porosity.

MIP tests are shown in Figure 4.13. The characteristic peak of PC in pore size distribution is at 0.050 μm, while for all samples with BNC, it is shifted from 0.050 μm to 0.045 μm.

PC has an average of 19% capillary porosity, while BNC05 has an average of 12% and BNC15 of 16%. BNC containing samples show a significant reduction of porosity in some parts of the samples. Nanocellulose dispersion and distribution within the samples are key factors in obtaining homogeneous properties, but it cannot be easily measured. Dispersion depends on the chemical properties of BNC, while an uneven distribution can lead to scatter in measurements [169]. The ultrasonic scrubber allowed us to have a better distribution of BNC in the mix [127]. However, in Figure 4.13, MIP results for the non-carbonated cement with bacterial nanocellulose show some scatter, certainly due to heterogeneity.

Adding bacterial nanocellulose to Portland cement led to a lower porosity and a characteristic pore size peak shifted towards smaller pores (from 0.050 to 0.045 μm). Cellulose nanocrystals have been reported to reduce porosity in cement samples for pores smaller than 0.100 μm [170]. The hydrophilic properties of bacterial nanocellulose induce the precipitation of larger quantities of hydration products during the hydration process [171]. These products accumulate in the pores previously filled with water [144]. Furthermore, the fibers of the bacterial nanocellulose have significant mechanical strength characteristics

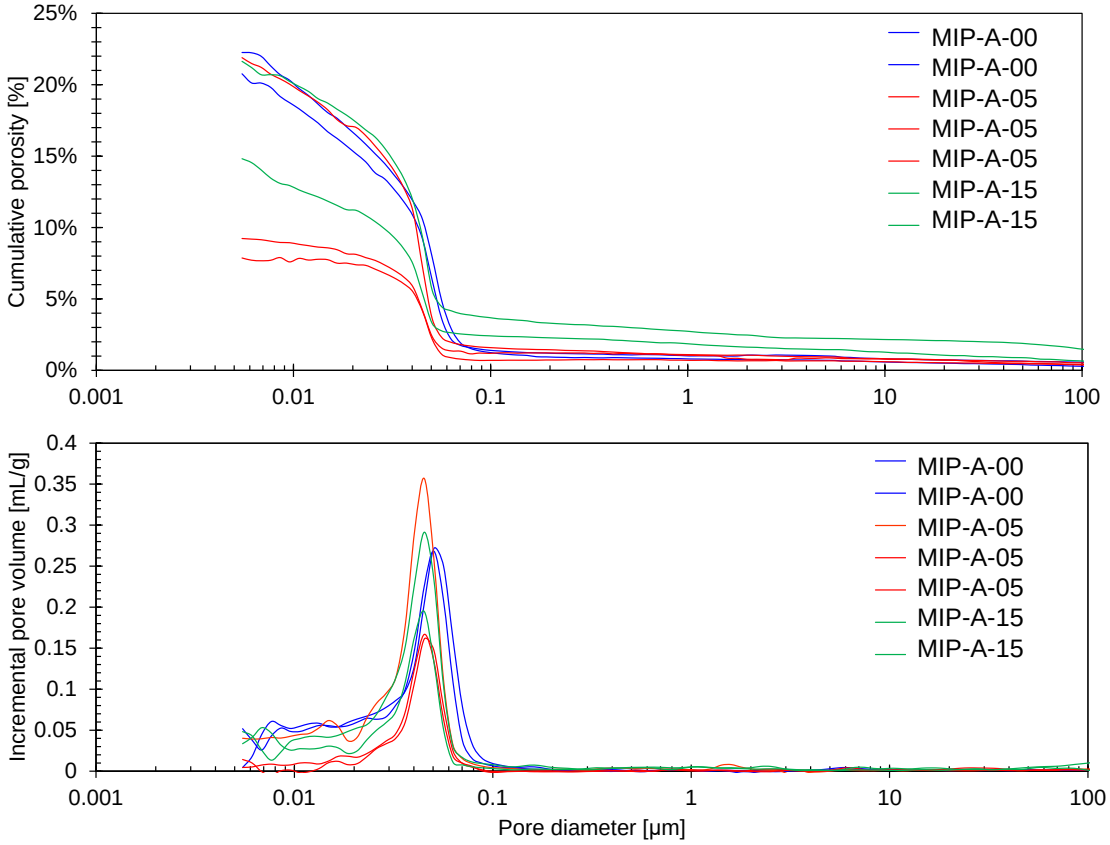

Fig. 4.13.: Cumulative porosity and pore size distribution of PC, BNC05 and BNC15 in non-carbonated samples. Results are shown up to values of 0.006 μm

[98], which during cement shrinkage, may decrease the probability of having micro-cracks, and thus reducing the final porosity [110].

4.2.8 Conclusion

Results indicate that the addition of BNC between 0.05% and 0.20% BWOC produces an important decrease in the amount of free fluid. The addition of BNC reduces the thickening time of cement slurry, and a dispersive agent is needed to maintain the fluidity of the mixture. Nevertheless, more significant amounts of dispersant increase the thickening time for the same amount of nanocellulose.

The thermogravimetric analysis shows an increment in portlandite content and hydration degree as the percentage of bacterial nanocellulose increases. The dynamic mechanical analysis shows an improvement in the thermoelastic behaviour of cement pastes when using large percentages of BNC, mainly induced by its thermal stability and its tensile reinforcement. The use of BNC in cement has shown an increment in strength development at 7 and 28 days.

All the mixtures using bacterial nanocellulose have shown an increase in their compressive strength development over time. Triaxial results also show an improvement in the compresibility moduli of cements with BNC, and similar or higher ultimate strengths. This is likely due to the tensile strength of NCB, which allows it to inhibit cracks. Another reason for this might be the increase in hydration degree, which generates more C-S-H that increase cement strength.

4.3 Effect of bacterial nanocellulose on carbonated cement

This section shows the results obtained for cement cured by method A (see Section 3.2). 18 specimens were carbonated from 3 different mixtures: PC, BNC05, and BNC15. Some were used for mechanical testing, while others were used for microstructural analysis of the core and areas near the CO_2 exposed surface of the specimen.

4.3.1 Supercritical carbonation test

Table 4.6 shows the density variation of samples after 30 and 120 days of carbonation. These values are the averages of all the samples tested, and the deviation does not exceed 2% of the averages.

PC bulk density increases by 1.4% and 2.5% after 30 and 120 days of carbonation, respectively. BNC05 was the lightest compared to the other two types of cement, and showed an increase of its density by 1.5% and 2%, respectively. BNC15 initial density was higher than BNC05, and showed an increase by 1.3% and 3.6%.

		30 Days of carbonation		120 Days of carbonation	
Samples (I)	Initial density $[g/cm^3]$	Mass uptake [g]	Density variation [%]	Mass uptake [g]	Density variation [%]
PC	1.99	2.7	+1.4	4.0	+2.5
BNC05	1.93	2.8	+1.5	3.3	+2.0
BNC15	1.97	2.1	+1.3	7.5	+3.6

Tab. 4.6.: Average values of density and mass uptake after carbonation.

Calcium hydroxide (CH) is dissolved from its solid form into Ca^{2+} and OH^- ions which are dissolved in water. The saturation of these ions in the acidified medium containing HCO_3^- provokes the precipitation of calcium carbonates ($CaCO_3$) in pores and water formation (Equation 2.17). In this reaction, the stoichiometric relation between the solid phases CH and $CaCO_3$ is one. As the density of CH is 2.23 g/cm^3, and $CaCO_3$ is 2.71 g/cm^3 (or 2.93

g/cm^3 for aragonite or 2.54 g/cm^3 for vaterite), density will inevitably increase during the reaction (this is actually due to the input of carbon dioxide which precipitates into $CaCO_3$). C-S-H is an amorphous material that may have different phases with different densities, ranging from 2.6 g/cm^3 to 2.86 g/cm^3 [172]. The C-S-H chemical balance of Equation 2.18 indicates that density will also increase due to the formation of $CaCO_3$ with a relation of 1.7 mol of $CaCO_3$ per 1 mol of C-S-H carbonated.

As shown in Figure 4.14, the degraded zone (brown zone) has a slow penetration rate, and no change can be seen in the center of the sample. However, in the top part, an important penetration is observed. In the case shown in Figure 4.14, BNC05 cement was less degraded than PC. Lower amounts of calcium hydroxides and a lower Ca/Si ratio in the C-S-H structure characterize this carbonated zone [85].

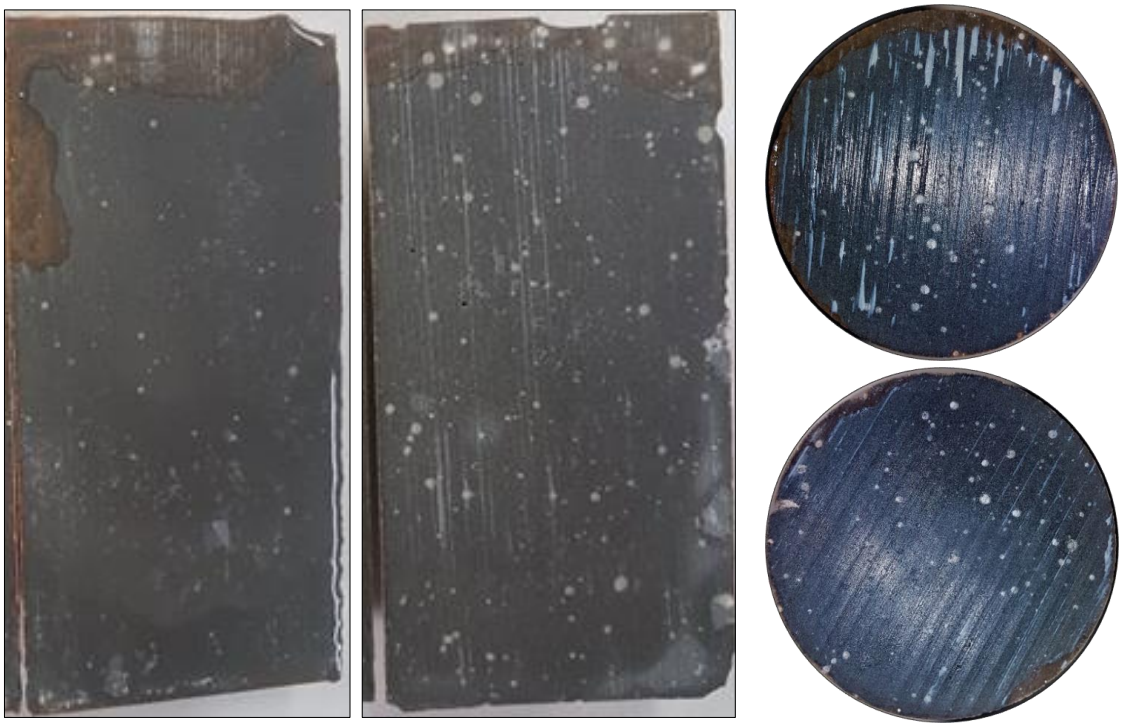

Fig. 4.14.: Cross section of PC (longitudinal on the left and radial at the top) and BNC05 (longitudinal on the right and radial at the bottom) samples after 120 days of carbonation.

The top degraded zone observed in Figure 4.14 might result from sedimentation during the cement setting, which leaves a more porous area at the top of the sample. The degraded zone penetrates 8.7 mm inwards from the top of this PC specimen, while a value of 5.6 mm is measured for this BNC05 specimen. The porosity of BNC05 in the upper part was lower than for PC, due to BNC's ability to diminish cement sedimentation by reducing the free water content, thus allowing this part to have more cement hydrates and less porosity. After carbonation, the pH of the remaining fluid at the bottom of the cell was reduced from 13 to 7, similar to studies made by Barlet-Gouédard [73]. Unfortunately, the pH could not be

measured during the carbonation test. In fact, the pH during the carbonation process could be reduced to 2.9 [69] or 3.2 [173], depending on the solubility of CO_2 in water. Solubility increases with pressure, with temperature up to a certain degree, and decreases with the salinity of the water. According to Duan and Carey's model [173, 174], the solubility of CO_2 in our experiment was 1.1 mol/kg.

Hydration conditions before carbonation are essential, and they determine the amount of cement hydrates and porosity. Overall, temperature and curing time are parameters that will change porosity and pore size distribution [54, 60]. In this work, curing conditions are optimal for having a high hydration level and low porosity cement after 28 days of curing [60], so the hydration process during supercritical carbonation is not substantial. By considering these conditions, the transport properties for diffusion [175] and advection phenomena [176], which are linked with the porosity and pore interconnections, are considerably reduced. Some authors have performed tests with similar curing conditions [69, 177]. Nevertheless, the pH of the curing conditions they considered was around 7 using freshwater or water with NaCl, which is not in equilibrium with the cement pore solution pH of 12.5. This allows Ca^{2+} ions to be leached during hydration. In the present study, the lime-saturated water is in equilibrium with the cement paste during curing, making possible to study the effect of supercritical carbonation on sound cement samples.

Carbonation conditions are critical to obtaining more or less penetration as well. There have been reports on how carbonation effects are affected by temperature or pressure variations by maintaining one of these parameters constant [178]. It was shown that, by increasing pressure and keeping the temperature constant, the penetration depth was smaller and compressive strength was larger. On the other hand, when the pressure was maintained constant and the temperature increased, cement was more affected with a larger penetration depth and a further reduction in compressive strength, probably due to more cracks propagating caused by higher carbonation temperature and enhanced chemical reactions.

At the end of the 120 days of carbonation, the samples have not been completely carbonated. Therefore, the results shown here correspond to cement samples that are not totally carbonated in the interior, and that are more carbonated in the areas close to the surface in contact with CO_2. The carbonation conditions adopted in the current work are similar to those considered by Barlet-Gouédard and Fabbri [73, 30], where larger penetrations or complete penetration have been observed after 30 days of carbonation. However, the carbonation effect in our samples is different, similar to the small penetrations observed by Kutchko and Gu [69, 179]. The slow advancement rate of the degraded zone in our samples is explained by their low capillary porosity (19%, Section 4.3.2) compared to the other authors [73, 30] (33% - 41%).

It is interesting to note the difference between Duguid's experiments [82] and this work. After 12 months of curing in a NaCl solution, the samples were exposed to CO_2-saturated brine at 50 °C for 30 days. Nevertheless, the authors used HCl to lower the pH of the brine solution to simulate the sequestration of CO_2 in a sandstone formation. Under these conditions, they observed a considerable penetration length of the reactive front, with several regions characterized by different colors behind the front. However, these reactions could have been due to the attack of a strong acid in conjunction with carbonation rather than pure carbonation, which could not be quantified. It is then not possible to know what influence each reaction had on the degradation process. The difference between static and agitated conditions between in the carbonation cell the two experiences could also influence the outcome. In our work, carbonation induces a change in the color of the external surface from initial grey to light brown at 30-days and dark orange after 120-days (Figure 4.15). The samples have a thin brown outer ring, and a thinner darker brown ring was observed surrounding the interior part of the brown ring in some samples. The change in color in the altered zones might result from the release of Fe^{3+} ions, which can react chemically and form iron hydroxides [13]. This probably comes from the fact that the brownmillerite begins to carbonate, because a decrease of its content is seen near the exposed area in XRD tests in section (see in Section 4.4.4).

Fig. 4.15.: Variation in the coloration of carbonated samples at 30 and 120 days.

4.3.2 Microstructural analysis

Figure 4.16 shows the cumulative intrusion and pore size distribution of the zone near the exposed surface of the PC's samples at different carbonation times. Figure 4.17 and Figure 4.18 also show these results for BNC05 and BNC15, respectively.

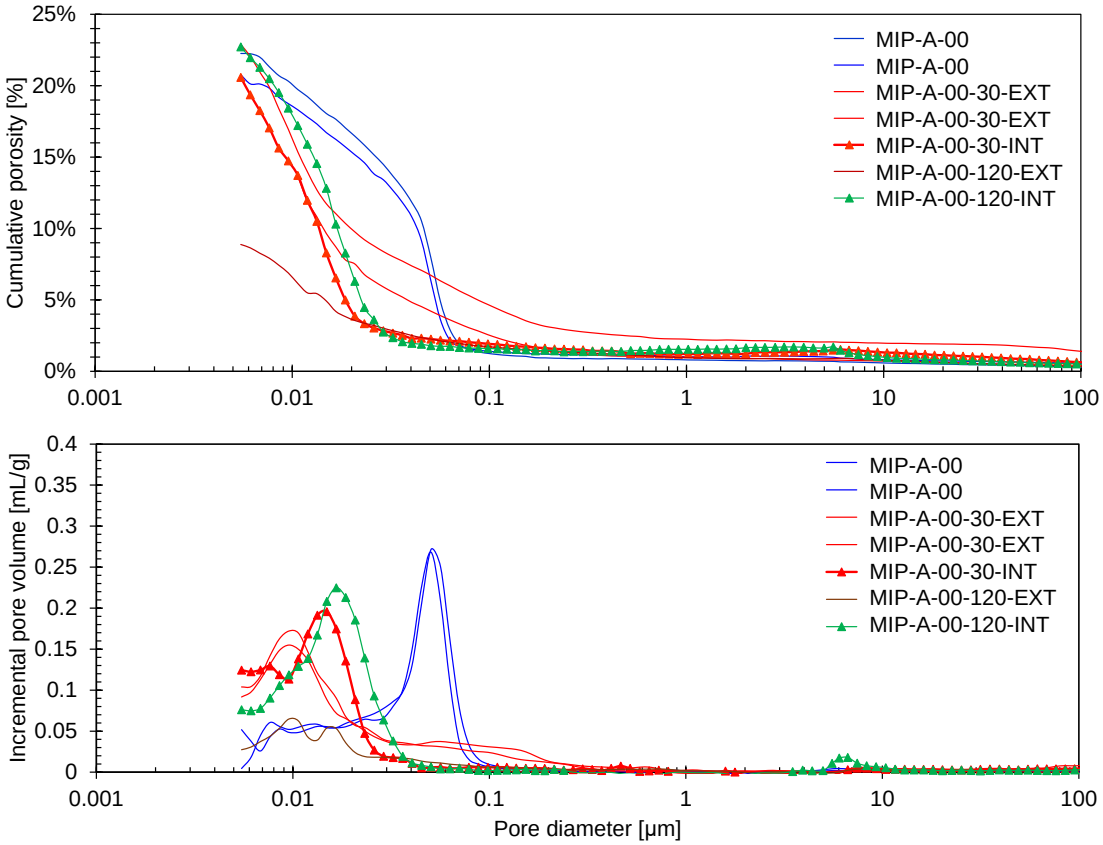

Fig. 4.16.: Cumulative porosity and pore size distribution of PC before and after 30 and 120 days of carbonation.

The cumulative porosity prior to carbonation shows a concave downward curve for all types of cement. This curve for the material closest to the exposed surface, after 30 days of carbonation, it changes in shape to a concave upwards curve. After 120 days, this shape is still observed but with a lesser slope.

The results near the exposed surface after 30 days of carbonation show that the characteristic pore size peak initially at 0.050 μm has moved to 0.010 μm for the samples studied. After 120 days, the distribution is similar, however, the incremental pore volume smaller, and so does the cumulative porosity. A peak in incremental pore volumes are observed at 0.100 μm after 30 days of carbonation, but the corresponding pores disappear at 120 days.

A porosity decrease is shown on the exterior part of the sample after 30 days of carbonation, diminishing down to averages of 14.5% for PC, 10.6% for BNC05, and 13% for BNC15. After 120 days of carbonation, the porosity near the outer rim has continued dropping to 5% for PC, 6% for BNC05, and 4.5% for BNC15.

Capillary porosity at the cement core has not decreased much compared to non-carbonated cement after 120 days of carbonation. In that region, capillary porosities for PC, BNC05, and BNC15 are 17%, 19%, and 18%, respectively. However, the pore size distribution has changed. The characteristic peak has shifted from 0.050 μm to 0.015 μm for BNC-cement samples while it has shifted to 0.020 μm for PC samples. The difference in the final characteristic peak position between PC and BNC-cement samples (0.020 μm and 0.015 μm, respectively) is analogous to the difference measured for non-carbonated samples (0.050 μm and 0.045 μm for PC and BNC-cement samples, respectively).

The variation in the shape of MIP curves means that the characteristic peak of PSD tends to disappear, and smaller pores (less than 0.010 μm) begin to appear after 30 days. As carbonation continues towards 120 days, this 0.010 μm pore population starts to be reduced.

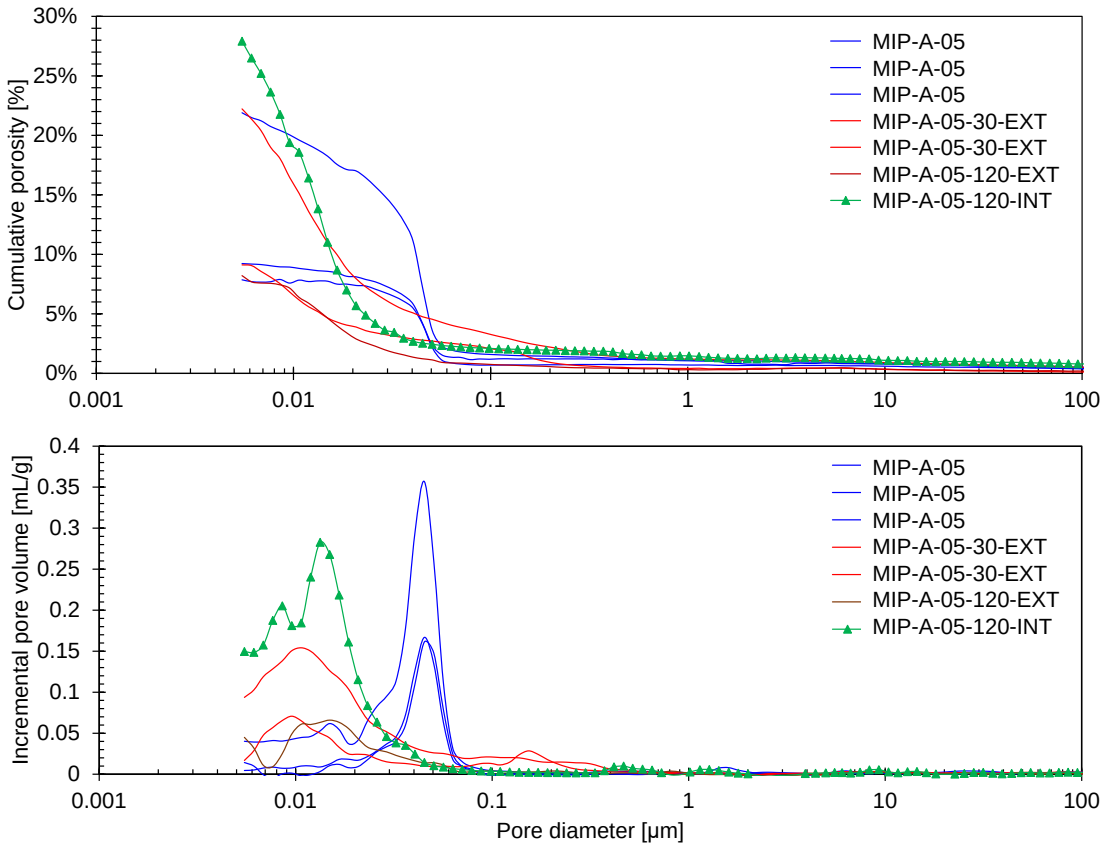

Fig. 4.17.: Cumulative porosity and pore size distribution of BNC05 before and after 30 and 120 days of carbonation.

Cement with BNC show some heterogeneity. One MIP test showed a porosity value of 6.2% after carbonation, indicating that this sample contained BNC at the beginning (non-modified samples had 18% or more porosity). After 30 days of carbonation, this portion was also affected by calcite precipitation, which induced a further decrease of its porosity.

After 30-days carbonation, PC, BNC05 and BNC15 samples show an increase of the population of pores having a diameter close to 0.100 μm. That population was quasi inexistent in pre-carbonated samples. Some authors have confirmed the occurrence of nano-cracks and micro-cracks after carbonation shrinkage [180], probably induced by calcite crystallization in pores [181]. However, this specific increment of the pore volume could be due to CH dissolution or C-S-H decalcification. In fact, studies on the dissolution of CH and C-S-H indicate a similar porosity increment at 0.100 μm [182]. The process of calcite precipitation and hydrates dissolution may be happening at the same time. Once the pH drops in the pore solution, due to the CH dissolution, the dissolution of ettringite (pH < 10.7) and C-S-H (pH < 10.5 or 8.8 depending on the study [183]) will begin.

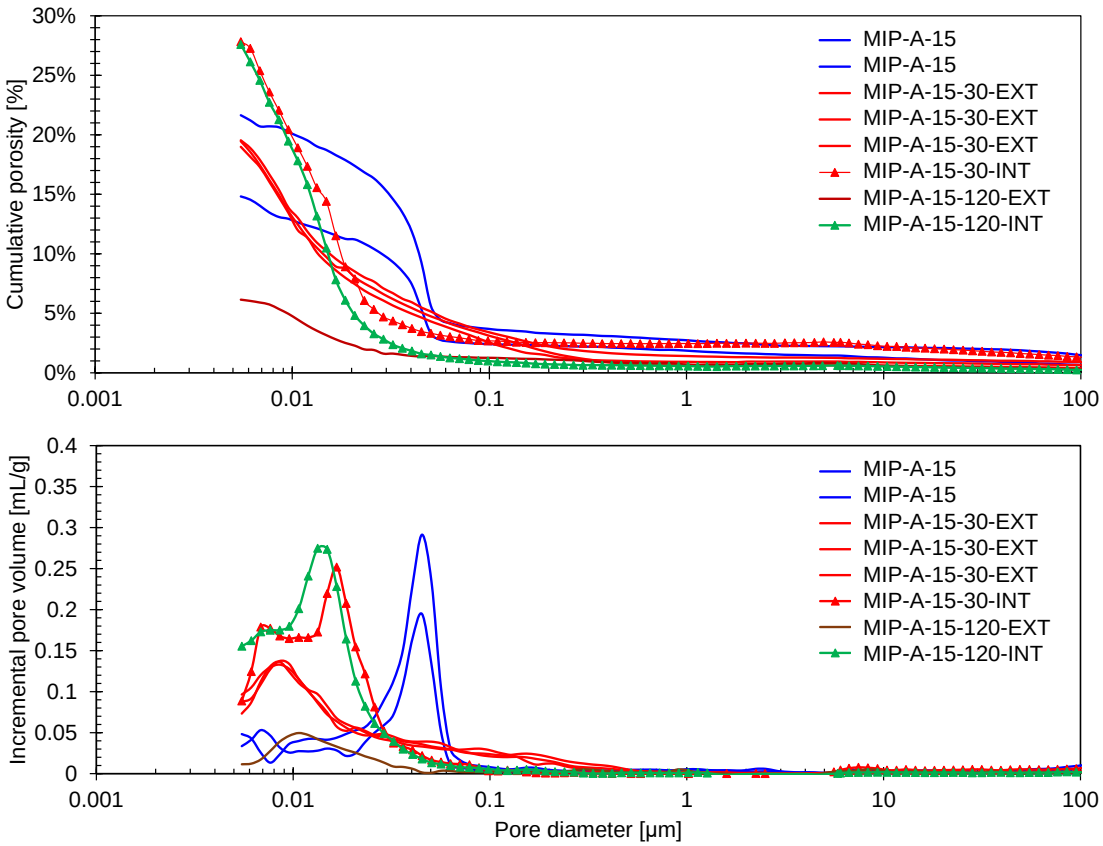

Fig. 4.18.: Cumulative porosity and pore size distribution of BNC15 before and after 30 and 120 days of carbonation.

Regardless of this porosity change at 30 days, samples carbonated for 120 days in Figure 4.16 to Figure 4.18 do not present this porosity increase around 0.100 μm. C-S-H

decalcification is the one that produces more $CaCO_3$ that further clogs the pores after 120 days of carbonation, according to Morandeau studies [184]. As samples were not underwater, dissolved ions could not be released out of the cement samples. Therefore, the $CaCO_3$ precipitation has been refilling these carbonation-induced cracks and blocking further carbonation inwards. This can be observed in SEM images in Figure 4.19, which shows the carbonation front. Behind the carbonation front, it can be observed a higher density due to carbonate precipitation, while in the innermost zone, the cementitious material is dissolving.

PC results show a porosity decrease at the cement core, suggesting that chemical reactions of carbonation have reached this point. This can also be observed in the pore distribution. Indeed, it seems that carbonation exists over the whole sample under supercritical carbonation, at a relatively slow rate at the center and a faster one near the outer rim, where a carbonation front can visually be identified. This was observed first by Rimmelé [32], who reported that CH depletion and $CaCO_3$ precipitation occurred at the cement core, ahead of the carbonation front. Later, Adeoye [92] noted that the Vickers hardness increases throughout the material after carbonation, indicating that there was precipitation of $CaCO_3$ at the cement core.

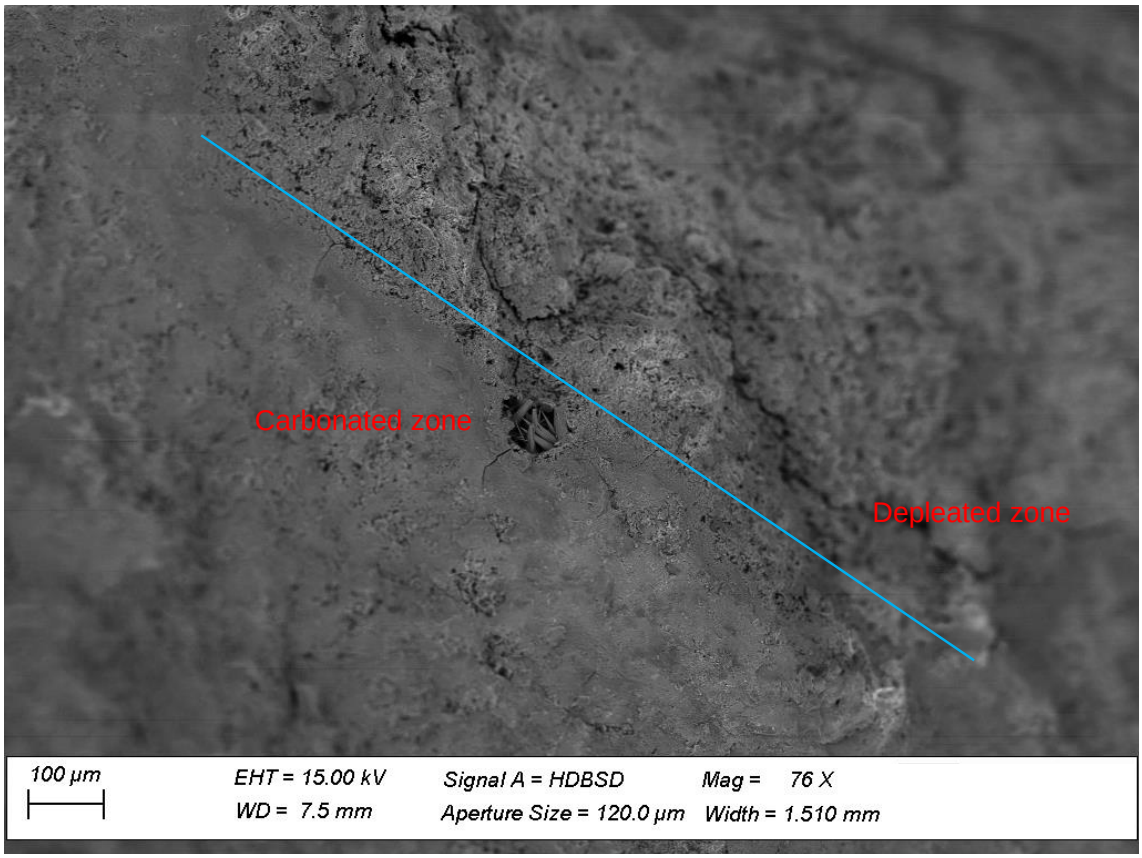

Fig. 4.19.: Carbonation front of BNC15 after 120 days of carbonation.

As in non-carbonated samples, when comparing BNC and PC samples, we can observe a shift of the characteristic peak at the core of carbonated samples in Figure 4.17 and Figure 4.18. The characteristic peak is centered on 0.015 μm for BNC and 0.020 μm for PC. This shows that the effects of nanocellulose remains during cement carbonation, maintaining a characteristic MIP peak at lower values than for ordinary PC. According to Kutchko [69], the carbonation causes a decrease in CH amount at the inner part of cement (Region 1), and a decrease in porosity over the carbonate barrier (Region 2). Although it is seen that there is precipitation of $CaCO_3$, a large number of pores smaller than 0.020 μm are observed.

On one hand, the porosity and the size of coarser pores have diminished because of the formation of $CaCO_3$. On the other hand, for the samples with BNC, the porosities and the quantity of smaller pores have increased due to hydrates depletion, and the characteristic peak has been shifted by $CaCO_3$ precipitation. This suggests that at the core of PC samples, the chemical process advanced towards Region 2 after 120 days of carbonation, while the samples with addition of BNC are in transition between Region 1 and Region 2 and have seen the carbonation advance delayed.

Figure 4.20 shows the pore size variation at a material point near the external surface of PC from the initial state (no carbonation) to 120 days of carbonation where: Time 1 is before carbonation, Time 2 is 30 days of carbonation and Time 3 is 120 days of carbonation.

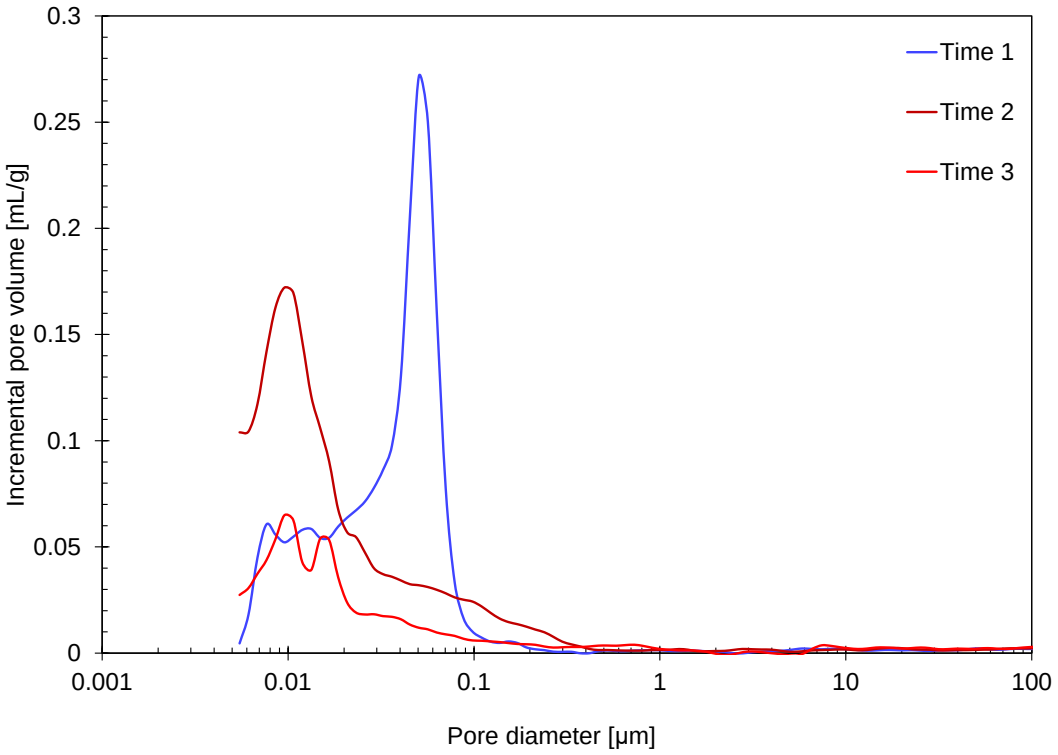

Fig. 4.20.: Pore size distribution variation in time for a point near the exposed surface of PC samples. Non-carbonated (Time 1), 30 days of carbonation (Time 2) and 120 days of carbonation (Time 3).

These times correspond to porosities of 19%, 14% and 5% for PC. All of our cement types behave in this manner with their corresponding capillary porosities. As seen before, the $CaCO_3$ growth in pores shifts the characteristic peak from 0.050 μm to 0.010 μm after 30 days, indicating an increase of the quantity of small pores. At this time, an increment of 0.100 μm pores is also observed. This is likely to be caused by micro-cracks originating from crystals growth ($CaCO_3$ precipitation) [185] or C-S-H decalcification. After 120 days of carbonation, depletion continues but towards smaller pores, as seen above by the increase of gel porosity, and $CaCO_3$ continues growing inside the smallest pores. At this point, no cracks are observed, the ones that appeared previously having been filled by $CaCO_3$ precipitation.

4.3.3 Porosity measurements by oven drying and porosity variation over time

Porosity for all non-carbonated samples has an average of 39%, with a maximum relative variation of 10% of this value (Table 4.7).

Samples	Initial [%]	30 days [%]	120 days [%]
PC	39.7	28.8	31.1
BNC05	39.2	27.3	29.1
BNC15	39.6	30.3	28.5

Tab. 4.7.: Total porosity near the exposed surface of the samples at different carbonation times.

Total porosity in the upper degraded part of the sample after 30 days of carbonation has decreased from (averages of three samples) 39% to 29% for PC, 27% for BNC05, and 30% for BNC15. After 120-days of carbonation, it increases back to 31% and 29% for PC and BNC05, respectively, but it diminishes further, down to 28.5% for BNC15 at 120 days. Adding bacterial nanocellulose to the cement mix does not appear to significantly change the total porosity of non-carbonated samples. Indeed, as the water to cement ratio is the same for all samples, total porosity will be the same. The fact that capillary porosity is reduced in BNC-cement samples might be related to the adsorption of water on the BNC surfaces. This adsorbed water is then no more available to create macropores, and it evaporates only after the oven drying, thus appearing as porosity not accessible by mercury intrusion.

The decrease in total porosity after 30 days of carbonation follows the reduction trend observed in the MIP tests. The increment of porosity from 30 days to 120 days is likely to be due to the dissolution of $CaCO_3$ in an acidified medium. In fact, the high pressure and zero salinity of the water increase the dissolution of CO_2 in the saturated samples, further reducing the pH, possibly down to values as low as 2.9 [69]. This is supported by previous works with similar conditions [71], where they locate the $CaCO_3$ dissolution front in a thin microscopic layer right next to the exposed surface. Figure 4.21 shows this layer which

is right next to the supercritical fluid. The white zone is carbonated material that has not yet begun to dissolve. This zone is very soft and highly porous [82], so its contribution to cement strength is reduced.

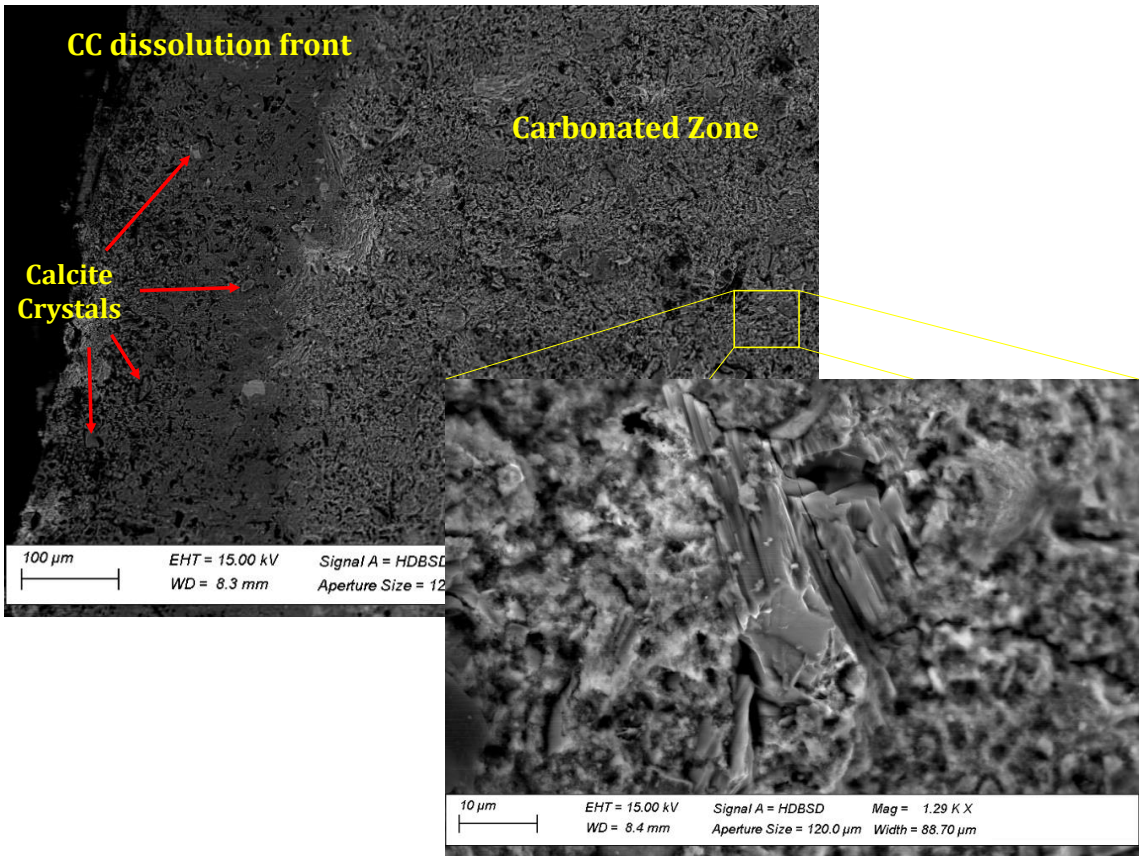

Fig. 4.21.: The outer rim shows larger calcite crystals in a more porous zone, while the carbonated zone shows fewer voids because the dissolution front has not yet reached this zone.

Figure 4.22 represents the total porosities of samples carbonated after 120 days. It is worth noting that in the degraded zone, porosity is lower than at initial state, but in the non-degraded core sample, the total porosity has increased, meaning that the core began to experience CH and C-S-H dissolution. The increase in total porosity, accompanied by the decrease in capillary porosity indicates that the macropores are being filled, and nanopores are beginning to predominate.

PC and BNC15 have similar behaviour, except in zone 2, where BNC15 has a smaller porosity value than PC. However, BNC05 has the smallest porosities for all zones except for zone 2, which is right after the degraded zone. In zone 1, total porosity was the lowest for BNC05, thus reducing the transport of ions into cement. Zone 2, zone 3 and zone 4 of BNC05 are very close to the original 39% non-carbonated porosity, meaning that these zones have not been as affected as in the case of PC and BNC15 samples. This is probably due to the porosity reduction in zone 1 (capillary and total).

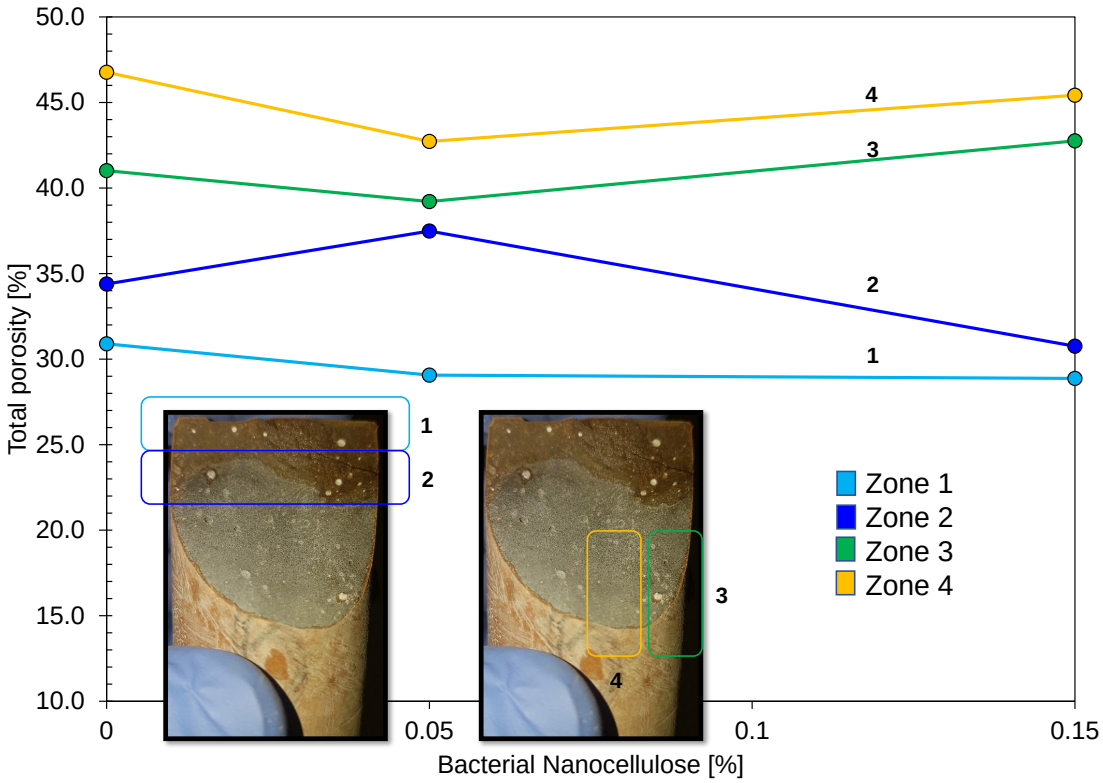

Fig. 4.22.: Total porosity of samples carbonated after 120 days (PC, BNC05, BNC15).

With our previous results, the variation of the total, capillary, and gel porosity along the carbonation time of the degraded zone can be obtained. Macropores or isolated pores were not considered. Total porosity (ϕ_T) was obtained from oven drying, capillary porosity(ϕ_C) was obtained from MIP test results of pores larger than 10 nm and gel porosity (ϕ_G) has been simply assumed to be the difference between the two other porosities:

$$\phi_G = \phi_T - \phi_C \tag{4.1}$$

Results for the outer rim are shown in Figure 4.23. All cement samples behave similarly; all porosities were reduced after 30 days of carbonation. Between days 30 and 120, capillary porosity continued to decline at a steady rate, while total porosity remained approximately constant, and gel porosity started increasing. The obtained values of the total, gel, and capillary porosities are similar to values previously reported by other authors for Class G cement before carbonation [60].

For data obtained after 30 days of carbonation, it is possible to observe that gel porosity approaches the capillary porosity values. The decreasing rate of capillary porosity is lower than the one of gel porosity. In PC samples, the capillary and gel porosities are the same,

while for BNC05 and BNC15 samples, the gel porosity is always larger. Indeed, as mentioned before, the BNC-adsorbed water leads to larger gel porosity at the expense of capillary porosity, which can be seen in the results before carbonation. Trends for BNC15 are similar for both curves (gel and capillary). BNC05 results show an important reduction in gel porosity, while the capillary porosity has not changed substantially.

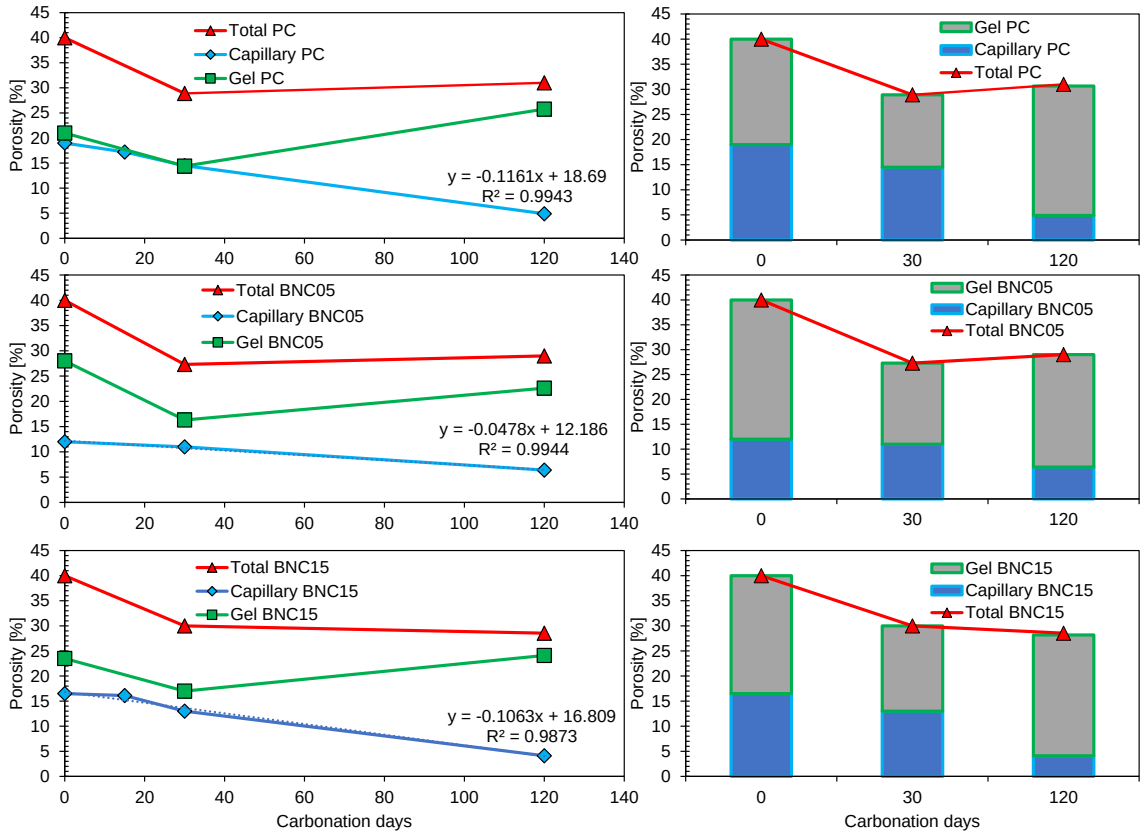

Fig. 4.23.: Variation of total, capillary and gel porosities over time for samples PC, BNC05 and BNC15 for 30 days and 120 days of carbonation (near the exposed surface)

For results at 120 days of carbonation, a linear regression can be accurately fitted to the MIP data. BNC05 has a negative slope of 0.05 %/day, while PC and BNC15 have a negative value of 0.11 %/day. This behaviour indicates that the addition of 0.05% bacterial nanocellulose has reduced the porosity changes compared to the other two mixtures. Of course, the fitted line should end at some point before porosity 0%, but this has not been seen during the experiment's duration. Finally, gel porosity starts growing up again in all samples between 30 days and 120 days, meaning that at a given point, C-S-H decalcification has started, creating new pores probably in its matrix [184]. Nevertheless, at 120 days of carbonation, total porosity remains below its initial value, and capillary porosity continues decreasing, clogging the invasion of CO_2 towards the inner parts of the cement matrix.

4.3.4 Unconfined compressive strength (UCS)

Figure 4.24 shows the compressive strength and Young's modulus development of cylindrical samples over time for PC, BNC05, and BNC15. These are average values of 3 specimens tested. PC has a strength of 53 MPa while BNC05 and BNC15 have 55 MPa. Young's modulus values are 25.7 GPa, 24.2 GPa, and 26.3 GPa for PC, BNC05, and BNC15, respectively.

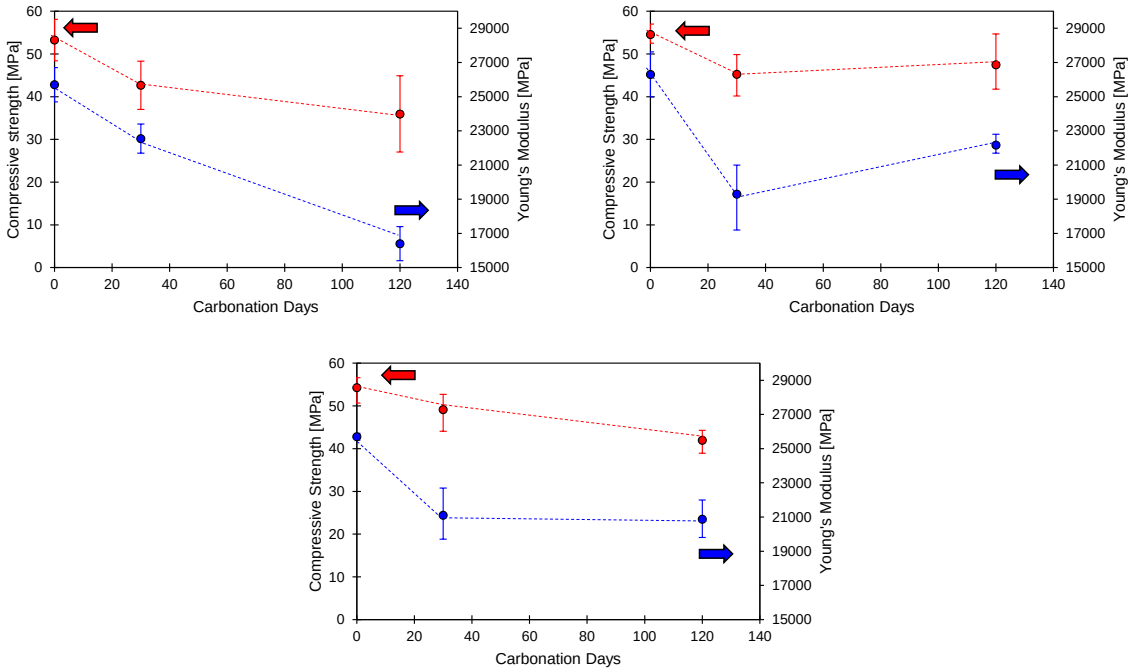

Fig. 4.24.: Development of the compressive strength (red) and Young's modulus (blue) of PC (a), BNC05 (b) and BNC15 (c) over the carbonation time.

After 30 days, PC suffers a drop in compressive strength of 20%, while BNC05, a drop of 17%, and BNC15, a drop of 10%. Results after 120-days of carbonation show that PC has lost 33% of its original strength while BNC has lost 13% and BNC15 23%. At this stage, the compressive strength is 36 MPa for PC, 48 MPa for BNC05, and 42 MPa for BNC15.

PC and BNC15 are continuously losing strength during the carbonation stages. However, BNC05 experiences a drop in strength after 30 days, but after 120 days, it regains 5% of strength compared to the 30 days' situation.

Young's modulus follows a trend similar to that of compressive strength. PC sees its Young's modulus diminishing by 13% after 30 days and 37% after 120 days. Modulus of BNC05 loses 20% after 30 days, but it increases again after 120 days, thus losing only 10% of the initial Young's modulus at this age. BNC15 had, like BNC05, a drop of 20%, but this value was maintained after 120 days. Young's moduli after 120 days are 16.5 GPa for PC, 22 GPa for BNC05, and 21 GPa for BNC15.

Considering cement carbonation in supercritical conditions, some authors have reported an increment in compressive strength [186, 35], while more recently researchers report a decrease in mechanical performance [30, 75, 187]. This contradiction stems from the different conditions of cement hydration before carbonation [91] and the subsequent carbonation conditions [186].

It is known that in the case of atmospheric carbonation, the precipitation of $CaCO_3$ in the material increases its strength [188]. In our experimental conditions, supercritical carbonation is adversely affecting the mechanical performance of cement. Several reasons may explain the strength decrease: micro-cracks due to pressure variation in the carbonation cell, the high porosity and softening of the outer layer due to $CaCO_3$ dissolution [82], the degradation of C-S-H [189], possible cracks due to crystallization stresses induced by of $CaCO_3$ precipitating in the pores [30, 75], or the preferential paths of the cracks through the different interfaces of the rings of the carbonated material [30].

C-S-H decalcification is mainly responsible for the strength loss during carbonation [190], and the Young's modulus in leached zones can decrease up to 80% [191]. It was observed by Hidalgo et al. [192] that CH is depleted rapidly and the remains are surrounded by carbonation products. Afterward, the process continues decalcifying and degrading the C-S-H phase, thus reducing the bonding strength of the material.

The discontinuities between the different rings of the carbonation zones (calcium depletion, $CaCO_3$ precipitation, and degradation zone) can generate stress concentrations and initiate failure during the compression test. Some of our samples broke parallel to the applied force and near the rim, as also observed by other authors [30], which supports this failure mechanism.

$CaCO_3$ precipitation can produce tensile stresses around the pores [193, 194]. A work carried out by Lesti highlighted the problems of pore crystallization [75]. It was noted that, even though the carbonation front did not advance very deeply, cracks were observed in the neat cement samples, which considerably increased their permeability and enhanced the failure probability of the sample. This can be observed in Figure 4.25, where the growth of calcium carbonates is observed. Qualitative chemical scanning outside the pore indicates that there are many components characteristic of the cementitious matrix, while in the interior only calcium, oxygen and carbonate are detected. The images found at the top of Figure 4.26 show that the calcium carbonates grow in the form of needle, while the photos at the bottom show that the carbonate grow in the form of sheets that overlap each other.

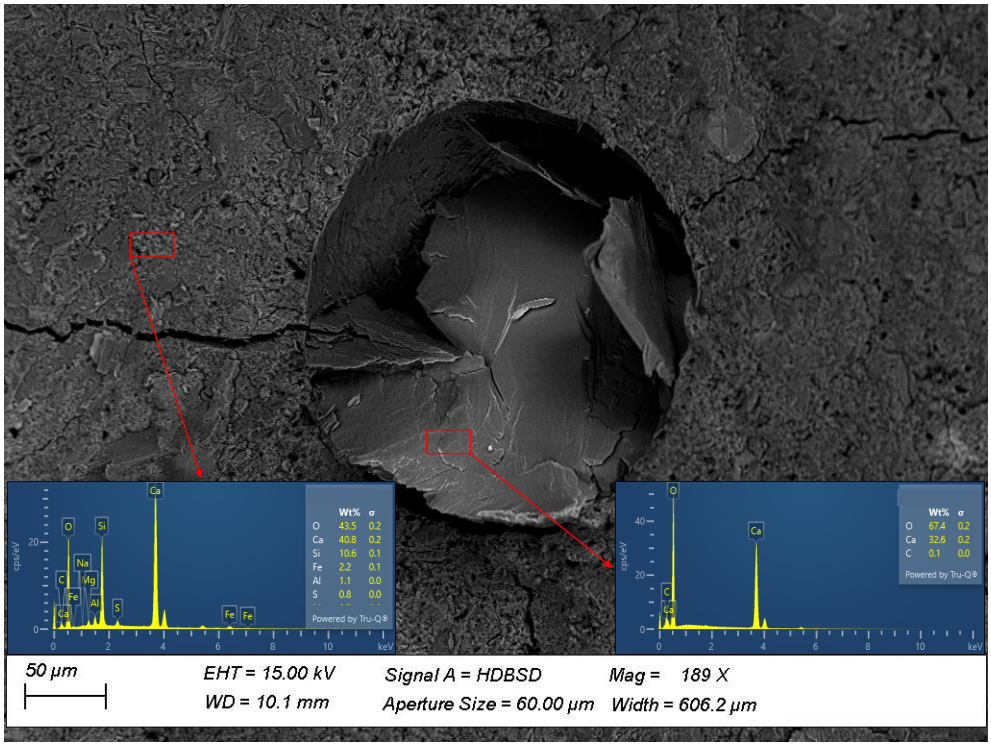

Fig. 4.25.: Cracks formed around a pore with calcium carbonate growth.

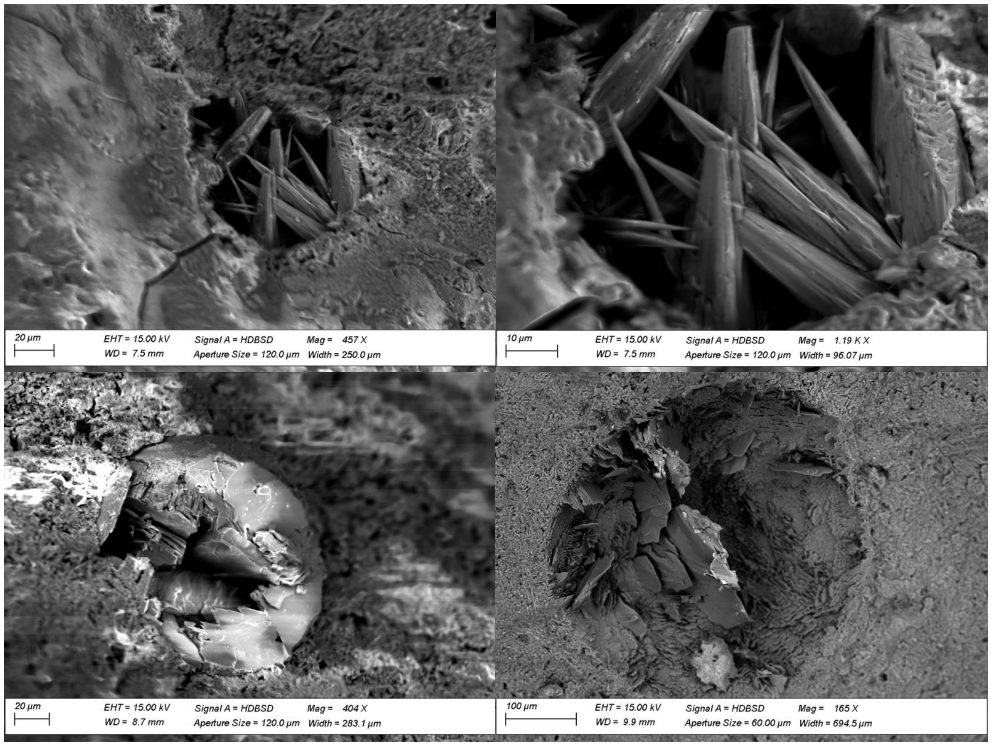

Fig. 4.26.: Cement samples being filled with calcium carbonates after 120 days of carbonation.

Nanocellulose has been reported incrementing mechanical properties when added to the cement mix [110, 117, 121]. Results in this work show an initial increment in strength by the addition of bacterial nanocellulose, while Young's modulus was not significantly affected. However, the effects of BNC are not as remarkable as the results previously obtained in Section 4.2.4, probably due to the use of different specimen sizes and shapes.

Samples with bacterial nanocellulose were less affected by carbonation at 30 and 120 days. After 120 days of carbonation, the PC strength is 36 MPa, while BNC05 and BNC15 strength is 48 MPa and 42 MPa. Young's modulus was also affected in PC to a value of 16.5 GPa, while BNC05 and BNC15 modulus are 22 and 21 GPa, respectively. The increased level of cement hydration from the hydrophilic characteristics of BNC probably reduced the progression of carbonation. Indeed, the lower capillary porosity due to the higher degree of hydration slows down the diffusion rate of carbonate ions [175]. Additionally, the high-resistant BNC fibers contribute to tensile strength, which can also translate into an increase in compressive strength.

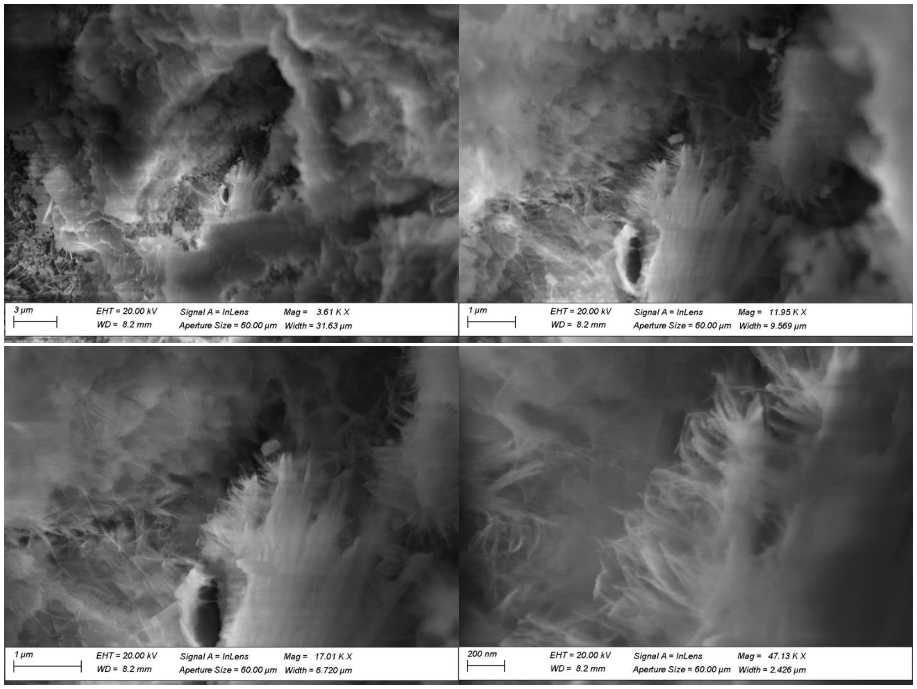

Fig. 4.27.: Pore with bacterial nanocellulose in carbonated cement (BNC15). A small network linking different vertices of the cement structure can be observed.

Figure 4.27 is an image of a carbonated BNC15 sample after 120 days. A material different in terms of shape and texture than the one generated by the carbonation of the cement can be observed. The matching size, the thread-like structure and the bonding between different points of the carbonated cement matrix allow to identify it as the bacterial nanocellulose. The BNC allows some interweaving of its threads, but most of it is agglomerated in a single sector, indicating that the dispersion and distribution within the mixture was not perfect.

4.3.5 Triaxial tests on carbonated samples

The list of isotropic triaxial tests performed for carbonated samples is given in Table 4.2.

Sample	Condition	Initial confinement pressure [MPa]	Final confinement pressure [MPa]	Bulk modulus [MPa]
PC 30d	Undrained	14.00	21.00	8.60
PC 30d		27.00	36.00	8.70
BNC05 30d		10.00	14.00	9.00
BNC05 30d		10.00	20.00	9.70
BNC05 120d		10.00	17.00	9.70
BNC05 120d		10.00	17.00	9.10
PC 30d	Drained	11.00	21.00	7.50
BNC05 30d		11.00	26.00	8.40
BNC05 120d		11.00	20.00	8.70
BNC05 120d		11.00	20.00	9.10

Tab. 4.8.: Bulk modulus values for carbonated specimens subjected to different confining pressures.

Figure 4.28 shows the bulk modulus of the carbonated samples determined during triaxial experiments. The outer rim of the carbonated samples is affected and presents various discontinuities, which could allow higher deformations when an isotropic loading is applied. Carbonation generates different fronts: leaching, precipitation, and re-dissolution [84]. These discontinuities in cement samples reduce their mechanical properties [187].

The averages values obtained from all the isotropic tests are listed in Table 4.9, which shows the bulk modulus of PC samples and BNC05 samples. Carbonation reduces drained and undrained bulk moduli by up to 40% for both mixtures.

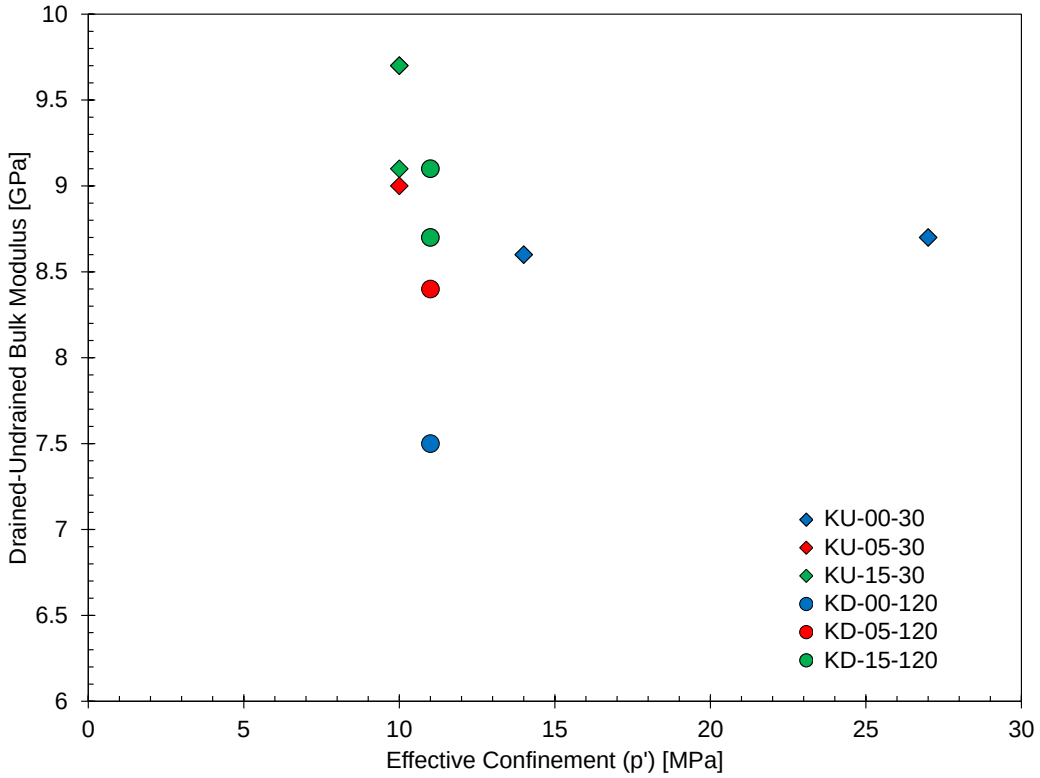

Fig. 4.28.: Bulk modulus of drained (Kd) and undrained (Ku) tests on carbonated (C) samples. Results are shown as a function of the initial confinement pressure of each test.

Sample	Parameter	Non-carbonated [GPa]	30-days carbonation [GPa]
PC	Ku [GPa]	15.30	8.60
	Kd [GPa]	12.00	7.50
BNC05	Ku [GPa]	16.30	9.40
	Kd [GPa]	12.50	8.70

Tab. 4.9.: Averages bulk modulus values of CP and BNC05 obtained from isotropic tests at different confinement pressures.

After 30 days of carbonation, Ku and Kd values decrease for PC and BNC05 cements, but the values of Ku are still greater than Kd. BNC05 modules are larger than PC modules. This indicate that samples with bacterial nanocellulose were less affected by carbonation. After 120 days, the moduli of BNC05 are slightly higher than the moduli at 30 days.

Additionally, the thin exterior front of re-dissolution is characterized by high porosity due to calcite leaching [71]. It is observed that the carbonated material experiences greater volumetric variation when an isotropic load is applied to the material, which leads to a decrease in the compressibility modulus. Indeed, SEM images at the outer edge show the $CaCO_3$ dissolution front (Figure 4.29). Ahead of this area is the carbonated cement (Figure 4.21). The former has a thickness of 250 μm and its porosity increases, while the carbonate zone is denser and with overlapping sheet-like crystals (Figure 4.30). It is also

observed how the material around the denser calcite crystals dissolves. This dissolution of material is what generates a lower apparent bulk modulus in the triaxial tests, since the outer edge is more deformable. The upper left picture of Figure 4.29 shows the outer rim of a carbonated sample. Some larger minerals are seen near the outer surface. The upper right image shows the same image but highlighting the pores. Here we see that there is a greater porosity in the external zone. Zooming in on the minerals near the outer edge shows that there is greater porosity around them. As calcite crystals are stable, they are the last to dissolve in the presence of CO_2.

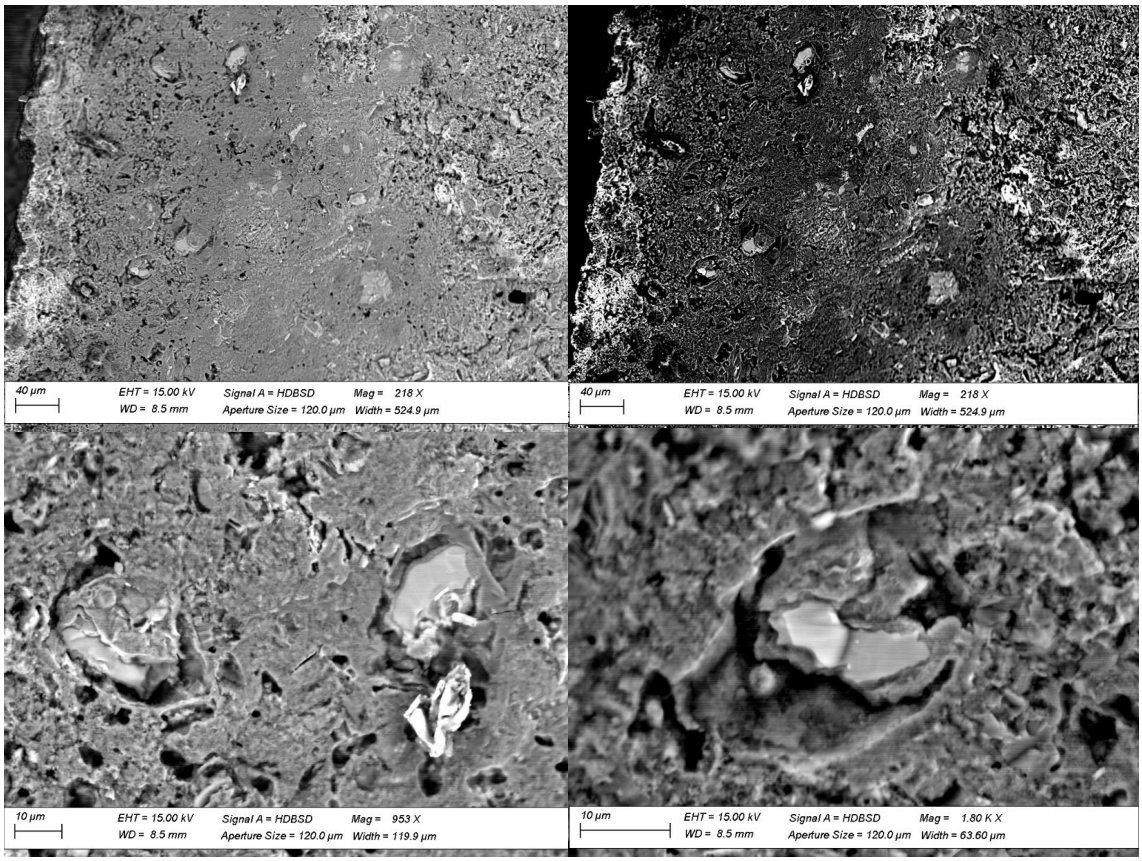

Fig. 4.29.: Edge exposed to CO_2 in supercritical state after 120 days of carbonation. It is observed that the zone closer to the surface has more voids, indicating that $CaCO_3$ is dissolving.

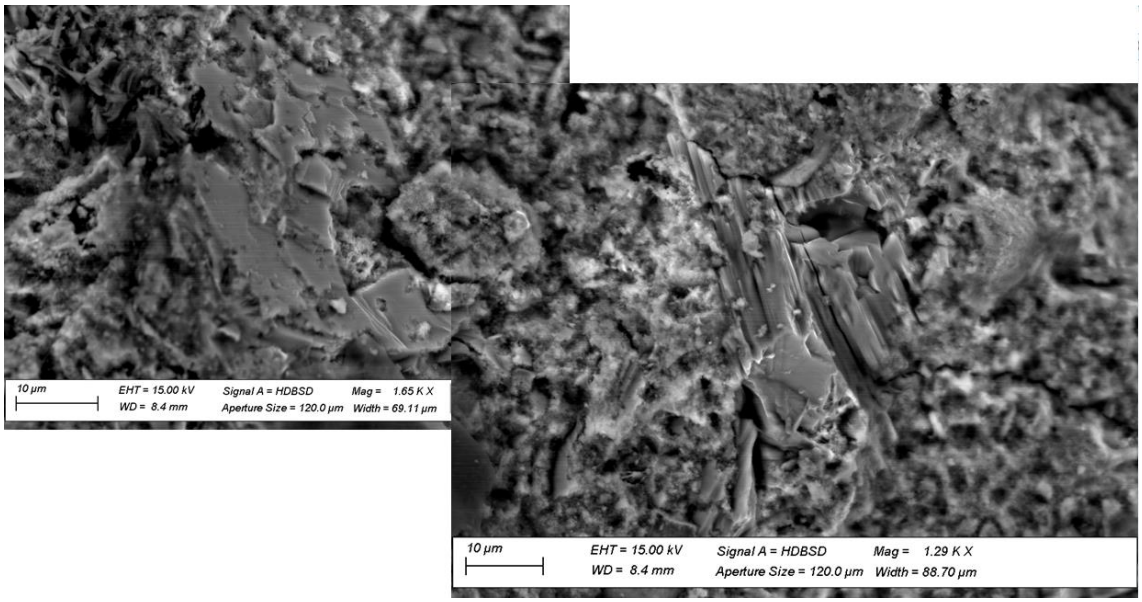

Fig. 4.30.: Structure of carbonated cement after 120 days. The precipitation of $CaCO_3$ crystals generates a zone with low porosity.

4.3.6 X-ray diffraction (XRD)

Figure 4.31 shows the XRD patterns of PC and BNC15, while Table 4.10 gives the relative percentages of the crystalline phases. The analyses show the contents of portlandite, katoite, brownmillerite, magnesite, aragonite, and calcite. Portlandite is one of the main cement hydration products with high crystallinity. In contrast, C–S–H is a low crystallinity amorphous material. Brownmillerite is a phase of clinker denominated as C_4AF. Aragonite and calcite are calcium carbonates of a different crystalline system with orthorhombic and rhombohedral shapes, respectively. Katoite is a calcium aluminate hydrate more stable at high temperatures than ettringite. Before carbonation, the samples with BNC have an increase in the relative crystalline amount of portlandite and a lower amount of brownmillerite. A certain percentage of the specimens was carbonated before exposure. Katoite and okenite are also detected here. After carbonation, the exposed surface of all cements seem to be similarly affected. The percentage of CH has almost entirely vanished, katoite has disappeared in PC and BNC15, and a considerable increase in aragonite is observed, but there is no calcite increase. The cement's cores do not show substantial changes in the relative percentage of calcite. A reduction is seen in the amount of portlandite

in BNC15 samples, while the katoite amount increased in both types of cement whereas the brownmillerite quantity decreased.

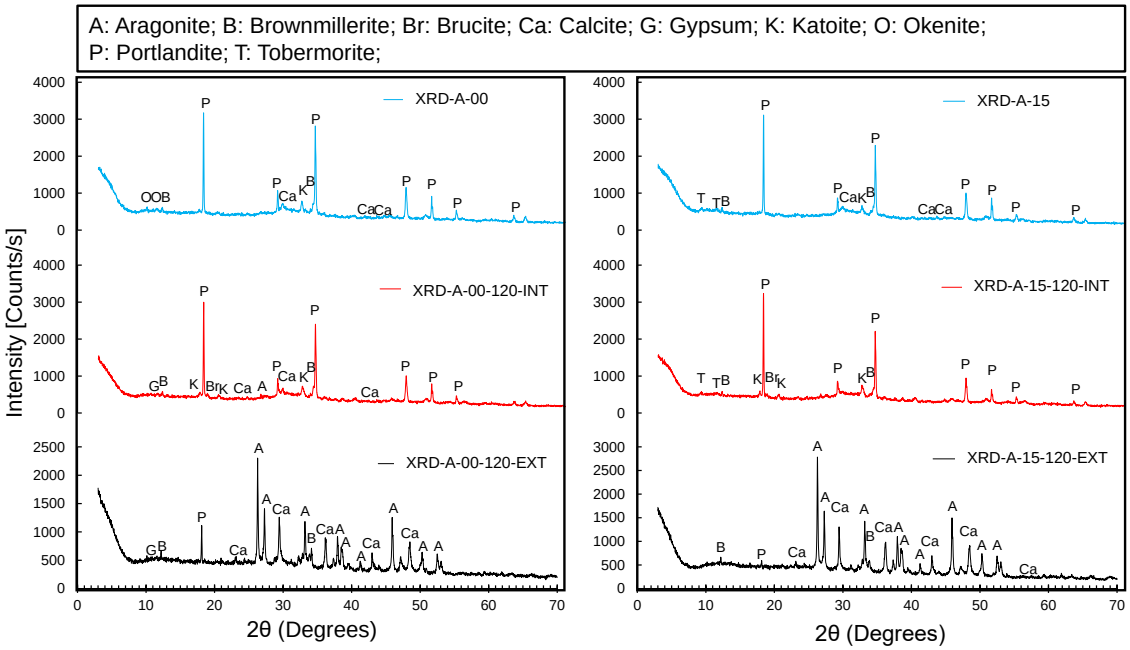

Fig. 4.31.: XRD patterns at the core (Int) and near the outer rim (Ext) of PC and BNC15 samples exposed to supercritical CO_2 for 120 days.

Crystalline phase	PC			BNC15		
	NC	Int (C)	Ext (C)	NC	Int (C)	Ext (C)
Portlandite	50	52	5	63	55	1
Katoite	16	23	-	14	26	-
gypsum	-	Traces	traces	-	-	-
Brownmillerite	16	11	9	12	10	5
Tobermorite	-	-	-	traces	traces	-
Brucite	-	3	-	-	traces	-
Okenite	5	-	-	-	-	-
Calcite	13	10	12	10	8	9
Aragonite	-	Traces	73	-	-	85

Tab. 4.10.: Quantification of crystalline phases from XRD results (120 days of carbonation).

For non-carbonated samples, the increase in the amount of portlandite and decrease in browmillerite in samples before carbonation reinforces the results reported in previous sections showing that BNC increases the degree of cement hydration. XRD curves are similar to other types of G-cements [58], showing similar crystals. The lack of ettringite and monosulfoaluminates may be due to the low content of C_3A and gypsum in the cement [58, 195]. Katoite or silicious hydrogarnet can be formed from C_2S and C_4AF. These products have a similar chemical formula depending on fluid condition, sulfate activity, and temperature [196]. Here, both are listed as katoite in Table 4.10. Additionally, the lack of

crystals related to C-S-H is due to the insufficient intensity of reflection of this amorphous material [197]. The CH and C-S-H structure can be observed in Figure 4.32, which shows a non-carbonated cement structure. The upper right image shows a CH crystal resting on the amorphous C-S-H surface.

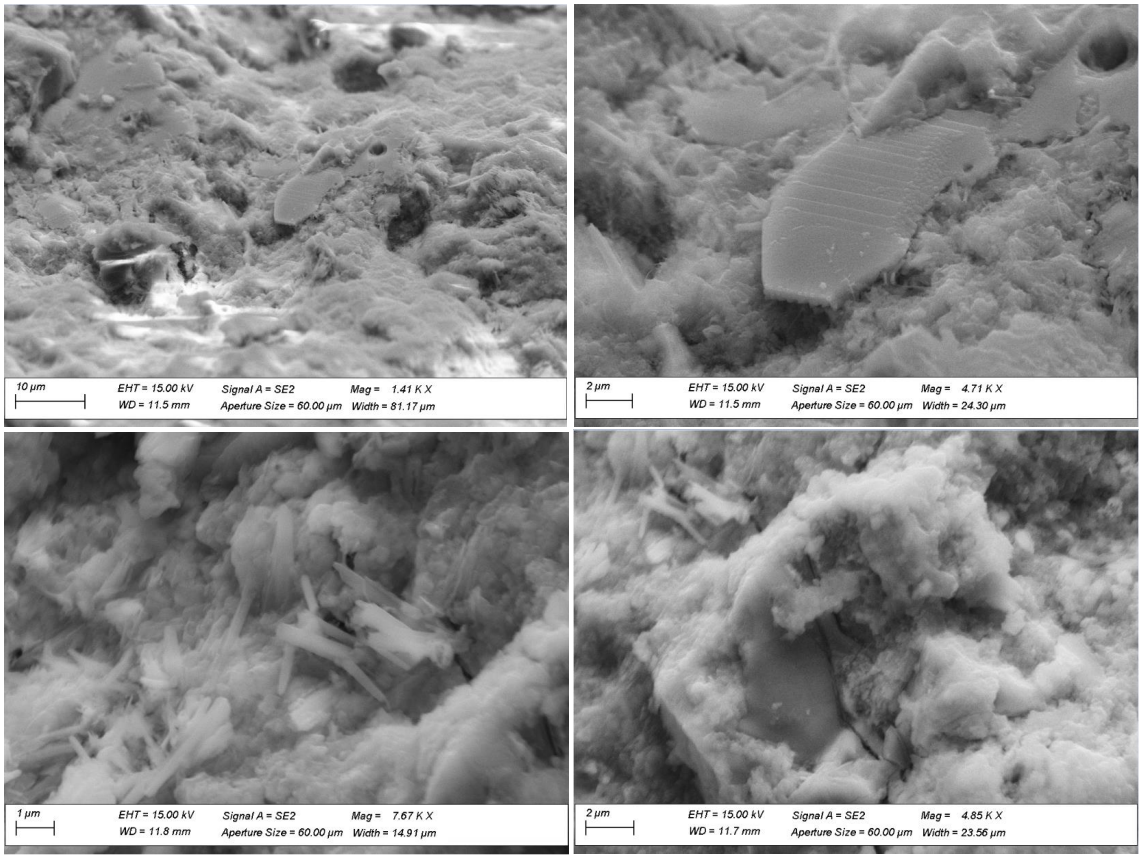

Fig. 4.32.: Non-carbonated cement structure. The images show portlandite crystals surrounded by C-S-H.

The post-carbonation XRD results on the exposed surface indicate almost complete carbonation of the cement hydrates, which confirms the MIP results. A large amount of aragonite in this area denotes higher chemical instability due to its high solubility. This may indicate that dissolution of the $CaCO_3$ crystals could take place if a suitable external fluid (water) were present. The core is less affected by carbonation, but the percentages of minerals have changed. The increase in katoite is probably a combination of temperature effect during carbonation, as this material is more stable at higher temperatures, and C_4AF hydration. In fact, katoite was found to increase significantly upon hydration of C_4AF [198].

Figure 4.33 shows the thermogravimetric results of the carbonated samples near the exposed surface.

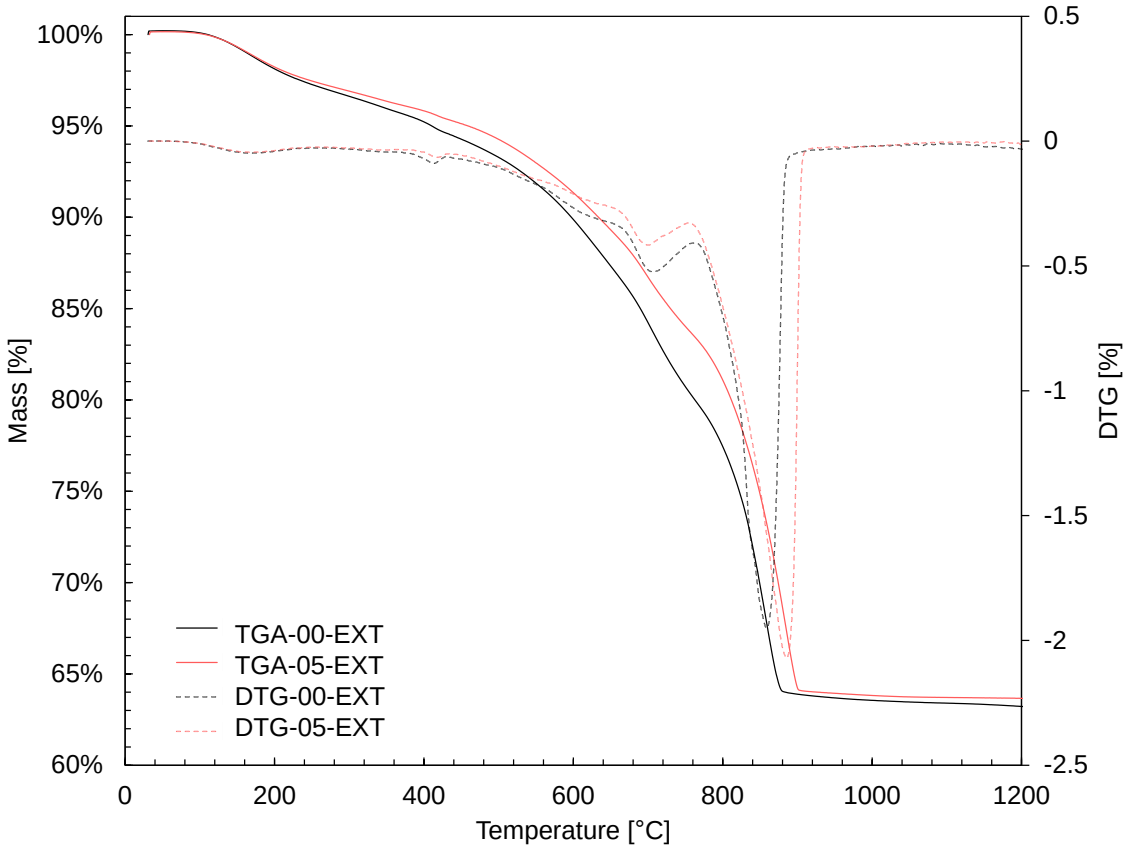

Fig. 4.33.: TGA results for Portland Cement (PC) and BNC05 near the exposed surface of samples carbonated for 120 days.

Results near the outer edge of the sample indicate that all of the portlandite was consumed. A small peak corresponding to katoite can be observed in the DTG graph. Two other peaks are seen in the DTG, one around 700 °C, and a larger one at 860 °C for PC and another at 900 °C for BNC05. Some authors [54, 67] agree on the fact that the first peak refers to less stable calcium carbonates such as aragonite or vaterite, while the higher temperature peak corresponds to a calcite of greater crystallization. Quantitative results are presented in Table 4.11 and give values of 51.9% carbonates for PC and 56.8% for BNC05. However, this technique does not allow to distinguish between calcium carbonates produced from CH or from C-S-H.

Component [%]	PC	BNC05
Portlandite	0	0
Aragonite/Vaterite	15.5	12.2
Calcite	36.4	44.6

Tab. 4.11.: Content of portlandite and calcium carbonates near the exposed surface after 120 days of carbonation

Figure 4.34 shows SEM images of the structure of a BNC15 sample carbonated for 120 days. Here we can see that the topography changed from a foamy form to a crystalline

form generated by calcite crystals, with no CH or C-S-H present. Zooming in further, in image b we observe calcium carbonates with a different crystalline system. These crystals have a shape similar to aragonite or vaterite. However, in the XRD analysis, only calcite or aragonite crystals are visible. Image c shows the different zones that are produced due to carbonation. The $CaCO_3$ redissolution zone is the most exposed to carbonic acid and it is here that calcite can be transformed into aragonite and then dissolved in the fluid. The carbonation front is a denser zone richer in calcium carbonates. The CH dissolution zone is characterized by being a more porous zone than the uncarbonated cement.

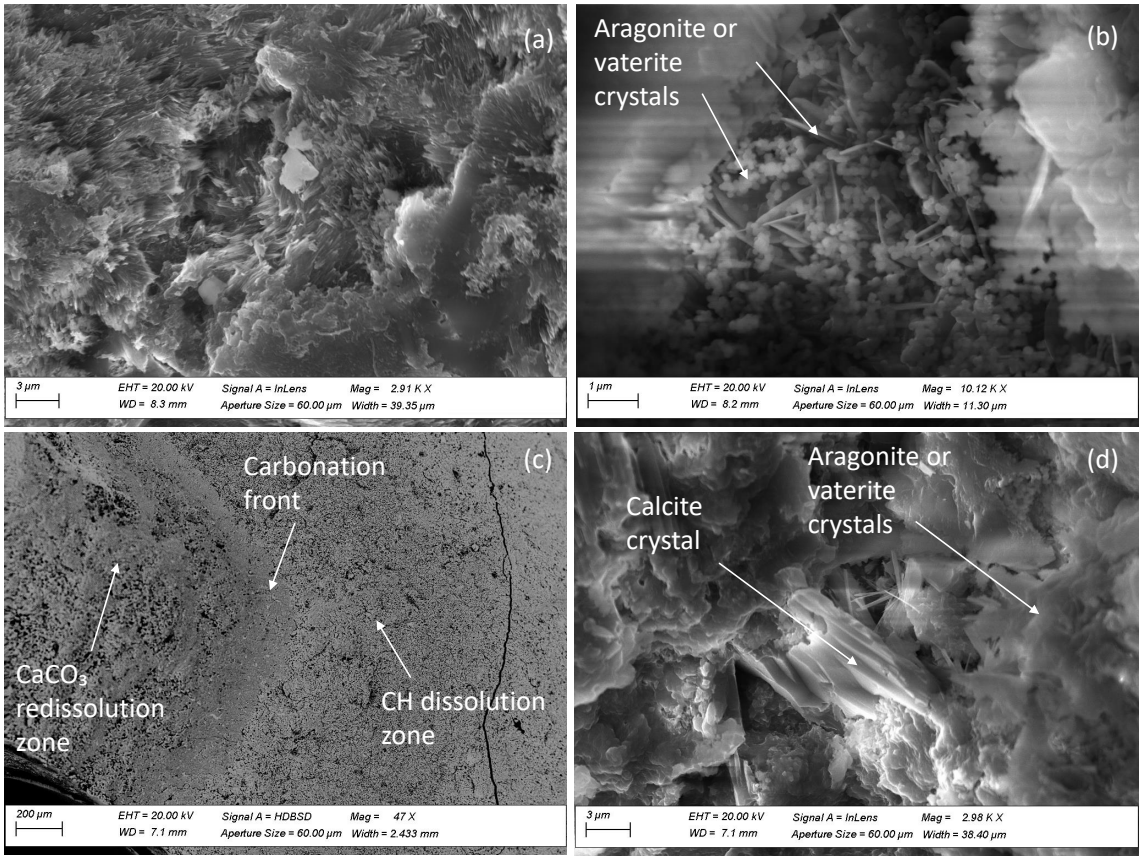

Fig. 4.34.: (a) Structure of the carbonated cementitious matrix (b) Types of calcium carbonate crystals (c) Carbonation zones of the cement (d) Calcite crystal in carbonated cementitious matrix.

BNC15 shows a decrease in portlandite, suggesting that CH dissolution has started. However, this is not observed in PC cement. Some aragonite traces are detected at the core of the PC sample. Carbonation and/or hydration during the test produced a change in the amount of katoite and brownmillerite, while portlandite and carbonates do not appear to have changed.

Figure 4.35 shows the thermogravimetry of the cement core after 120 days of carbonation. The results in 4.2.6 indicated very low amount of carbonates in non-carbonated samples. However, the carbonated samples at the core indicate some carbonation. The portlandite

peak is found around 500 °C, while carbonation peaks are observed between 750 and 800 °C for PC and BNC05 correspondingly, and at 900 °. It is worth noting the difference in temperature between these peaks on the outside and inside of the sample. Indeed, a carbonated cementitious material will have more chemically stable calcite crystals, so its mass loss will be at higher temperatures. On the other hand, a material at the cement core will have a lower CO_2 concentration, yielding metastable calcite carbonates, and lower decarbonation temperature, as shown in Figure 4.35. We observe that the percentage of portlandite in the core is 13% for PC and 14.8% for BNC05. The percentage of calcite are 10% for PC and 6.3% for BNC05. It is possible that the considerable katoite growth and brownmillerite reduction can affect the relative crystal proportions of portlandite and calcite concealing small carbonate precipitations.

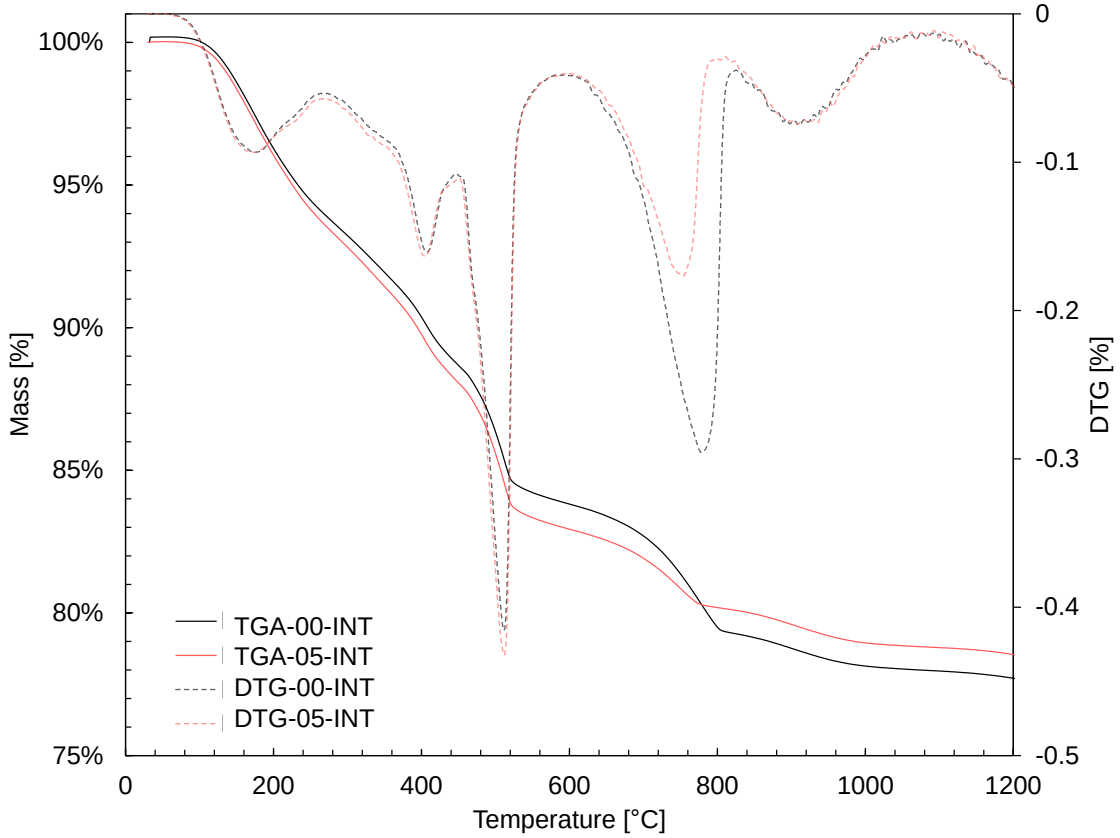

Fig. 4.35.: TGA results for PC and BNC05 at the core of samples carbonated for 120 days.

4.3.7 Conclusion

Density has increased in all samples, but cement with 0.05% of BNC was the lightest. An important degraded zone was seen at the top of the samples, but radially, the cement was less damaged.

BNC exchanges the capillary porosity (reducing it) by gel porosity (increasing it). By having smaller pores, the advance of CO_2 is slowed down in modified samples.

A linear reduction in capillary porosity was noted radially over the exterior of the samples during the 120 days of carbonation while gel porosity was decreased during the first 30 days of carbonation. Gel porosity increases again after 120 days of carbonation, suggesting C-S-H decalcification. Total porosity at the end of the experiments resulted in a lower value than the initial one.

At the core, capillary porosity was reduced in PC and BNC15 samples but not for BNC05. Pore size distribution has varied and oven porosity has increased, with a reduction of largest pores, and an increase in gel pores.

Carbonation generates a reduction in the mechanical strength and Young's modulus of all samples. This is probably due to the constant decalcification of C-S-H, which reduces the integrity of the cementitious matrix. Neat cement samples show a continuous decline in strength, while samples with BNC maintain the same strength from 30 to 120 days. Samples with BNC show higher values of their mechanical properties in absolute and relative terms before and after the carbonation process. A decrease in the compressibility modulus of cement in triaxial tests is also observed, although BNC05 maintains values higher than PC.

TGA results indicate that BNC05 cement has lower amounts of calcium carbonates, either in the core or near the surface exposed to CO_2.

XRD results show more crystalline phases of hydrated cement in samples with BNC before carbonation. A large amount of aragonite in the outer rim may indicate that dissolution of the $CaCO_3$ minerals might take place if external conditions allowed it.

SEM images show the initial foamy topography (amorphous C-S-H) of uncarbonated cement and the fully crystalline surface of carbonated cements for 120 days. They also show carbonates growing in the form of sheets overlapping each other, pore crystallization and dissolution of calcium carbonates near the exposed surface.

Cement with 0.05% of bacterial nanocellulose presents a lesser degraded zone and is not affected at the center of the sample as the other mixtures. PC and BNC15 share similarities in their behaviour when exposed to carbonation. However, porosity changes and lower density variation suggest that BNC05 allowed fewer chemical reactions. This was corroborated by the carbonation degree analysis and by the UCS results.

4.4 High temperature curing effect and carbonation

BNC-cement samples subjected to supercritical carbonation showed that their mechanical behaviour is less affected than non-modified cement. Nevertheless, their behaviour at different curing conditions like those in a reservoir is unknown.

Temperatures in the various geological reservoirs (coal beds, deep saline aquifers, or depleted oil and gas reservoirs) can vary depending on the depth at which they are found. In some reservoirs, the temperature can vary from 60 to 160 °C [29], being 90 °C a value often considered by other authors experimenting with oil well cement [30, 199, 32, 33].

The following analysis focuses on the microstructure and mechanical changes of cement pastes with added bacterial nanocellulose and cured at 90 °C for 30 and 120 days in the context of CO_2 reservoir conditions.

This section shows the results obtained for cement cured by method A (see Section 3.2). 16 specimens were carbonated from 2 different mixtures: PC and BNC05. Some were used for mechanical testing (6), while others were used for microstructural analysis of the core and areas near the CO_2 exposed surface of the specimen.

4.4.1 Supercritical carbonation test

Figure 4.36 shows a longitudinal cross section of samples after 30 days of carbonation. Brown color represents the most degraded part of cement due to carbonation, the color probably being due to iron hydroxide released from chemical reactions[13]. PC samples show a core with less change in coloration compared to BNC05. BNC05 presents some small voids in their interior, which could allow further CO_2 penetration. The penetration depth had important progress on the cement cured at 90 °C after 30 days of carbonation. These results are similar to values obtained by other authors considering similar curing and carbonating conditions[30, 73]. There are some uncertainties based on studies by previous authors, mainly from the curing conditions before carbonation. Indeed, water to cement ratio, curing temperature and pressure, and duration will affect the carbonation depth, so different curing conditions and equal carbonation procedures will yield different results. Some previous experiences used short curing times for the cement[30, 73], and show high CO_2 penetration, while some other authors performed longer curing periods[69, 179], showing less penetration. Recent works have shown that cement with lower density allows a higher CO_2 penetration[79]. Furthermore, a higher hydration degree is tied with density increase, and porosity reduction[60]. Thus maintaining a high temperature during a short curing period will allow deeper CO_2 penetration into the cement samples and more advanced chemical reactions.

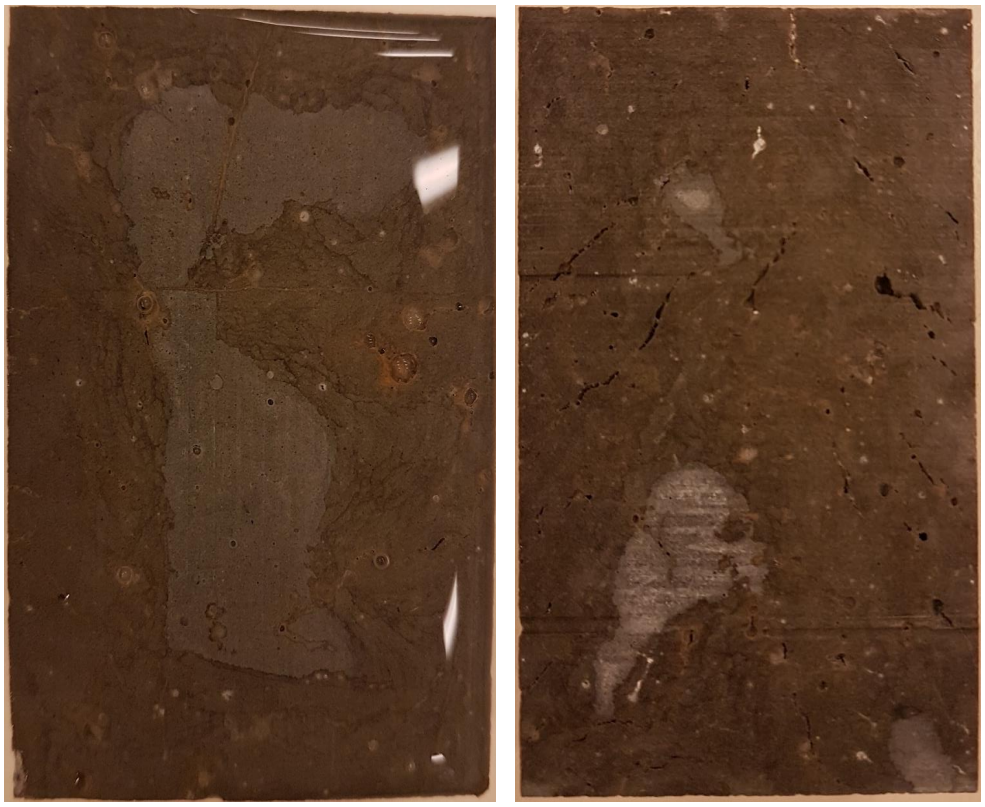

Fig. 4.36.: Samples cured at 90 °C and carbonated for 30 days (left: PC, and right: BNC05).

In this case, 30-days carbonation led to an increase in the density of PC and BNC05 samples. Before carbonation, a slight difference is noted between PC and BNC05 samples, with densities of 1.89 and 1.87 g/cm^3, respectively. Once the samples were carbonated, density increased until 2.13 and 2.11 g/cm^3 for PC and BNC05 (Table 4.12). PC shows an average mass uptake of 13.2% while BNC05 shows an average of 12.9%, meaning that fewer chemical reactions have taken place. The mass gain is similar to previous works under similar conditions[73], however, the penetration depth is different. Our results are closer to the penetrations observed by Fabbri and co-workers[30], even though our samples are not fully carbonated after 30 days. This is because our samples are larger, so that more CO_2 is needed to carbonate a larger volume, , while the diffusion of CO_2 limits chemical reactions. In addition, it was observed that a greater number of samples were damaged after the carbonation process that lasted 120 days, producing cracks or breaks (Figure 4.37).

Samples	Reference	Initial density [g/cm^3]	Final density [g/cm^3]	Mass gained [%]
1	PC-30 days	1.89	2.13	13.2
2	BNC05-30 days	1.87	2.11	12.9
3	PC-120 days	1.89	2.15	13.7
4	BNC05-120 days	1.85	2.16	16.6

Tab. 4.12.: Density and mass gained after carbonation.

After 120 days of carbonation, the density and mass uptake continued growing until 2.11 g/cm^3 for both cements. In this case, mass uptake is higher in samples with BNC05.

Fig. 4.37.: Cracks in samples of cement cured under unfavorable conditions and carbonated for 120 days.

4.4.2 Mercury intrusion porosimetry (MIP) and total porosity

Oven-drying for one week at 85 °C has not significantly affected the MIP porosity or the pore size distribution when compared to freeze-drying (not oven-dried for one week) (Figure 4.38). MIP porosity increased for both cement types from 33.7% (freeze-dried) to 34.5% (oven-dried), before the carbonation test, and the characteristic peak is approximately 0.050 μm. Bacterial nanocellulose did not significantly modify the cement in terms of porosity or pore size distribution when comparing to PC cement cured at 90 °C. Likely, bacterial nanocellulose does not have the same effect in inhibiting the larger cracks produced by the high curing temperature.

Calorimetry tests have shown that BNC initially acts as a cement retarder [167, 166]. As the curing time in this work is short, the porosity of BNC-cement is similar to PC with some coarser pores at 0.20 μm. Nevertheless, for longer curing periods (e.g. cement cured at 20 °C for 28 days), the cement structure is denser and more compact. In these conditions, bacterial nanocellulose is more likely be more intricate within a cement matrix and increase hydration degree [156, 171], as it tends to release adsorbed water, which contributes to the hydration [111].

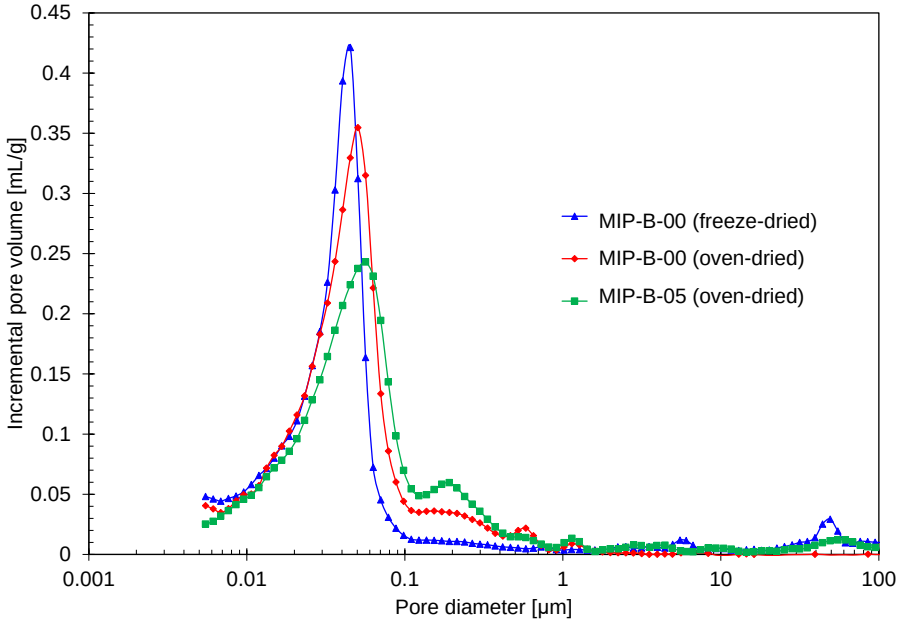

Fig. 4.38.: Pore size distribution of oven-dried (curing method B) and freeze-dried samples.

The MIP results after the carbonation of PC are presented in Figure 4.39. Here we can observe that the porosity variation along the radial direction leads to smaller pores and smaller porosity values. At the same time, the characteristic peak is shifted to pores smaller than 0.010 μm. After carbonation, no significant change is observed due to the addition of BNC. Porosity decreased to 24.5% at the core and to 21.5% near the exposed surface. BNC05 shows similar results to PC (Figure 4.40), and its porosity decreased at the core to 23.2% and near the exposed surface to 21%. The slight mass uptake is due to the consumption of CO_2 by the occurring chemical reactions and is reflected by these small porosity variations. Reduced porosities lead to less diffusion of CO_2 into the cement core and therefore increase the time to reach full carbonation of the samples. Table 4.13 shows the porosity values of the samples carbonated for 30 and 120 days.

Test	Sample	BNC [%]	Carbonation days	MIP porosity [%]
1	PC-Reference	0	0	33.7
2	PC-NC	0		34.6
3	BNC05-NC	0.05		34.5
4	PC-30INT	0	30	24.5
5	PC-30EXT	0		21.5
6	BNC05-30INT	0.05		23.2
7	BNC05-30EXT	0.05		21.0
8	PC-120INT	0	120	14.5
9	PC-120EXT	0		13.4
10	BNC05-120INT	0.05		14.6
11	BNC05-120EXT	0.05		15.2

Tab. 4.13.: MIP experiments on samples cured at 90 °C.

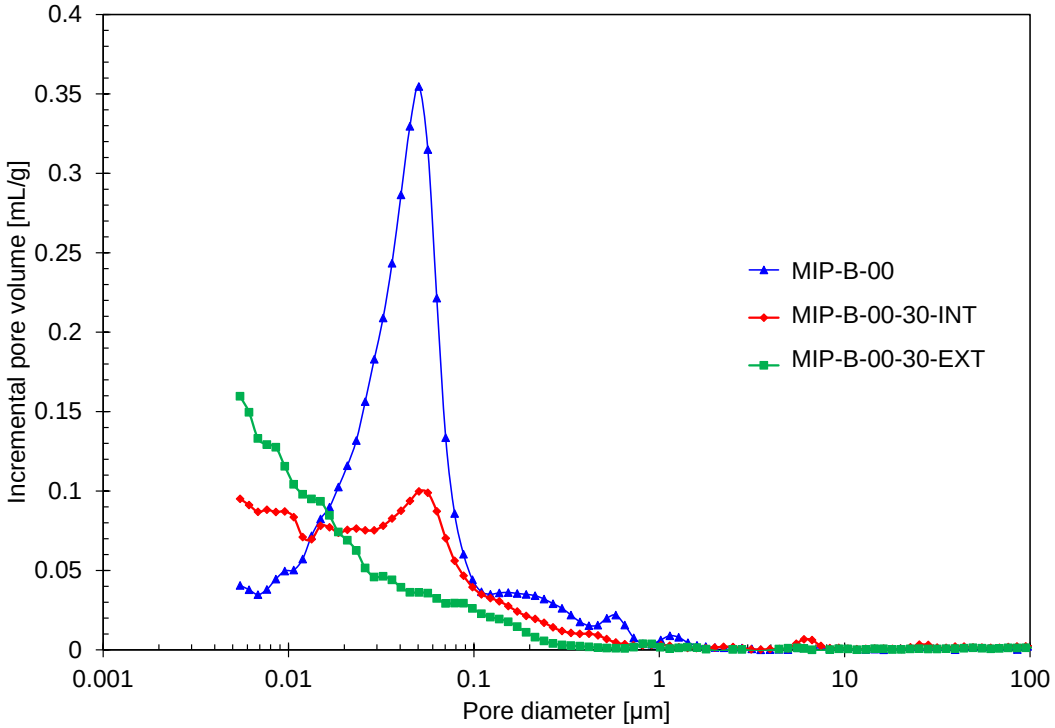

Fig. 4.39.: Pore size distribution of 30-days carbonated and non-carbonated PC samples cured at 90 °C. The red curve corresponds to the cement core, while the green curve corresponds to a sector near the exposed surface.

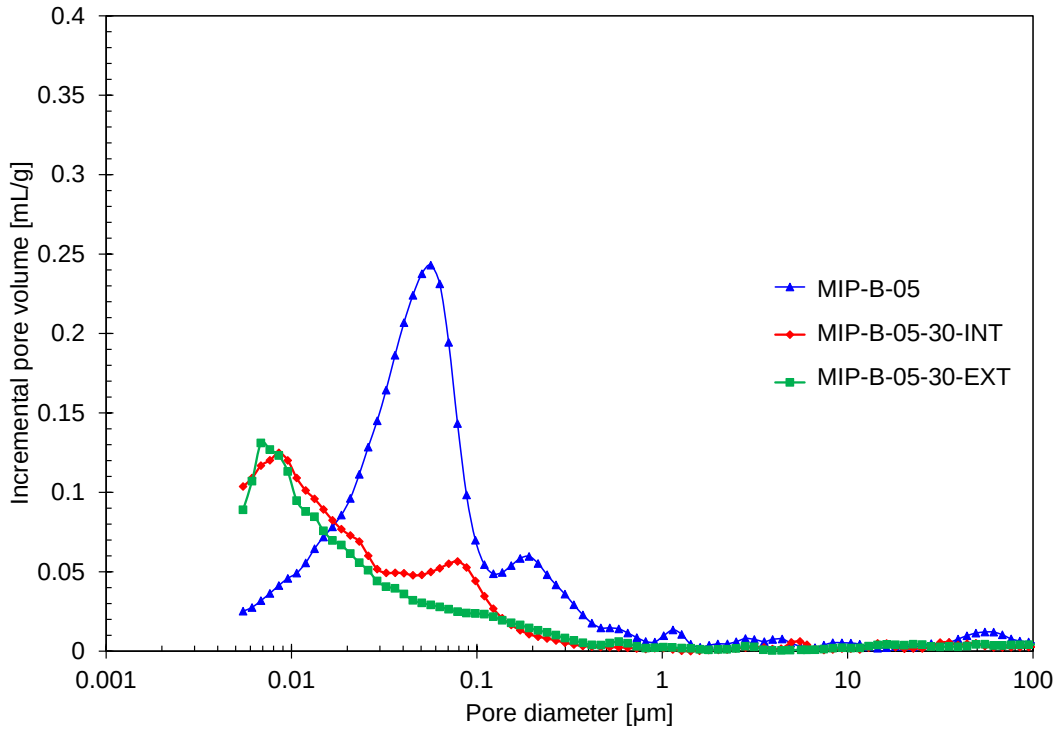

Fig. 4.40.: Pore size distribution of 30-days carbonated and non-carbonated BNC05 samples cured at 90 °C. The red curve corresponds to the cement core, while the green curve corresponds to a sector near the exposed surface.

After 120 days of carbonation, the pore size distributions are very similar in shape to each other for both PC (Figure 4.41) and BNC05(Figure 4.42). This can be due to two causes: that pore clogging prevents further precipitation or that there is a limit to the rate of calcium carbonate precipitation that prevents it from dropping below 14% porosity [68, 200]. PC MIP values reach 14.5% for the interior and 13.4% for the exterior, while BNC05 values reach 14.6% and 15.2%, respectively. The second is the most probable case, since in samples cured at 20 °C, values as low as 5% MIP porosity could be observed. This reduction rate may be due to the cement running out of portlandite and C-S-H, which limits chemical reactions, leaving only non-hydrated cement to carbonate. Indeed, the shorter time the cement had to hydrate means that there are fewer hydration products that can react with H_2CO_3.

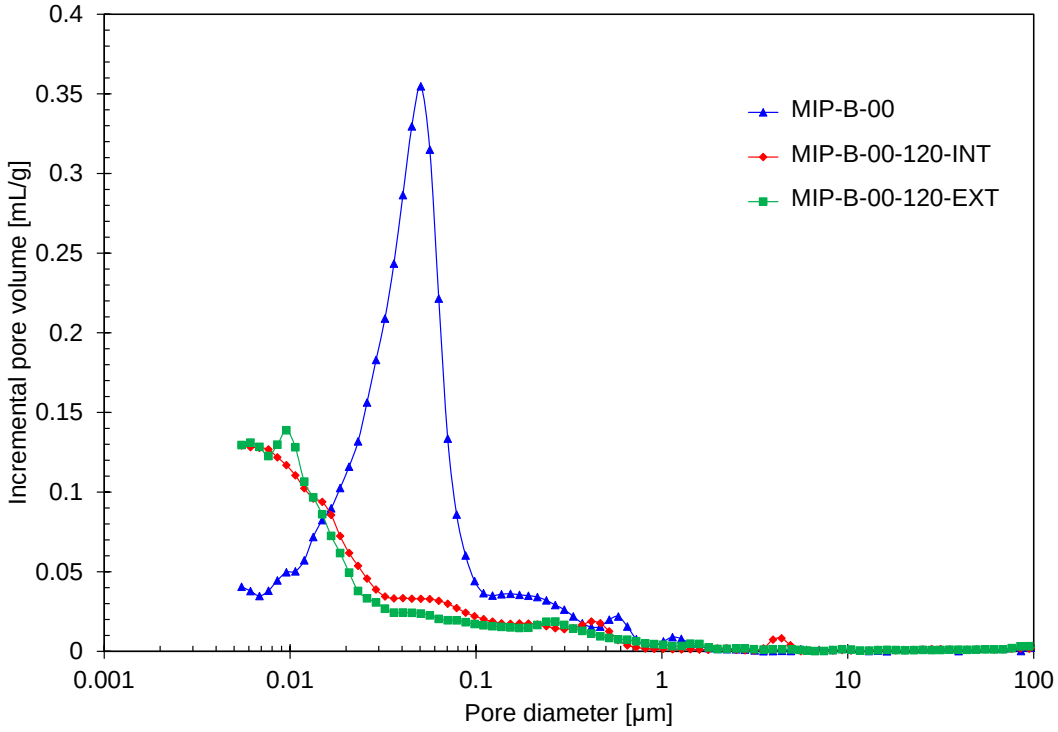

Fig. 4.41.: Pore size distribution of 120-days carbonated and non-carbonated PC samples cured at 90 °C. The red curve corresponds to the cement core, while the green curve corresponds to a sector near the exposed surface.

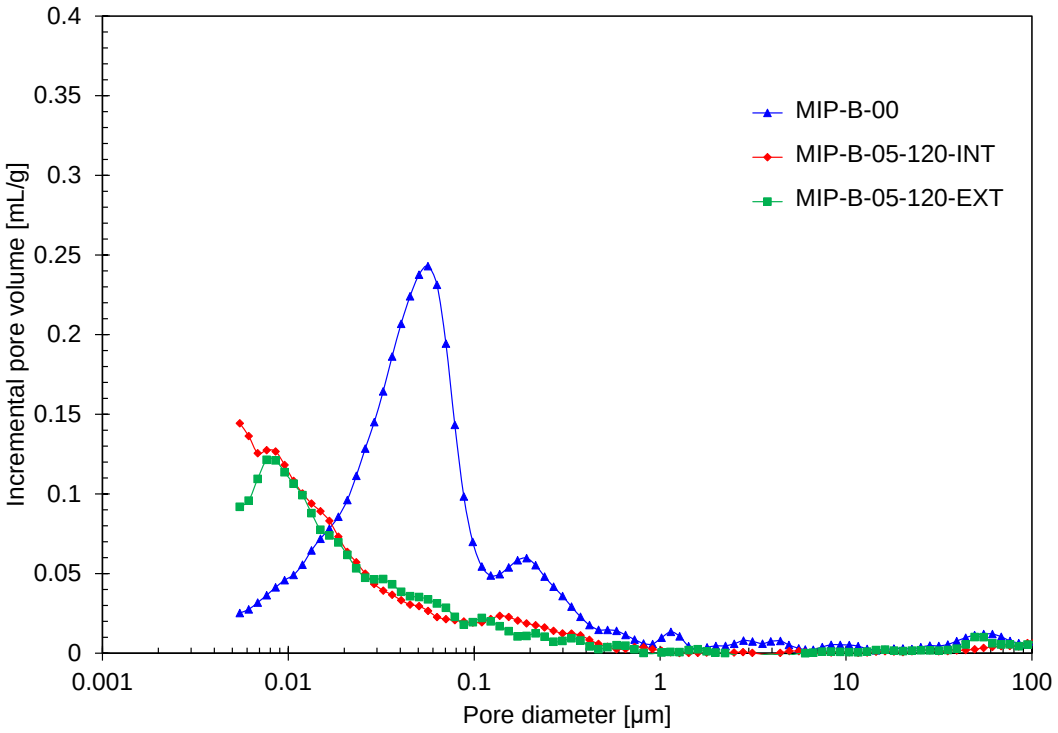

Fig. 4.42.: Pore size distribution of 120-days carbonated and non-carbonated BNC05 samples cured at 90 °C. The red curve corresponds to the cement core, while the green curve corresponds to a sector near the exposed surface.

In non-carbonated samples, the water porosity is higher in samples with BNC (Table 4.14). After carbonation, the total porosity is 30% in the interior of the sample, while it is 28% near the external surface. No major differences are observed in the two types of mixtures.

Test	Sample	BNC [%]	Carbonation days	Water porosity [%]
1	PC-NC	0	0	40.1
2	BNC05-NC	0.05	0	42.6
3	PC-120INT	0	120	29.6
4	PC-120EXT	0	120	28.3
5	BNC05-120INT	0.05	120	30.0
6	BNC05-120EXT	0.05	120	28.0

Tab. 4.14.: Water porosity on samples cured at 90 °C.

4.4.3 Measurement of elastic ultrasound waves and unconfined compressive strength (UCS)

Table 4.15 shows the mechanical properties determined from V_P and V_S measurements. Overall, mechanical properties increase during the carbonation process. UCS tests corroborate this statement. However, these results cannot be directly compared, since one is a dynamic method, and the other a static one. The carbonated samples show an increment in compressive strength (Figure 4.43) and their Young's modulus (Figure 4.44). PC strength initially was 31 MPa, and after the carbonation stage of 30 days, it increased by 44%, while BNC05 started with 24 MPa of strength, and it increased by 60%. Both types of cement initially had Young's modulus of 20 GPa, unlike the 25 GPa for long-cured specimens in previous sections, but after carbonation, this modulus increased by 11% for PC and by 18% for BNC05.

Sample	G [GPa]	K [GPa]	E [GPa]	ν
PC - NC	8.4	9.5	19.5	0.16
PC - 30-days C	8.9	12.7	21.3	0.22
BNC05 - NC	7.8	8.5	18	0.15
BNC05 - 30-days C	8.9	9.8	20.5	0.15

Tab. 4.15.: Elastic properties obtained from elastic waves velocities V_P and V_S.

Under these conditions, BNC05 samples initially have less compressive strength than PC samples and similar Young's modulus. These observations depart from the results previously obtained with cement cured at room temperature over a long period in the previous sections. Curing at a higher temperature is probably generating larger cracks in the cement, so the microstructural effect of BNC does not substantially improve the mechanical behaviour. This effect appears during the carbonation stage because of the retarder effect of BNC or the superplasticizer, which slow down the hydration rate of the modified cement, and thus the hydration degree at the end of the initial curing time.

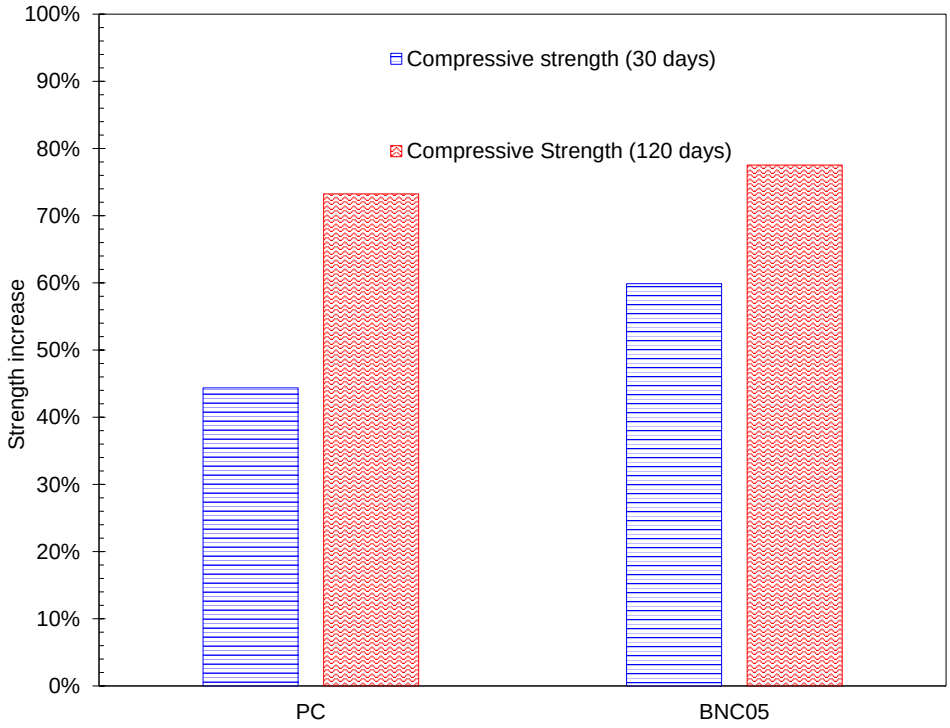

Fig. 4.43.: Compressive strength after carbonation of PC and BNC05 samples for 30 and 120 days.

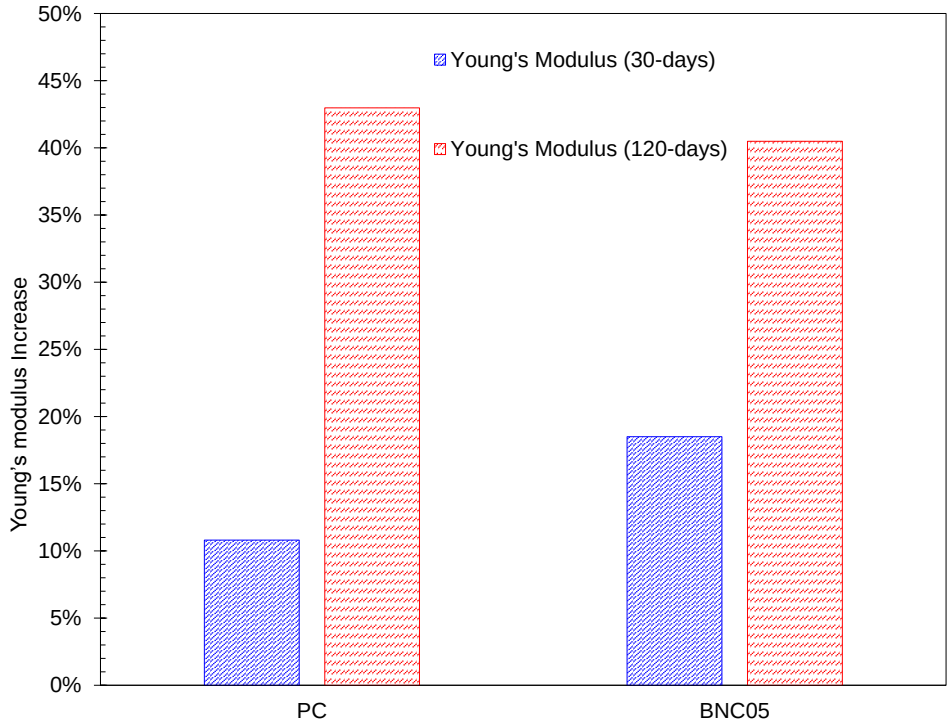

Fig. 4.44.: Young's Modulus after carbonation of PC and BNC05 samples for 30 and 120 days.

BNC enhanced the hydration kinetics due to: (1) the hydrophilic properties of the bacterial nanocellulose [171]; and (2) its ability to release water during hydration [111].

Nevertheless, after 120 days of carbonation, this effect is reduced and the strength increment is quite the same between both cement, with a 73% increment (53 MPa) and 78% (43 MPa) for PC and BNC05, respectively. In the case of Young's modulus, PC cement shows an increase in value by 43%, while BNC05 an increased by 41%.

From these results, and with reference to Section 4.3, we determined that mechanical properties (Young's modulus and strength) will increase during carbonation if the curing time is short prior to carbonation, while they will decrease if the curing time is longer. After short curing conditions (90 °C for 72 h), cement will not be fully hydrated. Therefore, the mechanical performance increment after carbonation will most likely be due to the cement matrix development by hydration acceleration imposed by temperature in the carbonation cell. At the same time, the results of the mechanical tests will be linked to the combination of the effects of cement hydration components and precipitated calcite produced during carbonation. A new question arise in this situation: for longer times in the carbonation cell, will the mechanical properties degrade again?. New experiments could determine whether this is the case or not. On the other hand, cements with a high degree of hydration before carbonation (cement cured for 28 days at 20 °C) will only experience a drop in strength due to C–S–H degradation and porosity increase over time [179, 187, 184]. These observations are intricately linked to the static carbonation conditions. In the present experiment, CO_2 penetrates the sample by diffusion in the pore fluid, which is not renewed. However, if cement carbonation is imposed by a continuously renewed fluid, then the products of carbonation (mainly carbonates), will in turn dissolve and be flushed out, leading to a strong increase in porosity of the cement, and degraded mechanical properties.

Since $C\bar{C}$ has better mechanical performance than CH, $C\bar{C}$ precipitation should increase mechanical performance and Young's modulus of carbonated cement. This effect can occur here because of the continuous hydration of cement inside the reactor, which links the precipitated $C\bar{C}$ with the cement matrix. These two effects increase mechanical properties, as seen by Fabbri et al. and Sauki et al.[30, 186], but cement hydration plays the most significant role during the carbonation process. This can also be observed from V_P and V_S wave data, where mechanical parameters increased during carbonation.

The moduli obtained from the measurement of elastic waves is dynamic, while that measured in UCS tests is static. Therefore, they cannot be directly compared, but a similar trend can be obtained in both tests. Young's moduli measured by elastic waves are 19.5 and 21.3 GPa for PC before and after carbonation, while for BNC05, measured values were 18 and 20.5 GPa. UCS tests gave values of 20 GPa for both types of cement samples before carbonation, while after carbonation, these values were 22.2 GPa and 23.6 GPa for PC and BNC05, respectively.

4.4.4 X-ray diffraction (XRD)

Figure 4.45 presents the XRD patterns of the samples cured at 90 °C before and after carbonation.

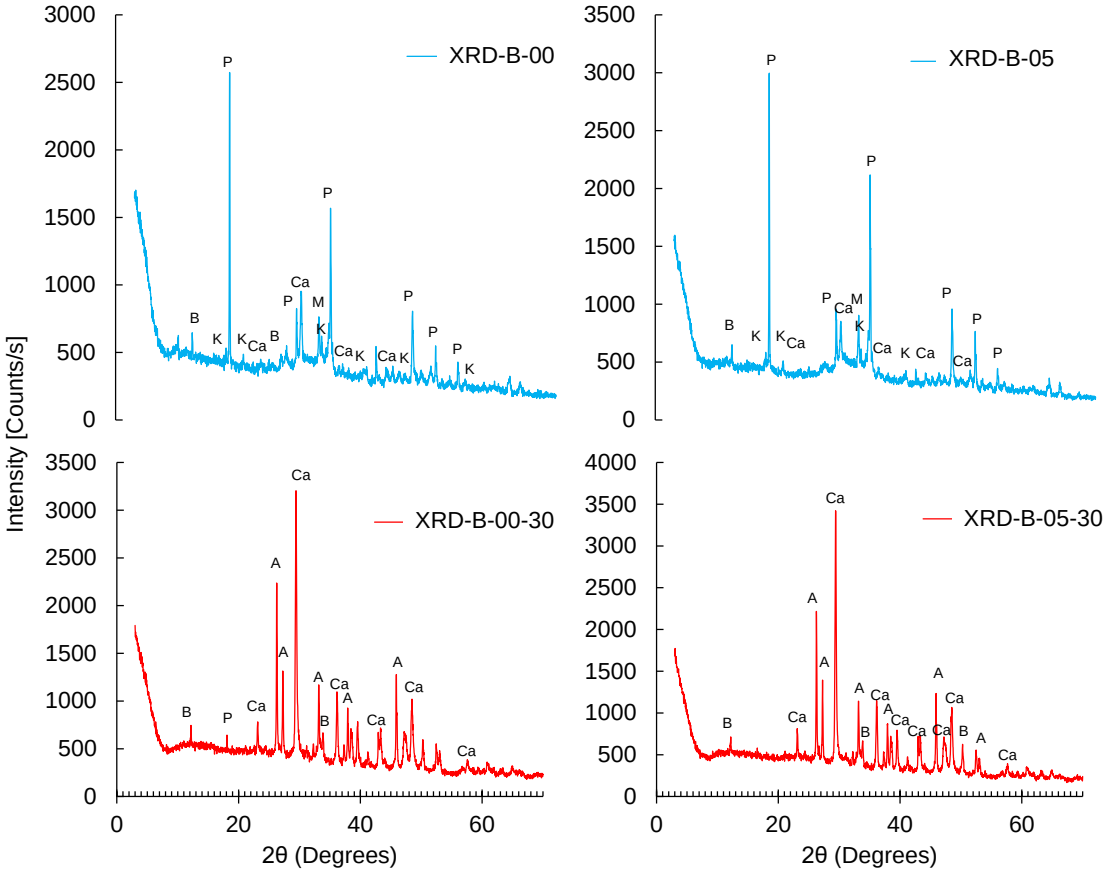

Fig. 4.45.: XRD patterns of non-modified cement (PC) and modified cement (BNC05) cured at 90°C before carbonation (NC), and after 30-days of carbonation (C).

XRD results on cement before supercritical carbonation (Table 4.16) show approximately 60% hydrated material (portlandite and katoite), 25% carbonated material (calcite and magnesite), and 15% non-hydrated and non-carbonated material (browmillerite).

Crystalline phase [%]	PC		BNC05	
	NC	C	NC	C
Portlandite	32	1	33	-
Katoite	28	-	29	-
Magnesite	10	-	5	-
Brownmillerite	16	6	15	7
Calcite	14	43	18	44
Aragonite	-	50	-	49

Tab. 4.16.: Quantification of crystalline phases from XRD results.

XRD results on cement after supercritical carbonation show no cement hydration materials (portlandite and katoite). Therefore, it means that complete carbonation is reached. Magnesite also seems to have been consumed, allowing the formation of more calcium carbonates. Crystalline carbonated materials amount to approximately 93% of the carbonated cement; the remaining 7% is C_4AF from the clinker phase that did not chemically react.

In this case, the generation of crystals can be seen directly if we cut longitudinally the sample (Figure 4.46). Up to 6 different zones with different colors can be observed. From left to center: light brown, beige, darker grey, dark brown, light grey and grey (Figure 4.47). The results of the PC and BNC05 samples before and after carbonation are similar to each other, suggesting that the BNC did not significantly affect the microcrystalline structure of the cement under these curing conditions.

Fig. 4.46.: BNC05 carbonated for 120 days. The image below shows a zoom of the red rectangle.

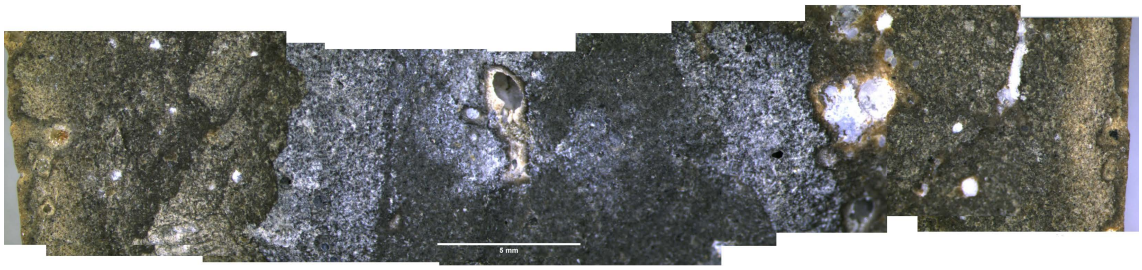

Fig. 4.47.: Zoom of a BNC05 sample carbonated for 120 days.

The carbonation process led to significant crystallization that is filling the pores of cement samples. Figure 4.48 and Figure 4.49 show two different pores one next to the other. One pore is completely filled, while the other shows that each crystal grows independently. This is similar to the situation in samples cured at 20 °C. At first, calcium carbonates grow separately and after certain carbonation time, these crystals start to merge and they develop a singular structure.

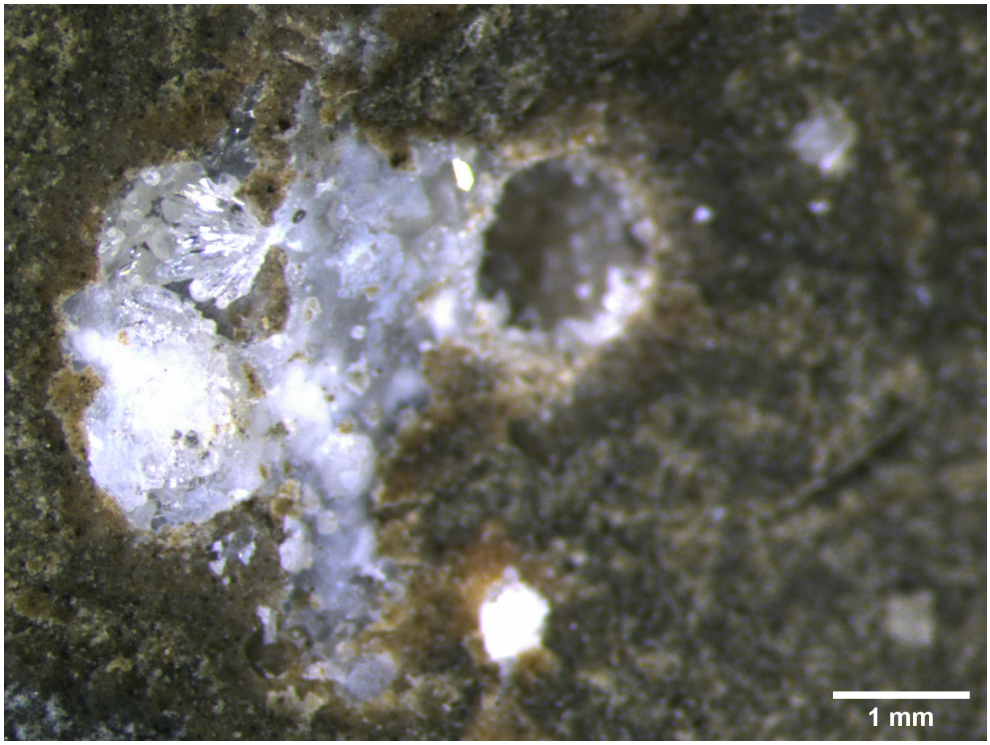

Fig. 4.48.: Crystal growth inside pores. BNC05 sample cured at 90 °C and carbonated for 120 days.

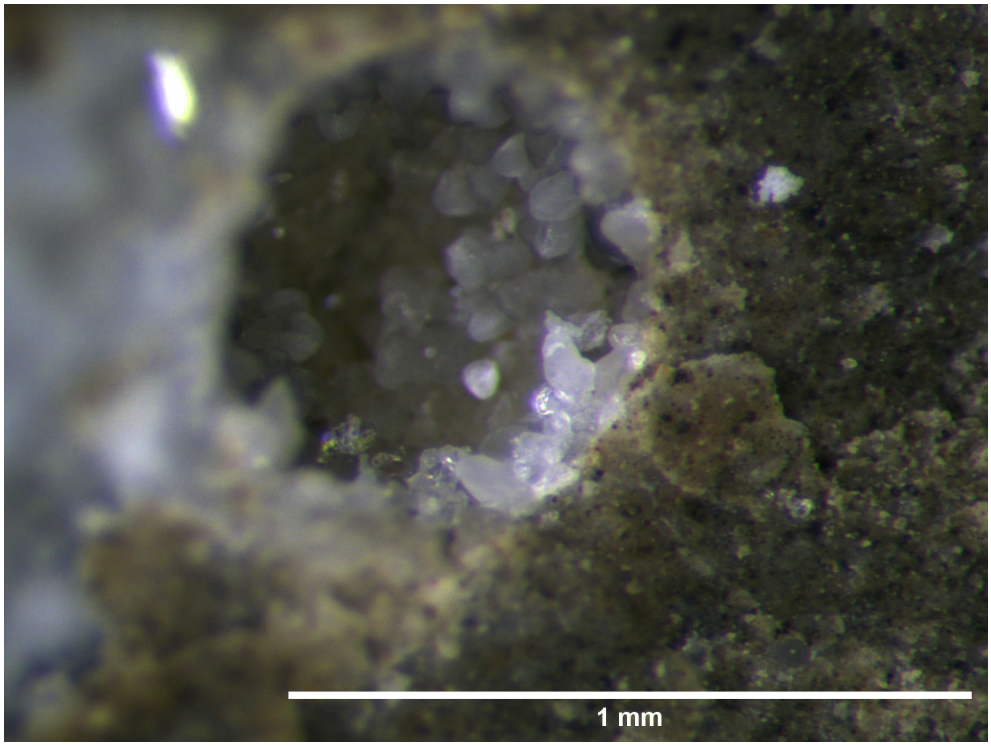

Fig. 4.49.: Crystal growth inside pores. BNC05 sample cured at 90 °C and carbonated for 120 days.

4.4.5 Conclusion

The microstructure and mechanical changes of cement with bacterial nanocellulose additions and cured at 90 °C in the context of reservoir conditions were analyzed. Mercury intrusion porosimetry (MIP), X-ray diffraction (XRD), ultrasonic wave measurements, and unconfined compressive strength (UCS) tests were performed on BNC-cement samples subjected to supercritical CO_2 conditions to determine their behaviour.

BNC-cement samples show a lower mass gain compared to PC after 30 days of carbonation. However, after 120 days of carbonation, BNC05 presents a higher mass uptake than PC. The BNC-cement longitudinal sections present some small voids in their interior, which could allow further CO_2 penetration.

The MIP results show that initially, samples with BNC have the same porosity as the cement without BNC addition. Lower porosity is observed in cement with BNC after carbonation for 30 days, either in the core or near the exposed surface. After 120 days, the porosity at the interior is the same for both cements, and is lower for PC near the exposed surface. It is observed that the reduction of porosity is limited to minimum values of 13/14%, probably due to total consumption of the hydrated components. Total porosity is higher in BNC05 before carbonation but it is the same at the interior and near the exposed surface after 120 days.

The XRD results of the PC and BNC05 samples before and after carbonation show no difference from each other. After carbonation, the dominant crystalline phases are calcite and aragonite, which indicates the complete carbonation of the material near the surface exposed to the supercritical fluid.

Unmodified cement samples show a better mechanical performance during carbonation. However, carbonation in samples with BNC indicates a higher increase in relative strength than in samples without additions due to the fact that BNC releases water during hydration inside the carbonation cell.

4.5 Integral assessment of the cement properties obtained

This section summarizes the effects of supercritical carbonation on cement, the effect of bacterial nanocellulose, and permeability analysis based on the results obtained from mercury intrusion porosimetry.

4.5.1 Microstructure and mechanical behaviour

Figure 4.50 shows the overall effects of carbonation on cement. Carbonation dissolves the portlandite and induces the precipitation of calcium carbonates, which fill the capillary pores. The effects of temperature in the carbonation cell, decalcification of C-S-H or interfaces produced by the carbonation front reduce the strength and Young's modulus of the material. Although porosity is reduced over time, this does not lead to an overall increase in strength. This indicates that the precipitation of stronger materials does not compensate for the loss of strength.

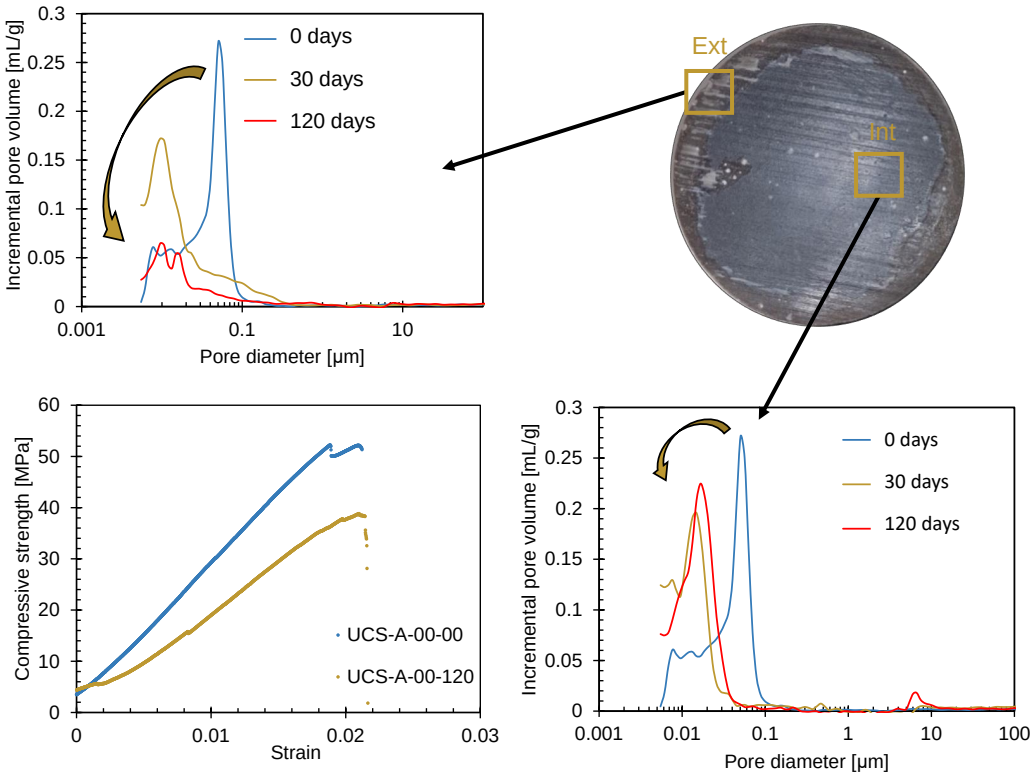

Fig. 4.50.: Effect of carbonation on porosity and mechanical strength of specimens cured at low temperature for 28 days.

SEM images of Figure 4.29 show greater porosity at the outer edges. In Figure 4.51 is also observed that the bulk modulus was reduced after carbonation, despite the fact that the outer edge is the one filled with calcium carbonates, which should resist the isotropic stress. XRD results show that aragonite is present, a mineral more prone to dissolve in water than calcite.

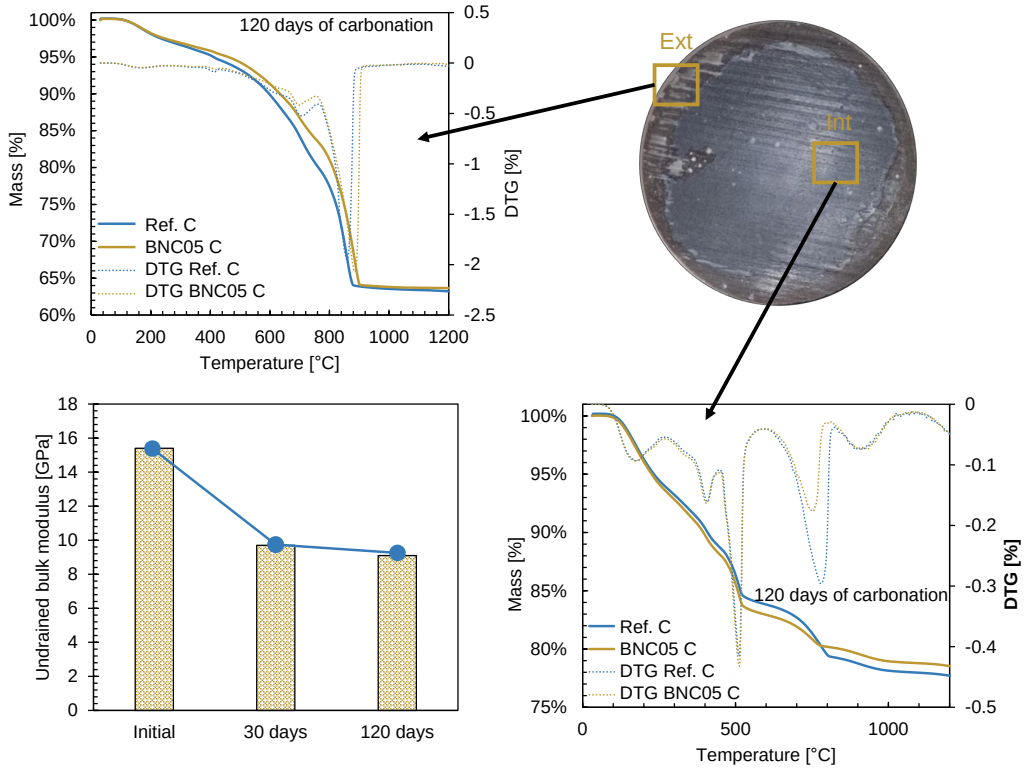

Fig. 4.51.: Effect of carbonation on chemical composition and bulk modulus of specimens cured at low temperature for 28 days. (Data from Section 4.3)

Bacterial nanocellulose reduced the amount of free water during initial mixing but increases the cement viscosity. It leads to higher hydration levels for the same curing conditions and reduced the capillary porosity of the specimens cured for 28 days. After carbonation, BNC-cement had similar behaviour to cement without addition, but with less effect on mechanical properties. This is due to the reduction of diffusion and permeability coefficients that depend on the porosity and tortuosity values.

In the absence of total carbonation of the specimens by this method, a second stage of carbonation was scheduled. A higher temperature was used (90 °C) for a shorter time to obtain higher levels of penetration. From this, the minerals present in this cement are different from the previous one, as well as their volumetric proportion and capillary porosity. These temperatures can be obtained in wells at great depths. During CO_2 injection, CO_2 can displace fluids around the wellbore. The porous medium will contain only supercritical CO_2 and a small amount of capillary water in the smaller pores and microcracks.

With this curing, greater penetration of the carbonation front and an increase in strength were observed. Large crystals were also observed in the pores, and XRD results showed a low percentage of portlandite and a high percentage of katoite. No influence of bacterial nanocellulose was observed in all experimental results. Short curing times and large pores/cracks inhibit the effect of nanocellulose, which seems to work better when the cement is cured at a lower temperature.

4.5.2 Permeability estimation

Permeability measures the ability of porous material to transmit fluids. It is a complex function of the properties of the material, such as porosity, pore geometry, pore size distribution and tortuosity. We can simplify the calculation to estimate permeability by assuming cylindrical interconnected pores. We can calculate the pore diameter corresponding to each mercury pressure step by:

$$p = -\frac{4\Upsilon\cos(\theta)}{d} \tag{4.2}$$

where Υ = mercury surface tension = 0.485 N/m, θ = mercury contact angle = 130°, p = mercury pressure, d = pore diameter [135].

An estimate of permeability can be made from the results obtained in the MIP test. This estimation is performed by considering the macro-scale flow with Darcy's law and the micro-scale flow with Poiseuille's law.

Each pore of class i of diameter d_i has an intrusion volume of mercury V_i, so a length L_i can be determined for each pore class i:

$$L_i = \frac{4V_i}{\pi d_i^2} \tag{4.3}$$

Assuming laminar flow, the Poiseuille's flow in a cylindrical tube depends on the difference of pressures at the tube ends, the dimensions of the tube, and the viscosity of the fluid. So the flow for each tube of diameter d_i is:

$$Q_{Poiseuille} = \frac{\Delta V}{\Delta t} = \frac{\Delta P_i(\pi d_i^4)}{128 L_i \eta} \tag{4.4}$$

Where ΔP_i is every mercury pressure step and η is the dynamic viscosity of the fluid.

Once the total flow rate is obtained, Darcy's law can be used to determine the permeability at the macro-scale. Let V_t be the total apparent volume of the MIP sample (ratio of total pore volume to porosity). The average pore length L_e is defined as:

$$L_e = \sqrt[3]{V_t} \tag{4.5}$$

The hydraulic gradient i is given by:

$$i = \frac{\Delta P_t}{L_e} \tag{4.6}$$

Where ΔP_t is the total pressure increase in meters' water column measured in the MIP.

Therefore, the intrinsic permeability of the material (independent of fluid conditions) is:

$$k = \frac{\sum_1^n Q_{Poiseuille}}{iS} \left(\frac{\eta}{\rho_f g} \right) \tag{4.7}$$

Where n is the total number of pores of different diameters, S is the cross-section of a cubic specimen with sides of length L_e, ρ_f is the density of the fluid and g is the gravity.

The calculated permeability accounts for an isotropic flux in a cubic sample. Hence, it needs to be divided by three to compare with the directional permeability obtained experimentally. This indicates that the fluid flows equally in the three directions of space [201].

The specimens analyzed to calculate permeability were carbonated and non-carbonated samples of both cement types (MIP-B-00, MIP-B-05, MIP-B-00-30-EXT, MIP-B-05-30-EXT).

The permeability results in Table 4.17 are consistent with the intrinsic permeability values of cement cured at a high temperature. This method simplifies the complexity of crosslinking between different cylinders of different pore diameters and considers a tortuosity of 1 [202]. The L_i values are very high for small diameter pores, so a higher deviation error is induced. For this reason, only the results obtained in samples cured at high temperature and carbonated for 30 days were analyzed.

sample	$k\,[\mathrm{m}^2]$
MIP-B-00	3.4 x 10^{-18}
MIP-B-00-30-EXT	3.1 x 10^{-19}
MIP-B-05	3.2 x 10^{-19}
MIP-B-05-30-EXT - C	2.6 x 10^{-19}

Tab. 4.17.: Intrinsic permeabilities.

In this analysis, cement with nanocellulose addition appears to have lower permeability than cement without additions. After carbonation, the permeability values of PC are reduced by one order of magnitude, while the permeability in cement with BNC addition is in the

same order of magnitude as the initial value. Experimental permeability tests on carbonated cement samples are necessary to validate these results.

4.5.3 Comparative overview

Experience	Reference cement	BNC-modified cement
Characterization of cement from specimens cured at low temperature (20 °C)	-	⩾ Higher viscosity. ⩾ Lower free fluid content. ⩾ Lower capillary porosity. ⩾ Enhanced hydration. ⩾ Higher strength.
Carbonation of specimens cured at low temperature (20 °C)	⩾ Carbonation increases density. ⩾ Total and capillary porosities decrease over time at the exposed edge. ⩾ Total porosity increases at the core while portlandite content decreases. ⩾ Strength and stiffness decrease. ⩾ The exposed edge is more porous.	⩾ The lower capillary porosity limits the entry of CO_2 into the core of the sample. ⩾ Shows higher values in its mechanical properties in absolute and relative terms after carbonation.
Carbonation of specimens cured at high temperature (90°C)	⩾ Capillary porosity is higher, so the carbonation process is faster. ⩾ Total and capillary porosities decrease over time. ⩾ Strength and stiffness increase.	⩾ BNC does not improve mechanical or microstructural properties of cement.

Tab. 4.18.: Summary based on the results obtained.

The overall parameters obtained from mechanical tests do not allow a carbonated specimen to be fully characterized. Therefore, a modeling tool is needed to simulate the advance of the carbonation front and to observe the variations in the physical properties of the material. For this to happen, the dissolution and precipitation process must be determined in order to estimate the material response to stresses.

Modeling the carbonation process

5

5.1 Introduction

This chapter is divided into two sections. In the first, the degree of carbonation of laboratory samples is determined from laboratory data, a hydration model and a stoichiometric balance. The second section performs a more complex simulation from a chemo-hydro-mechanical model implemented in a finite element code. With this code, carbonated specimens are represented and extrapolated to a possible carbonation scenario in an oil well.

5.2 Carbonation degree

The volumetric fractions of cement are calculated from the thermogravimetric analysis, MIP, total porosity measurements, and from Powers hydration model [203]. To verify these fractions, the total sample weight (m_T) is calculated in Equation 5.1 by adding the weight of each hydration product (m_i) and compared to the experimental weight.

$$m_T = \sum m_i = \sum f_{Vi} V_T \rho_i \tag{5.1}$$

where f_{Vi} is the volume fraction of each hydration product, V_T is the total sample volume and ρ_i is the bulk density of the hydration product. If we consider total carbonation, the CH, C-S-H will be completely carbonated, generating $C\bar{C}$ and AmSi (decalcified C-S-H, with a Ca/Si ratio constantly decreasing). Since our XRD does not detect ettringite or monosulfoaluminates, and their volumetric proportions in this type of cements are very small (< 4%) [54], we do not consider their influence during carbonation in this model. The increase of mass by precipitation corresponding to complete carbonation can be estimated from the stoichiometric balance of CH and C-S-H. For simplifying the calculation, and to compare the different cement mixtures, clinker carbonation is neglected. This assumption can be made considering that clinker (CL) grains are surrounded by the C-S-H layers that prevent its carbonation [68]. Thus, the calcite and amorphous silica fractions will be:

$$f_{V_{C\bar{C}}} = \left(1 \frac{f_{V_{CH}}}{V_{m_{CH}}} + 1.7 \frac{f_{V_{C-S-H}}}{V_{m_{C-S-H}}} \right) V_{m_{C\bar{C}}} \tag{5.2}$$

$$f_{V_{AmSi}} = \left(1 \frac{f_{V_{C-S-H}}}{V_{m_{C-S-H}}}\right) V_{m_{AmSi}} \tag{5.3}$$

where 1 and 1.7 are the CH and C-S-H coefficients of the stoichiometric balance. V_m is the molar volume of the corresponding components. The capillary porosity will therefore be:

$$\phi = 1 - f_{V_{CH}} - f_{V_{C-S-H}} - f_{V_{Al}} - f_{V_{CL}} - f_{C\bar{C}} \tag{5.4}$$

while the weight of every component will be:

$$m_i = f_{V_i} V_T \rho_i \tag{5.5}$$

The carbonation degree of the sample (C_D) will be the mass uptake of the sample at time t_i $(m_{(t_i)})$ with respect to the mass of precipitate necessary to obtain 100% carbonation (m_{FC}).

$$C_D = \frac{m_{(ti)}}{m_{FC}} \tag{5.6}$$

$$m_{FC} = \sum f_{V_i} V_T \rho_i - m_0 \tag{5.7}$$

where m_0 is the initial mass of the sample before carbonation. Table 5.1 shows the average (μ) and standard deviation (σ) of the carbonation degree. Some BNC15 samples were damaged after 120 days of carbonation, so their values cannot be entirely relied upon.

	30 days of carbonation			120 days of carbonation		
	PC	BNC05	BNC15	PC	BNC05	BNC15
μ	16,97%	10,23%	11,21%	19,06%	13,68%	27.59%
σ	4,12%	2,08%	1,56%	4,90%	3,02%	13.09%

Tab. 5.1.: Carbonation degree and its deviation after 30 and 120 days of carbonation calculated from the mass balance.

The PC samples show an increase of 17% of carbonation during the first 30 days, while after 120 days, the carbonation rate has decreased, and a carbonation degree of only 19% is observed. The BNC05 samples also show this behaviour, but with lower corresponding values. BNC15 samples have similar values to BNC05 at 30 days, but at 120 days we observed a considerable dispersion in the results, probably due to measurement errors. In addition, some samples were broken when the cell was opened. So the BNC15 samples are included in the table but less reliable than other samples; a new test on these samples should be performed.

The carbonation degree seems to have a logarithmic behaviour over time (see Figure 5.1). Initially, a clogging effect is caused by calcite precipitation, which reduces further advance of carbonation after 120 days [67]. This results in a lower carbonation rate over time. A

reduction in the degree of carbonation of samples with BNC additions is also observed. This is due to the increase in hydration degree that increased the number of cement hydrates. Even though the carbonatable compounds had increased and should influence the carbonation rate [204], they filled the pore spaces and reduced capillary porosity [60]. This affected the diffusion coefficients, which reduced the CO_2 income to the sample and carbonation reactions. An extrapolation to 100 years was made from these results. shows an improvement in carbonation resilience of samples with 0.05% of BNC, since PC shows a total carbonation degree of 35%, while BNC05 shows a carbonation degree of 25%. The results obtained for BNC15 at 30 days of carbonation are similar to those of BNC05. However, the results at 120 days make the fitted curve steeper and with higher carbonation levels.

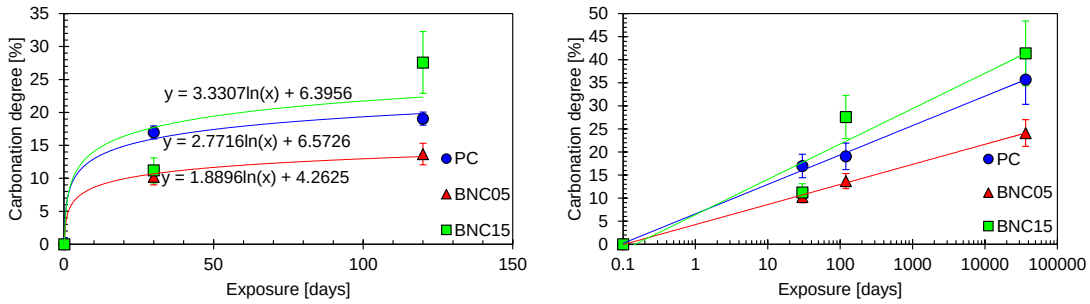

Fig. 5.1.: Results of the carbonation degree and extrapolation to 100 years for PC, BNC05 and BNC15.

5.3 Chemo-poro-mechanical model

5.3.1 Fundamentals

The experimental tests are simulated with a chemo-hydro-mechanical coupled model [205] implemented in a finite element code called BIL 2.3.0 [206].

The code allows to represent the carbonation advance in 1D, 2D o 3D materials. It contains the balance equations of porous continua based on conservation of mass and momentum [207]. This model is implemented specifically for class G cement and designed to be used in the context of CO_2 geological storage. It has been validated on a single test type performed under different curing and carbonation conditions. On this occasion, having all the initial and final parameters of our cements (volumetric proportions of the compounds, curing and carbonation conditions, porosities and mechanical strength), we can calibrate the model and analyze the results using our laboratory data.

For this model, cement is considered a porous multi-phase material composed of a solid matrix and water-saturated pores. The skeleton is composed of different materials, such as calcium hydroxide (CH), calcium silicate hydrate (C-S-H), aluminates, and calcite ($C\bar{C}$).

CO_2 is considered dissolved in the aqueous solution. The chemical reactions start when the CO_2 concentration reaches a threshold value. The chemical reactions are assumed to be instantaneously [205].

The CH is the first cement hydrate to react with CO_2, leading to precipitation of $C\bar{C}$. Once the pH level of the solution drops below 9, the carbonation will start to consume the C-S-H, also precipitating $C\bar{C}$ and amorphous silica [67].

During cement carbonation, porosity undergoes several variations. Some are due to chemical reactions, denoted ϕ_L for leaching of cement matrix and ϕ_C for calcite precipitation. The other variations of porosity are due to the deformation of the porous medium, with φ_F and φ_C as the deformation of the porosity filled by fluid phase and by calcite phase, respectively. The porosities involved can be written as follows:

$$\phi_F = \phi_0 + \phi_L - \phi_C + \varphi_F \tag{5.8}$$

$$\phi = \phi_F + \delta_C \tag{5.9}$$

$$\delta_C = \phi_C + \varphi_C \tag{5.10}$$

where ϕ_F corresponds to the pore volume occupied by the in-pore fluid per unit of initial volume of the porous medium, ϕ corresponds to the initial pore space per unit of initial volume of porous medium which is not occupied by the solid phase. The difference between these two porosities is denoted by δ_C, which is the pore volume occupied by carbonate crystals [194, 205].

The constitutive equations of isotropic linear poroelastic material of an infinitesimal representative volume element of a porous medium ($\partial\Omega_0$) are derived from Gibbs-Duhem equalities and Clausius-Duhem inequality assuming isothermal conditions.

$$\boldsymbol{\sigma} - \boldsymbol{\sigma_0} = \left(K - \frac{2}{3}G\right)(\varepsilon_v - \varepsilon_0)\,\mathbf{1} + 2G\,(\boldsymbol{\epsilon} - \boldsymbol{\epsilon_0}) - \sum_{k=F,C} b_k\,(p_k - p_{k,0})\,\mathbf{1} \tag{5.11}$$

$$\varphi_J - \varphi_{J,0} = b_J\,(\varepsilon_v - \varepsilon_0) + \sum_{k=F,C} \frac{p_k - p_{k,0}}{N_{JK}}; J = F, C \tag{5.12}$$

where: $\boldsymbol{\sigma}$: is the stress tensor, $\boldsymbol{\epsilon}$: is the infinitesimal strain tensor, ε_v: is the volumetric strain (tr($\boldsymbol{\epsilon}$)), K, G = are the bulk and shear modulus in drained conditions, φ_J: is the porous volume deformation occupied by the phase J, b_J: is the generalized Biot coefficient, N_{JK}: is the generalized poroelastic coupling moduli [208],

The mass conservation is applied to the fluid and to the molar amount of CO_2:

$$\left(\frac{\rho_f \phi_F}{K_f}\right) \frac{\partial p_f}{\partial t} + \rho_f \; b \; \text{div}\left(\frac{\partial \boldsymbol{u}}{\partial t}\right) + \rho_f \sum_{Ri} Y_{Ri} \frac{\partial \xi_{Ri}}{\partial t} - \text{div}\left(\rho_f \; \frac{k}{\eta} \; \text{grad} \; \rho_f\right) = 0 \tag{5.13}$$

$$\frac{\partial \left(\phi_F \; C_{CO_2}\right)}{\partial t} + \sum_{Ri} a_{Ri} \frac{\partial \xi_{Ri}}{\partial t} - \text{div}\left(d_{eff} \; \text{grad} \; C_{CO_2} + C_{CO_2} \; \frac{k}{\eta} \; \text{grad} \; \rho_f\right) = 0 \tag{5.14}$$

Where: ρ_f is the density of the fluid, ϕ_F is the fluid porosity, K_f is the bulk modulus of the fluid, p_f is the fluid pressure, a_{Ri} is the stoichiometric coefficient of the reaction Ri, C_{CO_2} is the CO_2 concentration in the fluid, η is the dynamic viscosity of the fluid phase, Y_{Ri} is a variable, function of the molar volumes of the reactive and produced species, allowing to evaluate the variation of pore pressure resulting from the reactions of leaching and precipitation reactions having impacted the pore volume. $\boldsymbol{u}$ is the skeleton displacement vector, ξ_{Ri} is the reaction advance depending on k and d_{eff}, which are the permeability and diffusion coefficients.

The kinetics of the chemical reactions are slowed down in order to soften the carbonation front (this can be seen as a numerical regularization):

$$\frac{\partial \xi}{\partial t} - \frac{(\xi_{max} - \xi)}{\tau} \frac{C_{CO_2}}{S_{CO_2}} = 0 \tag{5.15}$$

where: ξ_{max} corresponds to the maximum possible advancement calculated from the quantities of reactants present, S_{CO_2} is the threshold value of C_{CO_2} below which the carbonation reaction cannot occur, τ is a time constant allowing to more or less soften the carbonation front.

Chemical reactions (carbonation-dissolution) occurring in the system induce changes in the transport and mechanical properties of the system. Diffusion and permeability transport phenomena control the carbonation advance. Empirical permeability–porosity laws are commonly used for materials which exhibits time-dependent deformation. One can use a power law such as $k/k_0 = (\phi/\phi_0)^\alpha$. Ghabezloo et al. give an expression a class G cement [176]:

$$k = k_0 \left(\frac{\phi_F}{\phi_{init}} \right) \ 10^{-19} \tag{5.16}$$

where: k_0 is a parameter to calibrate, ϕ_{init} is the capillary porosity of cement before testing and ϕ_F is the porosity at a given time during the test. Similarly, the variation of the porosity must be taken into account in the expression of the effective diffusion coefficient considering a porous medium. The effective diffusion coefficient is ϕD, while D is the diffusion coefficient of the solute in the interstitial pore solution. Based on experimental data, Mainguy and Coussy [175] propose the following expression for the effective coefficient of diffusion:

$$d_{eff} = d^0_{eff} \exp(9.95\phi_F - 29.08) \tag{5.17}$$

where: d^0_{eff} is a parameter to calibrate. These equations are empirical and aimed at reasonably representing the transport phenomena occurring within the cement matrix. Parameters k_0 and d^0_{eff} can be modified to obtain values of intrinsic permeability and diffusivity suitable for class G or H cement.

5.3.2 Homogenization of the poroelastic parameters

In this section, a homogenization technique is used to calculate the poroelastic moduli of the cement paste during the dissolution/precipitation processes induced by its carbonation. All cement components (including CH, C-S-H, calcite, hydrated silicates and chemically inert phases) have to be considered in the homogenization analysis in terms of their mechanical contribution to the overall stiffness [205]. The poroelastic parameters can be then determined from the constituents properties following the relations [209]:

$$K_d^{hom} = \sum_r f_r k_r A_r^v \tag{5.18}$$

$$G_d^{hom} = \sum_r f_r g_r A_r^d \tag{5.19}$$

$$b^{hom} = 1 - \sum_r f_r A_r^v \tag{5.20}$$

$$\frac{1}{N^{hom}} = \sum_r f_r \frac{1 - A_r^v}{k_r} \tag{5.21}$$

where K_d^{hom} is the drained bulk modulus, G_d^{hom} is the drained shear modulus, b^{hom} is Biot's parameter, N^{hom} is the Biot skeleton modulus, f_r is the volumetric proportion of the phase

r, k_r and g_r are the elastic parameters of the solids r and A_r^v and A_r^d are the volumetric and deviatoric strain localization coefficients. In the current study, a homogenization formulation was implemented for this case, adding the BNC characteristics. As carbonation advances, homogenization allows us to know the poroelastic parameters of the cement paste at each step of time.

5.3.3 Isotropic damage

From a microscopic point of view, the damage corresponds to the creation of microcracks. In the theory of damage, effective stress, now called damaged stress, is based on a decrease of the effective area due to the appearance of micro-cavities [210]. Considering damage as isotropic, a simplification for calculating the damaged stress can be made:

$$\tilde{\boldsymbol{\sigma}} = \frac{\boldsymbol{\sigma'}}{1-d} \tag{5.22}$$

When $d = 0$, there is no damage. When damage is between 0 and 1, the material is in a damaged state. If $d = 1$, the material is broken.

A damage criterion is introduced via the definition of a yield surface in the stress space. The interior of the yield surface ($f_d < 0$) corresponds to the effective stress space for which no damage occurs, and the exterior ($f_d > 0$) the space for which the effective stress state cannot be reached. Thus, as long as the stress state remains within the yield surface, the damage will not evolve. Similarly, if the stress state reaches the loading surface, but the material point under study is subjected to unloading, there will be no evolution of the damage. On the other hand, if the stress state is on the yield surface and the loading increases, damage will occur.

The model adopts a Drücker-Prager criterion, suitable for the behaviour of geomaterials under high confinement [207]. The criterion takes the following form:

$$f_d = q \; + \; f_f \, \sigma_m \; - \; c_c \tag{5.23}$$

where q and σ_m are the deviatoric stress and effective mean stress, while f_f and c_c are parameters depending on the friction angle φ of the material and its cohesion c:

$$\begin{cases} f_f = \frac{6\sin\varphi}{3-\sin\varphi} \\ c_c = \frac{6\cos\varphi}{3-\sin\varphi} c \end{cases} \tag{5.24}$$

5.3.4 Damage evolution

The mean and deviatoric stresses are evaluated from the imposed deformation and the homogenized modulus

$$\sigma_m = \sigma_{m_0} + K_d^{hom} \Delta\varepsilon_v \tag{5.25}$$

$$q = q_0 + G_d^{hom} \Delta\varepsilon_s \tag{5.26}$$

with $\varepsilon_v = \text{tr}(\boldsymbol{\epsilon})$ and $\varepsilon_s = \sqrt{\frac{2}{3} J_2(\boldsymbol{\epsilon})}$. $\Delta\varepsilon_v$ and $\Delta\varepsilon_s$ are the increments of the volumetric and deviatoric strains.

Once the stress state reaches the Drücker-Prager criterion and f_d is greater than zero, the damage is calculated in function of an increment of deviatoric and volumetric deformations [207]:

$$d_{n+1} = 1 - \frac{c_c - q - f_f \sigma_m}{3G_c^{hom} \Delta\varepsilon_s + f f K_c^{hom} \Delta\varepsilon_v} \tag{5.27}$$

where K_c^{hom} and G_c^{hom} are the compressibility and shear modulus of the homogenized medium right before reaching the criterion. And the new damaged stress state will be:

$$\boldsymbol{\sigma'} = \boldsymbol{\sigma_0} + (1 - d_{n+1}) \{2G_c^{hom}(\boldsymbol{\varepsilon} - \boldsymbol{\varepsilon_0})(K_c^{hom} - \frac{2}{3} G_c^{hom})[\text{tr}(\varepsilon) - \text{tr}(\varepsilon_0)]\} \tag{5.28}$$

Finally, the mechanical modulus is affected with the calculated damage of Equation 5.27.

$$K_{n+1}^{hom} = (1 - d_{n+1})\, K_d^{hom} \tag{5.29}$$

$$G_{n+1}^{hom} = (1 - d_{n+1})\, G_d^{hom} \tag{5.30}$$

5.3.5 Dissolution and precipitation of CH, C-S-H and $C\bar{C}$

It has been observed that CH and C-S-H carbonate simultaneously [211], although thermodynamically CH should be consumed first so that C-S-H can carbonate. Morandeau et al. proves that there is a simultaneous carbonation of CH and C-S-H, indicating that the carbonation rate in both phases is similar at the beginning, and then the rate of CH decreases [67]. The decrease in the rate of CH carbonation is due to problems of CO_2

accessibility to carbonate this material, leaving residual CH at the outer edge. This was observed in our X-ray diffraction results. This points also highlights that C-S-H is the main responsible for the porosity variation.

We consider a rate of C-S-H variation based on Morandeau et al. tests, approximating a carbonation ratio between CH and C-S-H of 0.8. This ratio is conservative, but similar to the ones obtained from the TGA test and Gamma-ray attenuation method [67]. Once all the CH is consumed, the carbonation rate of C-S-H returns to 1 mole of C-S-H consumed per 1.7 moles of precipitated $C\bar{C}$, as indicated in Equation 2.18.

Calcite dissolution has been added to the code in order to contemplate this effect in the cement matrix. The equilibrium between CH and $C\bar{C}$ comes from the following relationships proposed by Shen [212]:

$$\frac{Q_{C\bar{C}}}{K_{C\bar{C}}} = \frac{Q_{CH}}{K_{CH}} \frac{\rho_{CO_2^0}}{\rho_{CO_2^0}^{CH}} \tag{5.31}$$

where Q_{CH} and $Q_{C\bar{C}}$ are the CH and $C\bar{C}$ ions activity. K_{CH} and $K_{C\bar{C}}$ are the equilibrium constants for CH and $C\bar{C}$ at a given temperature. $\rho_{CO_2^0}$ is the dissolved CO_2 concentration and $\rho_{CO_2^0}^{CH}$ is the dissolved CO_2 concentration for which $C\bar{C}$ is not stable.

There is a domain where only CH is stable $\left(\frac{Q_{CH}}{K_{CH}} = 1\right)$:

$$n_{CH} \geq 0, \rho_{CO_2^0} < \rho_{CO_2^0}^{CH}, \frac{Q_{C\bar{C}}}{K_{C\bar{C}}} < 1 \tag{5.32}$$

where n_{CH} is the number of moles of CH. And there is a domain where only $C\bar{C}$ is stable $\left(\frac{Q_{C\bar{C}}}{K_{C\bar{C}}} = 1\right)$ is:

$$n_{C\bar{C}} \geq 0, \rho_{CO_2^0} > \rho_{CO_2^0}^{CH}, \frac{Q_{CH}}{K_{CH}} < 1 \tag{5.33}$$

where $n_{C\bar{C}}$ is the number of moles of $C\bar{C}$. So the dissolution of CH and $C\bar{C}$ can be modeled with one variable ζ :

$$\zeta_{Ca} = \frac{n_{C\bar{C}} + n_{CH}}{n_{Ca}^0} + \log\left[\max\left(\frac{Q_{CH}}{K_{CH}}, \frac{Q_{C\bar{C}}}{K_{C\bar{C}}}\right)\right] \tag{5.34}$$

where n_{Ca}^0 is the initial content of CH (mol/L). The numbers of moles of the first term are known. If $\rho_{CO_2^0} \geq \rho_{CO_2^0}^{CH}$ there is no CH, and the $C\bar{C}$ dissolution can be calculated by the following expression:

$$\zeta_{Ca} = \frac{n_{C\bar{C}} + n_{CH}}{n^0_{Ca}} + \log\left(\frac{Q_{C\bar{C}}}{K_{C\bar{C}}}\right) \tag{5.35}$$

Calcite is dissolved in solution if ζ_{Ca} is less than or equal to zero. If we consider CO_2 and bicarbonate dissolved in water [213], we can obtain their equilibrium constants at 90 °C [212]:

$$K_{a1} = \frac{\left[HCO_3^-\right]\left[H^+\right]}{[CO_2]} = 10^{-6.37} \tag{5.36}$$

$$K_{a2} = \frac{\left[CO_3^{2-}\right]\left[H^+\right]}{\left[HCO_3^-\right]} = 10^{-10.13} \tag{5.37}$$

While the concentration of calcium carbonate is governed by the solubility product constant of the mineral:

$$K_{sp} = \left[Ca^{2+}\right]\left[CO_3^{2-}\right] = 10^{-9.12} \tag{5.38}$$

With these constants we can determine the concentrations of any of the species in solution as a function of the CO_2 concentration:

$$\left[H^+\right]^3 = \frac{[CO_2]^2 (K_{a1})^2 (K_{a2})}{2(K_{sp})} \tag{5.39}$$

$$\left[HCO_3^-\right] = \frac{[CO_2]^2 (K_{a1})}{[H^+]} = \frac{2(K_{sp})\left[H^+\right]^2}{(K_{a1})(K_{a2})[CO_2]} \tag{5.40}$$

$$\left[CO_3^{2-}\right] = \frac{[CO_2](K_{a1})(K_{a2})}{[H^+]^2} \tag{5.41}$$

So $Q_{C\bar{C}}$ for each given CO_2 concentration is given by:

$$Q_{C\bar{C}} = \left[Ca^{2+}\right]\left[CO_3^{2-}\right] = \left[CO_3^{2-}\right]^2 \tag{5.42}$$

To analyze these effects, a 1D carbonation model was analyzed. The problem is adapted to be solved with the finite element method, which is better suited to take into account the mechanical aspects, but is more unstable in the presence of steep fronts with respect to a variable. The model consists of 100 finite elements, which have properties of cement. On one side a CO_2 concentration of molarity 1.2 is placed as a boundary condition for 10 days

(Figure 5.2). In this case, the model only considers hydro-Chemical effects, and the rock is considered as inert.

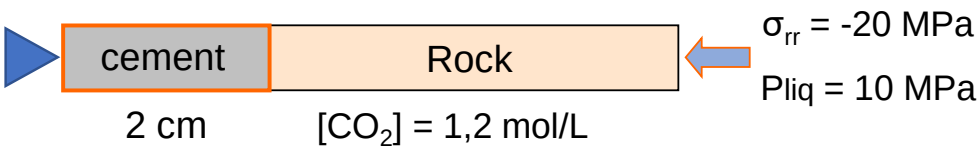

Fig. 5.2.: 1D cement carbonation model.

Figure 5.3 shows the dissolution of C-S-H simultaneously with CH, and the $C\bar{C}$ dissolution when the CO_2 concentration is higher than $\rho^{CH}_{CO_2^0}$, while Figure 5.4 the variation in the number moles of each cement component as a function of time.

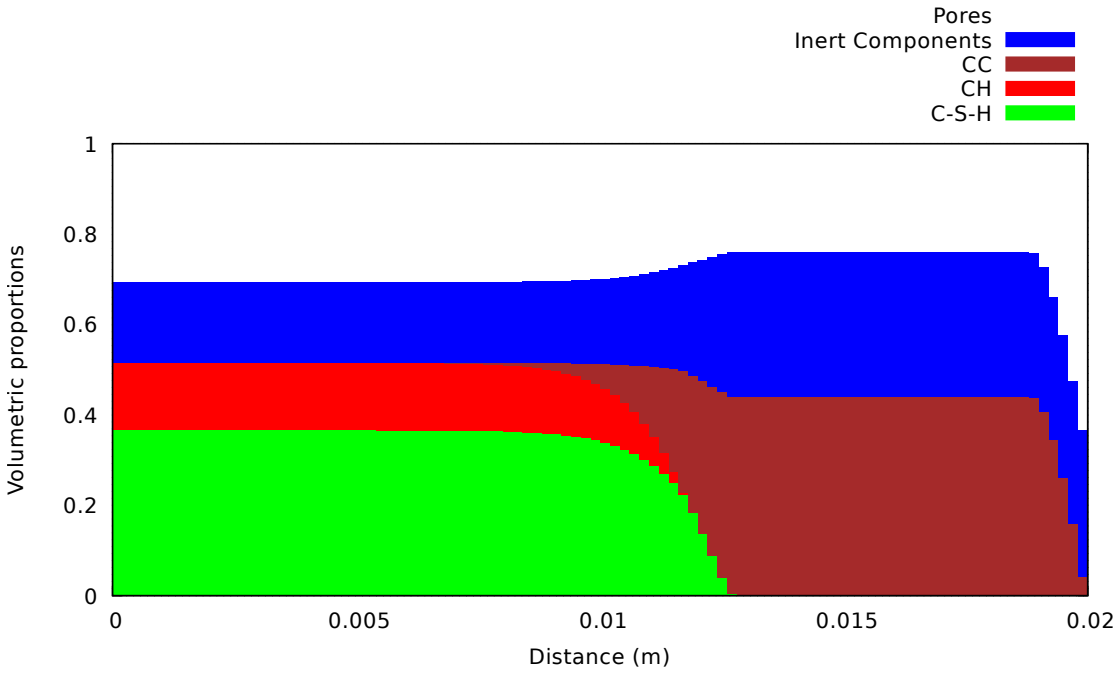

Fig. 5.3.: Volumetric proportions of the 1D carbonation model.

At the right outer edge (up to 0.1 mm), it can be observed that the porosity starts to increase. This is due to the dissolution of calcite from the criterion that was established. This results in only amorphous silica (inert components in the image) being present in the cement matrix, along with a small remaining percentage of calcium carbonates.

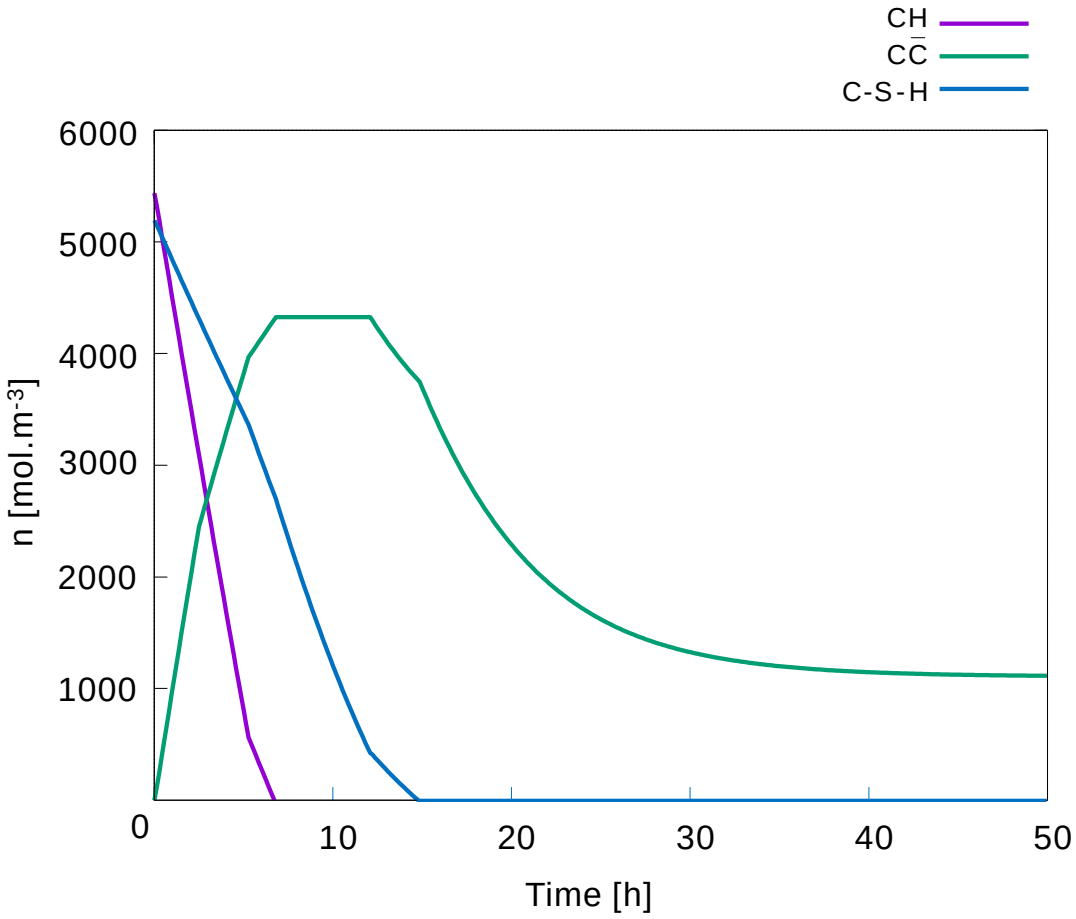

Fig. 5.4.: Variation in the number of moles as a function of time. These results are those obtained at the outer edge in contact with supercritical CO_2.

Not all calcium carbonates dissolve at the outer edge of the sample due to the established criterion that calcite remains in solid state while ζ_{Ca} is higher than 0. This determines a threshold of CO_2 concentration for the calcite dissolution, which depends on the initial conditions of the material.

This consideration allows to reproduce the simultaneous dissolution of CH and C-S-H, and calcite dissolution when the CO_2 concentration is high enough, which decreases the mechanical properties as observed in the experimental results.

5.3.6 Modeling in cement cured at room temperature

In this section, the numerical analysis of the samples cured at room temperature and then carbonated under supercritical condition was performed. The initial volumetric proportions were taken from the previous analysis in Section 5.2. Calcite is not considered to be present prior to carbonation.

The geometry chosen is one-quarter of the testing cement samples with axisymmetric conditions in X. Considering symmetries, a 2D rectangular shape model was used. The rectangular shape consisted of one-quarter of a sample (19 mm-radius by 38 mm-height) using a mesh of 22x11 elements (Figure 5.5). The bottom horizontal contour has restricted movements in the Y direction, while the left vertical contour has restricted movements in the X direction.

First, uniaxial compression is performed without carbonation on this geometry (case a). The confining pressure is the atmospheric pressure and a vertical deformation is applied by compressing the specimen at a constant rate until failure of the material.

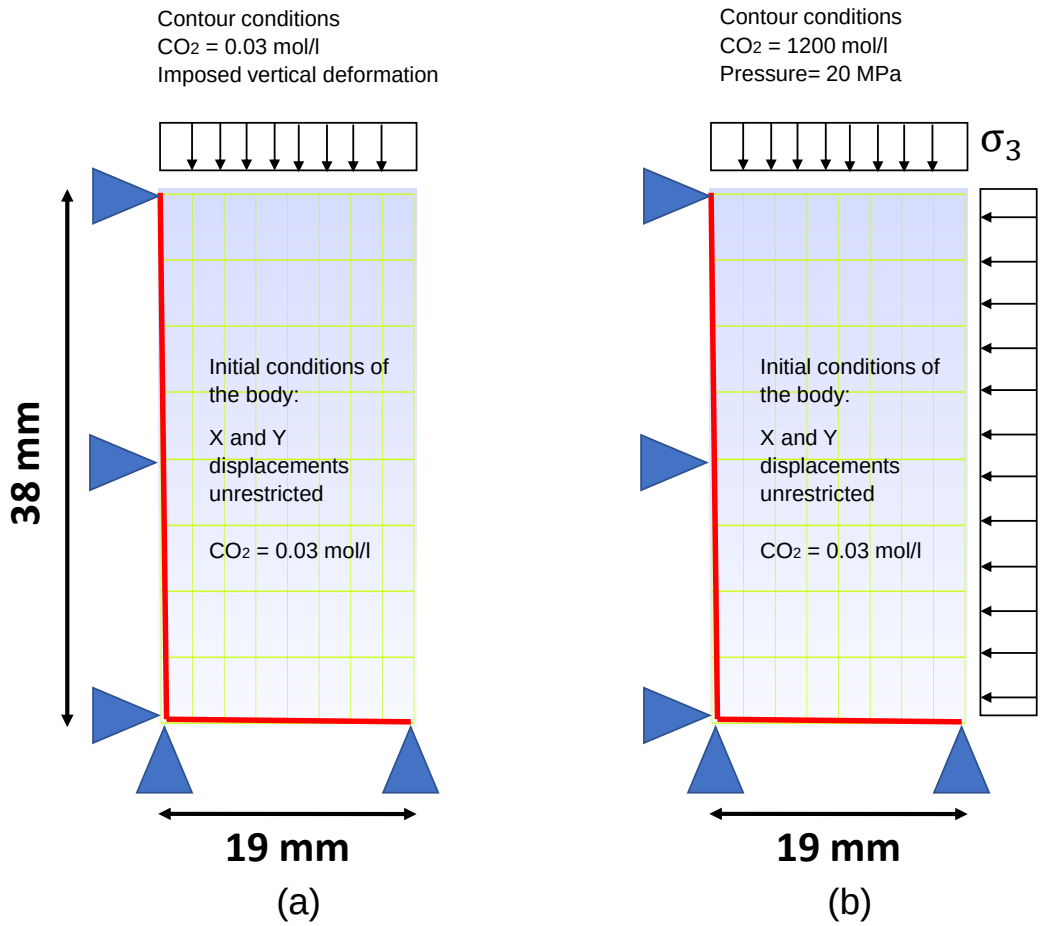

Fig. 5.5.: 2D model representation of one-quarter sample subjected to carbonation using the code BIL. Case (a) uniaxial test. Case (b) supercritical carbonation.

The volumetric proportions used for the case of samples with bacterial nanocellulose are shown in Table 5.2. The components considered inert are aluminates and clinker (See Section 5.2).

Inclusion	Volumetric Proportion	Bulk Modulus [GPa]	Shear Modulus [GPa]
Porosity	0.18	-	-
CH	0.22	33.00	14.50
C-S-H	0.51942	25.00	18.40
Inert components	0.08	27.00	9.50
$C\bar{C}$	0.00	69.00	37.40
BNC	0.00058	42.00	38.00

Tab. 5.2.: Initial properties of cement with bacterial nanocellulose cured at room temperature. BNC values are conservative and determined from the literature [214, 215, 216].

The stress-strain curves are linear up to the yield (damage) stress and thereafter are constant for the uniaxial test (Figure 5.6). This is due to the fact that the model does not calculate the material's plasticity, and only isotropic damage is considered from the elastic limit onwards. The displacements are shown in Figure 5.7, where uniaxial compression produces negative vertical displacements, while it produces positive horizontal displacements. The results are approximate to the maximum load of 55 MPa obtained in the uniaxial tests on cylindrical specimens.

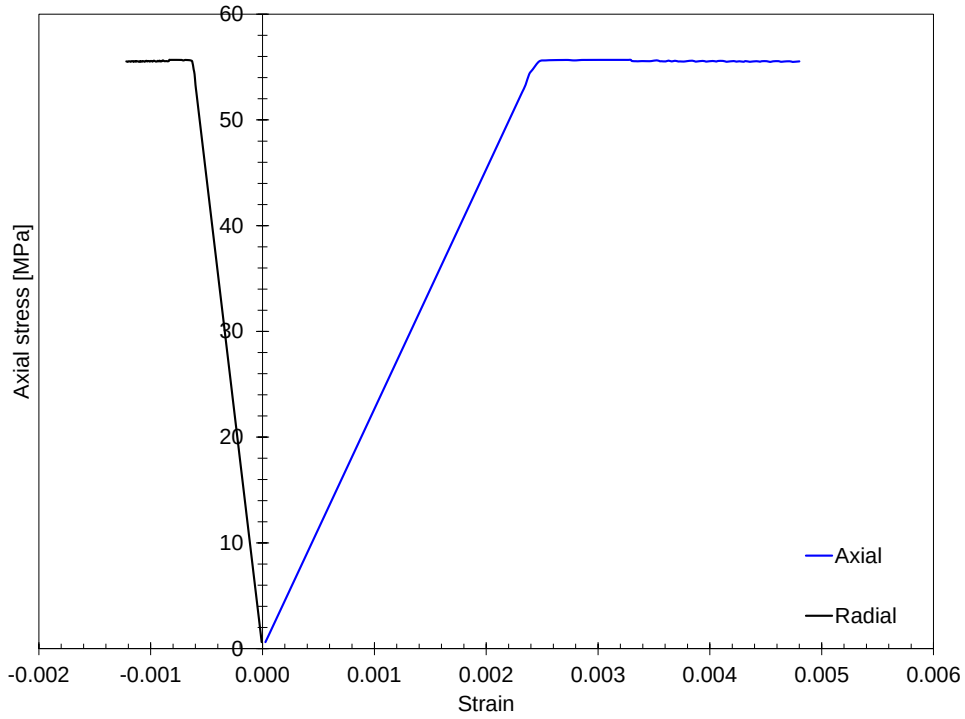

Fig. 5.6.: Uniaxial compressive stress for a non-carbonated sample.

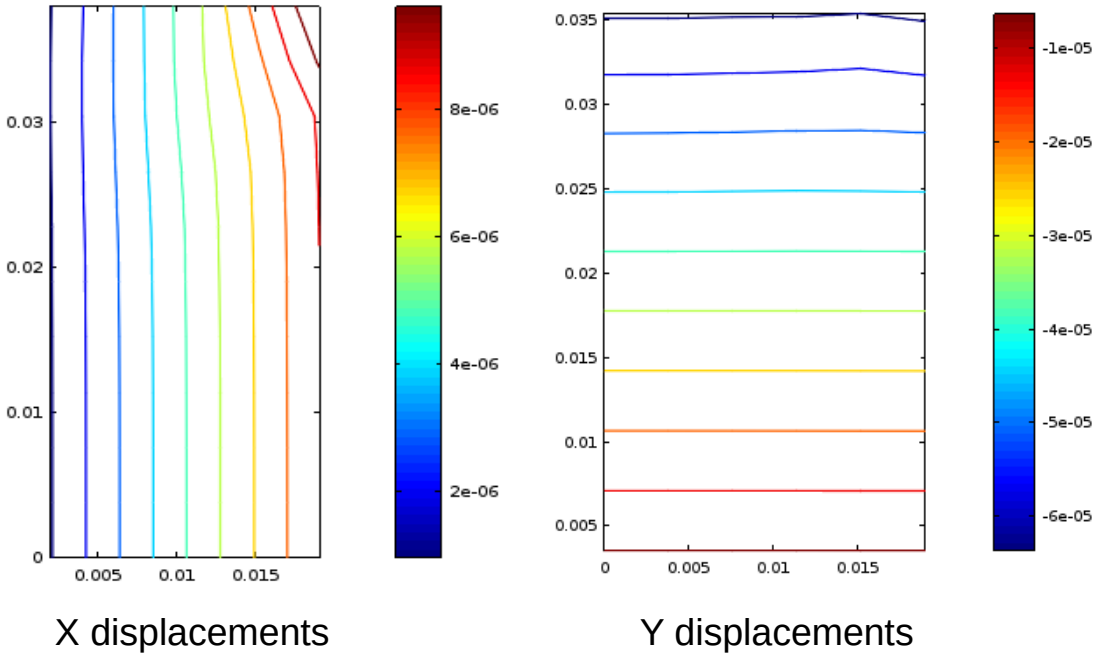

Fig. 5.7.: Total displacements in the X and Y direction.

The effect of isotropic damage can be seen in Figure 5.8. Assuming that it is loaded until the yield stress and then unload, damage occurs on the specimen, which reduces its elastic properties. When it is reloaded, the stress reaches the same maximum value, but with a different modulus of elasticity.

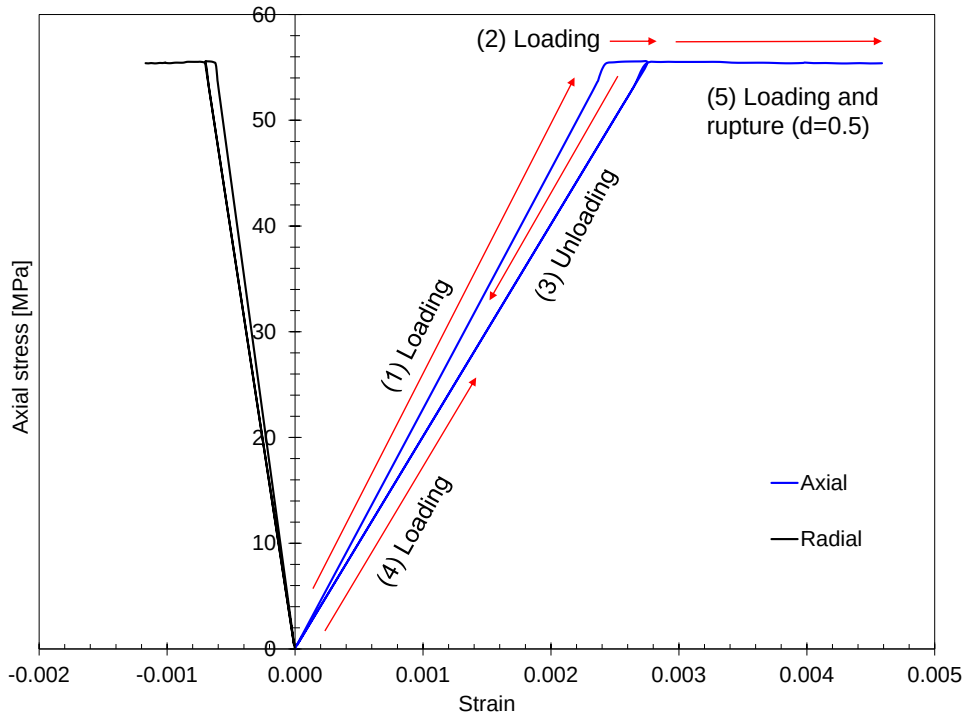

Fig. 5.8.: Behaviour of the elastic modulus when damage is applied to the sample.

From Equation 5.29 it is determined that the elastic moduli are directly affected by the damage produced. Figure 5.9 shows how the modulus of compressibility K varies with time, following the loading and unloading sequence plotted in Figure 5.8. In the elastic domain, there is no variation of the modulus until yield stress is reached. If the sample is compressed further, damage begins to occur and the compressibility modulus decreases (Figure 5.10). When unloaded, the compressibility modulus keeps the last value calculated from the damage, so when the sample is reloaded, the slope is less steep. The simulation continues until the moment when the damage is equal to 0.5 (Figure 5.11), so the deformation rate is maintained until that point is reached, calculating at each step the new damage and the new compressibility modulus, which is decreasing.

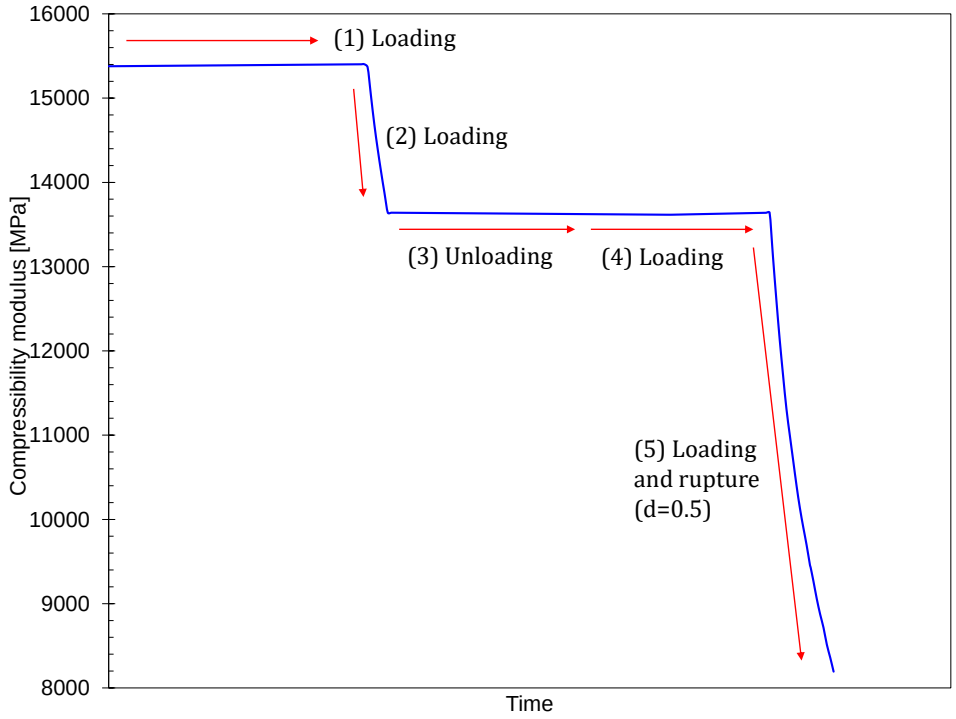

Fig. 5.9.: Behaviour of the compressibility modulus when damage is applied to the sample.

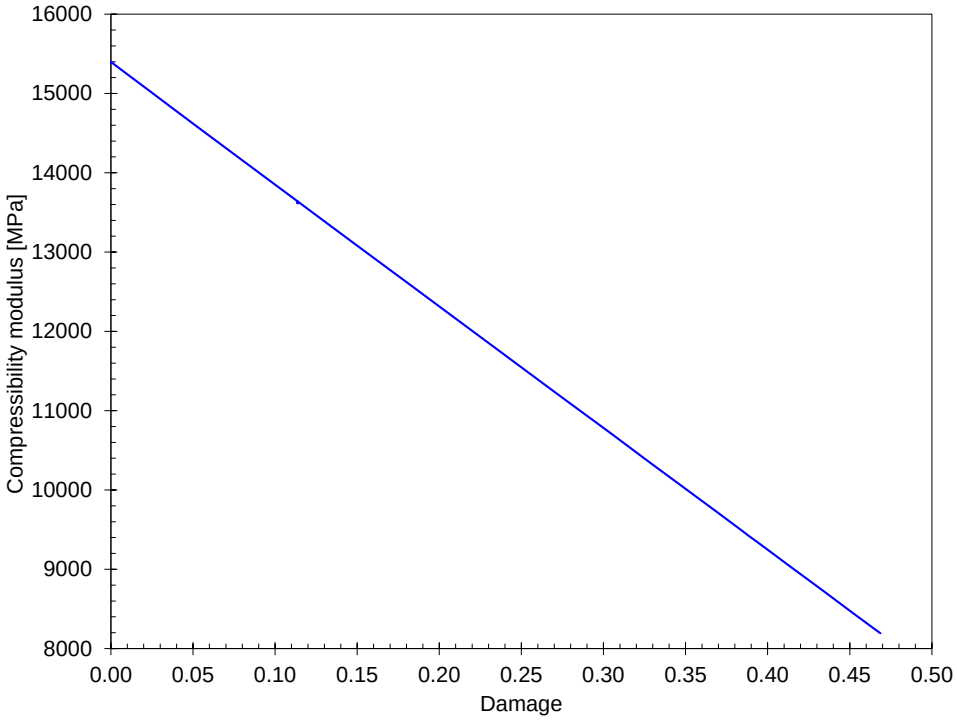

Fig. 5.10.: Variation of the modulus of compressibility as a function of damage.

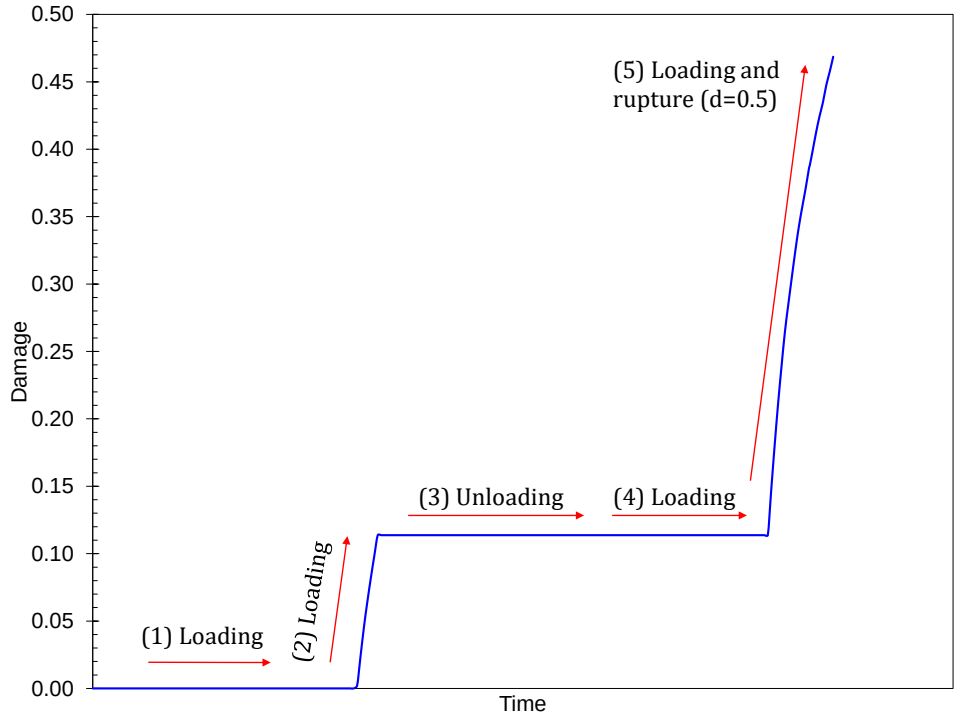

Fig. 5.11.: Damage evolution under uniaxial loading.

This geometry (Figure 5.5) is now tested at 20 MPa of confinement and a temperature of 90 °C for 30 days of carbonation (case b). As the code considers isothermal conditions, the fluid and gas conditions are set for a temperature of 90 °C. The top and right-hand contours are subjected to carbonation.

Figure 5.12 shows the advance of CO_2 concentration after 30 days of carbonation. The carbonic acid enters the sample by diffusion and reacts chemically with the hydration products. This causes a variation of porosity at the carbonation front and an increase of porosity at the calcite dissolution front as observed in the experimental results. Also it results in a reduction in the numbers of CH and C-S-H moles, and an increase in the number of $C\bar{C}$ moles at the carbonation front. Near the edge, where the CO_2 concentration is higher, calcite dissolves generating calcium ions and H_2O, so the number of $C\bar{C}$ moles decreases in this sector (see Figure 5.13).

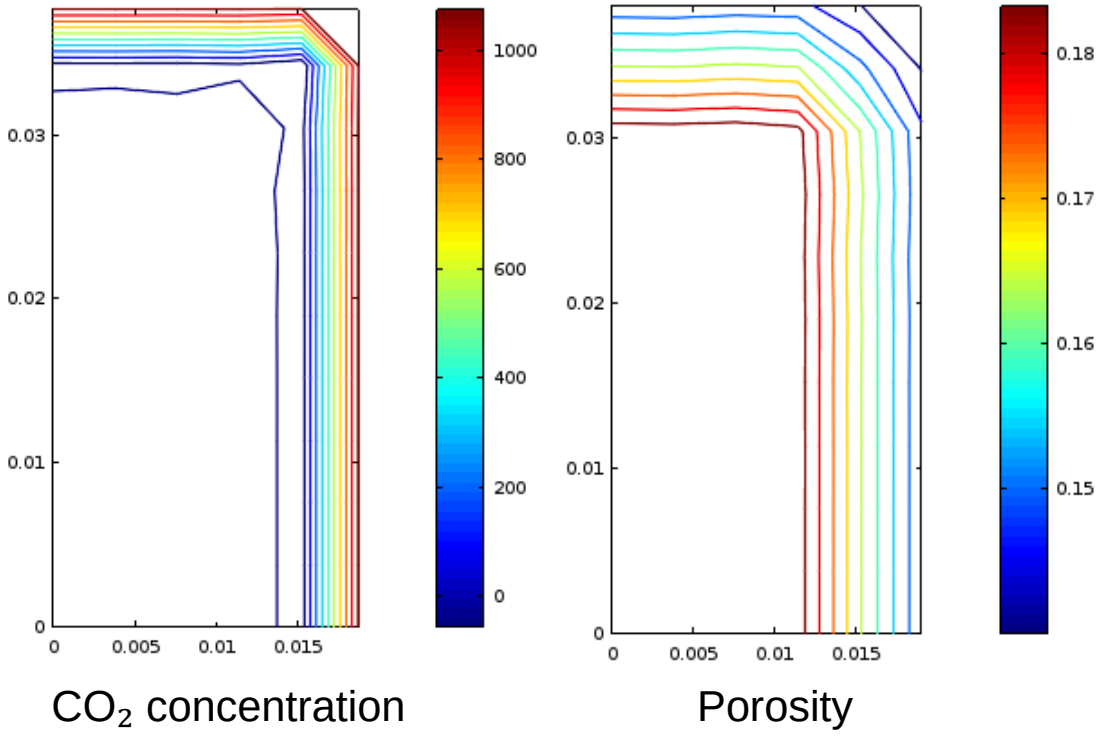

Fig. 5.12.: CO_2 concentration and capillary porosity after 30 days of supercritical carbonation.

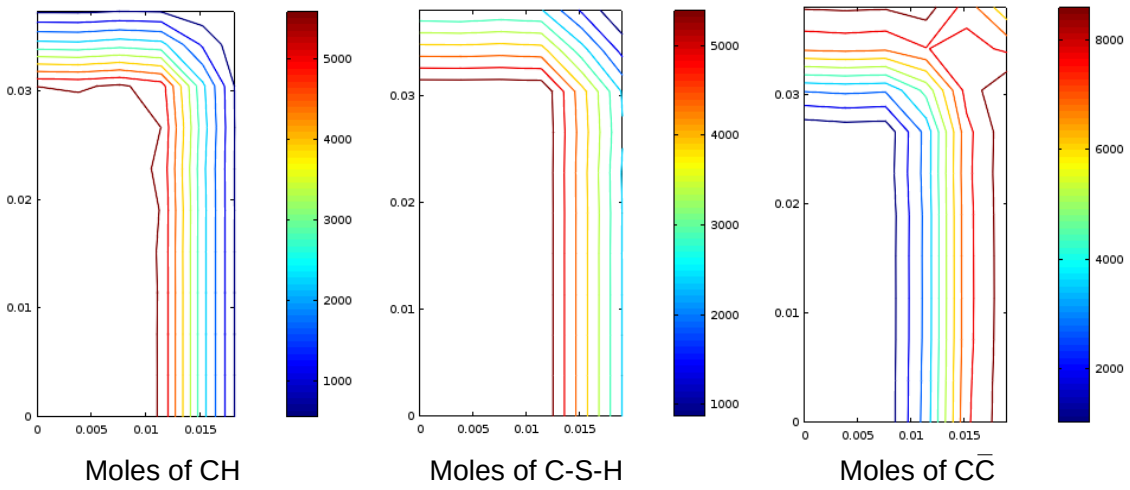

Fig. 5.13.: Number of moles of portlandite, C-S-H and calcite after 30 days of supercritical carbonation.

Because of carbonation, the mechanical properties of the cement are reduced, so the material breaks at lower stress and lower deformation. The results are similar to those obtained in laboratory experiments, as shown in Figure 5.14 below.

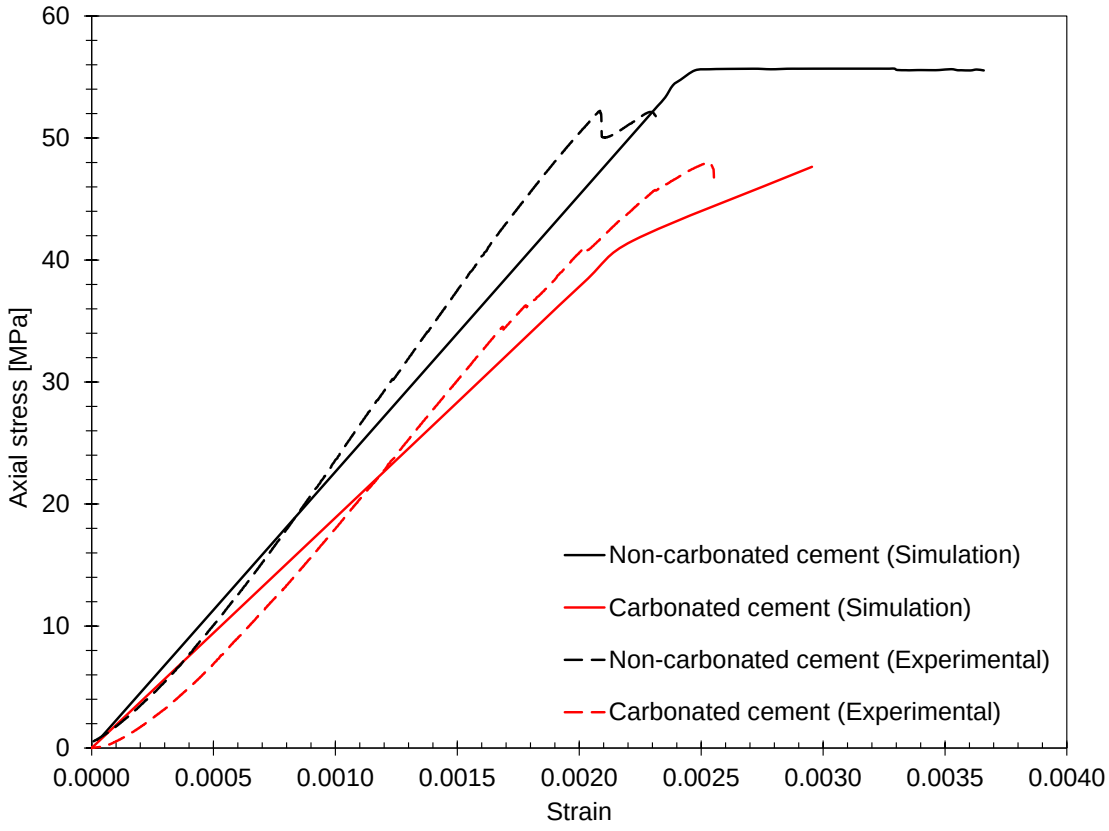

Fig. 5.14.: Variation in uniaxial strength after 30 days of carbonation.

The non-carbonate experimental specimens reach brittle fracture at the same time as when the model failure surface is reached. In this case, the model continues its calculation until damage = 0.5, so the material continues to deform. In the case of carbonate samples, the experiments and the model reach fracture at the same time, although the model experiences greater deformation.

5.3.7 Modeling cements with bacterial nanocellulose cured at reservoir temperature

In this section, the numerical analysis of the carbonated BNC samples is presented. A 2D analysis is performed simulating the experimental carbonation of the cylindrical samples cured at reservoir temperature (90 °C) and carbonated for 30 days. Calibration of the model is made by taking the porosity values obtained experimentally to estimate the intrinsic parameters of this cement. The calibrated model is extrapolated to simulate in 1D the cement carbonation in a wellbore system under downhole conditions.

Initial parameters and intrinsic properties of cement

In this section, we estimate the cement parameters from our experimental results and from the literature, since the previous model can only be used for room temperature curing. Porosity is very variable for cement and depends mainly on the water to cement ratio and on the type of curing in which the specimen is placed. Some authors estimate porosities greater than 30% [32, 73, 217, 218], while others and this work approximate it from 20% to 30% [219, 176, 58, 220]. Regardless of the kind of oil cement in question (G or H), it can be generalized that the capillary porosities of oil cement are around 20% to 35%. The initial porosity of the samples in this work before carbonation is 34.5% as indicated in Section 4.4.

The volumetric content of cement minerals depends substantially on the cement type, water to cement ratio, hydration degree, and curing temperature. So, it is necessary to estimate these proportions for the simulation. In some articles, the amount of Portlandite CH varies between 15 to 25% [176, 175], with commonly accepted values ranging from 18 to 20% [205]. In the results of the previous section, using the same cement and same water to cement ratio, a percentage of 20% was obtained by thermogravimetric analysis in a cement with a high level of hydration. Class G and H cement have very low initial aluminate contents following API requirements aiming at being resistant to sulfate attacks ($C_3A \leq 3\%$ and $C_4AF + 2\ C_3A \leq 24\%$). So the hydrated aluminate components have a low percentage, around 6 to 14% [205, 219, 221]. Finally, the most important phase of cement in terms of compressive strength, C-S-H, can vary between 60 to 27% in volume fraction [205, 221].

The intrinsic permeability is independent of the conditions to which the material is initially subjected, at least directly. Since cement is a heterogeneous material, there is no unique intrinsic permeability value for cement. Nelson et al.[39] in their experiments report values of 1x10^{-16} m^2 to 1x10^{-20} m^2. This is supported by Ghabezloo et al. [176] and Mainguy et al. [175], who obtain values in the order of 1x10^{-19} m^2 to 1x10^{-20} m^2. Sercombe et al. [220] show values of 1x10^{-16} m^2 after excessive heating on hardened cement paste, so it can be assumed that this order of magnitude refers to cracked cement.

The diffusivity of cement for class G and H has also been variable, as reported by different authors. Huet et al. [222] performs a compilation of the different transport mechanisms of cement G subjected to an environment of supercritical CO_2 and quotes diffusivity values of 1x10^{-12} m^{2}s^{-1} down to 1x10^{-14} m^{2}s^{-1}. Mainguy et al. [175] give an example of diffusion in the order of 1x10^{-12} m^{2}s^{-1}, and Vallin et al. [205] determine a value of 1x10^{-10} m^{2}s^{-1} from reverse analysis. Furthermore, Shen [223] quotes the values of different aqueous species in the order of 1x10^{-9} m^{2}s^{-1}.

To obtain the diffusion and permeability parameters for this particular cement for later use in the simulation at reservoir level, a porosity value equal to the experimental value of 34.5% for the first simulation is considered. As the rest of the volumetric proportions are variable, values were adopted from literature considering a 0.05% content of BNC: C-S-H 40.5%, CH 18%, aluminates 6.942%, and BNC 0.058%. The remaining compounds are classified as inert components, including amorphous silica which is a carbonation product. It is considered that there is no calcite prior to carbonation. CO_2 concentration is calculated considering: water volume, temperature, pressures, and mole fraction of CO_2 from experiments. The calculations give values of 1200 mol/m^3.

The initial parameters for fluid and cement are listed in Table 5.3, where η_{vis} is the fluid viscosity, K_F the fluid compressibility, ρ_F is the fluid density, R_c is cement compressive strength, and R_t the tensile strength.

η_{vis}[MPa.s]	K_F [MPa]	ρ_F[kg/m^3]	R_c[MPa]	R_t[MPa]	f_f	c_c
0.5 10^{-9}	2200	1000	24	2.4	1.135	31.35

Tab. 5.3.: Initial media properties for simulations.

Table 5.4 shows the molar volumes of the compounds involved.

ν^s_{CH}	$\nu^s_{C-S-H_{1.6}}$	ν^s_{CC}	ν^s_{AmSi}	$\nu^f_{H_2O}$
33.1	84.7	36.9	31	18.85

Tab. 5.4.: Molar volumes in cm^3/mol.

The 2D model is the same as in the previous section (Section 5.5). The lower horizontal contour has restricted movements in the Y direction, while the left vertical contour has restricted movements in the X direction. The top and right-hand contours are subjected to the carbonation conditions. Table 5.5 shows the initial conditions for modeling.

Inclusion	Volumetric Proportion	Bulk Modulus [GPa]	Shear Modulus [GPa]
Porosity	0.345	-	-
CH	0.18	33.00	14.50
C-S-H	0.405	25.00	18.40
Aluminates	0.06942	27.00	9.50
$C\bar{C}$	0.00	69.00	37.40
BNC	0.00058	42.00	38.00

Tab. 5.5.: Initial properties of cement with bacterial nanocellulose for the simulation under downhole conditions.

The well-system modeled consists of a CO_2 reservoir drilled and refilled with a steel casing protected by an annular cement geometry. We used the same transport values after determining the advection and diffusion parameters from the previous simulation. The model for the wellbore simulation assumes 1D axial symmetry under plane strain conditions in the axial direction. The mesh of ¾ of an inch (19 mm) represents the annular cement thickness and allows studying the progress of carbonation from the outer surface towards the inner cement. It consists of 502 elements that have the properties of the modified cement with BNC. Previous conditions for temperature and fluid pressure are considered (that is 90 °C and 20 MPa) with a 1.2 CO_2 molarity.

Results and discussion

First, a sensitivity analysis of parameters to calibrate the numerical model is made to reproduce the experimental penetration results. Table 5.6 and Table 5.7 show the values of the intrinsic permeability and diffusion coefficient varying k_0 and d^0_{eff}. As it can be observed, the values of permeability and diffusivity are in the range of the admissible values for cement class G previously mentioned.

Porosity	Parameter k_0 [m^2]					
	0.1	1	10	100	350	500
0.345	2.24^{-19}	2.24^{-18}	2.24^{-17}	2.24^{-16}	7.86^{-16}	1.12^{-15}

Tab. 5.6.: Values of k for different values of k_0.

Porosity	Parameter d^0_{eff} [m^2/s]					
	0.1	1	10	100	350	500
0.345	7.27^{-13}	7.27^{-12}	7.27^{-11}	7.27^{-10}	1.16^{-9}	2.18^{-9}

Tab. 5.7.: Values of d_{eff} for different values of d^0_{eff}.

By calibrating the model for $k_0 = 350$ and $d^0_{eff} = 160$, a representation of the entire sample consistent with the MIP experimental results of porosity can be observed in Figure 5.15. Results clearly show how the carbonation advanced into the core. The 1D image shows the porosity variation as a function of the radius. The material near the exposed surface is completely carbonated, and the porosity reaches 21%, while at the core, the porosity average is similar to the 23.2% from the MIP experiments.

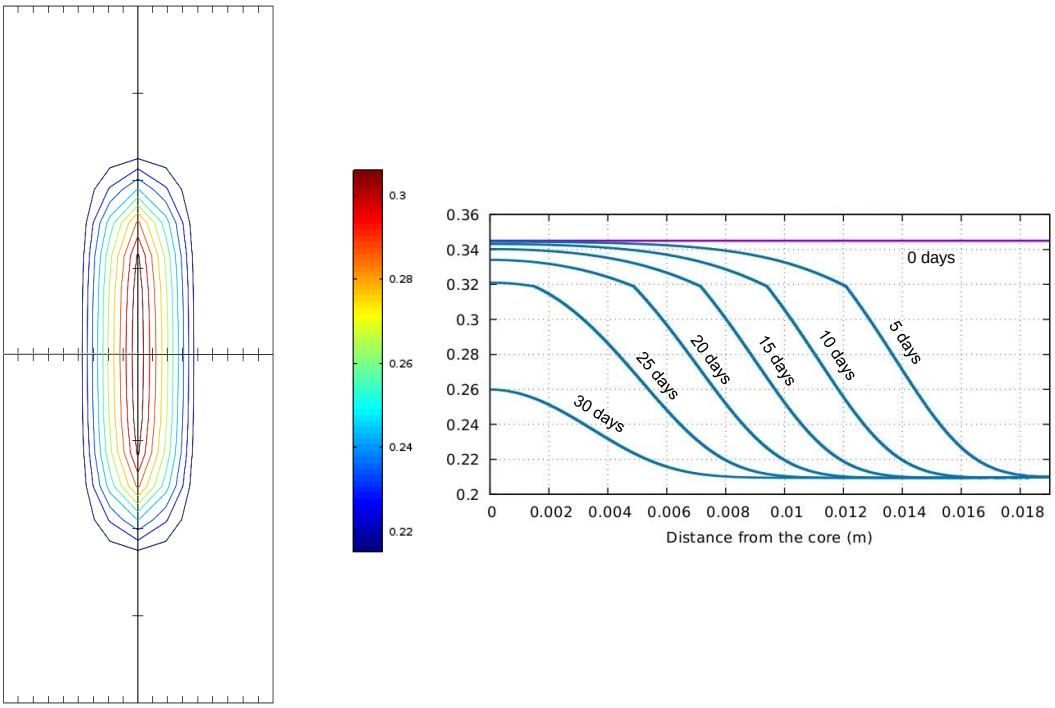

Fig. 5.15.: Left: Results of the simulation showing the variation of porosity in the experimental BNC05 sample of 38 mm by 78 mm for values of $k_0 = 350$ and $d^0_{eff} = 160$. Right: Results of porosity in 1D.

Figure 5.16 shows in more detail the dissolution and carbonation fronts. The blue line corresponds to the starting point of the chemical reaction of CH, while the red line is the limit between the carbonation process and where the hydrated products have already been carbonated. Some authors consider that the carbonation front or penetration depth follows a linear trend as a function of the square root of time (consistently with the fact that the chemical reactions are limited by the diffusion of CO_2 within the fluid phase)[84, 67]. Nevertheless, this is usually based on the phenolphthalein test which only considers the pH below 9. With the present model, we can distinguish the two fronts. In a first contact between the cement and supercritical CO_2, there is a significant decrease in CH and C-S-H content that lasts for the first few days. After 10 days, the dissolution front reaches the center of the cement sample. The fully carbonation front advances almost linearly in time but, it does not reach the cement center. Calcite is mostly deposited in the material near the exposed surface, decreasing its porosity, while in the core, it has not yet fully precipitated.

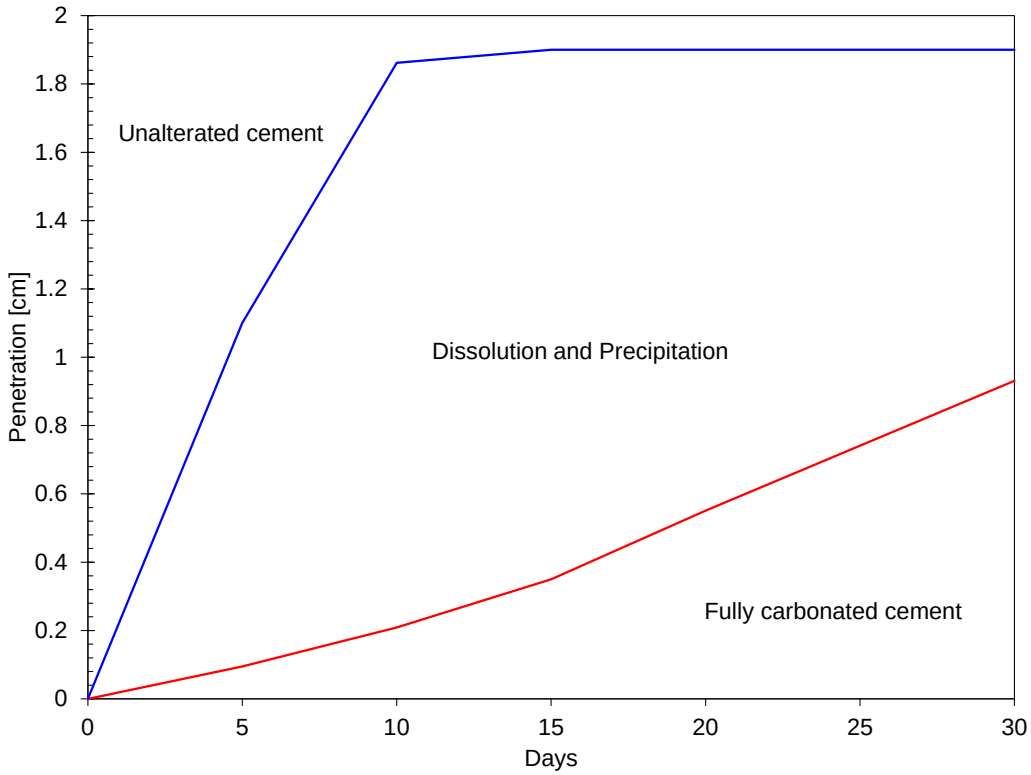

Fig. 5.16.: Dissolution and carbonation fronts development over time. The blue line corresponds to the starting point of the chemical reaction of CH, while the red line is the limit between the carbonation process and where the hydrated products have already been completely carbonated

Even though the dissolution front has reached the center, the chemical reactions between CO_2 and CH/C-S-H, which produce $C\bar{C}$ and water are still taking place in a region located 1 cm away from the center, meaning that all CH and C-S-H have not yet been completely leached after 30 days in these conditions.

The calibrated parameters are extrapolated to the cement submitted under downhole conditions in the context of CO_2 geological storage. We have to keep in mind that in the experimental results, curing and carbonation conditions are unfavorable to cement. However, the numerical model can be adapted to any condition considered. From this approach, additional characteristics of the variability of the carbonation front using these transport parameters can be obtained such as permeability variations throughout the sample (Figure 5.17). Carbonation advance forms calcite from CH and C-S-H, which grows inside the pores, this produces a reduction of the porosity and, as a consequence, a decrease in permeability and diffusivity, that slow down the entry of more CO_2 to the cement core. In Figure 5.17, this can be seen as a clogging effect. After 5 days of carbonation, we can observe a considerable CO_2 penetration, but after 5 more days, the penetration rate has significantly slowed down.

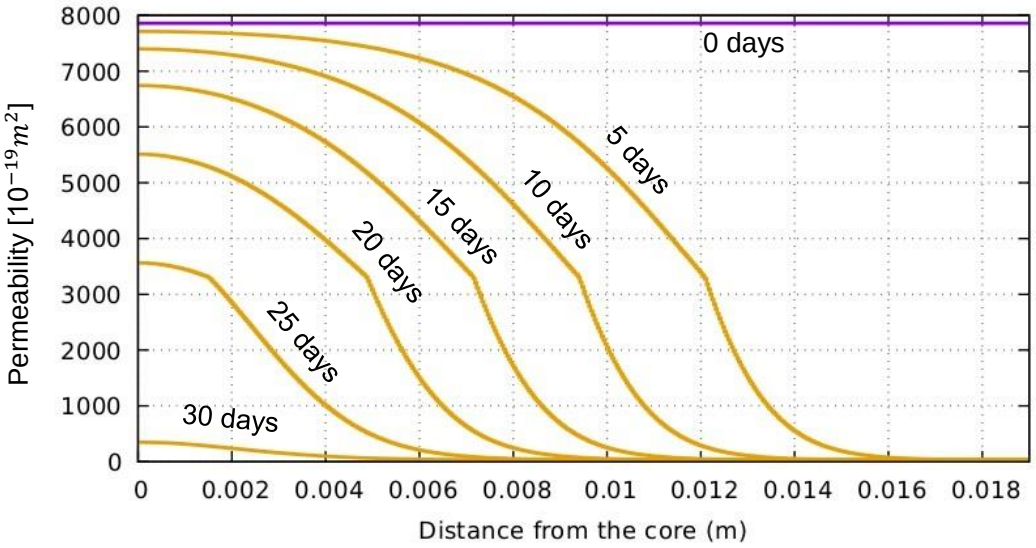

Fig. 5.17.: Permeability variation over time along the annular cement thickness of 3/4 inch

5.3.8 Conclusion

By performing a mass calculation and stoichiometric balance of the carbonation process in the samples, the carbonation degree of the experimental samples was calculated. The carbonation degree of BNC05 and BNC15 turned out to be less than for PC after 30 days of carbonation. After 120 days of carbonation, BNC05 continues having less carbonation than PC. BNC15 increases its carbonation level greatly, although this value is questionable since some specimens were broken when the cell was opened and measurement errors are likely to have occurred.

A chemo-poro-mechanical model of $scCO_2$ attack on a cement annulus of an abandoned oil well in the context of CO_2 storage was presented. A modification on the formulation was implemented to add the nanocellulose characteristics. Modifications were made to the base code to account for the simultaneous dissolution of CH and C-S-H, and also the dissolution of calcite when the supercritical CO_2 concentration is high enough.

The experimental data and simulation results were back analyzed to determine the properties of the cement used. Once these properties were known, a simulation under downhole conditions in the context of CO_2 geological storage was represented.

Results show a decrease in permeability and hydration products over time and the advance of the dissolution and carbonation fronts. The numerical study shows the advantage of the use of this type of tool for the study of possible real scenarios of CO_2 injection processes in deep wells. It can be adapted to different systems under different established conditions.

Conclusions and perspectives

6

6.1 Conclusions

Rheological, mechanical, thermal, and microstructural tests were performed on samples with different percentages (0%, 0.05%, 0.10%, 0.15%, 0.20%) of bacterial nanocellulose (BNC). 11 free fluid and 6 thickening-time tests were performed to characterize the slurry with BNC. The mechanical behaviour of the hardened state was investigated through the dynamical mechanical analysis (DMA) of 20 samples, measurements of 32 elastic ultrasound waves, 84 unconfined compressive strength (UCS) and 25 triaxial experiments (21 isotropic and 4 compressive tests). A total of 64 cylindrical specimens were subjected to supercritical CO_2 conditions (20 MPa and 90 °C) for 30 and 120 days with several percentages of nanocellulose using two curing methods, one long-term curing at low temperature (36 specimens) and one short-term curing at high temperature (32 specimens). The microstructure and crystalline characterization were studied by means of thermogravimetric analysis (TGA) of 9 samples, mercury intrusion porosimetry (MIP) of 52 samples, water porosity of 60 samples, scanning electron microscopy (SEM) and X-ray diffraction (XRD) of 10 samples.

The conclusions from the tests and simulations performed can be separated into four sections:

Effect of nanocellulose on non-carbonated cement.

Results indicate that the addition of BNC between 0.05% and 0.20% BWOC produces a significant decrease in the amount of free fluid and reduces the thickening time of cement slurry, but retains a greater amount of water which aids in its subsequent hydration. It was necessary to use up to 0.35% superplasticizer for the cement to have a viscosity similar to that of the reference cement. The gydration improvement was observed in its microstructure, where a higher degree of hydration, and a decrease in porosity were observed. This increase in hydration was likely the reason that cements with nanocellulose had a uniaxial compressive strength up to 20% higher than neat cement. It was also observed that higher BNC contents improve the thermomechanical behaviour under oscillating bending stress. Triaxial results also show an improvement in the compressibility moduli of cements with BNC and similar or higher ultimate strength. The MIP results show that the samples with BNC have lower capillary porosity, although with some heterogeneity because the distribution of

BNC in the mixture was not perfect. BNC exchanges the capillary porosity (reducing it) by gel porosity (increasing it).

Effect of carbonation on cements with added bacterial nanocellulose cured at room temperature.

Density increased in all specimens, but cement with 0.05% of BNC was the lightest. An extensive degraded zone was seen at the top of the specimens, but radially, the cement was less damaged. Cement with 0.05% of bacterial nanocellulose presents a lesser degraded zone and is not affected at the center of the sample as the other mixtures.

The microstructure shows that the capillary porosity decreases steadily to values of 5% during 120 days of carbonation, which reduces the penetration of carbonic acid into the specimen, while gel porosity was decreasing during the first 30 days of carbonation. Gel porosity increases again after 120 days of carbonation, suggesting C-S-H decalcification. Total porosity at the end of the experiments resulted in a lower value than the initial one. At the core, capillary porosity was reduced in neat cement (PC) and BNC15 samples but not for BNC05. Here, the pore size distribution has varied and oven porosity has increased, with a reduction of largest pores, and an increase in gel pores.

Carbonation generates a reduction in the mechanical strength and Young's modulus of all specimens. Neat cement shows a continuous decline in strength, while specimens with BNC maintain the same strength from 30 to 120 days. Specimens with BNC show higher values of their mechanical properties compared to PC in absolute and relative terms before and after the carbonation process. A decrease in the compressibility modulus of cement in triaxial tests is also observed, although BNC05 maintains values higher than PC.

TGA results indicate that BNC05 cement has lower amounts of carbonates with respect to PC, mostly aragonite, either in the core or near the surface exposed to CO_2. XRD results show higher amount of CH in samples with BNC before carbonation. SEM images on all carbonated cement samples show fully crystalline surface after 120 days of carbonation, instead of the amorphous surface observed in non-carbonated cement. They also show carbonates growing in the form of sheets overlapping each other, pore crystallization, and dissolution of calcium carbonates near the exposed surface.

Effect of carbonation on cements with added bacterial nanocellulose cured at high temperature (90 °C).

BNC specimens show a lower mass gain compared to PC after 30 days of carbonation. However, after 120 days of carbonation, BNC05 presents a higher mass uptake than PC. The BNC-cement longitudinal sections reveal some small voids in their interior, which could allow further CO_2 penetration. The considerable increase in porosity dulls the short-term

hydration effects and the strength of cements with nanocellulose is lower prior to the carbonation process.

The MIP results show that initially, BNC-cement samples own the same porosity as the cement without BNC addition. Lower porosity is observed in cement with BNC after being carbonated for 30 days, either in the core or near the exposed surface. After 120 days, the porosity at the interior is the same for both cement (PC and BNC05) and is lower for PC near the exposed surface. It is observed that the reduction of porosity is limited to minimum values of 13/14%, probably due to the total consumption of the hydrated components. Total porosity is higher in BNC05 before carbonation, but it is the same at the interior and near the exposed surface after 120 days.

The XRD results of the PC and BNC05 samples before and after carbonation show no difference between them. After carbonation, the dominant crystalline phases are calcite and aragonite, which indicates the complete carbonation of the material near the surface exposed to the supercritical fluid.

Unmodified specimens show a better mechanical performance during carbonation. However, carbonation in specimens with BNC indicates a higher increase in relative strength than in cements without additions.

Numerical simulations of cements with bacterial nanocellulose.

The carbonation degree of BNC05 and BNC15 turned out to be less than for PC after 30 days of carbonation. After 120 days of carbonation, BNC05 continues to have less carbonation than PC. BNC15 showed great increase in its carbonation level, although this value is questionable since some specimens were broken when the cell was opened and measurement errors are likely to have occurred.

A chemo-poro-mechanical model of $scCO_2$ attack on a cement annulus of an abandoned oil well in the context of CO_2 storage was presented. A modification on the formulation was implemented to add the nanocellulose characteristics. Adjustments were made to the base code to account for the simultaneous dissolution of CH and C-S-H, and also the dissolution of calcite when the $scCO_2$ concentration is high enough.

The experimental data and simulation results were back analyzed to determine the properties of the cement used. Once these properties were known, a simulation under downhole conditions in the context of CO_2 geological storage was represented.

Results show a decrease in permeability and hydration products over time and the advance of the dissolution and carbonation fronts. The numerical study shows the advantage of the use of this type of tool for the study of possible real scenarios of CO_2 injection processes in deep wells. It can be adapted to different systems under different established conditions.

6.2 Perspectives

More detailed work on the effect of nanocellulose at different curing temperatures would be relevant to perform, also considering different water-cement ratios. The present work only evaluated the influence of nanocellulose after curing the cement for 28 days, so more information is needed to have a better understanding at early ages.

It would also be of interest to make a comparison between cements cured at different ages and carbonate them under the same condition. Here we have performed carbonation only for two curing conditions, so the effect of hydration/carbonation could be studied to have more information regarding the microstructure and mechanical behaviour before and after carbonation.

Tests studying the permeability of cement during the carbonation process would be of value to evaluate possible gas migrations due to microstructural variations.

More focused work on the study of crystallization pressure could determine its effects on cement. From there, this model could be added to the code to assess the damage caused to the sample during carbonation. Additionally, this numerical code could be extended so that the temperature is coupled to it.

Bibliography

[1]M. D. Aminu, S. A. Nabavi, C. A. Rochelle, and V. Manovic. „A review of developments in carbon dioxide storage“. *Applied Energy* 208.December 2016 (2017), pp. 1389–1419 (cit. on pp. 1, 6).

[2]W. Chen and R. Xu. „Clean coal technology development in China“. *Energy Policy* 38.5 (2010). Greater China Energy: Special Section with regular papers, pp. 2123–2130 (cit. on p. 1).

[3]K. Michael, A. Golab, V. Shulakova, J. Ennis-king, G. Allinson, S. Sharma, and T. Aiken. „Geological storage of CO 2 in saline aquifers — A review of the experience from existing storage operations“. *International Journal of Greenhouse Gas Control* 4.4 (2010), pp. 659–667 (cit. on pp. 1, 6).

[4]J. M. Belbute and A. M. Pereira. *ARFIMA Reference Forecasts for Worldwide CO2 Emissions and the Need for Large and Frontloaded Decarbonization Policies*. Tech. rep. Lisboa: Gabinete de Estratégia e Estudos do Ministério da Economia, 2019, p. 31 (cit. on p. 5).

[5]R. Afroz, M. N. Hassan, and N. A. Ibrahim. „Review of air pollution and health impacts in Malaysia“. *Environmental Research* 92.2 (2003), pp. 71–77 (cit. on p. 5).

[6]V. Masson-Delmotte, P. Zhai, H.-O. Pörtner, et al. *IPCC, 2018: Global Warming of 1.5°C. An IPCC Special Report on the impacts of global warming of 1.5°C above pre-industrial levels and related global greenhouse gas emission pathways, in the context of strengthening the global response to the threat of cli*. Tech. rep. Geneva, 2018, p. 616 (cit. on p. 5).

[7]Philip Ringrose. *How to Store CO2 Underground: Insights from early-mover CCS Projects*. Springer, 2020, p. 129 (cit. on pp. 5–7).

[8]B. Metz, O. Davidson, H. Coninck, M. Loos, and L. Meyer. *La captación y el almacenamiento de dióxido de carbono*. 2005, p. 57 (cit. on p. 6).

[9]S. Bachu, D. Bonijoly, J. Bradshaw, R. Burruss, S. Holloway, N. P. Christensen, and O. M. Mathiassen. „CO2 storage capacity estimation: Methodology and gaps“. *International Journal of Greenhouse Gas Control* 1.4 (2007), pp. 430–443 (cit. on p. 6).

[10]A. Lokhorst and T. Wildenborg. „Introduction on CO2 geological storage. Classification of storage options“. *Oil and Gas Science and Technology* 60.3 (2005), pp. 513–515 (cit. on p. 6).

[11]S. Ó. Snæbjörnsdóttir, F. Wiese, T. Fridriksson, H. Ármansson, G. M. Einarsson, and S. R. Gislason. „CO2 storage potential of basaltic rocks in Iceland and the oceanic ridges“. *Energy Procedia* 63 (2014). 12th International Conference on Greenhouse Gas Control Technologies, GHGT-12, pp. 4585–4600 (cit. on p. 6).

[12]D. Civile, M. Zecchin, E. Forlin, F. Donda, V. Volpi, B. Merson, and S. Persoglia. „CO2 geological storage in the Italian carbonate successions“. *International Journal of Greenhouse Gas Control* 19 (2013), pp. 101–116 (cit. on p. 6).

[13]J. W. Carey, M. Wigand, S. J. Chipera, G. WoldeGabriel, R. Pawar, P. C. Lichtner, S. C. Wehner, M. A. Raines, and G. D. Guthrie. „Analysis and performance of oil well cement with 30 years of CO2 exposure from the SACROC Unit, West Texas, USA“. *International Journal of Greenhouse Gas Control* 1.1 (2007), pp. 75–85 (cit. on pp. 6, 71, 95).

[14]F. A. Rahman, M. M. A. Aziz, R. Saidur, W. A. W. A. Bakar, M. R. Hainin, R. Putrajaya, and N. A. Hassan. „Pollution to solution: Capture and sequestration of carbon dioxide (CO2) and its utilization as a renewable energy source for a sustainable future“. *Renewable and Sustainable Energy Reviews* 71.January (2017), pp. 112–126 (cit. on p. 7).

[15]S. T. McCoy and E. S. Rubin. „An engineering-economic model of pipeline transport of CO2 with application to carbon capture and storage“. *International Journal of Greenhouse Gas Control* 2.2 (2008), pp. 219–229 (cit. on p. 7).

[16]Y. Huang, S. Rebennack, and Q. P. Zheng. „Techno-economic analysis and optimization models for carbon capture and storage: A survey“. *Energy Systems* 4.4 (2013), pp. 315–353 (cit. on p. 7).

[17]D. N. Espinoza and J. C. Santamarina. „CO2 breakthrough—Caprock sealing efficiency and integrity for carbon geological storage“. *International Journal of Greenhouse Gas Control* 66.October (2017), pp. 218–229 (cit. on p. 8).

[18]V. Vilarrasa and L. Laloui. „Potential fracture propagation into the caprock induced by cold CO2 injection in normal faulting stress regimes“. *Geomechanics for Energy and the Environment* 2 (2015), pp. 22–31 (cit. on p. 8).

[19]L. Urpi, A. Rinaldi, J. Rutqvist, F. Cappa, and C. J. Spiers. „Dynamic simulation of CO2-injection-induced fault rupture with slip-rate dependent friction coefficient“. *Geomechanics for Energy and the Environment* 7 (2016), pp. 47–65 (cit. on p. 8).

[20]H. E. Mason, W. L. D. Frane, S. D. C. Walsh, Z. Dai, S. Charnvanichborikarn, and S. A. Carroll. „Chemical and Mechanical Properties of Wellbore Cement Altered by CO 2 - Rich Brine Using a Multianalytical Approach“. *Environmental Science & Technology* 47 (2013), pp. 1745–1752 (cit. on p. 9).

[21]M. Recasens, S. Garcia, E. Mackay, J. Delgado, and M. M. Maroto-Valer. „Experimental Study of Wellbore Integrity for CO2 Geological Storage“. *Energy Procedia* 114.November 2016 (2017), pp. 5249–5255 (cit. on p. 9).

[22]S. E. Gasda, S. Bachu, and M. A. Celia. „Spatial characterization of the location of potentially leaky wells penetrating a deep saline aquifer in a mature sedimentary basin“. *Environmental Geology* 46.6-7 (2004), pp. 707–720 (cit. on pp. 9, 10).

[23]S. Adjei and S. Elkatatny. „A highlight on the application of industrial and agro wastes in cement-based materials“. *Journal of Petroleum Science and Engineering* 195.June (2020), p. 107911 (cit. on p. 10).

[24]D. Calvert and D. K. Smith. „API Oilwell Cementing Practices“. *Journal of Petroleum Technology* 42.11 (Nov. 1990), pp. 1364–1373 (cit. on p. 11).

[25]M. Al Ramadan, S. Salehi, G. Kwatia, C. Ezeakacha, and C. Teodoriu. „Experimental investigation of well integrity: Annular gas migration in cement column“. *Journal of Petroleum Science and Engineering* 179.January (2019), pp. 126–135 (cit. on p. 11).

[26]R. Kiran, C. Teodoriu, Y. Dadmohammadi, R. Nygaard, D. Wood, M. Mokhtari, and S. Salehi. „Identification and evaluation of well integrity and causes of failure of well integrity barriers (A review)“. *Journal of Natural Gas Science and Engineering* 45 (2017), pp. 511–526 (cit. on p. 11).

[27]G. Carter and D. K. Smith. „Properties of Cementing Compositions at Elevated Temperatures and Pressure“. *32nd Annual Fall Meeting of Society of Petroleum Engineers*. 1957, pp. 20–27 (cit. on p. 11).

[28]N. Banthia and N. Nandakumar. „Crack growth resistance of hybrid fiber reinforced cement composites“. *Cement and Concrete Composites* 25.1 (2003), pp. 3–9 (cit. on pp. 11, 59).

[29]X. Liu, G. Falcone, and C. Alimonti. „A systematic study of harnessing low-temperature geothermal energy from oil and gas reservoirs“. *Energy* 142 (2018), pp. 346–355 (cit. on pp. 11, 95).

[30]A. Fabbri, J. Corvisier, A. Schubnel, F. Brunet, B. Goffé, G. Rimmele, and V. Barlet-Gouédard. „Effect of carbonation on the hydro-mechanical properties of Portland cements“. *Cement and Concrete Research* 39.12 (2009), pp. 1156–1163 (cit. on pp. 11, 25, 70, 82, 95, 96, 104).

[31]I. Yurtdas, S. Y. Xie, N. Burlion, J. F. Shao, J. Saint-Marc, and A. Garnier. „Influence of chemical degradation on mechanical behavior of a petroleum cement paste“. *Cement and Concrete Research* 41.4 (2011), pp. 412–421 (cit. on p. 11).

[32]G. Rimmelé, V. Barlet-Gouédard, O. Porcherie, B. Goffé, and F. Brunet. „Heterogeneous porosity distribution in Portland cement exposed to CO2-rich fluids“. *Cement and Concrete Research* 38.8-9 (2008), pp. 1038–1048 (cit. on pp. 11, 23, 75, 95, 134).

[33]M. Samudio. „Modelling of an oil well cement paste from early age to hardened state : hydration kinetics and poromechanical behaviour“. PhD thesis. Université Paris-Est, 2018, p. 231 (cit. on pp. 11, 60, 62, 95).

[34]X. Zhang, S. Heinonen, and E. Levänen. „Applications of supercritical carbon dioxide in materials processing and synthesis“. *RSC Adv.* 4 (105 2014), pp. 61137–61152 (cit. on p. 11).

[35]R. Bruckdorfer. „Carbon Dioxide Corrosion in Oilwell Cements“. *Society of Petroleum Engineers* (1986) (cit. on pp. 12, 82).

[36]G. W. Scherer. „Leakage of CO2 through abandoned wells: Role of corrosion of cement“. *Carbon Dioxide Capture for Storage in Deep Geologic Formations*. Elsevier Ltd., 2005, pp. 827–848 (cit. on p. 12).

[37]M. Bai, Z. Zhang, and X. Fu. „A review on well integrity issues for CO2 geological storage and enhanced gas recovery“. *Renewable and Sustainable Energy Reviews* 59 (2016), pp. 920–926 (cit. on p. 12).

[38]American Petroleum Institute. *Specification for Cements and Materials for Well Cementing 10A*. 2019, p. 62 (cit. on pp. 13, 18, 33, 35, 36).

[39]E. B. Nelson. *Well Cementing*. Elsevier, 1990 (cit. on pp. 14, 16, 51, 135).

[40]A. M. Neville and J. J. Brooks. *Concrete technology*. Longman Scientific & Technical, 2010, p. 442 (cit. on p. 14).

[41]D. J. M. Guitart. „Durabilidad de morteros de cemento en contacto con purines de cerdo“. PhD thesis. Universidad Politécnica de Madrid, 2010, p. 265 (cit. on p. 14).

[42]A. Vázquez and T. Piqué. „Biotech admixtures for enhancing portland cement hydration“. *Biopolymers and Biotech Admixtures for Eco-Efficient Construction Materials* (2016), pp. 81–98 (cit. on p. 15).

[43]J. R. Niño Hernandez. *Tecnología de concreto: Tomo 1 Materiales, propiedades y diseño de mezclas*. Vol. I. Bogotá: Asociación Colombiana de Productores de Concreto - ASOCRETO, 2010, p. 228 (cit. on p. 15).

[44]H. J. Brouwers. „The work of Powers and Brownyard revisited: Part 1“. *Cement and Concrete Research* 34.9 (2004), pp. 1697–1716 (cit. on p. 16).

[45]F. Young and W. Hansen. „Volume relationships for C-S-H formation based on hydration stoichiometries“. *Materials Research Society* 85 (1987), pp. 5–24 (cit. on p. 16).

[46]I. Soroka. *Portland Cement Paste and Concrete*. 1979, p. 338 (cit. on p. 16).

[47]K. A. Slagle. „Rheological Design of Cementing Operations“. *36 th Annual Full Meeting of SPE*. Vol. 36. 1962, pp. 323–328 (cit. on p. 18).

[48]API. „Recommended Practice for Testing Well Cements: API Recommended practice 10B“. November (2000), p. 134 (cit. on p. 18).

[49]T. Nguyen-Sy, T.-K. Nguyen, V.-D. Dao, K. Le-Nguyen, N.-M. Vu, Q.-D. To, T.-D. Nguyen, and T.-T. Nguyen. „A flexible homogenization method for the effective elastic properties of cement pastes with w/c effect“. *Cement and Concrete Research* 134 (2020), p. 106106 (cit. on p. 19).

[50]J. Sanahuja, L. Dormieux, and G. Chanvillard. „Modelling elasticity of a hydrating cement paste“. *Cement and Concrete Research* 37.10 (2007), pp. 1427–1439 (cit. on p. 19).

[51]B. Pichler, C. Hellmich, and J. Eberhardsteiner. „Spherical and acicular representation of hydrates in a micromechanical model for cement paste: Prediction of early-age elasticity and strength“. *Acta Mechanica* 203.3-4 (2009), pp. 137–162 (cit. on p. 19).

[52]S. Ghabezloo. „Association of macroscopic laboratory testing and micromechanics modelling for the evaluation of the poroelastic parameters of a hardened cement paste“. *Cement and Concrete Research* 40.8 (2010), pp. 1197–1210 (cit. on p. 19).

[53]S. Ghabezloo, J. Sulem, S. Guédon, F. Martineau, and J. Saint-Marc. „Poromechanical behaviour of hardened cement paste under isotropic loading“. *Cement and Concrete Research* 38.12 (2008), pp. 1424–1437 (cit. on pp. 20, 62).

[54]S. Bahafid, S. Ghabezloo, M. Duc, P. Faure, and J. Sulem. „Effect of the hydration temperature on the microstructure of Class G cement: C-S-H composition and density“. *Cement and Concrete Research* 95 (2017), pp. 270–281 (cit. on pp. 20, 21, 70, 91, 115).

[55]P. Garcés, E. Alcocel, S. Chinchón, C. Andreu, and J. Alcaide. „Effect of curing temperature in some hydration characteristics of calcium aluminate cement compared with those of portland cement“. *Cement and Concrete Research* 27.9 (1997), pp. 1343–1355 (cit. on p. 21).

[56]Y. Maltais and J. Marchand. „Influence of curing temperature on cement hydration and mechanical strength development of fly ash mortars“. *Cement and Concrete Research* 27.7 (1997), pp. 1009–1020 (cit. on p. 21).

[57]K.-h. Yang, J.-s. Mun, and M.-s. Cho. „Effect of Curing Temperature Histories on the Compressive Strength Development of High-Strength Concrete“. *Advances in Materials Science and Engineering* 2015 (2015), p. 12 (cit. on p. 21).

[58]S. Bahafid, S. Ghabezloo, P. Faure, M. Duc, and J. Sulem. „Effect of the hydration temperature on the pore structure of cement paste: Experimental investigation and micromechanical modelling“. *Cement and Concrete Research* 111.June (2018), pp. 1–14 (cit. on pp. 21, 89, 134).

[59]M. Röβler and I. Odler. „Investigations on the relationship between porosity, structure and strength of hydrated portland cement pastes I. Effect of porosity“. *Cement and Concrete Research* 15.2 (1985), pp. 320–330 (cit. on p. 21).

[60]S. Bahafid. „A multi-technique investigation of the effect of hydration temperature on the microstructure and mechanical properties of cement paste“. PhD thesis. 2017, p. 154 (cit. on pp. 21, 70, 79, 95, 117).

[61]M. Bagheri, S. M. Shariatipour, and E. Ganjian. „A review of oil well cement alteration in CO2-rich environments“. *Construction and Building Materials* 186 (2018), pp. 946–968 (cit. on p. 22).

[62]M. Fernández Bertos, S. J. Simons, C. D. Hills, and P. J. Carey. „A review of accelerated carbonation technology in the treatment of cement-based materials and sequestration of CO2“. *Journal of Hazardous Materials* 112.3 (2004), pp. 193–205 (cit. on p. 22).

[63]R. Chang, S. Kim, S. Lee, S. Choi, M. Kim, and Y. Park. „Calcium carbonate precipitation for CO 2 storage and utilization: A review of the carbonate crystallization and polymorphism“. *Frontiers in Energy Research* 5.JUL (2017), pp. 1–12 (cit. on p. 22).

[64]B. Šavija and M. Luković. „Carbonation of cement paste: Understanding, challenges, and opportunities“. *Construction and Building Materials* 117 (2016), pp. 285–301 (cit. on p. 22).

[65]L. Urbonas, V. Leno, and D. Heinz. „Effect of carbonation in supercritical CO2 on the properties of hardened cement paste of different alkalinity“. *Construction and Building Materials* 123 (2016), pp. 704–711 (cit. on p. 22).

[66]Y. Li, W. Liu, F. Xing, S. Wang, L. Tang, S. Lin, and Z. Dong. „Carbonation of the synthetic calcium silicate hydrate (C-S-H) under different concentrations of CO2: Chemical phases analysis and kinetics“. *Journal of CO2 Utilization* 35 (2020), pp. 303–313 (cit. on p. 22).

[67]A. Morandeau, M. Thiéry, and P. Dangla. „Investigation of the carbonation mechanism of CH and C-S-H in terms of kinetics, microstructure changes and moisture properties“. *Cement and Concrete Research* 56 (2014), pp. 153–170 (cit. on pp. 22, 91, 116, 118, 122, 123, 137).

[68]V. Shah, K. Scrivener, B. Bhattacharjee, and S. Bishnoi. „Changes in microstructure characteristics of cement paste on carbonation“. *Cement and Concrete Research* 109.April (2018), pp. 184–197 (cit. on pp. 22, 25, 100, 115).

[69]B. G. Kutchko, B. R. Strazisar, D. A. Dzombak, G. V. Lowry, and N. Thauiow. „Degradation of well cement by CO2 under geologic sequestration conditions“. *Environmental Science and Technology* 41.13 (2007), pp. 4787–4792 (cit. on pp. 22–24, 26, 27, 70, 76, 77, 95).

[70]E. N. Matteo, B. Huet, C. F. Jové-Colón, and G. W. Scherer. „Experimental and modeling study of calcium carbonate precipitation and its effects on the degradation of oil well cement during carbonated brine exposure“. *Cement and Concrete Research* 113.May 2017 (2018), pp. 1–12 (cit. on p. 23).

[71]Y. J. Jeong, K. S. Youm, and T. S. Yun. „Effect of nano-silica and curing conditions on the reaction rate of class G well cement exposed to geological CO2-sequestration conditions“. *Cement and Concrete Research* 109.September 2017 (2018), pp. 208–216 (cit. on pp. 23, 24, 77, 86).

[72]D. Buhmann and W. Dreybrodt. „The kinetics of calcite dissolution and precipitation in geologically relevant situations of karst areas. 2. Closed system“. *Chemical Geology* 53.1-2 (1985), pp. 109–124 (cit. on p. 23).

[73]V. Barlet-Gouédard, G. Rimmelé, B. Goffé, and O. Porcherie. „Well Technologies for CO2 Geological Storage: CO2-Resistant Cement“. *Oil & Gas Science and Technology* 62.3 (2007), pp. 325–334 (cit. on pp. 23, 25, 27, 69, 70, 95, 96, 134).

[74]S. Kim and J. C. Santamarina. „Reactive fluid flow in CO 2 storage reservoirs: A 2-D pore network“. *Greenhouse Gases: Science and Technology* 473.5 (2015), pp. 462–473 (cit. on p. 23).

[75]M. Lesti, C. Tiemeyer, and J. Plank. „CO2 stability of Portland cement based well cementing systems for use on carbon capture & storage (CCS) wells“. *Cement and Concrete Research* 45.1 (2013), pp. 45–54 (cit. on pp. 23, 82).

[76]K. Abid, R. Gholami, P. Choate, and B. H. Nagaratnam. „A review on cement degradation under CO2-rich environment of sequestration projects“. *Journal of Natural Gas Science and Engineering* 27 (2015), pp. 1149–1157 (cit. on p. 24).

[77]C. Teodoriu and O. Bello. „A review of cement testing apparatus and methods under CO2 environment and their impact on well integrity prediction – Where do we stand?“ *Journal of Petroleum Science and Engineering* 187 (2020), p. 106736 (cit. on p. 24).

[78]N. Neuville, E. Lécolier, G. Aouad, A. Rivereau, and D. Damidot. „Effect of curing conditions on oilwell cement paste behaviour during leaching: Experimental and modelling approaches“. *Comptes Rendus Chimie* 12.3-4 (2009), pp. 511–520 (cit. on p. 24).

[79]B. L. S. Costa, J. C. O. Freitas, D. M. A. Melo, R. G. S. Araujo, Y. H. Oliveira, and C. A. Simão. „Evaluation of density influence on resistance to carbonation process in oil well cement slurries“. *Construction and Building Materials* 197 (2019), pp. 331–338 (cit. on pp. 24, 95).

[80]M. Bagheri, S. M. Shariatipour, and E. Ganjian. „Prediction of the lifespan of cement at a specific depth based on the coupling of geomechanical and geochemical processes for CO2 storage“. *International Journal of Greenhouse Gas Control* 86.April (2019), pp. 43–65 (cit. on p. 24).

[81]J. B. Laudet, A. Garnier, N. Neuville, Y. Le Guen, D. Fourmaintraux, N. Rafai, N. Burlion, and J. F. Shao. „The behavior of oil well cement at downhole CO2 storage conditions: Static and dynamic laboratory experiments“. *Energy Procedia* 4.December (2011), pp. 5251–5258 (cit. on p. 25).

[82]A. Duguid and G. W. Scherer. „Degradation of oilwell cement due to exposure to carbonated brine“. *International Journal of Greenhouse Gas Control* 4.3 (2010), pp. 546–560 (cit. on pp. 25, 27, 28, 71, 78, 82).

[83]N. J. Huerta, M. A. Hesse, S. L. Bryant, B. R. Strazisar, and C. Lopano. „Reactive transport of CO2-saturated water in a cement fracture: Application to wellbore leakage during geologic CO2 storage“. *International Journal of Greenhouse Gas Control* 44 (2016), pp. 276–289 (cit. on p. 25).

[84]B. Kutchko, B. Strazisar, G. Lowry, D. Dzombak, and N. Thaulow. „Rate of CO2 Attack on Hydrated Class H Well Cement under Geologic Sequestration Conditions“. *Environmental Science & Technology* 42.16 (2008), pp. 6237–6242 (cit. on pp. 25, 85, 137).

[85]H. B. Jung and W. Um. „Experimental study of potential wellbore cement carbonation by various phases of carbon dioxide during geologic carbon sequestration“. *Applied Geochemistry* 35 (2013), pp. 161–172 (cit. on pp. 25, 69).

[86]B. G. Kutchko, B. R. Strazisar, N. Huerta, G. V. Lowry, D. A. Dzombak, and N. Thaulow. „CO2 reaction with hydrated class H well cement under geologic sequestration conditions: Effects of flyash admixtures“. *Environmental Science and Technology* 43.10 (2009), pp. 3947–3952 (cit. on p. 25).

[87]V. Barlet-Gouédard, G. Rimmelé, B. Goffé, and O. Porcherie. „Mitigation strategies for the risk of CO2 migration through wellbores“. *SPE/IADC Drilling Conference, Proceedings*. 2006, pp. 405–421 (cit. on pp. 25, 27).

[88]„Wellbore integrity in a saline aquifer: Experimental steel-cement interface degradation under supercritical CO2 conditions representative of Brazil's Parana basin“. *International Journal of Greenhouse Gas Control* 98.October 2019 (2020) (cit. on p. 25).

[89]M. Zhang and S. Bachu. „Review of integrity of existing wells in relation to CO2 geological storage: What do we know?“ *International Journal of Greenhouse Gas Control* 5.4 (2011), pp. 826–840 (cit. on pp. 25, 27).

[90]B. L. de Sena Costa, J. C. de Oliveira Freitas, P. H. Silva Santos, R. Gomes da Silva Araújo, J. F. dos Santos Oliveira, and D. M. de Araújo Melo. „Study of carbonation in a class G Portland cement matrix at supercritical and saturated environments“. *Construction and Building Materials* 180 (2018), pp. 308–319 (cit. on p. 25).

[91]B. L. d. S. Costa, J. C. d. O. Freitas, P. H. S. Santos, D. M. d. A. Melo, R. G. d. S. Araujo, and Y. H. de Oliveira. „Carbonation in oil well Portland cement: Influence of hydration time prior to contact with CO2“. *Construction and Building Materials* 159 (2018), pp. 252–260 (cit. on pp. 25, 82).

[92]J. T. Adeoye, A. B. R. Ellis, and P. Northwest. „Application of Engineered Cementitious Composites for Enhanced Wellbore Integrity During Geologic Carbon Sequestration“ (2019) (cit. on pp. 25, 75).

[93]N. Jacquemet, J. Pironon, V. Lagneau, and J. Saint-Marc. „Armouring of well cement in H2S–CO2 saturated brine by calcite coating – Experiments and numerical modelling“. *Applied Geochemistry* 27.3 (2012), pp. 782–795 (cit. on p. 25).

[94]N. J. Huerta, S. L. Bryant, and L. Conrad. „Cement core experiments with a conductive leakage pathway, under confining stress and alteration of cement's mechanical properties via a reactive fluid, as an analog for CO2 leakage scenario“. *Proceedings - SPE Symposium on Improved Oil Recovery* 2 (2008), pp. 643–655 (cit. on p. 25).

[95]I. Siró and D. Plackett. „Microfibrillated cellulose and new nanocomposite materials : a review“. *Cellulose* 17 (2010), pp. 459–494 (cit. on p. 29).

[96]D. Klemm, D. Schumann, F. Kramer, et al. „Nanocelluloses as Innovative Polymers in Research and Application“. *Advances in Polymer Science* August (2006), pp. 49–96 (cit. on p. 29).

[97]N. Muhd Julkapli and S. Bagheri. „Nanocellulose as a green and sustainable emerging material in energy applications: a review“. *Polymers for Advanced Technologies* 28.12 (2017), pp. 1583–1594 (cit. on p. 29).

[98]P. Gatenholm and D. Klemm. „Bacterial Nanocellulose as a Reneable Material for Biomedical Applications“. *MRS Bulletin* 35 (2010), pp. 208–213 (cit. on pp. 29, 62, 67).

[99]S. Keshk. „Bacterial Cellulose Production and its Industrial Applications“. *Journal of Bioprocessing & Biotechniques* 04.02 (2014) (cit. on p. 29).

[100]D. Mikkelsen, B. M. Flanagan, G. A. Dykes, and M. J. Gidley. „Influence of different carbon sources on bacterial cellulose production by Gluconacetobacter xylinus strain ATCC 53524“. *Journal of Applied Microbiology* 107.2 (2009), pp. 576–583 (cit. on p. 29).

[101]A. Vazquez, M. L. Foresti, P. Cerrutti, and M. Galvagno. „Bacterial Cellulose from Simple and Low Cost Production Media by Gluconacetobacter xylinus“. *Journal of Polymers and the Environment* 21.2 (2013), pp. 545–554 (cit. on pp. 29, 31, 32).

[102]M. Foresti, P. Cerrutti, and A. Vázquez. „Bacterial Nanocellulose: Synthesis, Properties and Applications“. *Polymer nanocomposites based on inorganic and organic nanomaterials*. 2015, p. 581 (cit. on p. 30).

[103]P. Cerrutti, P. Roldán, R. M. García, M. A. Galvagno, A. Vázquez, and M. L. Foresti. „Production of bacterial nanocellulose from wine industry residues: Importance of fermentation time on pellicle characteristics“. *Journal of Applied Polymer Science* 133.14 (2016) (cit. on pp. 30, 34, 53).

[104]A. F. Jozala, L. C. D. Lencastre-novaes, A. M. Lopes, V. D. C. Santos-ebinuma, P. G. Mazzola, and A. Pessoa-jr. „Bacterial nanocellulose production and application : a 10-year overview“. *Applied Microbiology and Biotechnology* 100.5 (2016), pp. 2063–2072 (cit. on p. 30).

[105]S. Sheykhnazari, T. Tabarsa, A. Ashori, A. Shakeri, and M. Golalipour. „Bacterial synthesized cellulose nanofibers; Effects of growth times and culture mediums on the structural characteristics“. *Carbohydrate Polymers* 86.3 (2011), pp. 1187–1191 (cit. on p. 30).

[106]O. R. Ilesanmi, B. Hilal, S. Gill, H. Leigh, A. Brandl, B. Hughes, M. A. Mazrouei, A. Abdullah, A. Omar, and A. Halim. „Long Term Wellbore Isolation in Corrosive Environments“. *SPE Heavy Oil Conference - Canada, 2013* June (2013), pp. 1–14 (cit. on p. 30).

[107]V. Barlet-Gouédard, S. James, B. Drochon, B. Piot, and C. Jean-Philippe. *Cement composition for carbon dioxide supercritical enviroment*. 2012 (cit. on p. 30).

[108]Y. Yang, B. Yuan, Y. Wang, S. Zhang, and L. Zhu. „Carbonation resistance cement for CO2 storage and injection wells“. *Journal of Petroleum Science and Engineering* 146 (2016), pp. 883–889 (cit. on p. 30).

[109]H. Charreau, M. L. Foresti, and A. Vazquez. „Nanocellulose Patents Trends: A Comprehensive Review on Patents on Cellulose Nanocrystals, Microfibrillated and Bacterial Cellulose“. *Recent Patents on Nanotechnology* 7.1 (2012), pp. 56–80 (cit. on pp. 30, 34).

[110]O. A. Hisseine, W. Wilson, L. Sorelli, B. Tolnai, and A. Tagnit-Hamou. „Nanocellulose for improved concrete performance: A macro-to-micro investigation for disclosing the effects of cellulose filaments on strength of cement systems“. *Construction and Building Materials* 206 (2019), pp. 84–96 (cit. on pp. 30, 32, 58, 59, 65–67, 84).

[111]O. A. Hisseine, A. F. Omran, and A. Tagnit-Hamou. „Influence of cellulose filaments on cement paste and concrete“. *Journal of Materials in Civil Engineering* 30.6 (2018), pp. 1–14 (cit. on pp. 30, 32, 66, 97, 103).

[112]X. Sun, Q. Wu, S. Lee, Y. Qing, and Y. Wu. „Cellulose Nanofibers as a Modifier for Rheology, Curing and Mechanical Performance of Oil Well Cement“. *Scientific Reports* 6 (2016), pp. 1–9 (cit. on pp. 31, 45, 53, 59, 64, 65).

[113]J. N. de Paula, J. M. Calixto, L. O. Ladeira, P. Ludvig, T. C. C. Souza, J. M. Rocha, and A. A. de Melo. „Mechanical and rheological behavior of oil-well cement slurries produced with clinker containing carbon nanotubes“. *Journal of Petroleum Science and Engineering* 122 (2014), pp. 274–279 (cit. on p. 31).

[114]C. Gómez Hoyos, E. Cristia, and A. Vázquez. „Effect of cellulose microcrystalline particles on properties of cement based composites“. *Materials and Design* 51 (2013), pp. 810–818 (cit. on pp. 31, 52, 65).

[115]R. Mejdoub, H. Hammi, J. J. Suñol, M. Khitouni, and S. Boufi. „Nanofibrillated cellulose as nanoreinforcement in Portland cement : Thermal , mechanical and microstructural properties“. *Journal of Composite Materials* 51.17 (2017), pp. 2491–2503 (cit. on pp. 31, 32, 58).

[116]H. Savastano, P. G. Warden, and R. S. Coutts. „Microstructure and mechanical properties of waste fibre-cement composites“. *Cement and Concrete Composites*. Vol. 27. 5. 2005, pp. 583–592 (cit. on p. 31).

[117]X. Sun, Q. Wu, J. Zhang, Y. Qing, Y. Wu, and S. Lee. „Rheology, curing temperature and mechanical performance of oil well cement: Combined effect of cellulose nanofibers and graphene nano-platelets“. *Materials and Design* 114 (2017), pp. 92–101 (cit. on pp. 31, 84).

[118]F. Mohammadkazemi, K. Doosthoseini, E. Ganjian, and M. Azin. „Manufacturing of bacterial nano-cellulose reinforced fiber-cement composites“. *Construction and Building Materials* 101 (2015), pp. 958–964 (cit. on p. 31).

[119]F. Mohammadkazemi, R. Aguiar, and N. Cordeiro. „Improvement of bagasse fiber–cement composites by addition of bacterial nanocellulose: an inverse gas chromatography study“. *Cellulose* 24.4 (2017), pp. 1803–1814 (cit. on pp. 31, 66).

[120]J. Ramasamy and M. Amanullah. „Nanocellulose for oil and gas field drilling and cementing applications“. *Journal of Petroleum Science and Engineering* 184.July 2019 (2020) (cit. on p. 31).

[121]M. A. Akhlaghi, R. Bagherpour, and H. Kalhori. „Application of bacterial nanocellulose fibers as reinforcement in cement composites“. *Construction and Building Materials* 241 (2020), p. 118061 (cit. on pp. 31, 84).

[122]M. S. El-Feky, P. Youssef, A. M. El-Tair, S. Ibrahim, and M. Serag. „Effect of nano silica addition on enhancing the performance of cement composites reinforced with nano cellulose fibers“. *AIMS Materials Science* 6.6 (2019), pp. 864–883 (cit. on p. 31).

[123]A. Vázquez and T. M. Pique. „Biobased Additives in Oilwell Cement“. *Industrial Applications of Renewable Biomass Products. Past, Present and Future*. 2017, pp. 179–198 (cit. on p. 32).

[124]M. Panchuk, L. Shlapak, A. Panchuk, M. Szkodo, and W. Kiełczy. „Perspectives of use of nanocellulose in oil and gas industry“. *Journal of Hydrocarbon Power Engineering* 3.2 (2016), pp. 79–84 (cit. on p. 32).

[125]O. A. Hisseine, N. Basic, A. F. Omran, and A. Tagnit-Hamou. „Feasibility of using cellulose filaments as a viscosity modifying agent in self-consolidating concrete“. *Cement and Concrete Composites* 94.September (2018), pp. 327–340 (cit. on p. 32).

[126]C. G. Hoyos, R. Zuluaga, P. Gañán, T. M. Pique, and A. Vazquez. „Cellulose nanofibrils extracted from fique fibers as bio-based cement additive“. *Journal of Cleaner Production* 235 (2019), pp. 1540–1548 (cit. on pp. 32, 52, 53, 55).

[127]V. A. Barbash, O. V. Yaschenko, S. V. Alushkin, A. S. Kondratyuk, O. Y. Posudievsky, and V. G. Koshechko. „The Effect of Mechanochemical Treatment of the Cellulose on Characteristics of Nanocellulose Films“. *Nanoscale Research Letters* 11.1 (2016), pp. 16–23 (cit. on pp. 34, 66).

[128]F. Puertas, H. Santos, M. Palacios, and S. Martínez Ramos. „Polycarboxylate superplasticiser admixtures: effect on hydration, microstructure and rheological behaviour in cement pastes“. *Advances in Cement Research* 17.2 (2005), pp. 77–89 (cit. on p. 35).

[129]C. García. „Caracterización térmica y mecánica de polibutilentereftalato (PBT)“. PhD thesis. Universidad Politécnica de Cartagena, 2012, p. 100 (cit. on p. 38).

[130]M. Jawaid, H. P. S. A. Khalil, A. Hassan, R. Dungani, and A. Hadiyane. „Composites : Part B Effect of jute fibre loading on tensile and dynamic mechanical properties of oil palm epoxy composites“. *Composites Part B* 45.1 (2015), pp. 619–624 (cit. on p. 38).

[131]N. Saba and P. M. Tahir. „A Review on Dynamic mechanical analysis of natural fibre reinforced polymer composites“. *Construction and Building Materials* 106 (2016), pp. 149–159. arXiv: 9809069v1 [arXiv:gr-qc] (cit. on p. 38).

[132]ASTM International. „ASTM C109: Standard Test Method for Compressive Strength of Hydraulic Cement Mortars“. *American Society for Testing and Materials.* 04.May (1999), pp. 1–6 (cit. on p. 40).

[133]M. T. Palou, F. Šoukal, M. Boháč, P. Šiler, T. Ifka, and V. Živica. „Performance of G-Oil Well cement exposed to elevated hydrothermal curing conditions“. *Journal of Thermal Analysis and Calorimetry* 118.2 (2014), pp. 865–874 (cit. on pp. 45, 64).

[134]I. Pane and W. Hansen. „Investigation of blended cement hydration by isothermal calorimetry and thermal analysis“. *Cement and Concrete Research* 35.6 (2005), pp. 1155–1164 (cit. on p. 46).

[135]S. Diamond. „Pore Size Distributions in Clays“. *Clays and Clay Minerals* 18.1 (1970), pp. 7–23 (cit. on pp. 46, 112).

[136]P. Delage, D. Tessier, and M. Marcel-Audiguier. „Use of the Cryoscan apparatus for observation of freeze-fractured planes of a sensitive Quebec clay in scanning electron microscopy“. *Canadian Geotechnical Journal* 19.1 (1982), pp. 111–114 (cit. on p. 47).

[137]M. B. Pinson, E. Masoero, P. A. Bonnaud, H. Manzano, Q. Ji, S. Yip, J. J. Thomas, M. Z. Bazant, K. J. Van Vliet, and H. M. Jennings. „Hysteresis from multiscale porosity: Modeling water sorption and shrinkage in cement paste“. *Physical Review Applied* 3.6 (2015), pp. 1–17 (cit. on pp. 48, 66).

[138]C. Gallé. „Effect of drying on cement-based materials pore structure as identified by mercury intrusion porosimetry - A comparative study between oven-, vacuum-, and freeze-drying“. *Cement and Concrete Research* 31.10 (2001), pp. 1467–1477 (cit. on p. 48).

[139]D. Moore and R. Reynolds. *X-Ray Diffraction and the Identification and Analysis of Clay Minerals*. 1989, p. 371 (cit. on p. 49).

[140]P. E. Biscaye. „Geological Society of America Bulletin Mineralogy and Sedimentation of Recent Deep-Sea Clay in the Atlantic Ocean and Adjacent Seas and Oceans“. *Geological Society American Bulletim* 76.7 (1965), pp. 803–832 (cit. on p. 49).

[141]A. Bonett and D. Pafitis. „Getting to the root of gas migration“. *Oilfield Review* 8.1 (1996), pp. 36–49 (cit. on p. 51).

[142]S. Salehi, M. Khattak, N. Ali, and H. Rizvi. „Laboratory Investigation of High Performance Geopolymer Based Slurries AADE-16-FTCE-88“. *American Association of Drilling Engineers* April (2016) (cit. on p. 51).

[143]M. Moumin and J. Plank. „Effectiveness of Polycarboxylate Dispersants in Enhancing the Fluid Loss Performance of Cellulose Ethers“. *SPE International Conference on Oilfield Chemistry* (2017) (cit. on p. 51).

[144]A. Balea, E. Fuente, A. Blanco, and C. Negro. „Nanocelluloses: Natural-based materials for fiber- reinforced cement composites. A critical review“. *Polymers* 11.3 (2019) (cit. on pp. 52, 59, 66).

[145]G. Abbas, S. Irawan, S. Kumar, and A. A. Elrayah. „Improving Oil well Cement Slurry Performance Using Hydroxypropylmethylcellulose Polymer“. *Advanced Materials Research* 787 (2013), pp. 222–227 (cit. on p. 53).

[146]Z. Li, K. Ahadi, K. Jiang, B. Ahvazi, P. Li, A. O. Anyia, K. Cadien, and T. Thundat. „Free-standing hierarchical porous carbon film derived from hybrid nanocellulose for high-power supercapacitors“. *Nano Research* 10.5 (2017), pp. 1847–1860 (cit. on p. 53).

[147]P. J. Sereda, R. F. Feldman, and E. G. Swenson. „Effect of sorbed water on some mechanical properties of hydrated Portland cement pastes and compacts“. *Highway Research Board . . .* 90 (1966), pp. 58–73 (cit. on p. 55).

[148]R. H. Evans and M. S. Marathe. „Microcracking and stress-strain curves for concrete in tension“. *Matériaux et Constructions* 1.1 (1968), pp. 61–64 (cit. on p. 55).

[149]G. Foray-thevenin, G. Vigier, R. Vassoille, and G. Orange. „Characterization of cement paste by dynamic mechanical Part I : operative conditions“. 56 (2006), pp. 129–137 (cit. on p. 55).

[150]R. Alizadeh, J. J. Beaudoin, and L. Raki. „Mechanical properties of calcium silicate hydrates“. *Materials and Structures/Materiaux et Constructions* 44.1 (2011), pp. 13–28 (cit. on pp. 55, 56).

[151]F. Radjy and C. W. Richards. „Effect of curing and heat treatment history on the dynamic mechanical response and the pore structure of hardened cement paste“. *Cement and Concrete Research* 3.1 (1973), pp. 7–21 (cit. on p. 55).

[152]P. Pourbeik, R. Alizadeh, J. J. Beaudoin, D. T. Nguyen, and L. Raki. „Microindentation creep of 45 year old hydrated Portland cement paste“. *Advances in Cement Research* 25.5 (2013), pp. 301–306 (cit. on p. 57).

[153]M. Jamshidi and M. Karimi. „Characterization of Polymeric Fibers as Reinforcements of Cement-Based Composites“. *Journal of Applied Polymer Science* 115.5 (2009), pp. 2779–2785 (cit. on p. 57).

[154]S. Parveen, S. Rana, R. Fangueiro, and M. Conceiç. „A novel approach of developing micro crystalline cellulose reinforced cementitious composites with enhanced microstructure and mechanical performance“. *Cement and Concrete Composites* 78 (2017) (cit. on p. 57).

[155]C. Xiaofeng, G. Shanglong, D. Darwin, and S. L. McCabe. „Role of silica fume in compressive strength of cement paste, mortar, and concrete“. *ACI Materials Journal* 89.4 (1990), pp. 375–387 (cit. on p. 58).

[156]H. J. Lee, S. K. Kim, H. S. Lee, and W. Kim. „A Study on the Drying Shrinkage and Mechanical Properties of Fiber Reinforced Cement Composites Using Cellulose Nanocrystals“. *International Journal of Concrete Structures and Materials* 13.1 (2019) (cit. on pp. 58, 59, 66, 97).

[157]Y. Cao, P. Zavaterri, J. Youngblood, R. Moon, and J. Weiss. „The influence of cellulose nanocrystal additions on the performance of cement paste“. *Cement and Concrete Composites* 56 (2015), pp. 73–83 (cit. on pp. 58, 66).

[158]A. W. Skempton. „The pore-pressure coefficients a and b“. *Geotechnique* 4.4 (1954), pp. 143–147 (cit. on p. 60).

[159]R. L. Day and B. K. Marsh. „Measurement of porosity in blended cement pastes“. *Cement and Concrete Research* 18.1 (1988), pp. 63–73 (cit. on p. 64).

[160]S. Wild and J. M. Khatib. „Portlandite consumption in metakaolin cement pastes and mortars“. *Cement and Concrete Research* 27.1 (1997), pp. 137–146 (cit. on p. 64).

[161]M. J. DeJong and F. J. Ulm. „The nanogranular behavior of C-S-H at elevated temperatures (up to 700 °C)“. *Cement and Concrete Research* 37.1 (2007), pp. 1–12 (cit. on p. 64).

[162]K. De Weerdt, M. B. Haha, G. Le Saout, K. O. Kjellsen, H. Justnes, and B. Lothenbach. „Hydration mechanisms of ternary Portland cements containing limestone powder and fly ash“. *Cement and Concrete Research* 41.3 (2011), pp. 279–291 (cit. on p. 64).

[163]K. Tuutti. „Corrosion of Steel in Concrete“. *Swedish Cement and Concrete Research Institute* 0346-6906 CBI forskning/research (1982), p. 469 (cit. on p. 64).

[164]L. Liu, J. Ha, T. Hashida, and S. Teramura. „Development of a CO2solidification method for recycling autoclaved lightweight concrete waste“. *Journal of Materials Science Letters* 20.19 (2001), pp. 1791–1794. eprint: 0005074v1 (arXiv:astro-ph) (cit. on p. 64).

[165]B. Ma, Z. Ou, S. Jian, and R. Xu. „Influence of cellulose ethers on hydration products of portland cement“. *Journal Wuhan University of Technology, Materials Science Edition* 26.3 (2011), pp. 588–593 (cit. on p. 64).

[166]Y. Cao, N. Tian, D. Bahr, P. D. Zavattieri, J. Youngblood, R. J. Moon, and J. Weiss. „The influence of cellulose nanocrystals on the microstructure of cement paste“. *Cement and Concrete Composites* 74 (2016), pp. 164–173 (cit. on pp. 66, 97).

[167]T. Fu, F. Montes, P. Suraneni, J. Youngblood, and J. Weiss. „The influence of cellulose nanocrystals on the hydration and flexural strength of Portland cement pastes“. *Polymers* 9.9 (2017) (cit. on pp. 66, 97).

[168]I. Gaus, P. Audigane, L. André, J. Lions, N. Jacquemet, P. Durst, I. Czernichowski-Lauriol, and M. Azaroual. „Geochemical and solute transport modelling for CO2 storage, what to expect from it?“ *International Journal of Greenhouse Gas Control* 2.4 (2008), pp. 605–625 (cit. on p. 66).

[169]G. Chauve and J. Bras. „Industrial Point of View of Nanocellulose Materials and Their Possible Applications“ (2014), pp. 233–252 (cit. on p. 66).

[170]M. R. Dousti, Y. Boluk, and V. Bindiganavile. „The effect of cellulose nanocrystal (CNC) particles on the porosity and strength development in oil well cement paste“. *Construction and Building Materials* 205 (2019), pp. 456–462 (cit. on p. 66).

[171]Y. Cao, P. Zavaterri, J. Youngblood, R. Moon, and J. Weiss. „The influence of cellulose nanocrystal additions on the performance of cement paste“. *Cement and Concrete Composites* (2014) (cit. on pp. 66, 97, 103).

[172]J. J. Thomas, H. M. Jennings, and A. J. Allen. „Relationships between composition and density of tobermorite jennite CSH“. *Journal of Physical Chemistry C* 114 (2010), pp. 7594–7601 (cit. on p. 69).

[173]J. W. Carey. „Geochemistry of Wellbore Integrity in CO2 Sequestration: Portland Cement-Steel-Brine-CO2 Interactions“. *Reviews in Mineralogy and Geochemistry* 77.1 (2013), pp. 505–539 (cit. on p. 70).

[174]Z. Duan and R. Sun. „An improved model calculating CO2 solubility in pure water and aqueous NaCl solutions from 273 to 533 K and from 0 to 2000 bar“. *Chemical Geology* 193.3-4 (2003), pp. 257–271 (cit. on p. 70).

[175]M. Mainguy. „Modeles de diffusion non-lineaires en milieux poreux. Applications a la dissolution et au sechage des materiaux cimentaires“. PhD thesis. 1999 (cit. on pp. 70, 84, 120, 134, 135).

[176]S. Ghabezloo, J. Sulem, and J. Saint-Marc. „Evaluation of a permeability-porosity relationship in a low-permeability creeping material using a single transient test“. *International Journal of Rock Mechanics and Mining Sciences* 46.4 (2009), pp. 761–768 (cit. on pp. 70, 119, 134, 135).

[177]A. Duguid. „Degradation of Well Cements Exposed to Carbonated Brine“. *Fourth Annual Conference on Carbon Capture and Sequestration Doe/Netl* May (2005), pp. 1–12 (cit. on p. 70).

[178]A. Sauki, M. H. Md. Shahid, K. H. Ku Hamid, A. Azizi, S. K. Jamaludin, T. A. Tengku Mohd, and N. H. Alias. „Utilization of Agarwood Distillation Waste in Oilwell Cement and Its Effect on Free Water and Porosity“. *International Journal of Science and Engineering* 5.2 (2013), pp. 61–65 (cit. on p. 70).

[179]T. Gu, X. Guo, Z. Li, X. Cheng, X. Fan, A. Korayem, and W. H. Duan. „Coupled effect of CO2 attack and tensile stress on well cement under CO2 storage conditions“. *Construction and Building Materials* 130 (2017), pp. 92–102 (cit. on pp. 70, 95, 104).

[180]B. Wu and G. Ye. „Development of porosity of cement paste blended with supplementary cementitious materials after carbonation“. *Construction and Building Materials* 145 (2017), pp. 52–61 (cit. on p. 74).

[181]D. Manzanal, V. Vallin, and J. M. Pereira. „A chemo-poromechanical model for well/caprock interface in presence of CO2“. *Poromechanics V - Proceedings of the 5th Biot Conference on Poromechanics* (2013), pp. 1470–1477 (cit. on p. 74).

[182]K. Haga, S. Sutou, M. Hironaga, S. Tanaka, and S. Nagasaki. „Effects of porosity on leaching of Ca from hardened ordinary Portland cement paste“. *Cement and Concrete Research* 35.9 (2005), pp. 1764–1775 (cit. on p. 74).

[183]M. Alexander, A. Bertron, and N. D. Belie. *Performance of Cement-Based Materials in Aggressive Aqueous Environments*. Vol. 10. 2013, p. 462 (cit. on p. 74).

[184]A. Morandeau, M. Thiéry, and P. Dangla. „Impact of accelerated carbonation on OPC cement paste blended with fly ash“. *Cement and Concrete Research* 67 (2015), pp. 226–236 (cit. on pp. 75, 80, 104).

[185]M. Bongué Boma and A. Alaoui. „A constitutive model for micro-cracked bodies with growing inclusions“. *Continuum Mechanics and Thermodynamics* 24.1 (2012), pp. 49–61 (cit. on p. 77).

[186]A. Sauki and S. Irawan. „Effects of Pressure and Temperature on Well Cement Degradation by Supercritical CO2“. *International Journal of Engineering & Technology IJET-IJENS* 10.4 (2010), pp. 53–61 (cit. on pp. 82, 104).

[187]B. Xu, B. Yuan, Y. Wang, S. Zeng, and Y. Yang. „Nanosilica-latex reduction carbonation-induced degradation in cement of CO2 geological storage wells“. *Journal of Natural Gas Science and Engineering* 65.February (2019), pp. 237–247 (cit. on pp. 82, 85, 104).

[188]W. Ashraf. „Carbonation of cement-based materials: Challenges and opportunities“. *Construction and Building Materials* 120 (2016), pp. 558–570 (cit. on p. 82).

[189]O. Omosebi, H. Maheshwari, R. Ahmed, S. Shah, S. Osisanya, A. Santra, and A. Saasen. „Investigating temperature effect on degradation of well cement in HPHT carbonic acid environment“. *Journal of Natural Gas Science and Engineering* 26 (2015), pp. 1344–1362 (cit. on p. 82).

[190]C. Carde and R. François. „Modelling the loss of strength and porosity increase due to the leaching of cement pastes“. *Cement and Concrete Composites* 21.3 (1999), pp. 181–188 (cit. on p. 82).

[191]E. Stora, B. Bary, Q. C. He, E. Deville, and P. Montarnal. „Modelling and simulations of the chemo-mechanical behaviour of leached cement-based materials: Interactions between damage and leaching“. *Cement and Concrete Research* 40.8 (2010), pp. 1226–1236 (cit. on p. 82).

[192]A. Hidalgo, C. Domingo, C. Garcia, S. Petit, C. Andrade, and C. Alonso. „Microstructural changes induced in Portland cement-based materials due to natural and supercritical carbonation“. *Journal of Materials Science* 43.9 (2008), pp. 3101–3111 (cit. on p. 82).

[193]A. Fabbri, N. Jacquemet, and D. M. Seyedi. „A chemo-poromechanical model of oilwell cement carbonation under CO 2 geological storage conditions“. *Cement and Concrete Research* 42.1 (2012), pp. 8–19 (cit. on p. 82).

[194]D. Manzanal and J. M. Pereira. „Effects of the presence of CO2 at the well/caprock interface: Crystallization damage“. *Proceedings of the International Conference on Offshore Mechanics and Arctic Engineering - OMAE*. Vol. 6. 2013, pp. 1–7 (cit. on pp. 82, 118).

[195]L. Black, C. Breen, J. Yarwood, C.-S. Deng, J. Phipps, and G. Maitland. „Hydration of tricalcium aluminate (C3A) in the presence and absence of gypsum—studied by Raman spectroscopy and X-ray diffraction“. *J. Mater. Chem.* 16 (13 2006), pp. 1263–1272 (cit. on p. 89).

[196]P. Lalan, A. Dauzères, L. D. Windt, D. Bartier, J. Sammaljärvi, J.-d. Barnichon, I. Techer, and V. Detilleux. „Impact of a 70 °C temperature on an ordinary Portland cement paste/claystone interface: An in situ experiment“. *Cement and Concrete Research* 83 (2016), pp. 164–178 (cit. on p. 89).

[197]R. Melzer and E. Eberhard. „Phase identification during early and middle hydration of tricalciumsilicate (Ca3SiO5)“. *Cement and Concrete Research* 19.c (1989), pp. 411–422 (cit. on p. 90).

[198]G. Álvarez-Pinazo, I. Santacruz, L. León-Reina, M. A. Aranda, and A. G. De La Torre. „Hydration reactions and mechanical strength developments of iron-rich sulfobelite eco-cements“. *Industrial and Engineering Chemistry Research* 52.47 (2013), pp. 16606–16614 (cit. on p. 90).

[199]I. Yurtdas, S. Y. Xie, N. Burlion, J. F. Shao, J. Saint-Marc, and A. Garnier. „Influence of chemical degradation on mechanical behavior of a petroleum cement paste“. *Cement and Concrete Research* 41.4 (2011), pp. 412–421 (cit. on p. 95).

[200]S. Steiner, B. Lothenbach, T. Proske, A. Borgschulte, and F. Winnefeld. „Effect of relative humidity on the carbonation rate of portlandite, calcium silicate hydrates and ettringite“. *Cement and Concrete Research* 135.January (2020), p. 106116 (cit. on p. 100).

[201]F. Khaddour, D. Grégoire, and G. Pijaudier-Cabot. „A Hierarchical Model for the Computation of Permeation Properties of Porous Materials and Their Enhancement due to Microcracks“. *Journal of Engineering Mechanics* 144.2 (2018), p. 04017160 (cit. on p. 113).

[202]L. Ecay, D. Grégoire, and G. Pijaudier-Cabot. „On the prediction of permeability and relative permeability from pore size distributions“. *Cement and Concrete Research* 133.March (2020), p. 106074 (cit. on p. 113).

[203]T. C. Hansen. „Physical Structure of Hardened Cement Paste“. *Materials and Structures* 19.6 (1986), pp. 423–436 (cit. on p. 115).

[204]M. Boumaaza, P. Turcry, B. Huet, and A. Aït-Mokhtar. „Influence of carbonation on the microstructure and the gas diffusivity of hardened cement pastes“. *Construction and Building Materials* 253 (2020), p. 119227 (cit. on p. 117).

[205]V. Vallin, J. M. Pereira, A. Fabbri, and H. Wong. „Numerical modelling of the hydro-chemo-mechanical behaviour of geomaterials in the context of CO 2 injection“. April (2013), pp. 3052–3069 (cit. on pp. 117, 118, 120, 134, 135).

[206]P. Dangla and A. Bonnard. *Ifsttar/bil: first version in github (Version v2.4)*. *Zenodo*. 2017 (cit. on p. 117).

[207]V. Vallin. „Modélisation chimio poromécanique du comportement des géomatériaux dans le contexte du stockage géologique du dioxyde de carbone : Application au puits d'injection“. PhD thesis. Université Paris-Est, 2014, p. 144 (cit. on pp. 117, 121, 122).

[208]O. Coussy. *Mechanics and Physics of Porous Solids*. 2010 (cit. on p. 119).

[209]F. J. Ulm, G. Constantinides, and F. H. Heukamp. „Is concrete a poromechanics material? - A multiscale investigation of poroelastic properties“. *Materials and Structures/Materiaux et Constructions* 37.265 (2004), pp. 43–58 (cit. on p. 120).

[210]L. Kachanov. „Introduction to Continuum Damage Mechanics“ (1971), p. 132 (cit. on p. 121).

[211]G. Villain, M. Thiery, and G. Platret. „Measurement methods of carbonation profiles in concrete: Thermogravimetry, chemical analysis and gammadensimetry“. *Cement and Concrete Research* 37.8 (2007), pp. 1182–1192 (cit. on p. 122).

[212]J. Shen. „Reactive transport modeling of CO2 through cementitious materials under CO2 geological storage conditions“. PhD thesis. Unieversité Paris–Est, 2013, p. 152 (cit. on p. 123).

[213]W. Mook. „Química Del ácido Carbónico Del Agua“. *Isótopos Ambientales en el Ciclo Hidrológico* (2002), pp. 101–111 (cit. on p. 123).

[214]Y. C. Hsieh, H. Yano, M. Nogi, and S. J. Eichhorn. „An estimation of the Young's modulus of bacterial cellulose filaments“. *Cellulose* 15.4 (2008), pp. 507–513 (cit. on p. 128).

[215]K. Y. Lee and A. Bismarck. *Bacterial NanoCellulose as Reinforcement for Polymer Matrices*. Elsevier B.V., 2016, pp. 109–122 (cit. on p. 128).

[216]Q. Wang, Q. Yao, J. Liu, J. Sun, Q. Zhu, and H. Chen. *Processing nanocellulose to bulk materials: a review*. Vol. 26. 13-14. Springer Netherlands, 2019, pp. 7585–7617 (cit. on p. 128).

[217]V. Ershadi, E. Ebadi, A. R. Rabani, L. Ershadi, and H. Soltanian. „Reduction of set cement permeability in oil well to decrease the pollution of receptive environment using spherical nanosilica“. *2nd International Conference on Environmental Science and Technology*. Vol. 6. 2. 2011, pp. 101–104 (cit. on p. 134).

[218]K. J. Krakowiak, J. J. Thomas, S. Musso, S. James, A.-t. Akono, and F.-j. Ulm. „Nano-chemo-mechanical signature of conventional oil-well cement systems : Effects of elevated temperature and curing time“. *Cement and Concrete Research* 67 (2015), pp. 103–121 (cit. on p. 134).

[219]A. Neves, J. Romildo, D. Toledo, and F. Jo. „A study of CO2 capture by high initial strength Portland cement pastes at early curing stages by new non-conventional thermogravimetry and non-conventional differential thermal analysis“. *Journal of Thermal Analysis and Calorimetry* (2017) (cit. on p. 134).

[220]J. Sercombe and C. Galle. „Rehydration and microstructure of cement paste after heating at temperatures up to 300 ° C“. 33 (2003), pp. 1047–1056 (cit. on pp. 134, 135).

[221]S. Ghabezloo. „Cement and Concrete Research Effect of the variations of clinker composition on the poroelastic properties of hardened class G cement paste“. *Cement and Concrete Research* 41.8 (2011), pp. 920–922 (cit. on p. 134).

[222]B. Huet, V. Tasoti, and I. Khalfallah. „A review of Portland cement carbonation mechanisms in CO2 rich environment“. *Energy Procedia* 4 (2011), pp. 5275–5282 (cit. on p. 135).

[223]J. Shen, P. Dangla, and M. Thiery. „Reactive transport modeling of CO2 through cementitious materials under CO2 geological storage conditions“. *International Journal of Greenhouse Gas Control* 18 (2013), pp. 75–87 (cit. on p. 135).

Publications and participation in conferences

Journal papers

- Barría, J.C.; Manzanal, D.; Cerrutti, P.; Pereira, J. (2021). Cement with bacterial nanocellulose cured at reservoir temperature: Mechanical performance in the context of CO_2 geological storage. Geomechanics for Energy and the Environment. https://doi.org/10.1016/j.gete.2021.100267
- Barría, J.C.; Vázquez, A., Pereira, J.; Manzanal, D., (2021). Effect of bacterial nanocellulose on the fresh and hardened states of oil well cement. J. Pet. Sci. Eng. 199. https://doi.org/10.1016/j.petrol.2020.108259.
- Barría, J.C.; Bagheri, M; Manzanal, D.; Shariatipour, S.; Pereira, J. (2021). Poromechanical analysis of oil well cements in CO_2-rich environments. International Journal of Greenhouse Gas Control (Under review).
- Barría, J.C.; Manzanal, D.; Ghabezloo, S.; Pereira, J.M. (2021). Effect of supercritical carbonation on porous structure and mechanical strength of cementitious materials modified with bacterial nanocellulose. Materials and structures. (Under review).

Conference papers

- Barría, J.C.; Manzanal, D.; Guerreiro R.; Pereira, J.M.; Orlandi, S. (2022). Mechanical properties of cement under supercritical carbonation. 20th International Conference on Soil Mechanics and Geotechnical Engineering. Sydney, Australia. May 1-6, 2022.
- Barría, J.C.; Manzanal, D.; Ghabezloo, S.; Pereira, J.M. (2022). Triaxial tests on carbonated cement samples in the context of carbon capture and storage. 7th International Young Geotechnical Engineers Conference. Sydney, Australia. April 29 - May 1, 2022.
- Barría, J.C.; Manzanal, D.; Guerreiro, R.; Pereira, J.; Orlandi, S. (2021). Resultados experimentales y simulaciones numéricas para el geo-almacenamiento de dióxido de carbono. Congreso Argentino de Mecánica de Suelos e Ingeniería Geotécnica. Posadas, Argentina. November 24-26, 2021.
- Vázquez, A.; Piqué, T; Barría, J.C.; Spinazzola, F.; Martín, C; Gómez Hoyos, C.; Cerrutti, P.; Manzanal, D. (2021). Uso de nanocelulosa como aditivo para la extracción de Petróleo y Gas. Congreso Argentino de Ingeniería (CADI/CLADI/CAEDI). Buenos Aires, Argentina. October 5-7, 2021.
- Barría, J.C.; Manzanal, D.; Pereira, J.; Ghabezloo, S., (2020). CO_2 geological storage: Microstructure and mechanical behavior of cement modified with a biopolymer after carbonation. 2nd International Conference on Energy Geotechnics (ICEGT 2020). La

Jolla, USA. April 10-13, 2022. E3S Web Conf. 205.
https://doi.org/10.1051/e3sconf/202020502007

- Barría, J.C.; Espelet, A; Miura, O.; Piqué, T.; Cerrutti, P.; Rodríguez, M.; Manzanal, D. (2020). Cementos modificados con biopolímeros para el geoalmacenamiento de CO_2. IX Congreso Internacional y 23° Reunión Técnica. La Plata, Buenos Aires, Argentina. November 2-6, 2020.
- Barría, J.C.; Manzanal, D.; Pereira, J. (2019) CO_2 geological storage: Performance of Cement-Rock interface. XVI Pan-American Conference on Soil Mechanics and Geotechnical Engineering. Cancún, Mexico. November 17-20, 2020.
- Barría, J.C.; Manzanal, D.; Martín, C.; Piqué, T.; Pereira, J. (2019). Cement-rock interface subjected to $SCCO_2$, in: Rock Mechanics for Natural Resources and Infrastructure Development. Proceedings of the 14th International Congress on Rock Mechanics and Rock Engineering. pp. 3196–3203. Foz do Iguassu, Brazil. September 13-18, 2019.
- Barría, J.C.; Manzanal, D.; Martín, C.; Piqué, T.; Pereira, J. (2018) Analysis of modified cement paste in the context of CO_2 geological storage. International Symposium of Energy Geotechnics SEG-2018. Pages 402-409. Lausanne, Switzerland. 25-28 September, 2018. https://doi.org/10.1007/978-3-319-99670-7. Publisher: Springer, Cham. Online ISBN 978-3-319-99670-7

Posters and oral presentations

- Barría, J.C.; Manzanal, D.; Pereira, J. (2021). Nanomaterials for CO_2 injection well technology. E-Poster Contest Award Research Conference - Enabling CO_2 Geological Storage within a Low-Carbon Economy. 2nd award. 22-24 February. Ali I. Naimi Petroleum Engineering Research Center's - Saudi Arabia.
- Barría, J.C.; Manzanal, D.; Pereira, J. (2019) Poromechanics behavior of cement modified with biopolymer under carbonation in supercritical conditions. 30th ALERT Geomaterials workshop. Poster session. September 30-October 2. Aussois, France. Pp. 48-49. ISBN 978-2-95661359-1

Appendix

A

A.1 Unconfined compressive strength (UCS)

Test	Reference	Curing days	Quantity	BNC content [%]	Strength [MPa]
1	UCS-00-01	1	3	0.00	6.9
2	UCS-05-01	1	3	0.05	6.3
3	UCS-10-01	1	3	0.10	6.1
4	UCS-15-01	1	3	0.15	6.1
5	UCS-20-01	1	3	0.20	5.9
6	UCS-00-07	7	3	0.00	32.5
7	UCS-05-07	7	3	0.05	38.4
8	UCS-10-07	7	3	0.10	38.7
9	UCS-15-07	7	3	0.15	29.3
10	UCS-20-07	7	3	0.20	33.8
11	UCS-00-28	28	3	0.00	46.4
12	UCS-05-28	28	3	0.05	53.4
13	UCS-10-28	28	3	0.10	53.0
14	UCS-15-28	28	3	0.15	54.5
15	UCS-20-28	28	3	0.20	53.5

Tab. A.1.: UCS test results on cubic specimens.

Test	Reference	Quantity	BNC [%]	Strength [MPa]	Young's modulus [GPa]
1	UCS-A-00-00	3	0.00	53.2	25.7
2	UCS-A-05-00	3	0.05	54.6	24.3
3	UCS-A-15-00	3	0.15	54.3	26.3
4	UCS-A-00-30	3	0.00	42.6	22.5
5	UCS-A-05-30	3	0.05	45.3	19.3
6	UCS-A-15-30	3	0.15	49.4	21.1
7	UCS-A-00-120	3	0.00	35.9	16.4
8	UCS-A-05-120	3	0.05	47.4	22.1
9	UCS-A-15-120	3	0.15	42.0	20.8
10	UCS-B-00-00	3	0.00	30.8 (21.3)	20.0 (23.5)
11	UCS-B-05-00	3	0.05	24.0 (19.6)	20.0 (22.3)
12	UCS-B-00-30	3	0.00	44.5 (-)	22.1 (-)
13	UCS-B-05-30	3	0.05	38.4 (-)	23.7 (-)
14	UCS-B-00-120	3	0.00	- (36.9)	- (33.6)
15	UCS-B-05-120	3	0.05	- (34.8)	- (31.3)

Tab. A.2.: UCS test results on cylindrical specimens.

A.2 Isotropic experiments

Specimen	Condition	Initial σ_3 [MPa]	Final σ_3 [MPa]	u_i [MPa]	u_f [MPa]	K [MPa]
KU-00 *	Undrained	5.00	12.00	2.00	5.00	16.60
KU-00 *		6.00	10.00	3.00	5.00	14.10
KU-00		30.00	40.00	1.00	1.10	17.00
KU-05		5.00	9.00	1.00	1.20	15.50
KU-05		11.00	21.00	3.00	4.00	15.40
KU-05		11.00	21.00	3.00	4.00	15.80
KU-05		28.00	36.00	3.20	3.50	18.00
KU-05		28.00	36.00	1.50	1.70	17.20
KU-15		27.00	36.00	3.00	3.80	18.00
KD-00	Drained	5.00	12.00	2.00	2.00	11.60
KD-00		29.00	39.00	1.00	1.00	12.50
KD-05		10.00	20.00	3.00	3.00	12.80
KD-05		10.00	27.00	3.00	3.00	12.10

Tab. A.3.: Bulk modulus values for non-carbonated specimens subjected to several confining pressures. (*) Skempton coefficient = 0.32 (**) Skempton coefficient = 0.30.

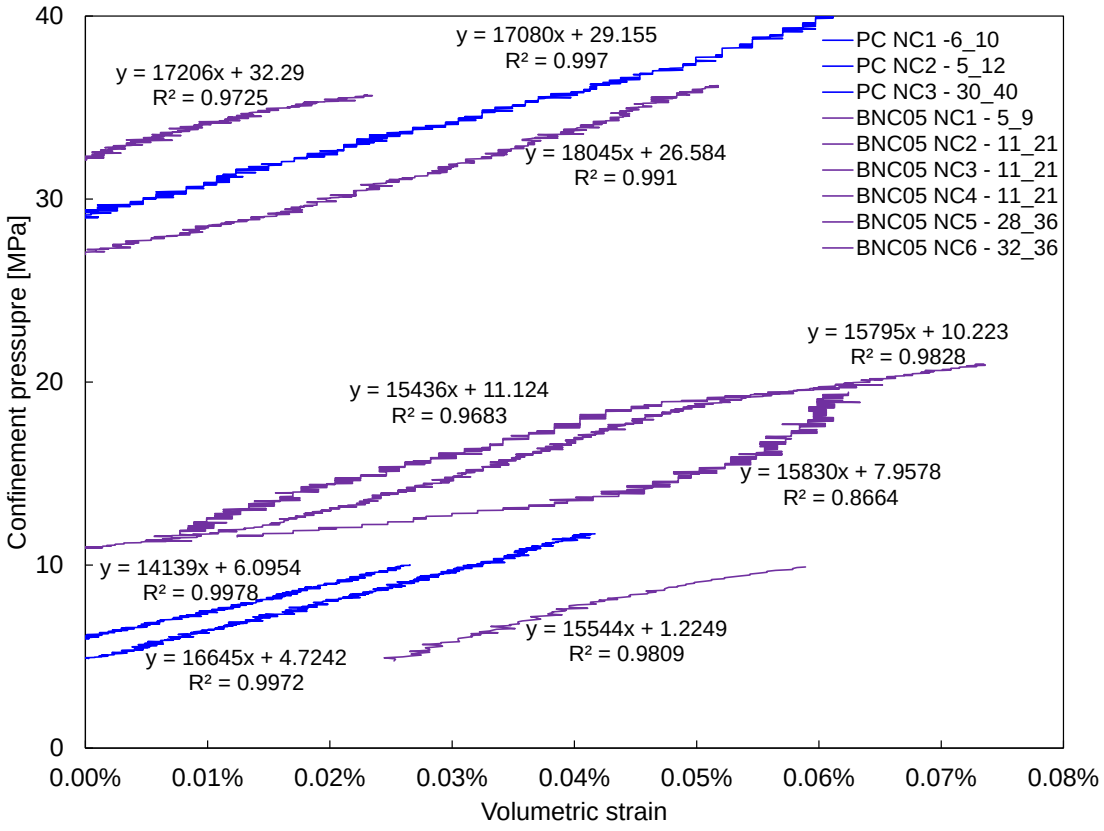

Fig. A.1.: Isotropic triaxial tests on non-carbonated specimens (undrained tests)

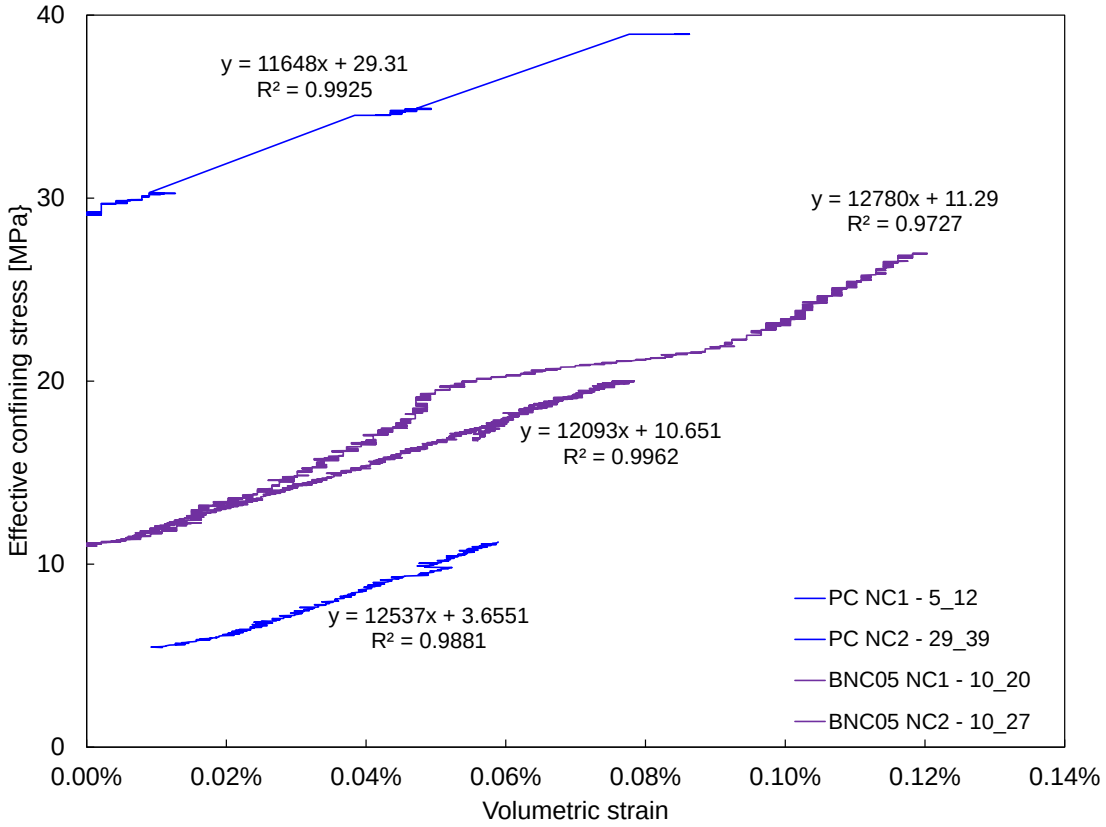

Fig. A.2.: Isotropic triaxial tests on non-carbonated specimens (drained tests)

Specimen	Condition	Initial σ_3 [MPa]	Final σ_3 [MPa]	u_i [MPa]	u_f [MPa]	K [MPa]
KU-00-30	Undrained	14.00	21.00	3.00	3.40	8.60
KU-00-30		27.00	36.00	3.00	3.90	8.70
KU-05-30*		10.00	14.00	4.00	6.3	9.00
KU-05-30**		10.00	20.00	4.00	9.50	9.70
KU-05-120		10.00	17.00	4.00	5.4	9.70
KU-05-120		10.00	17.00	4.00	5.4	9.10
KD-00-30	Drained	11.00	21.00	3.00	3.00	7.50
KD-05-30		11.00	26.00	4.00	4.00	8.40
KD-05-120		11.00	20.00	4.00	4.00	8.70
KD-05-120		11.00	20.00	4.00	4.00	9.10

Tab. A.4.: Bulk modulus values for carbonated specimens subjected to several confining pressures.(*) Skempton coefficient = 0.34 (**) Skempton coefficient = 0.35.

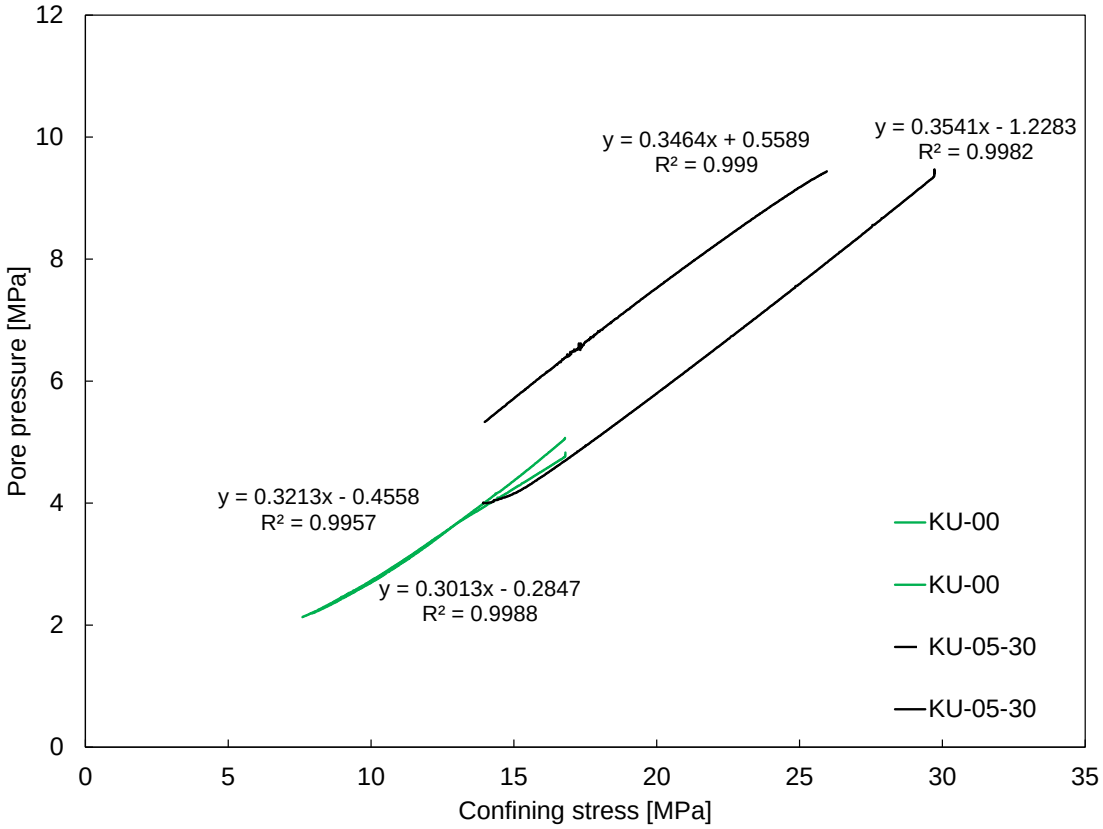

Fig. A.3.: Isotropic undrained tests. The slopes correspond to Skempton coefficient B

A.3 Triaxial experiments

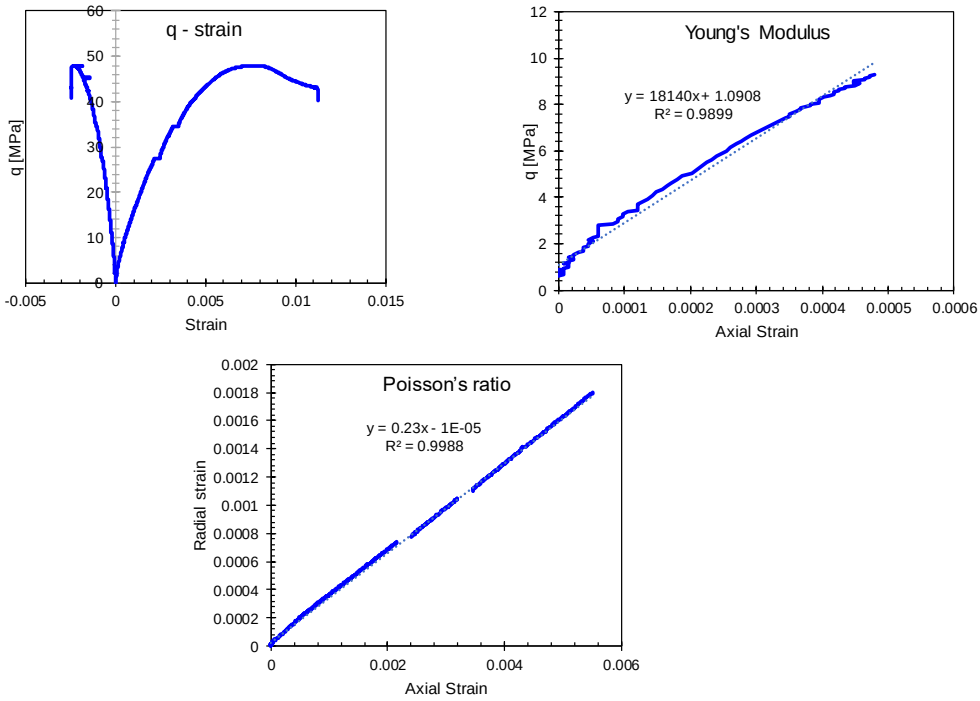

Fig. A.4.: Undrained triaxial test on DEV-00-U (σ_3 = 14 MPa)

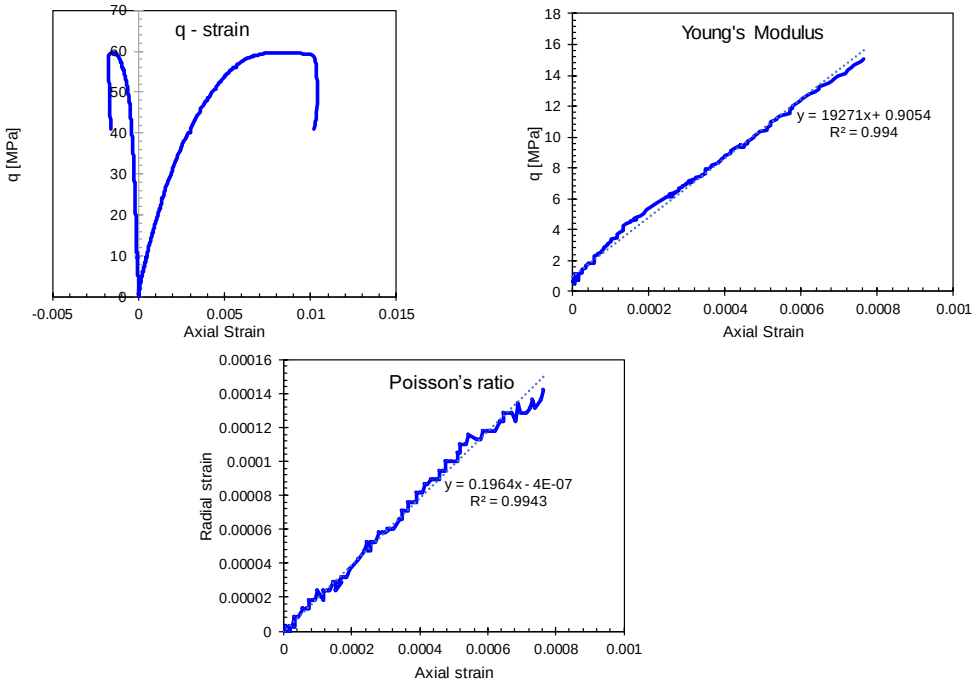

Fig. A.5.: Undrained triaxial test on DEV-00-U (σ_3 = 30 MPa)

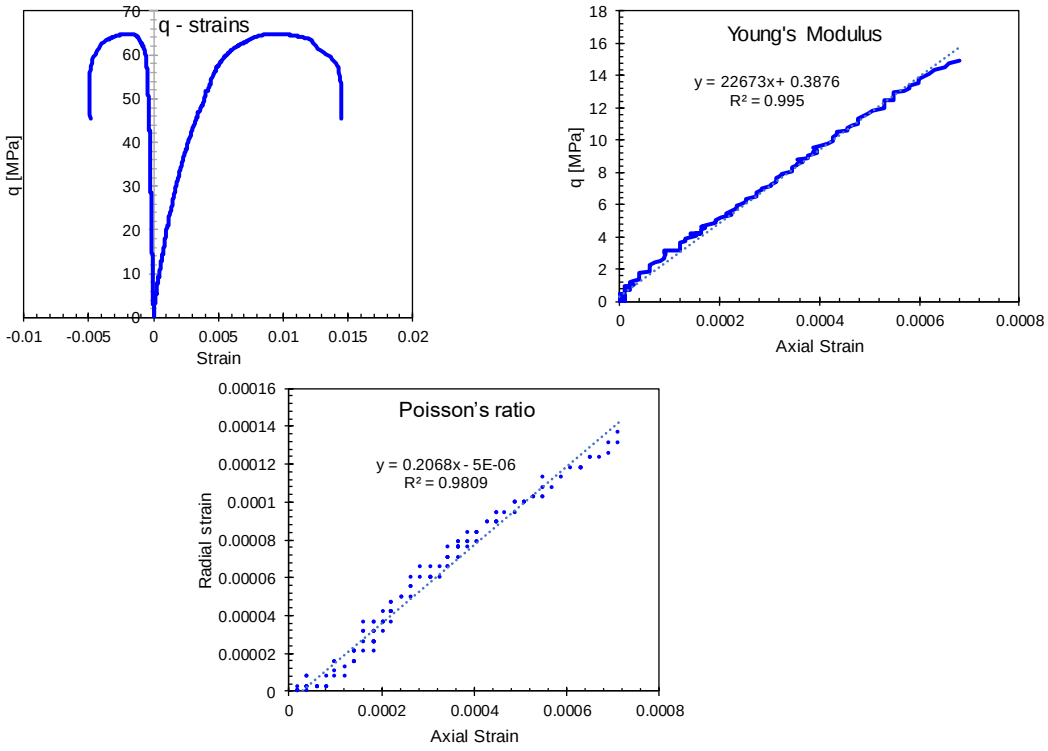

Fig. A.6.: Undrained triaxial test on DEV-05-U ($\sigma_3 = 30$ MPa)

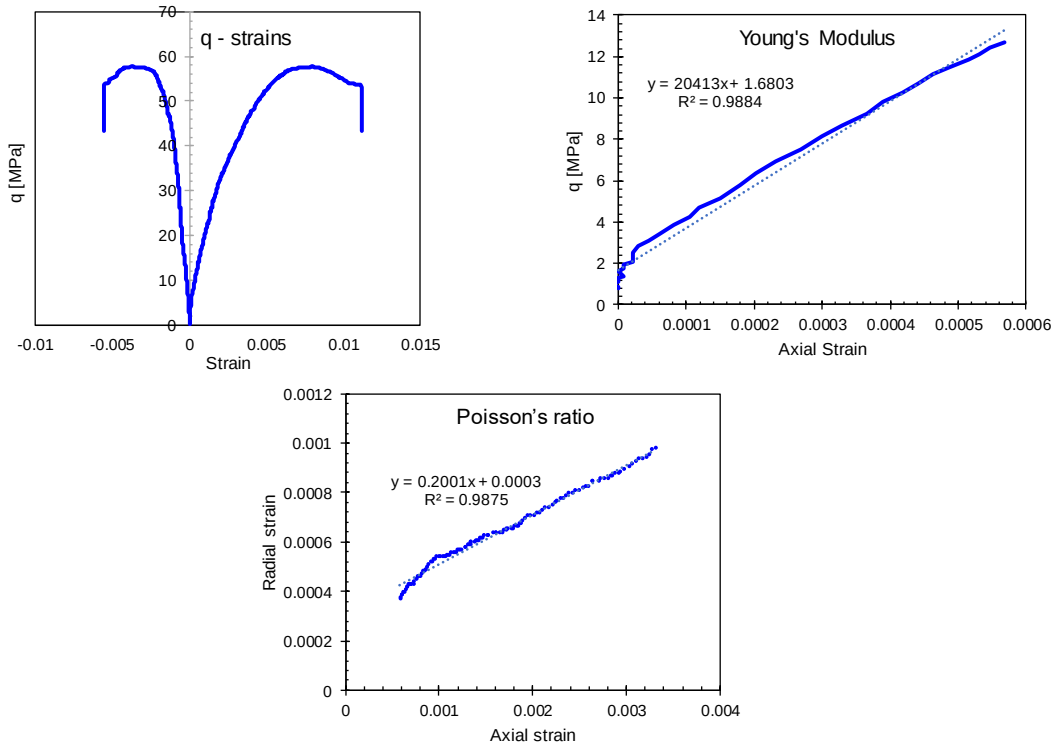

Fig. A.7.: Undrained triaxial test on DEV-15-U ($\sigma_3 = 30$ MPa)

A.4 Measurement of elastic ultrasound waves

Specimen	Height	Total height	Density [g/cm^3]	V_P [m/s]	V_S [m/s]
UWM-B-00-00	70.93	80.93	1.89	3317	2108
UWM-B-05-00	71.01	81.01	1.87	3189	2046
UWM-B-00-30	71.75	81.75	2.13	3378	2019
UWM-B-05-30	67.20	77.20	2.11	3203	2053

Tab. A.5.: Elastic ultrasound waves of cylindrical specimens after 30 days of carbonation (curing method B).

Specimen	Height	Total height	Density [g/cm^3]	V_P [m/s]	V_S [m/s]
UWM-B-00-00	72.00	82.00	1.90	3216	1767
UWM-B-00-00	71.00	81.00	1.89	3176	1767
UWM-B-00-00	71.90	81.90	1.90	3174	1773
UWM-B-00-00	71.80	81.80	1.87	3190	1770
UWM-B-00-00	72.50	82.50	1.88	3210	1774
UWM-B-00-00	72.80	82.80	1.89	3209	1769
UWM-B-05-00	72.00	82.00	1.85	3191	1723
UWM-B-05-00	73.70	83.70	1.86	3170	1740
UWM-B-05-00	72.70	82.70	1.85	3156	1752
UWM-B-05-00	73.50	83.50	1.84	3093	1740

Tab. A.6.: Elastic ultrasound waves of cylindrical specimens before 120 days of carbonation (curing method B).

Specimen	Height	Total height	Density [g/cm^3]	V_P [m/s]	V_S [m/s]
UWM-B-00-120	72.00	82.00	2.16	3374	1726
UWM-B-00-120	71.00	81.00	2.15	3418	1796
UWM-B-00-120	71.90	81.90	2.17	3398	1808
UWM-B-00-120	71.80	81.80	2.14	3396	1756
UWM-B-00-120	72.50	82.50	2.18	3395	1752
UWM-B-00-120	72.80	82.80	2.15	3352	1758
UWM-B-05-120	72.00	82.00	2.15	3361	1715
UWM-B-05-120	73.70	83.70	2.18	3375	1762
UWM-B-05-120	72.70	82.70	2.16	3376	1756
UWM-B-05-120	73.50	83.50	2.16	3422	1773

Tab. A.7.: Elastic ultrasound waves of cylindrical specimens after 120 days of carbonation (curing method B).

A.5 Density variation after supercritical carbonation

Curing method A:

Specimen	Non-carbonated specimens [g/cm^3]						Average [g/cm^3]
A-00-00	1.98	1.99	1.99	1.99	1.99	2.00	1.99
A-05-00	1.96	1.90	1.93	1.92	1.91	1.95	1.93
A-15-00	1.98	1.98	1.97	1.97	1.97	1.97	1.97

Tab. A.8.: Density values of cylindrical specimens before 30 days of carbonation (curing method A)

Specimen	Carbonated specimens [g/cm^3]						Average [g/cm^3]
A-00-30	2.02	2.02	2.04	2.02	2.02	2.02	2.02
A-05-30	1.98	1.96	1.95	1.95	1.94	1.98	1.96
A-15-30	2.01	2.00	1.99	2.00	2.00	1.99	2.00

Tab. A.9.: Density values of cylindrical specimens after 30 days of carbonation (curing method A)

Specimen	Carbonated specimens [g]						Average [g]
A-00-30	3.77	2.34	3.89	2.65	2.33	1.35	2.72
A-05-30	1.64	5.16	1.87	2.81	2.49	2.82	2.80
A-15-30	2.04	1.69	1.93	2.55	2.42	2.25	2.14

Tab. A.10.: Mass uptake of cylindrical specimens after 30 days of carbonation (curing method A)

Specimen	Non-carbonated specimens [g/cm^3]						Average [g/cm^3]
A-00-00	1.93	1.94	1.97	1.96	1.96	1.96	1.95
A-05-00	1.92	1.91	1.91	1.92	1.92	-	1.92
A-15-00	1.92	1.91	1.93	-	1.96	-	1.93

Tab. A.11.: Density values of cylindrical specimens before 120 days of carbonation (curing method A)

Specimen	Carbonated specimens [g/cm^3]						Average [g/cm^3]
A-00-120	1.99	1.98	2.00	2.01	2.00	2.02	2.00
A-05-120	1.96	1.97	1.94	1.97	1.95	-	1.95
A-15-120	2.04	2.04	1.98	-	2.02	-	2.02

Tab. A.12.: Density values of cylindrical specimens after 120 days of carbonation (curing method A)

Specimen	Carbonated specimens [g]						Average [g]
A-00-120	5.14	3.34	2.13	4.78	4.08	4.61	4.06
A-05-120	3.23	4.29	2.68	3.72	2.67	-	3.32
A-15-120	9.96	11.54	3.98	-	4.72	-	7.55

Tab. A.13.: Mass uptake of cylindrical specimens after 120 days of carbonation (curing method A)

Curing method B:

Specimen	Non-carbonated specimens [g/cm^3]				Average [g/cm^3]
B-00-00	1.89	1.89	1.89	1.89	1.89
B-05-00	1.87	1.87	1.88	1.87	1.87

Tab. A.14.: Density values of cylindrical specimens before 30 days of carbonation (curing method B)

Specimen	Non-carbonated specimens [g/cm^3]				Average [g/cm^3]
B-00-30	2.14	2.15	2.13	2.15	2.13
B-05-30	2.12	2.13	2.12	2.09	2.11

Tab. A.15.: Density values of cylindrical specimens after 30 days of carbonation (curing method B)

Specimen	Carbonated specimens [g]				Average [g]
B-00-30	21.83	21.77	17.45	19.10	20.04
B-05-30	22.22	22.69	20.50	16.35	20.44

Tab. A.16.: Mass uptake of cylindrical specimens after 30 days of carbonation (curing method B)

Specimen	Non-carbonated specimens [g/cm^3]					Average [g/cm^3]
B-00-00	1.90	1.89	1.90	1.87	1.89	1.89
B-05-00	1.85	1.86	1.85	1.84	-	1.85

Tab. A.17.: Density values of cylindrical specimens before 120 days of carbonation (curing method B)

Specimen	Carbonated specimens [g/cm^3]					Average [g/cm^3]
B-00-120	2.15	2.15	2.16	2.14	2.15	2.15
B-05-120	2.15	2.18	2.16	2.16	-	2.16

Tab. A.18.: Density values of cylindrical specimens after 120 days of carbonation (curing method B)

Specimen	Carbonated specimens [g]					Average [g]
B-00-120	21.65	21.42	22.52	22.45	23.09	22.89
B-05-120	25.99	27.72	26.87	27.41	-	27.00

Tab. A.19.: Mass uptake of cylindrical specimens after 120 days of carbonation (curing method B)

A.6 Water Porosity

Specimen	Initial weight [g]	Final weight [g]	Porosity [%]
WP-00-00	5.3384	4.2616	40.14
WP-00-00	5.7614	4.6039	39.11
WP-00-00	6.2667	5.0075	39.99
WP-00-30-EXT	12.5262	10.7367	28.86
WP-00-30-EXT	7.3315	6.3512	30.10
WP-00-30-EXT	3.5056	3.0287	27.50

Tab. A.20.: Water porosity of PC samples (curing method A)

Specimen	Initial weight [g]	Final weight [g]	Porosity [%]
WP-05-00	3.1330	2.487	39.80
WP-05-00	3.2691	2.6043	39.25
WP-05-00	11.4102	9.1210	38.72
WP-05-30-EXT	17.3268	14.8900	27.28
WP-05-30-EXT	16.3251	14.0051	27.57
WP-05-30-EXT	15.6314	13.4467	27.11

Tab. A.21.: Water porosity of BNC05 samples (curing method A)

Specimen	Initial weight [g]	Final weight [g]	Porosity [%]
WP-15-00	6.2714	4.9622	41.13
WP-15-00	2.1447	1.6995	40.89
WP-15-00	9.2213	7.4925	36.93
WP-15-30-EXT	13.5827	11.8018	26.22
WP-15-30-EXT	15.2478	12.6216	34.45
WP-15-30-EXT	1.9907	1.6930	30.21

Tab. A.22.: Water porosity of BNC15 samples (curing method A)

Specimen	Initial weight [g]	Final weight [g]	Porosity [%]
WP-00-00	2.14	1.69	39.70
WP-00-00	3.40	2.65	41.70
WP-00-00	2.36	1.86	40.0
WP-00-00	3.59	2.85	39.00
WP-00-120-EXT	6.25	5.40	29.10
WP-00-120-EXT	6.94	6.02	28.40
WP-00-120-EXT	6.55	5.69	28.10
WP-00-120-EXT	8.11	7.05	28.00
WP-00-120-EXT	6.04	5.25	28.00
WP-00-120-EXT	4.47	3.88	28.20
WP-00-120-INT	7.15	6.19	28.70
WP-00-120-INT	7.33	6.30	30.10
WP-00-120-INT	7.79	6.70	29.90

Tab. A.23.: Water porosity of PC samples (curing method B)

Specimen	Initial weight [g]	Final weight [g]	Porosity [%]
WP-05-00	1.38	1.06	43.40
WP-05-00	1.19	0.92	42.40
WP-05-00	2.09	1.61	42.90
WP-05-00	3.22	2.50	41.80
WP-05-120-EXT	5.08	4.44	26.70
WP-05-120-EXT	5.50	4.75	28.90
WP-05-120-EXT	7.06	6.13	27.90
WP-05-120-EXT	3.50	3.06	26.70
WP-05-120-EXT	7.02	6.06	29.00
WP-05-120-EXT	4.71	4.07	28.80
WP-05-120-INT	4.16	3.54	31.60
WP-05-120-INT	4.53	3.92	28.50
WP-05-120-INT	3.85	3.31	29.70

Tab. A.24.: Water porosity of BNC05 samples (curing method B)